



HAL
open science

Modeling and characterization of mode coupling in next generation of few mode optical fibers

Carina Castiñeiras Carrero Castiñeiras

► To cite this version:

Carina Castiñeiras Carrero Castiñeiras. Modeling and characterization of mode coupling in next generation of few mode optical fibers. Optics / Photonics. Université de Lille, 2018. English. NNT : 2018LILUR030 . tel-04213062

HAL Id: tel-04213062

<https://theses.hal.science/tel-04213062>

Submitted on 21 Sep 2023

HAL is a multi-disciplinary open access archive for the deposit and dissemination of scientific research documents, whether they are published or not. The documents may come from teaching and research institutions in France or abroad, or from public or private research centers.

L'archive ouverte pluridisciplinaire **HAL**, est destinée au dépôt et à la diffusion de documents scientifiques de niveau recherche, publiés ou non, émanant des établissements d'enseignement et de recherche français ou étrangers, des laboratoires publics ou privés.

Université de Lille - sciences et technologies

Doctoral School **ED SMRE**

Science de la matière du rayonnement et de l'environnement

THESIS

Thesis defended by **Carina Castiñeiras**

In order to become Doctor from University of Lille

Academic Field **Physics**

Specialty **Diluted media and fundamental physics**

**Modeling and characterization of mode
coupling in next generation of few mode
optical fibers**

Thesis supervised by Yves Quiquempois and Laurent Bigot

Prepared in Laboratoire de physique des lasers, atomes et molécules (PhLAM)

Committee members

<i>Referees</i>	Monique Thual	<i>University of Rennes 1 – Foton Institute</i>
	Yann Frignac	<i>Télécom Sud Paris</i>
<i>Examiners</i>	Christian Simonneau	<i>Nokia Bell-Labs – Nozay France</i>
	Nathalie Rolland	<i>University of Lille</i>
<i>Supersivors</i>	Yves Quiquempois	<i>University of Lille</i>
	Laurent Bigot	<i>PhLAM Laboratory</i>
<i>Invited member</i>	Pierre Sillard	<i>Prysmian Group</i>

Université de Lille - sciences et technologies

École doctorale **ED SMRE**

Science de la matière du rayonnement et de l'environnement

THÈSE

Présentée et soutenue par **Carina Castiñeiras**

Pour obtenir le titre de Docteur de l'Université de Lille

Mention **Physique**

Spécialité **Milieus dilués et optique fondamentale**

Modélisation et caractérisation du couplage de modes dans la prochaine génération de fibres optiques légèrement multimode

Thèse dirigée par Yves Quiquempois et Laurent Bigot

Préparée au Laboratoire de Physique des Lasers, Atomes et Molécules (PhLAM)

Composition du jury

<i>Rapporteurs</i>	Monique Thual	<i>Université de Rennes 1 – Institut Foton</i>
	Yann Frignac	<i>Télécom Sud Paris</i>
<i>Examineurs</i>	Christian Simonneau	<i>Nokia Bell-Labs – Nozay France</i>
	Nathalie Rolland	<i>Université de Lille</i>
<i>Directeurs</i>	Yves Quiquempois	<i>Université de Lille</i>
	Laurent Bigot	<i>Laboratoire PhLAM</i>
<i>Membre invité</i>	Pierre Sillard	<i>Prysmian Group – Haisnes France</i>

ACKNOWLEDGEMENTS

First and foremost, I have to thank my research supervisors, Pierre Sillard, Yves Quinquenpois and Laurent Bigo. Without their assistance and dedicated involvement in every step throughout the process, this thesis would have never been accomplished. I would like to thank you very much for your support and understanding over these past four years.

Besides my advisors, I would like to thank the rest of my thesis committee: Dra. Monique Thual, Dr. Yann Frignac, Dra. Monique Thaul, Dr. Christian Simonneau, and Dra Nathalie Rolland, for their insightful comments and encouragement, but also for the interesting questions which incited me to widen my research from various perspectives.

I would like to thank all the members of Prysmian group and the photonique group of the IRCICA laboratory. I would like to thank Denis Molin, Benoit Seigny and Guillaume Le Cocq for the experimental and theoretical assistance they offered and the stimulating discussions. I sincerely thank Arno Mussot, Pierre Samsonetti, Francois Copie, Jean Paul Yehouessi, Assaad Baz, Julie Beauce Remi Habert, Le Rouge Antoine, Aurelie Paquet, Esben Ravn Andresen, Jean-Baptiste Trinel, Flavie Braud, Geraud Bouwmans, Rédha Kassi, Pierre Gouriou, Valentin Constance for their valuable discussions and suggestions.

Getting through my dissertation required more than academic support, and I have many, many people to thank for listening to and, at times, having to tolerate me over the past four years. I cannot begin to express my gratitude and appreciation for their friendship. Tomy Marest, Benjamin Samson, Romain, Karim, Viktor, Amanda Sprigmann, Sebastien Milleville, Laurie, Thiari Grecia Romero, Diana Garcia, Lecciones de viaje de Tito, Francis Abrante, Glenda Gonzalez, Melina Nunez, Ender, Anna Horcada, Ramon Salazar (Mi nano), Meraldo Velez (Mi portorro), Juan Navarro, have been unwavering in their personal and professional support during the time I spent at the University. For many memorable evenings out and in, I must thank everyone above as well as Xu Gang, Carlos Mas Arabi, Florent Bessin, Corentin Naveau and Patrick Bulot.

Last but not the least, I would like to thank my family: my parents, Angel, Fabi, BBgr, Primo Manolito, Tia Maruja, Prima Cleo, Charito, Kather, Jesus Manuel, Tia Q and Gonzalez family and for supporting me spiritually throughout writing this thesis and my my life in general.

ABSTRACT

Résumé : Les fibres optiques légèrement multimodes (FMF) sont une classe de fibres optiques multimodes. Dans le domaine de la télécommunication, chaque mode d'une FMF peut être utilisé comme un canal indépendant de transmission, ainsi, des débits bien supérieurs aux fibres optiques conventionnelles pourraient être atteints. Cependant, des problèmes inhérents à l'utilisation de ce type de fibre sont le couplage de mode et la dispersion de mode qui dégradent les performances de transmission. Cette thèse entre dans le cadre de l'étude du couplage de mode de différents profils de fibre. Ce travail se décompose en deux axes : i) la modélisation du couplage de mode qui est effectuée en considérant la fibre comme une concaténation de plusieurs segments courbés, dont chaque segment est associé à un rayon de courbure aléatoire. ii) La mesure du couplage localisé qui est basée sur la méthode expérimentale A-S2. À l'aide de ce modèle et de ces mesures, nous pouvons confirmer l'absence ou la présence de couplage d'une fibre exposée à des micro-courbures ou à une perturbation aléatoire.

Abstract: Few multimode fiber (FMF) is a class of multimode fiber. Each mode of a FMF is considered as an independent transmission channel in telecommunication field. Thus, much higher rates than conventional optical fibers could be achieved. However, this fiber can present the mode coupling and mode dispersion that can degrade the transmission performance. The mode coupling over different fiber profiles is studied in this thesis. This work is divided into two parts: i) the modeling of the mode coupling considering the fiber as a concatenation of several curved segments, and each piece is associated with a random bending radius R . ii) The measurement of localized coupling which is based on the experimental method A-S2. Using this model and these measurements, we can demonstrate the absence or the presence of coupling of a fiber exposed to micro-curvatures or a random perturbation.

TABLE OF CONTENTS

ACKNOWLEDGEMENTS	6
ABSTRACT	7
TABLE OF CONTENTS	8
ACRONYMS AND ABBREVIATIONS	12
LISTE OF FIGURES	14
INTRODUCTION	23
1 Generalities of the optical communication transmission	27
1.1 A brief history of optical fiber	27
1.2 Single mode fiber optical transmission system.....	31
1.2.1 Transmitter	32
1.2.2 Modulator	33
1.2.3 Receiver (coherent detection).....	37
1.2.4 Transmission	38
1.3 Physical transmission constraint in Single Mode Fiber	40
1.3.1 Linear effect	41
1.3.2 Nonlinear effects	45
1.4 How to increase capacity in optical communications systems	47
1.4.1 Wavelength division multiplexing (WDM)	47
1.4.2 Polarization division multiplexing (PDM).....	48
1.4.3 Compensation of linear impairments	49
1.5 Toward spatial division multiplexing (SDM)	50
1.5.1 Components used in core multiplexing and MDM.	52
1.5.2 Few modes fiber (FMF) and Multicore fiber on transmission	56
1.6 Summary	60

TABLE OF CONTENTS

2	Propagation in the Few Modes Fiber (FMF)	61
2.1	Propagation in Optical fiber	64
2.1.1	Homogeneous vector wave equations	65
2.1.2	Translation-invariant optical fiber	66
2.1.3	Modal vector equation	68
2.1.4	Scalar modes	73
2.1.5	Laguerre and Hermite modes (graded index profile)	78
2.2	Group velocities	80
2.3	Numerical method	81
2.4	Few modes fibers	81
2.4.1	Rayleigh scattering losses	82
2.4.2	Microbending losses	82
2.4.3	Macrobending losses	82
2.4.4	Design of trench on refractive index of FMF	83
2.5	Example GI FMF with trench	85
2.5.1	Study of trench depth	86
2.5.2	Impact of differential TD by the modification of the Δn_{eff}	87
2.5.3	Guided modes	89
2.5.4	Leaky modes	91
2.6	Summary	96
3	Coupled mode in the emerging MDM communication systems	97
3.1	State of the art	100
3.2	Coupled mode theory applied to FMF	103
3.2.1	Coupled modes theory	106
3.2.2	Ideal mode propagation applied to an FMF	111
3.3	Group delay operator	117
3.4	Principal modes (PM)	121

TABLE OF CONTENTS

3.5	Coupling regime.....	124
3.6	Study of 10-spatial-mode fibers with trench-assisted graded-index-core profiles ...	124
3.6.1	Validation of the tools	126
3.6.2	Group delay as a function of the curvature	127
3.6.3	Study of the group delay variation as a function of the distance	130
3.6.4	Influence of coupling regimes on the electrical field.....	134
3.7	Summary	137
4	Localized mode coupling measurement in FMF	139
4.1	A brief review of coupling measurement.....	139
4.1.1	Method for measuring the modal content of a fiber.....	139
4.1.2	Method for measuring the mode coupling	147
4.2	Advanced S2 and principal component analysis	148
4.3	Schematic representation of the localized coupling in a two-mode fiber	152
4.4	Experimental setup.....	158
4.5	Experimental setup for studying the localized coupling in a two-mode fiber	159
4.6	Modeling the localized perturbation (wire-mesh).....	162
4.7	Experimental result for s2 measurement.....	165
4.8	A-S2 from S2	166
4.9	Experimental result for A-s2 measurement	168
4.9.1	Effect of the weight on the optical fiber.....	169
4.9.2	A splice as localized perturbation	181
4.6-	Summary.....	184
5	CONCLUSION AND OUTLOOKS.....	185
	What are the limitations of our study?	187
	Recommendations for further research	187
6	APPENDIX.....	188
A.	Normalization	188

TABLE OF CONTENTS

B.	Shooting method.....	188
B.1.	Using the shooting method (Runge kutta 4) to find the radiation modes.....	189
B.2.	Using the shooting method to find the leaky modes	191
C.	Radiation modes	191
D.	Galerkin method.....	195
E.	MIMO-DSP in MDM transmission system.....	196
E.1.	MIMO-DSP complexity	200
E.2.	MIMO in weakly coupled.....	203
F.	DGD in stochastic differential equation	205
NOTATIONS.....		208
BIBLIOGRAPHY		211

ACRONYMS AND ABBREVIATIONS

CD	Chromatic Dispersion
CW	Continuous wave
DGD	Differential Group Delay
DMDG	Differential Mode Group Delays
DSF	Dispersion Shifted Fiber
DSP	Digital Signal Processing
EDFA	Erbium-Doped Fiber Amplifier
FMF	Few Mode Fiber
GD	Group Delay
GDS	Group Delay Spread
GI	Graded Index
HOM	Highest Order Modes
LP	Linearly Polarized
MCF	Multicore Fiber
MDM	Mode Division Multiplexing
MIMO	Multiple-input Multiple-output
MMF	Multimode Fiber
MPLC	Multi-Plane Light Conversion
NA	Numerical Aperture
NRZ	Non Return to Zero
PDG	Polarization Dependent Gain
PDL	Polarization Dependent Loss
PMD	Polarization Mode Dispersion
PSP	Principal State of Polarization
RZ	Return to Zero
SDM	Space Division Multiplexing
SE	Spectral Efficiency
SMF	Single Mode Fiber

ACRONYMS AND ABBREVIATIONS

SNR	Signal-to-Noise Ratio
TD	Time Delay
TE	Transverse Electric Modes
TM	Transverse Magnetic Modes
WDM	Wavelength Division Multiplexing
PM	Principal Modes
OAM	Orbital Angular Momentum
MG	Multi-Group

LISTE OF FIGURES

Figure 1-1: MMF system evolution	29
Figure 1-2: SMF system evolutions	30
Figure 1-3: Optical transmission system (top) and evolution of per channel bit rate as a function of years (bottom).....	31
Figure 1-4: Spontaneous and stimulated emission.....	32
Figure 1-5: Schematic of NRZ, RZ and duobinary codes.....	34
Figure 1-6: Schematic constellations of advanced multilevel modulation formats.	36
Figure 1-7: QPSK modulator.	36
Figure 1-8: Coherent receiver.	37
Figure 1-9: DSP and ADC configuration.....	38
Figure 1-10: Snell law in the optical fiber.....	39
Figure 1-11: Step index profile (SI) and graded index profile (GI) are the most well-known refractive index profile.	39
Figure 1-12: Effect of non-linearity over fiber capacity.	40
Figure 1-13: Attenuation as a function of wavelength (SMF).	41
Figure 1-14: PDM impact on the transmitted pulse.	44
Figure 1-15: Nonlinear Effect in the optical fiber. Stimulated Light Scattering, Stimulated Brillouin Scattering, Stimulated Raman Scattering, Nonlinear Phase Modulation (Self-Phase Modulation, Cross-Phase Modulation), and Four-Wave Mixing.....	46
Figure 1-16: Optical transmission system with WDM.....	48
Figure 1-17: Digital equalization with dual polarization.	49
Figure 1-18: Capacity limit for single mode fiber [Mizuno, 2017].	51
Figure 1-19: Fibers proposals based on SDM to achieve high spectral efficiency (HSE).....	52
Figure 1-20: Phase-plate based SMUX.....	54
Figure 1-21: Multiplexer for MCF.	54
Figure 1-22: Photonic lanterns	55
Figure 1-23: The waveguide is inscribed in 3-dimensional by a femto second laser.	55
Figure 1-24: 3-dimensional waveguide a) Left: SMUX for 7-core MCF and b) Right: SMUX for 6-mode FMF [Chen, 2014]......	56
Figure 1-25: Decreasing the DGD	57

LISTE OF FIGURES

Figure 1-26: Spectral efficiency between different technologies [Sillard, 2016]	58
Figure 2-1: Graded index profile $n(x,y)$ with variations only over the core.	61
Figure 2-2: Exemplary refractive graded index profile $n(x,y)$. The infinite parabolic profile used by the Laguerre-Gauss method.	63
Figure 2-3: Modes inside an optical fiber.	68
Figure 2-4: The intensity is represented by the shadow and direction of the vector field by the arrows (TE_{01} and TE_{02}).	72
Figure 2-5: The intensity is represented by the shadow and direction of the vector field by the arrows (TM_{01} and TM_{02}).	72
Figure 2-6: The intensity is represented by the shadow and direction of the vector field by the arrows. To be noted that HE_{11} odd and HE_{11} even are linearly polarized.....	73
Figure 2-7: Step index fiber with 2 LP modes (LP_{01} and spatial degenerate LP_{11}). LP_{11} mode is obtained by superimposing the vector mode pairs (TE_{01} , HE_{21}) or (TM_{01} , HE_{21}).	76
Figure 2-8: Normalized propagation constant vs normalized frequency for a) a step index. b) a graded index($\alpha=2$) obtained by numerical tools. The x-axis corresponds to the normalized frequency and the y-axis corresponds to the normalized propagation constant, $B=(n_{eff}^2 - n_2^2)/(n_1^2 - n_2^2)$ [Sillard,	77
Figure 2-9: a) Laguerre-Gaussian modes b) Hermite-Gaussian modes.	79
Figure 2-10: Normalized propagation constant vs normalized frequency for a graded index with 9 multi-group [Molin, 2016].	80
Figure 2-11: Refractive index with trench. r_1 is the length between $R=0$ and the end of the parabolic shape, r_2 is the length between $R=0$ and the beginning of the trench, r_3 is the radius distance between $R=0$ and the end of the trench. Δn_{eff1} is the differential refractive index of the parabolic shape, and Δn_{eff2} is the differential refractive index of the trench. w_1 is width after parabolic shape and before trench. w_2 is width of the trench.	84
Figure 2-12: Index profile difference for both profiles. Here, LP_{01} , LP_{11} , LP_{02} , LP_{21} , LP_{12} and LP_{31} correspond to six guided modes groups, the rest of the modes correspond to the leaky modes. It should be noted that the amount of leaky modes is different between both profiles. Note that the leaky modes appear at $\Delta n_{eff} < 0$, whereas the guided modes exist for $\Delta n_{eff} > 0$	86
Figure 2-13: Modeling of differential time delay as a function of trench depth for: a) $\Delta n_{eff}=2.1 \times 10^{-3}$ and b) $\Delta n_{eff}=3.3 \times 10^{-3}$	87
Figure 2-14: Time delay for each modes a) core radius= $14\mu m$ ($\Delta n_{eff}=2.1 \times 10^{-3}$) b) core radius= $11\mu m$ ($\Delta n_{eff}=3.3 \times 10^{-3}$). Here, we have grouped into 4 multi-group (MG) taking into	

LISTE OF FIGURES

account almost the same Δ_{neff} . Thus, LP01(MG1), LP11(MG2), LP02(MG3), LP21(MG3), LP12(MG4)	88
Figure 2-15: Maximum time delay for the different profiles of the table 2.1.	89
Figure 2-16: F(R) of the 6-LP modes with a-c) R=14 μm ($\Delta_{\text{neff}}=2.1\times 10^{-3}$) and b-d) R=11 μm ($\Delta_{\text{neff}}=3.3\times 10^{-3}$).....	90
Figure 2-17: Rayleigh losses in guided modes for the profile of the Fig. 2.12.....	91
Figure 2-18: Refractive index profile for a) $\Delta_{\text{neff}}=2.1\times 10^{-3}$ and b) $\Delta_{\text{neff}}=3.3\times 10^{-3}$	92
Figure 2-19: a-b) Intensity field of leaky modes for a) R=14 μm ($\Delta_{\text{neff}}=2.1\times 10^{-3}$) and b) R=11 μm ($\Delta_{\text{neff}}=3.3\times 10^{-3}$). c-d) Field Intensity of leaky modes for a) R=14 μm ($\Delta_{\text{neff}}=2.1\times 10^{-3}$) and b) R=11 μm ($\Delta_{\text{neff}}=3.3\times 10^{-3}$).....	93
Figure 2-20: Time delay for each leaky modes a) core radius=11 μm ($\Delta_{\text{neff}}=3.3\times 10^{-3}$), b) core radius=14 μm ($\Delta_{\text{neff}}=2.1\times 10^{-3}$).....	94
Figure 2-21: a-b) Leakage loss in leaky modes for both studied profile. c) (Rayleigh + Leakage) in leaky modes for the profile of the Fig. 2.12.	95
Figure 3-1: General scheme of a) MDM using an FMF with 2 LP modes. b) WDM using an SMF with 2 wavelengths (it was discussed in chapter 1). Here, a laser is used as transmitter divided into N number of modulators. Modulator encodes different data to obtain a modulated optical signal. A basis LP for example is multiplexed (M-MUX) and transmitted on FMF. At the end of the transmission, each mode is de-multiplexed (M-DEMUX) and detected by the photodiodes	98
Figure 3-2: Crosstalk in a) MDM using an FMF with 2 LP modes and b) WDM using an SMF with 2 wavelength.	99
Figure 3-3: Perturbation in the optical fiber. The dotted line corresponds to the unperturbed fiber, whereas the continuous corresponds to the perturbation. a) Splices b) perturbed core, c) tapered core.	100
Figure 3-4: Coupling model for FMF. b) Microbending in FMF can be modeled as a set of very small random radius (bends) in the fiber core.....	103
Figure 3-5: Gaussian distribution related with the inverse of bending for different standard deviation of curvature $\sigma 1/R$. The x-axis is the inverse of the bending (1/R) and the y-axis is the amplitude of the distribution.	104
Figure 3-6: Equivalence of a perturbed fiber. It describes the equivalent model of a bend fiber. In a bent fiber, the optical path followed by light is longer at the outside of the concavity than at the inside, meaning that the equivalent wavelength in the material is modified through the cross-section.	105

LISTE OF FIGURES

Figure 3-7: a-b) Coupling matrices and intensity of the electric field for a) straight fiber b) slightly perturbed fiber. c) Coupling matrices and intensity of the electric field for a perturbed fiber in x-axis. d) Coupling matrices and intensity of the electric field for a perturbed fiber in y-axis.	116
Figure 3-8: Group delay for a) straight fiber b) slightly perturbed fiber and c) perturbed fiber.	121
Figure 3-9: Evolution of group delay (delay) of the PMs as a function of standard deviation of the curvature for a trench-assisted 6-LP graded-index fiber of a) 13 μm core radius. b) 12 μm core radius c) 10 μm core radius. Here, a coupling model using ideal mode was considered. The bending radius follows a Gaussian distribution with the given standard deviation of the curvature. GD of PMs over 100 segments.	123
Figure 3-10: Group delay operator calculation	125
Figure 3-11: a-b) Evolution of group delay of the PM modes as a function of curvature (1/R).	128
Figure 3-12: a-b) Evolution of attenuation (guided PMs modes without leaky modes) as a function of curvature.	129
Figure 3-13: a-b) Evolution of attenuation (guided modes with leaky modes) as a function of curvature. To make the graph, a linear interpolation between the calculated points was realized.	129
Figure 3-14: The linear and square root behaviors in the coupling regime curve.	130
Figure 3-15: Max-Min GD as a function of the propagation distance for different coupling strengths $\sigma 1/R$ for 10-spatial-mode fibers with $\Delta n_{\text{eff}} = 2.4 \times 10^{-3}$	131
Figure 3-16: Max-Min GD as a function of the propagation distance for different coupling strengths $\sigma 1/R$ for 10-spatial-mode fibers with $\Delta n_{\text{eff}} = 4.4 \times 10^{-3}$	132
Figure 3-17: Max-Min GD as a function of Δn_{eff} for $\sigma 1/R = 10^{-20}$ and 10^2 and propagation distance of 1km and 1000km for 10-spatial-mode fibers.	133
Figure 3-18: Max-Min GD as a function of Δn_{eff} for $\sigma 1/R = 10^{-20}$ and 10 and propagation distance of 1km and 1000km for 10-spatial-mode fibers.	134
Figure 3-19: Evolution of electric field vector as a function of curvature for a) $\Delta n_{\text{eff}} = 2.1 \times 10^{-3}$	135
Figure 4-1: a) The correlated filter method scheme to obtain the modal content. [Flamm, 2012]. b Left) Phase-hologram (encoded phase modulation) example for the six first guided modes by using an SLM as correlation filter. Right) Modal analysis with HM content, a) measured near-field intensity by measuring of the power as intensity of the diffracted signal	

LISTE OF FIGURES

(red cross). b-g) Signal after correlation for the phase-hologram of figure-left. H) Measured modal power spectrum. Here, 60% of the total power is guided by HOM.	140
Figure 4-2: a- Left) The C2 imaging scheme to obtain the cross-correlation trace [Schimpf, 2011]. SLD: super luminescent diode. Right) Cross-correlation trace at one pixel of the images group. b- Left) Cross-correlation trace between the reference field and the output of the fiber by integrating over all pixels recorded by the camera. The peaks in the trace correspond to the two different modes (LP_{01} and LP_{02}) in the fiber.	142
Figure 4-3: Left) Example of an optical spectrum. Right) its Fourier transform with multiple beat frequencies [Nguyen, 2012]. These peaks correspond to each beats between the fundamental modes and each higher order modes.	143
Figure 4-4: Amplitude profile for a bi-mode fiber.	146
Figure 4-5: Schematic of the S2 imaging setup [Sévigny, 2015].	149
Figure 4-6: Beat resolution by the advanced S2 method.	152
Figure 4-7: a) Diagram of an unperturbed FMF. b) α beat corresponding to one interference between 2 paths.	153
Figure 4-8: Fourier transform of the optical spectra of an unperturbed 2 modes FMF.	154
Figure 4-9: a) Coupling diagram of a perturbed FMF. b) beats corresponding to six interferences between 4 paths.	155
Figure 4-10: Coupling diagram and coupling matrix of a perturbed FMF.	156
Figure 4-11: Fourier transform of the optical spectra of a perturbed 2 modes FMF.	157
Figure 4-12: a) Experimental setup. a) Localized coupling generated by an offset splice. b) localized coupling generated by a mesh grid and weights	161
Figure 4-13: a) Wire-mesh system. b) Fibers setting in the wire mesh: straight fiber (9.8cm), big loop (24cm) and small loop (12cm).	162
Figure 4-14: Modeling the grid of wire-mesh system.	163
Figure 4-15: Evolution of the amplitude of the modes as a function of standard deviation of curvature for perfect step index profile, and fiber length of 90mm. Perturbation is considered in Rx. a-b) Section number=30 and 45. LP_{01} and LP_{11}	165
Figure 4-16: Fourier transform of the optical spectra by S2 a) Left: without perturbation (0kg) b) Right: with perturbation (6kg).	166
Figure 4-17: a-b) Upper: Spatial and spectral eigenvectors (LP_{01} - LP_{11} beats) obtained by S2 and A-S2 analysis for uncoupled case. a) Lower-left: $LP_{01}+LP_{11e}$. b) Lower -right: $LP_{01}+LP_{11o}$	167

LISTE OF FIGURES

Figure 4-18: Spatial and spectral eigenvectors obtained by S2 and A-S2 analysis for the fiber A ($\Delta n \sim 15 \times 10^{-3}$). We use a wire-mesh with a weight of 8kg and a straight fiber position inside to the mesh. a) Left: LP01+LP11e. b) Right: LP01+LP11o.	169
Figure 4-19: Evolution of the beats and frequency spectra (μ , $\beta + \delta$ and α) as a function of the weight applied to fiber B.	170
Figure 4-20: a) Evolution of the amplitude of the peaks as a function of weight in S2. b) Evolution of the coupling coefficient as a function of weight.	171
Figure 4-21: a-b) Evolution of the amplitude of the peaks as a function of weight in A-S2 for LP01+LP11e (upper-left) and LP01+LP11o (upper-right). c-d) Evolution of the amplitude of the μ peak as function of weight in A-S2 for LP01+LP11e (lower-left) and LP01+LP11o (lower-right).	171
Figure 4-22: a-b) Evolution of the coupling coefficient deduced by equation 4.18 as a function of weight for eigenvectors LP01+LP11e (upper-left) and LP01+LP11o (upper-right).	172
Figure 4-23: a-b) Evolution of the eigenvalue as a function of weight, LP01+LP11e (lower-left) and LP01+LP11o (lower-right).	172
Figure 4-24: a) Evolution of the power in each mode as function of the weight (upper). b)-d) Evolution of the power in LP01 (lower-left), LP11e (lower-middle) and LP11o (lower-right) as function of the weight.	173
Figure 4-25: a) Evolution of the amplitude of the peaks as a function of weight in S2. b) Evolution of the coupling coefficient as a function of weight.	174
Figure 4-26: a-b) Evolution of the amplitude of the peaks as a function of weight in A-S2 for LP01+LP11e (upper-left) and LP01+LP11o (upper-right). c-d) Evolution of the coupling coefficient as a function of weight for eigenvectors LP01+LP11e (lower-left) and LP01+LP11o (lower-right).	174
Figure 4-27: Evolution of the power in each mode as function of the weight (mesh 3, radius of curvature of 98mm).	175
Figure 4-28: a) Evolution of the amplitude of the peaks as a function of weight in S2. b) Evolution of the coupling coefficient as a function of weight.	176
Figure 4-29: a-b) Evolution of the amplitude of the peaks as a function of weight in A-S2 for LP01+LP11e (upper-left) and LP01+LP11o (upper-right). c-d) Evolution of the coupling coefficient as a function of weight for eigenvectors LP01+LP11e (lower-left) and LP01+LP11o (lower-right).	176
Figure 4-30: Evolution of the power in each mode as a function of weight (mesh 3, length fiber).	177

LISTE OF FIGURES

Figure 4-31: a) Evolution of the amplitude of the peaks as a function of weight in S2. b) Evolution of the coupling coefficient as a function of weight. The experimental setup uses mesh 4.	178
Figure 4-32: a-b) Evolution of the amplitude of the peaks as a function of weight in A-S2 using mesh 4 for LP01+LP11e (upper-left) and LP01+LP11o (upper-right). c-d) Evolution of the coupling coefficient as function of weight for eigenvectors LP01+LP11e (lower-left) and LP01+LP11o (lower-right). The experimental setup uses mesh 4.	178
Figure 4-33: Evolution of the power in each mode as a function of weight. The experimental setup uses mesh 4.	178
Figure 4-34: a-b) Evolution of the amplitude of the peaks as a function of weight in A-S2 for LP01+LP11e (upper-left) and LP01+LP11o (upper-right). c-d) Evolution of the coupling coefficient as a function of weight for eigenvectors LP01+LP11e (lower-left) and LP01+LP11o (lower-right). The experimental setup uses mesh 1.	179
Figure 4-35: a-b) Evolution of the amplitude of the peaks as a function of weight in A-S2 for LP01+LP11e (upper-left) and LP01+LP11o (upper-right). c-d) Evolution of the coupling coefficient as a function of weight for eigenvectors LP01+LP11e (lower-left) and LP01+LP11o (lower-right). The experimental setup uses mesh 2.	180
Figure 4-36: Deformation as function of the wire diameter.	180
Figure 4-37: Localized perturbation by splice.	181
Figure 4-38: a-b) Evolution of the amplitude as function of the splice condition for LP01+LP11e (upper-left) and LP01+LP11o (upper-right). c-d) Evolution of the A_{μ}/A as function of the splice condition for LP01+LP11e (lower-left) and LP01+LP11o (lower-right).	182
Figure 6-1: $Z_{\nu}(R)$ of the 6-LP modes with $R=14\mu\text{m}$ $\nu=0$ b) field of the 6-LP modes with for $\Delta n_{\text{eff}}=-0.084$ for $R=14\mu\text{m}$	192
Figure 6-2.	194
Figure 6-3: a-h) $Z_{\nu}(R)$ and radiation field of 6-LP modes, $R=14\mu\text{m}$ and $\nu=0$ for different propagation constants.	194
Figure 6-4: a) $Z_{\mu}(R)$ and radiation field of 6-LP modes, for different radiation modes. B) Radiation field for higher modes.	194
Figure 6-5: MDM system using MIMO-DSP.	197
Figure 6-6: A simple MIMO Wiener system. Here, $T(\omega)$ is the transfer function of the propagation channel. $h^{-1}(t)$ represents the estimated inverse channel impulse response and $e(t)$ is the error. [Manolakis, 2005]	198

LISTE OF FIGURES

Figure 6-7: FIR filter for signal de-convolution.....	201
Figure 6-8: FIR filter for signal de-convolution.....	202

INTRODUCTION

Optical links provide an enormous bandwidth and the optical fiber is the only medium that can meet the communication capacity needs of our modern society. This demand of high bandwidth involved by applications like video on-demand, cloud computing, social network, online games amongst others is the mainstream of the constantly growing telecommunication market which in a way is a master piece of the economic activity of our societies.

Optical fibers used in communication systems are divided into two categories: Single Mode Fiber (SMF) for long and mid -haul communications (submarine and terrestrial solutions) and, Multi-Mode Fiber (MMF) mainly used in short distance communication (less than 1km), as is the case for the data-centers

Regardless of the efforts of improvements in long-haul optical communication equipment, researchers and industry are betting on new long distance fibers based on spatial division multiplexing, because these solutions could provide a higher capacity-distance product. The fibers developed in this context are known as few mode fiber (FMF) and multi-core fiber (MCF). As FMF supports multiple transmission modes in a single core, it is more attractive from an industrial point of view because the manufacturing methods are similar to the one developed for conventional fibers. FMF in Mode Division Multiplexing (MDM) operation could be a possible candidate to increase the transmission capacity for long-haul optical communication, and for satisfying the demand of short high capacity optical transmission links. Nevertheless, the elements must be adapted to these emergent optical fibers.

As conventional fibers, FMF capacity is restricted by linear and nonlinear effects. For MDM operations, the mode coupling and intermodal dispersion are the main parameters to control. The intermodal dispersion in FMF is produced when several modes propagate with different group velocities, arriving at the reception at different times. This time delay between the slowest and fastest modes produce a spreading of the optical pulses as they travel along the fiber and set a limit to the maximum achievable transmission distance without distortion, which is one of the problems to reach maximal rates. To quantify the intermodal dispersion, the parameter known as the Differential Mode Group Delays (DMGD) – the difference between the maximum and minimum time delay (group delay) in a given length of the optical fiber – is generally used. This effect obviously accumulates during the propagation.

Another impairment is the mode coupling that occurs because as light is guided by the different modes (or by the orthogonal combinations of these modes), it can be randomly exchanged along the fiber between the spatial channels, due to perturbations in the fiber. In some cases that will be introduced in the present thesis, the impact of this coupling is considered as a strong drawback and must be controlled.

By employing a multiple-input multiple-output (MIMO) equalization digital signal processing (DSP) at the receiver, mode dispersion and mode coupling can be mitigated. However, the complexity of the MIMO equalizer results in a quadratic growth with the number of spatial channels. For instance, for the optical fibers that support 10 spatial modes like the ones theoretically studied in this thesis, the size of the MIMO should be 20x20 if we consider the polarization, which is a 100 times larger than the ones used for SMFs (2x2). Additionally, the equalizer complexity can also be affected by long values of the DMGD. If we consider a 4x4 MIMO (two spatial mode and two polarizations), the equalization filter windows (or taps) needed to cover the time delay between two modes, has to be longer than the delay between these modes. Thus, this window can be reduced by controlling the coupling or by reducing the DMGD. Hence, the FMF design can be adapted to decrease the constraints on the MIMO equalizer or its complexity. As we will show in this thesis, a step refractive index profile can be adopted in order to reduce the coupling, whereas a graded refractive index profile can be used to reduce the DMGD. Moreover, we will see later that the highest capacity per distance is reached by using graded-index FMF. Consequently, we studied 10-mode fibers applying a coupled-mode model based on random perturbations to estimate the impact of different coupling regimes on the DMGD.

In a second part of this work, to validate our model, we developed an experimental method combining spatially and spectrally resolved images (S2) with a wire-mesh approach to produce different coupling states. S2 is a powerful technique that can measure the modal content and mode-coupling quantitatively in a simple experimental setup. Mode coupling in two types of 2-mode step-index fibers has been experimentally observed.

This thesis is organized as follows:

Chapter 1 focuses on the history of SMF and MMF and on the impairments and constraints associated to light transmission in SMF. Then, we will present the emergent optical fibers, called FMF and MCF that today appear as possible candidates to overcome the capacity limits of SMF.

In chapter 2, we will introduce the wave equations and the scalar wave equations from the Maxwell's equations and present the notion of optical modes, either vector modes and LP (Linearly Polarized) modes. Here, we will study two types of fiber with well-known refractive index profiles: the step-index and the graded-index profiles. For step-index profile, we will analytically obtain the eigenmodes whereas, for graded-index profiles, we will use a semi-analytical model based on the Laguerre-Gauss or Hermite-Gauss functions. Besides, we will include the notion of weakly-guided and radiative modes and will describe the different 6-LP modes fibers used in the simulation of Chapter 3.

In chapter 3, we will compare the main coupling-models and describe the multi-segment coupling model developed for the FMFs studied in this Thesis. Indeed, we will compute the group operator and find its eigenvectors that are the principal modes. The principal modes are potential candidates as data carriers instead of the conventional ones (especially the LP modes) as they are robust against modal dispersion. Besides, we will simulate six 10-spatial-mode fibers with trench-assisted graded-index-core profiles in order to study the dependences of the group delay on the fiber bending and length in different coupling regimes (weak and strong coupling). Finally, we will demonstrate that the fibers with a large difference of effective index between modes (Δn_{eff}) are more resilient to the strong-coupling.

In chapter 4, we will describe the different methods to measure the coupling, and will develop a method based on S2 imaging and the wire-mesh. Finally, we will prove that a 2-mode step-index fiber with a large index difference between modes (Δn_{eff}) does not present coupling under the conditions of the experiment.

1 Generalities of the optical communication transmission

This chapter will briefly review the fundamental capacity limit in the optical transmission using single mode and multimode fiber, and some proposal based on spatial division multiplexing (SDM) to overcome the capacity crunch of conventional systems. I will start by some general concepts and carry on with some of the emerging solutions (new optical fibers), as Few Mode Fiber (FMF).

1.1 A brief history of optical fiber

Our ancestors used smoke and fire to relay messages between cities separated by mountains. Such communication systems were limited in distance and not secured, because anyone could see the message, decipher it or worse intercept it and alter it. Throughout the years, the transmission of data was possible over radius (Marconi, 1901), copper cable and optics (1920), allowing to substitute the archaic communication systems and services by more sophisticated techniques, such as the telegraph (Morse, 1799), telephony (Graham Bell, 1876), television (Logie, 1925), the internet (ARPANET, 1960), cellphones (Cooper, 1973) and videoconference.

To date, optical communication systems reach a higher throughput than the others. This dates back to 1961 and 1964 when Elias Snitzer published a theoretical description of a fiber with a core so small that it could carry light with only one waveguide mode. Later, Dr. Charles Kao established that the light loss (10 or 20dB/km) can be reduced in a purer form of glass [ITU-T, 2009].

In 1970, Corning glass researchers invented an optical fiber with loss of 17dB/km at 633 nm by adding titanium into the fiber core. Two years later, this group invented a multimode germanium-doped fiber with a step index profile and 4dB/km of loss. Not satisfied with the low bandwidth of the multimode index fiber, researches concentrated on multi-mode fibers with a gradual refractive index increase between the core and the coating, and core diameters of 50 or 62.5 micrometers. In 1974, they succeeded in massive manufacturing of high quality optical fiber by the modified chemical vapor deposition MCVD [MacChesney and Bell Labs].

Generalities of the optical communication transmission

In 1977 in Long Beach, California and later in Chicago, the telephony company used fibers with loss around 2dB/km and GaAlAs laser diodes at 850 nm. Afterwards, an InGaAsP laser at 1300 nm was used and an improvement of fiber attenuation was reached as low as 0.5dB/km, likewise the dispersion of the pulse was reduced to 850 nm. At the beginning of the 1980s, the world networks began to use single-mode fiber at 1300 nm.

For years, researchers have worked on improving the single-mode fiber properties because it could transmit higher data rates over longer distances, especially at wavelengths of 1550nm, where the attenuation is lower. In 1985 the dispersion shifted Fiber (DSF) was introduced allowing the minimum attenuation in the 1550 nm window with zero dispersion at the same wavelength.

In the early 1990, the Erbium-doped fiber (EDFA) seemed to revolutionize the optical system thanks to the capability to amplify light and raise the speed limitation imposed for electronic regeneration. Likewise, it allowed the development of the wavelength division multiplexing (WDM) technique, currently used.

The deployment of these new technologies brought with it nonlinear effects in the transmission as a consequence of the extra power that the fiber had to carry through the use of several amplifiers with a larger number of wavelengths. One of the most damaging effects to appear is the four-wave mixing, because multiple wavelengths combine to create new wavelengths that can potentially interfere with the transmission. The effect is more noticeable when the dispersion is close to zero. Thereby, the development of the non-zero dispersion fiber industry (NZDSF) was a direct response to the non-linear effects of propagation. Later, the effective mode area was increased to reduce the nonlinear effects in the fiber design.

Even if studies on the Raman amplification started around the 1970', it was not industrially used before the development of suitable high power pumps. Since 2000, most of the submarine fiber-optic transmission systems (typically, above 800km) use Raman amplification.

In the 1980s, the coherent detection became more attractive, principally in a WDM configuration, because it enables higher spectral efficiency through electrical domain channel selectivity, compared to direct detection in the optical domain and it also allows a higher sensitivity. Finally this technique provides access to modulation schemes with more bits per symbols. However, the coherent detection is more complex to implement.

Generalities of the optical communication transmission

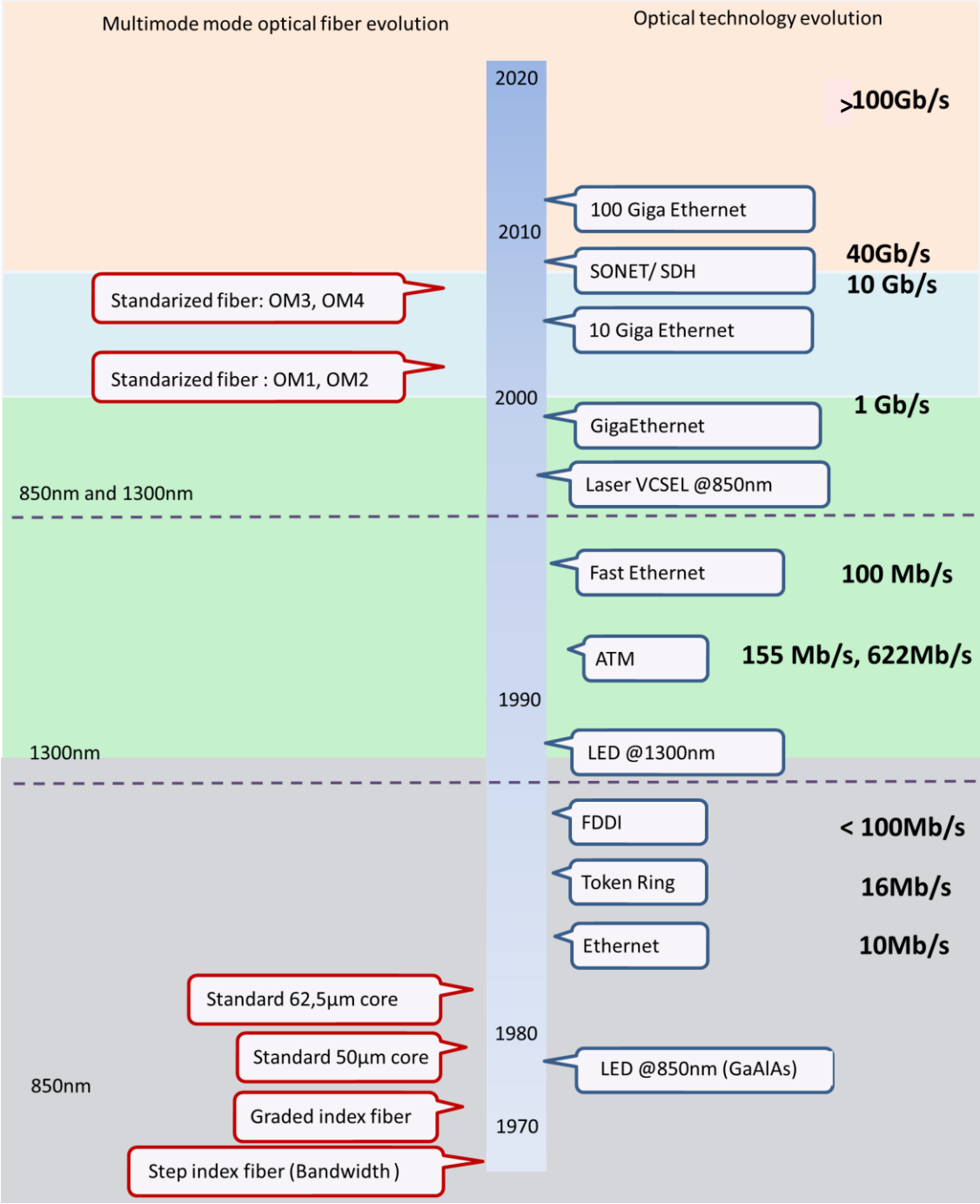


Figure 1-1: MMF system evolution. [ISO/IEC 11801, 2011] [IEC 60793-2-10, 2011]

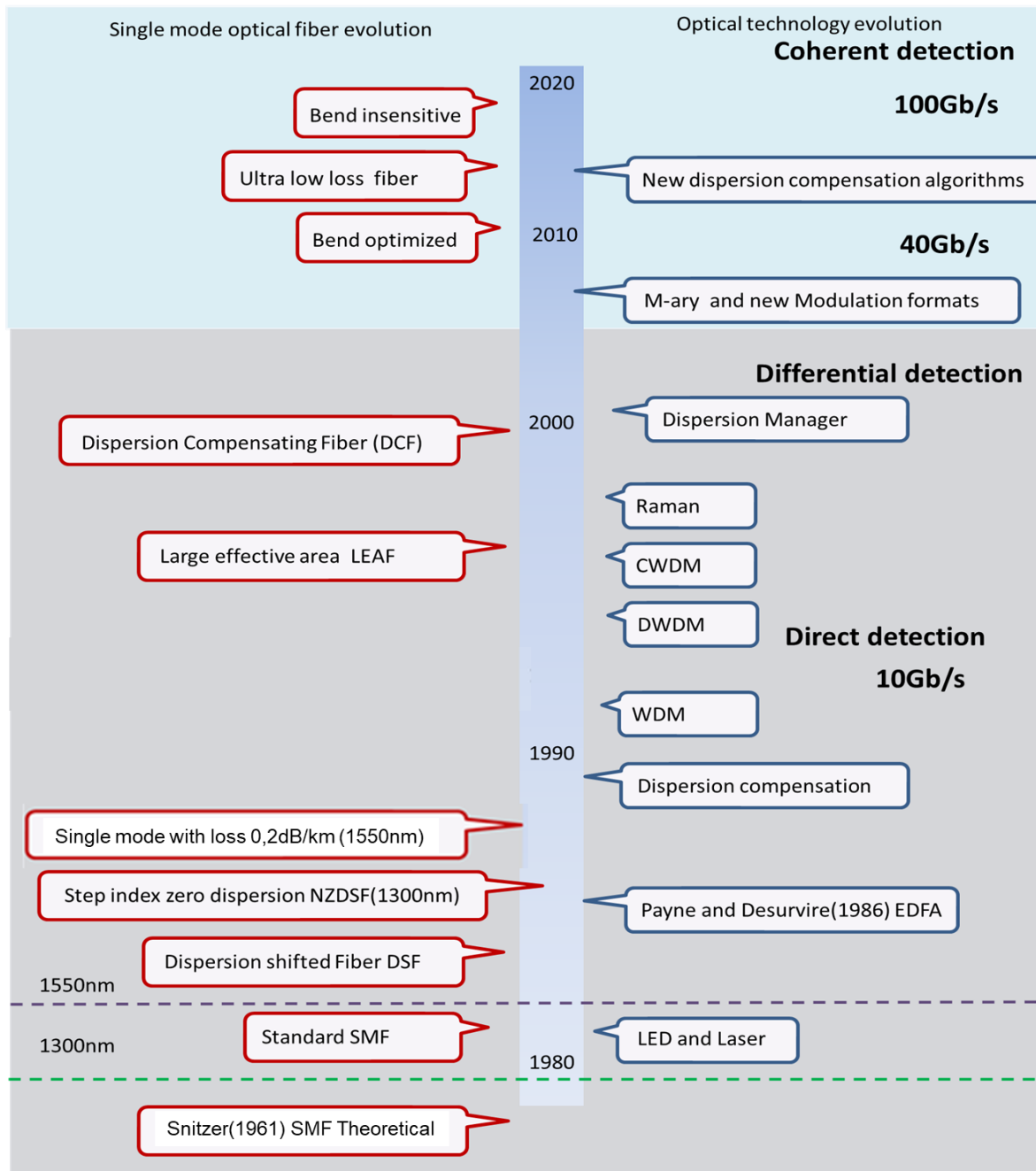


Figure 1-2: SMF system evolutions

Recently SMF fibers with ultra-low losses (losses less than 0.2dB/km) and low bends radii have been introduced on the optical network market especially for metro-access, FTTH/P networks (Local Area Network). Likewise, MMF has evolved on bend-insensitive fiber to enhance macro-bending performance and thus to eliminate the cable bending challenges of the installations (standards: OM3, OM4).

The fiber and optical technology evolutions is shown in the Fig. 1.1 and 1.2 for MMF and SMF fibers. Although the optical communication systems can have higher capacity (40 and 100 Gb/s), the new services and traffic requirements are reaching its limitation suggesting to the researchers the use of new technologies and fibers based on spatial division multiplexing (SDM).

1.2 Single mode fiber optical transmission system

A digital optical transmission system consists of a transmitter and a receiver connected between them by a single mode fiber (SMF). The transmitter converts binary data into a modulated optical signal with a particular bit rate ($\sim 100\text{Gb/s} +$) on a given wavelength channel. Once the signal is modulated, it is sent through an optical link, often composed of several spans of optical fiber cascaded with other optical elements (fiber optical, add-drop devices and amplifiers) in order to overcome the attenuation signal without optoelectronic signal regeneration. In the end, the receiver recovers the binary signal over long distances (more than 1000km) by using a digital signal processing (DSP) and error correction techniques. An overview of the optical transmission system and its bit rate evolution per channel is shown in Fig. 1.3.

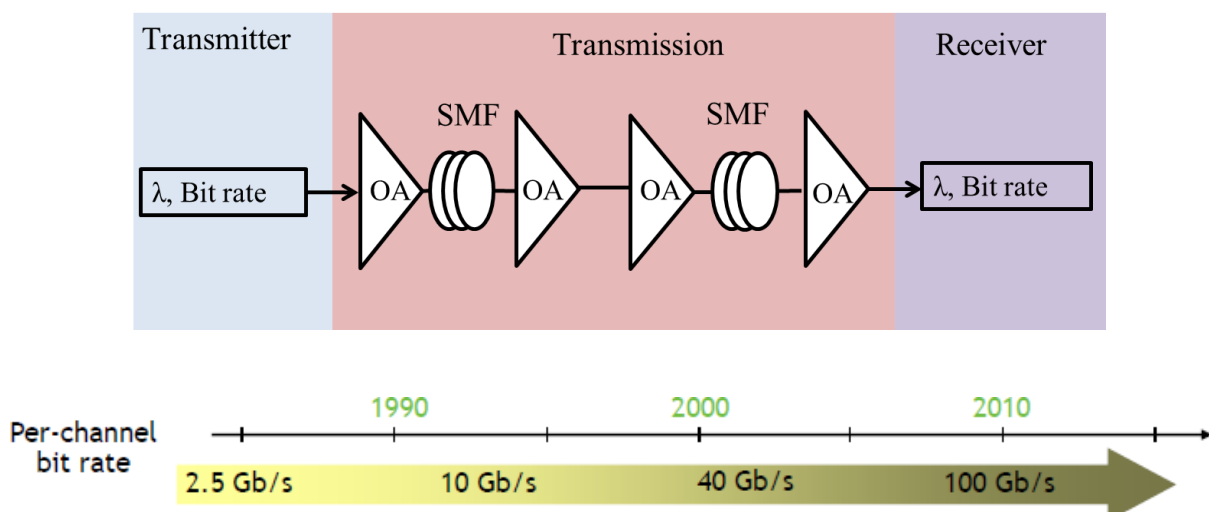


Figure 1-3: Optical transmission system (top) and evolution of per channel bit rate as a function of years (bottom)

1.2.1 Transmitter

An optical transmitter generates the optical signal using light-emitting diodes (LEDs) or LASERS. The generated optical light by LEDs or LASERS can be later modulated. The light generation depends on the recombination process in semiconductor materials; the light interacts with the material by absorption, spontaneous and stimulated emissions. Therefore, LED converts electrical energy in optical energy through the spontaneous emission resulting from spontaneous recombination of the excess carriers, whereas LASER does it by stimulated emission. These two different mechanisms of interaction between an atom and a photon for LED and LASER respectively are shown in Fig. 1.4. Here, $h\nu$ is photon energy and corresponds to the Planck constant (h) multiplied by the optical frequency (ν) which is proportional to the energy difference between the energy levels E_2 and E_1 .

More specifically, the spontaneous emission occurs when an electron drops from an excited state to ground state without any external mechanism. Lasers begin by spontaneous emission, and then work by stimulated emission. In stimulated emission, a photon interacts with an electron in excited state that drops to ground state to emit a photon coherent with the entrance photon.

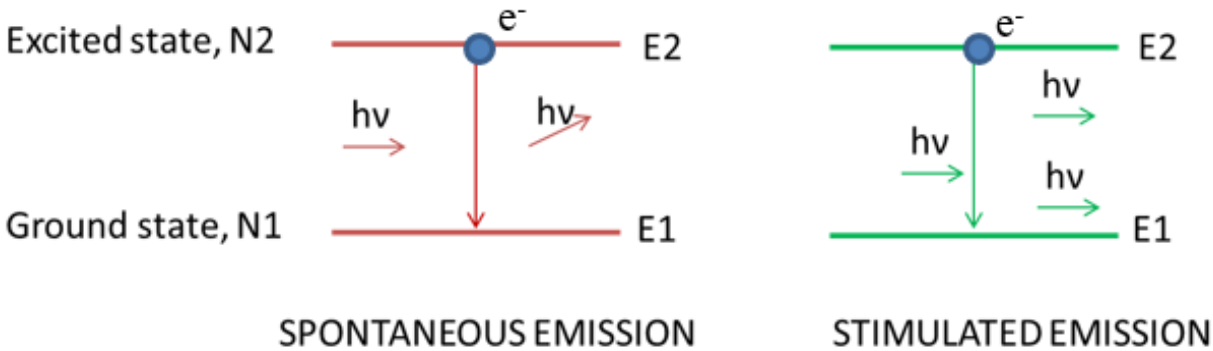


Figure 1-4: Spontaneous and stimulated emission.

One of the drawbacks of LED is that the emitted radiation is spontaneous and incoherent. LED have a spectral width of $\Delta\lambda = 50-60$ nm, with powers below $100 \mu\text{W}$ and

beam directivity lower than laser, making them impractical to use for long distance communications. Although the lasers are more complex devices than LED, their characteristics are the most used in communications at high speeds and long distances. The radiation is coherent which cause their spectral width to be much narrower and their directivity higher. As a matter of fact, they are 10 times more efficient than a LED (Pout~ 100 mW) [Djafar, 2001] and can be modulated directly at higher rates. In this way optical transmitters for long haul distance are based mostly on semiconductor lasers (VCSELs in the MMF case), and optical modulators.

Lasers can be divided into three main categories: continuous wave (CW), pulsed and ultrafast. The continuous-wave lasers produce a continuous beam of light, ideally with a very stable output power. A pulsed laser (produce pulses of 0.5 ns to 500 ns) is a system that will emit light in the form of optical pulses, rather than a continuous wave (CW). Ultrafast lasers are a special case of pulsed laser generally defined as lasers that produce pulses in the range of 5fs to 100ps.

For many applications, pulsed laser systems are advantageous compared to CW lasers, because they generate extremely high radiation intensities, even at moderate average laser power. However, the VCSELs (CW and Quantum-CW) or laser diode have a truly massive use throughout telecommunications and data storage (DVDs, CDs), because of the high beam quality and that they can be modulated with high frequencies.

Some transmitters implement a modulation stage to manipulate the output power in accordance to an input triggering signal. In the section below, the modulation will be presented.

1.2.2 Modulator

- **Modulation format**

Modulation makes the information signal more compatible with the medium (optical fiber). This process can be used to transmit coded information in binary format, because the optical fiber can recognize the absence or presence of light. In addition, the complex modulation format can increase the capacity. Thus, an optical communication system can have two modulations, the simple and complex modulation.

Generalities of the optical communication transmission

The first one is known as simple modulation because signal is directly proportional to the LED or laser response via amplitude modulation, and therefore the optical and electrical signal are modulated as a function of the transmitted data. Three types of base modulation are possible in optical communication systems: the format Return to Zero (RZ), Non Return to Zero (NRZ) and optical duobinary. In NRZ, a bit of logical value 1 (a pulse of light) changes its value from 1 (light) to 0 (no-light) or vice versa on a bit period. By contrast, the pulse of light in RZ is narrower than the bit period which allows less energy than a NRZ format (See Fig. 1.5). Like RZ, duobinary transmission are transmitted in a reduced bit period, and it can be understood as a multilevel transmission with phase encoded bits that are produced by adding one-bit-delayed data to the present data bit to give levels 0, 1, and 2.

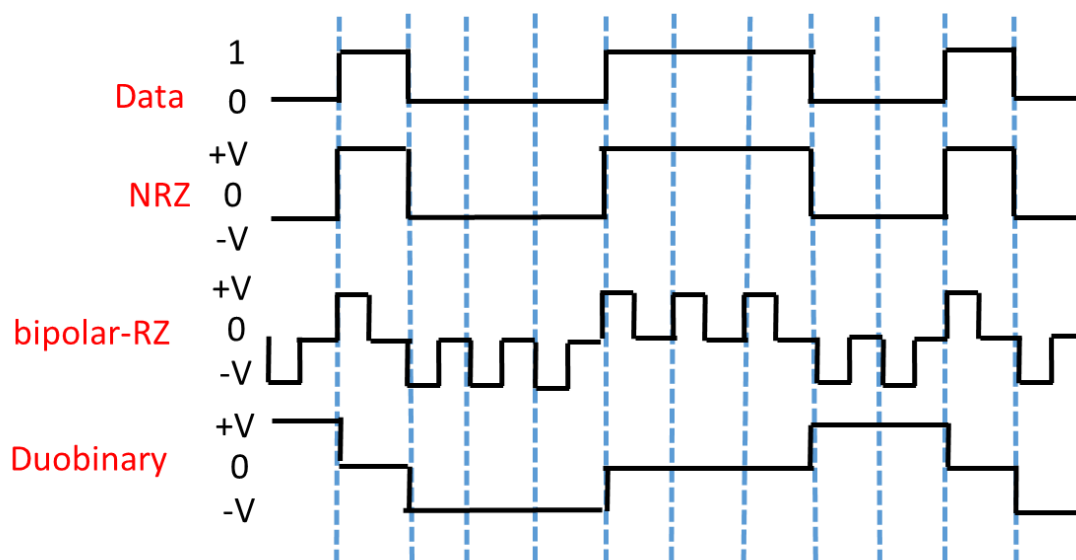


Figure 1-5: Schematic of NRZ, RZ and duobinary codes

Note that scheme signal in RZ does not need to send a separate clock along with the signal, because it has more transition than the NRZ. However, RZ signals involve a periodic return to a zero signal value and thus signal bandwidth is cut in half because half of the bandwidth is used to this return the signal to zero volts. That is, RZ decreases the symbol rate of the transmission.

In other words, as the data rate increases, the NRZ and RZ signals could gradually achieve the bandwidth limit, and the duobinary signals can be an appropriate alternative because of the efficient utilization of the bandwidth and the increase of the spectral efficiency. More specifically, [Phogat, 2013] demonstrated that on the simple modulations et at 10 Gbps, the duobinary is a much more resilient modulation format as compared to NRZ and RZ, because of its higher dispersion tolerance.

- **External modulation**

The first modulation format discussed above typically used the simplest modulation system called on-off keying (OOK), where the light beam is simply "turned on or off" depending on whether the information bit is a 1 or a 0 (binary information).

This type of modulation can be performed in two ways, by direct modulation or by external modulation. To avoid the frequency variation of the signal or chirp, an external modulation is recommended. The chirp is a phenomenon where the frequency and phase of the carrier of transmitted pulses varies with time generating a greater dispersion during its transmission. At speeds above 10 Gbps the chirp is so high that the direct modulation of semiconductor lasers is very seldom used [Agrawal, 2000].

In optical long-haul transmission systems, coherent continuous-wave lasers (CW) with external Mach–Zehnder modulators are used. These modulators are based on Mach–Zehnder interferometer between two waveguides with adjustable phase shifts. Consequently, an external electric field will generate changes in the refractive index of the material. Here, two cases are possible depending on the absence or presence of an external field. In the first case, the interference contributes constructively, because the optical field of the signal from the laser will have an equal phase change in the two arms. In the second case, the interference contributes destructively because the phase shift between the both arms can be equal to π .

- **High-order modulation for optical fiber transmission**

Even more sophisticated modulation schemes are used to increase the capacity by using multilevel modulation formats with $M=2^n$ bits per symbol. Thereby, we transmit more bits on an optical symbol by coding n bits through a sequence of 1 and 0. In this case, the amplitude and phase modulation can be used to obtain symbols with 2^n different forms.

Generalities of the optical communication transmission

Phase shift keying (PSK) modulates the optical signal by changing the phase of the signal. The PSK constellation symbols are positioned with uniform spacing around a circle and its performance decays as the number of symbols increases around the circle, because the effect of noise is more visible between each other due to their near position. To avoid that the symbols be located all around the circle, we can use the constellations based in quadrature and amplitude modulation (QAM) whose symbols can be more spaced. Here, the symbols in QAM can be distributed in amplitude and phase, by using I and Q orthogonal components separated 90 degrees between them (See Fig. 1.6).

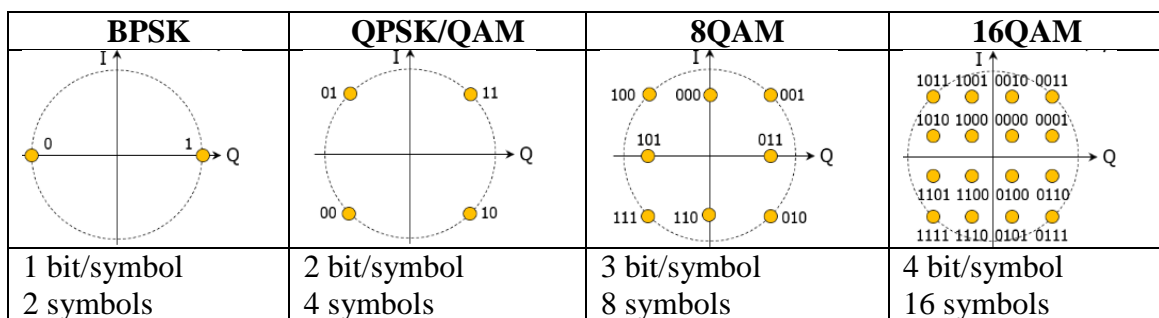


Figure 1-6: Schematic constellations of advanced multilevel modulation formats.

Figure 1.7 shows the block diagram of an optical transmitter adapted to QPSK modulation. In the transmitter, the laser signal is fed by the electrical signal current which allows to generate modulated light power. The transmission is ensured by the phase electrical-optical modulator MZM that allows the amplitude and phase modulation. Each MZM has 2 levels of voltage that give 2 points in the constellation; however one of the arms should be shifted in phase $\pi/2$ to allow moving the others points of constellation around 90° .

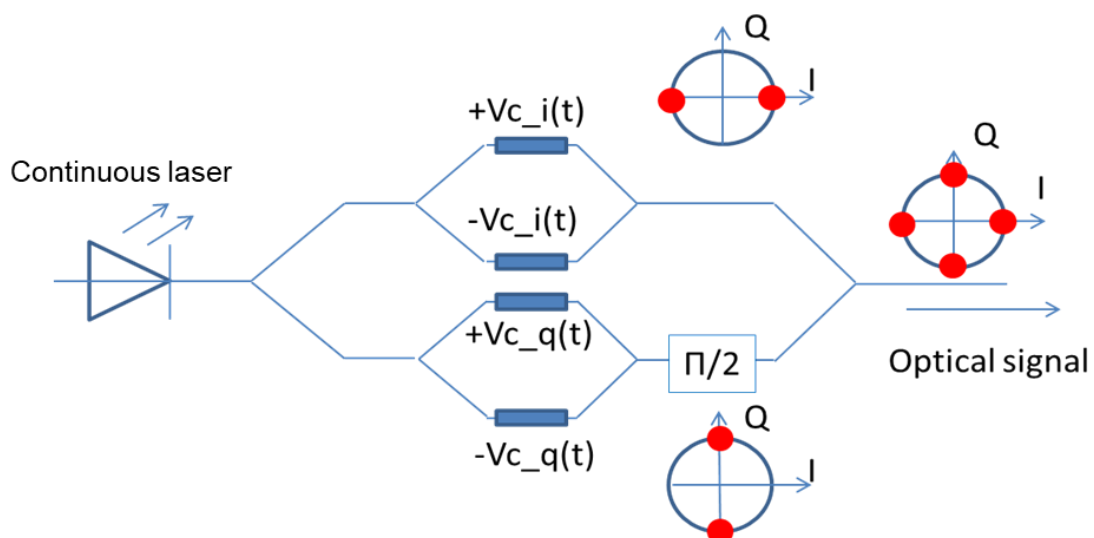


Figure 1-7: QPSK modulator.

1.2.3 Receiver (coherent detection)

At the reception, the optical signal is converted back into an electrical signal. The nature of the receiver depends on the modulation format. For example to detect modulated signal in OOK, it can be sufficient to use a simple photodiode, because it is not necessary to follow the signal phase. A photodiode gives only information about the intensity of the optical field making impossible the recovery of phase information, this modulation is well-known as direct modulation. However, sophisticated modulation schemes use coherent detections that allow the detection of the amplitude and phase of the incoming optical signal by using the polarization diversity receive. Such detectors use interferometric methods.

Figure 1.8 shows a coherent receiver scheme. Here, an optical input signal interferes with an unmodulated or laser local oscillator (LO) by using a coherent mixer. Note that each arm in the coherent mixer has a polarizer that is positioned to have the same field in the x and y axis. In addition, the wave-plate $\lambda/4$ produces a phase shift of $\pi/2$ only in the x-polarization. Thereby, polarization of the LO becomes circular, while the signal remains linearly polarized and its polarization angle is 45 with respect to the principal axis of polarization beam splitters. After passing through the half mirror, the Polarization Beam Splitter (PBS) separates the light into two orthogonal polarizations, while the interference and difference of phase between LO and the modulated signal are detected by the photodiodes PD1, PD2, PD3 and PD4.

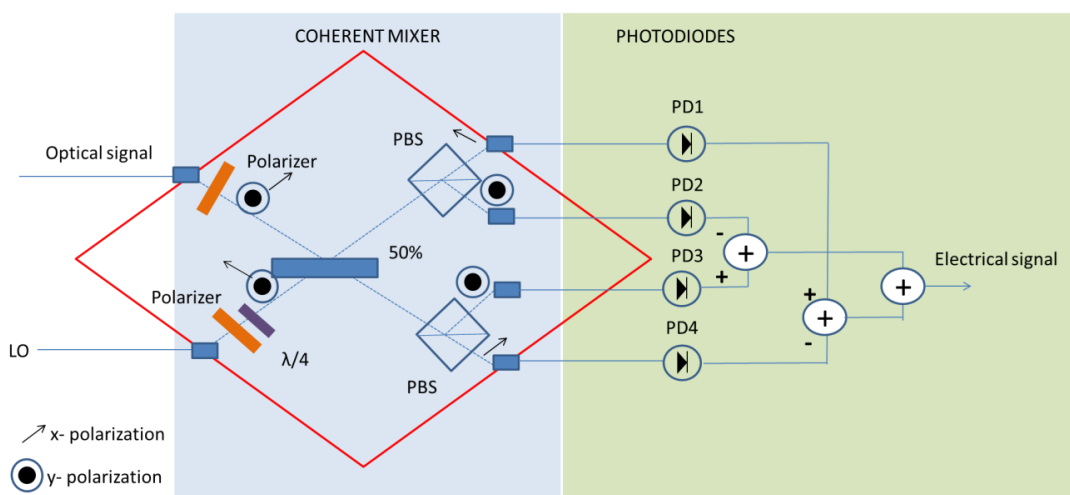


Figure 1-8: Coherent receiver.

Coherent detection together with Digital Signal Processing (DSP) technology is actually used to provide a solution to the detection problem of long-haul transmission systems [Ly-Gagnon, 2004]. Analog-to-digital conversion (ADC) and DSP compensate the imperfections of the coherent receiver and the other signal impairments coming from fiber propagation. Besides, coherent detection with DSP algorithms provides potential for superior receiver sensitivity. The common scheme of a DSP is shown in Fig. 1.9. Let's describe briefly each block.

CD compensation block is used to compensate the impairments produced by the chromatic dispersion (Section 1.3.1), clock recovery allows to correct the digital sampling error made by ADC. Polarization de-multiplexing block (Section 1.4) uses an algorithm to find principal of polarization. Phase and frequency recovery block corrects the phase and frequency difference between received signal and LO.

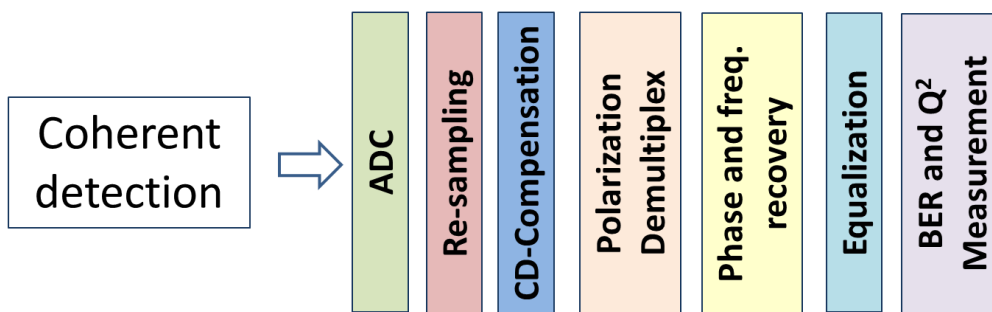


Figure 1-9: DSP and ADC configuration.

1.2.4 Transmission

- **Optical channel**

To explain the propagation inside the optical fiber, we will start by introducing the ray optic study (Snell law) by supposing that three layers of different refractive index materials can model the fiber. Snell law (equation 1.1) schematically explains how light behaves in the optical fiber. This behavior depends on the refractive index of the material, which is the ratio light velocity in vacuum and in the medium.

$$n_{air} \sin \theta = n_{core} \sin \theta_1 \quad (1.1)$$

To make sure to trap the light inside the core, the cladding refractive index (n_{cladding}) should be smaller than the core refractive index (n_{core}), and the light must be incident on an optical fiber with an angle of incidence smaller than the critical angle. Thereby, the critical angle must be only defined when $n_{\text{cladding}} / n_{\text{core}}$ is less than 1. To accept maximum incident light, we can measure how much light can be collected by an optical fiber through the numerical aperture (NA).

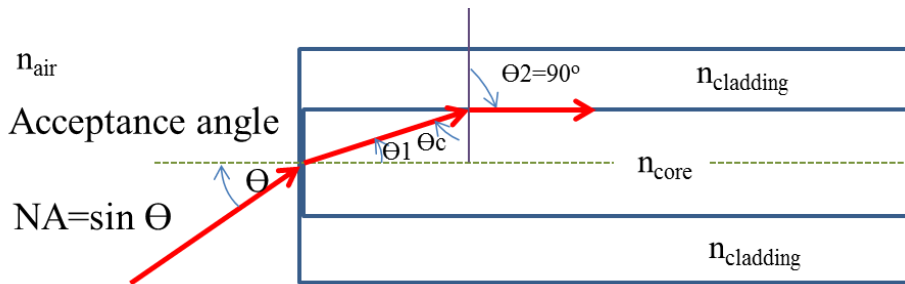


Figure 1-10: Snell law in the optical fiber.

The core refractive index profile is fundamental for light propagation and describes the radial change of the refractive index from the fiber to towards the cladding. Thus, the rays can be propagated as in a straight line or zig-zag, because the refractive index is homogenous in the core (step-index SI), or in parabolic form because the refractive index continually decreases from the fiber axis to the cladding (graded index GI).

According to the propagating modes, the optical fibers can be divided in single mode and multimode. In the former, one only mode should travel the length of the fiber. The number of modes of an optical fiber depends on its dimension and the variation of the refractive indices of both core and cladding across the cross section. This will be detailed in chapter 2.

Two classic profiles are shown in the Fig. 1.11.

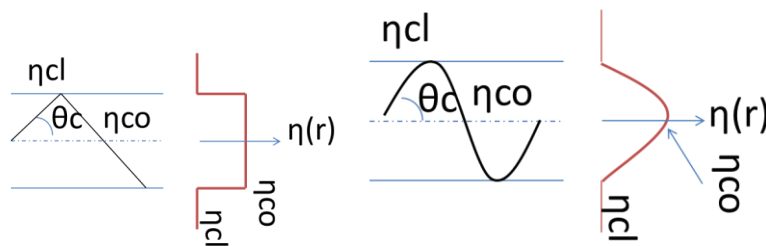


Figure 1-11: Step index profile (SI) and graded index profile (GI) are the most well-known refractive index profile.

1.3 Physical transmission constraint in Single Mode Fiber

Light is affected by the linear effects (chromatic dispersion (CD) and polarization mode dispersion (PMD)) that transform the signal linearly, or nonlinear effects (Kerr effect) as a result of the nonlinear behavior of the material.

The nonlinear effect represents one of the main reasons of the capacity limitation in long haul optical transmission system. In figure 1.11, the y axis represents the maximal channel capacity without error and the x axis the signal-to-noise ratio (SNR). According to the Shannon theory [Shannon, 1948], for a linear transmission system with a given SNR, the optical channel capacity is given $B \cdot \log_2(1+SNR)$ [bits/s] and the spectral efficiency (SE) by $\log_2(1+SNR)$ [bits/s/Hz] by dividing the channel capacity by spectral bandwidth B.

Figure 1.12 shows the capacity as a function of the SNR for an optical system. Here, the curve can be separated in one linear and one nonlinear part, the first one corresponding to the positive slope of the curve, where the capacity is only limited by the amount of amplified spontaneous emission noise [Tang, 2006] without the intervention of the non-linear effects. The second is the negative slope parts whose capacity deterioration is in large part due to the non-linear effects.

As an illustration, for a typical optical amplifier with a SNR of 40dB, we expect a theoretical limit for the capacity of 13 bits/s/Hz if the Kerr nonlinear effect is absent. However, for a given SNR the non-linear effects [Ellis, 2010] could appear and affect capacity nonlinearly, as is shown in the Fig. 1.12.

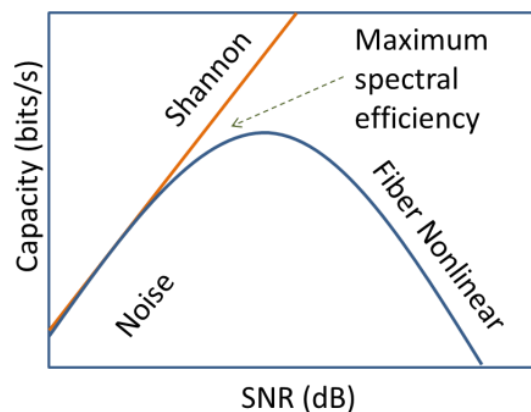


Figure 1-12: Effect of non-linearity over fiber capacity.

SE (bits/s/Hz) generally corresponds to the ratio between the channel bit rate and channel spacing. It is to be noted that the only way to increase the SNR is to increase the input optical power, but as input power increases, fibers cease to be a linear transmission media. That is, the nonlinear distortions are strongly dependent on the signal power. In this section, we will study the different effects that degrade the optical transmission performance.

1.3.1 Linear effect

- **Attenuation**

Attenuation (α) is the signal energy reduction during propagation. It varies as a function of wavelength (near infrared region). Typically, optical fibers work in the infrared region (850nm, 1300nm and 1550nm), however the lowest loss attenuation is found at 1550nm (less than 0.2dB/km [Agrawal, 2010]), as is shown in Fig. 1.13. In the end, this parameter will depend on the fiber length.

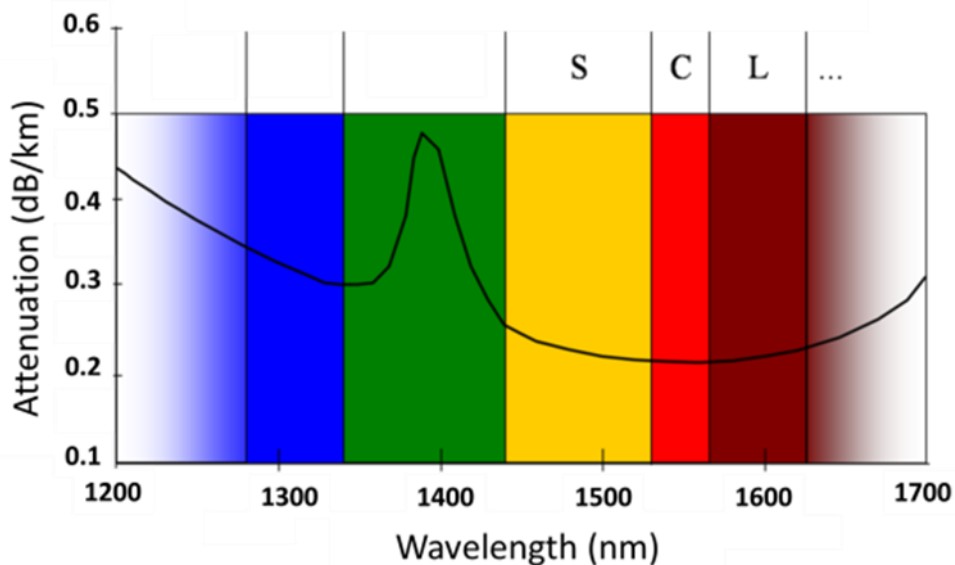


Figure 1-13: Attenuation as a function of wavelength (SMF).

To compensate the attenuation, current transmission systems use optical amplifiers (OA) without optoelectronic regeneration. However, all amplifiers degrade the signal-to-noise ratio (OSNR) of the amplified signal because a part of the amplification energy is naturally used to produce amplified spontaneous emission (ASE) during the amplification process. This OSNRs degradation is quantified by the noise figure (NF), which relates the input and output

signal-to-noise ratios of an amplifier. The ASE can be a dominant source of noise, because it is usually cumulative. It is an unwanted effect that limits the amplifier gain by increasing its noise level.

Erbium Doped Fiber Amplifiers (EDFA) and Raman amplifiers are the most popular amplifiers. EDFA are mostly used in terrestrial links and they work in the C-band (between 1530 and 1565 nm) and L-band. Raman amplifiers are most often used in submarine links.

- **Chromatic dispersion (CD)**

In bulk materials, chromatic dispersion is the signature of the dependence of the refractive indices of core and cladding on the wavelength. In optical waveguide, the dispersion may be due to the optical geometry and the material properties. To study the CD, we will consider the combination of both dispersion sources. To characterize this phenomenon, we can use the dispersion parameter D (See Eq.1.4). It can be described as the derivative of the inverse of group velocity with respect to the angular frequency, with a β_2 dispersion factor (ps^2/km) and is measured per unit length ($\text{ps}/(\text{nm}\cdot\text{km})$). The dispersion ($\text{ps}/(\text{nm}\cdot\text{km})$) is the propagation time difference that is observed around a kilometer of optical fiber between two spectral component spaced by 1nm.

$$v_g = \frac{\partial \omega}{\partial \beta} \quad (1.2)$$

$$\beta_2 = \frac{\partial \beta_1}{\partial \omega} = \frac{\partial \frac{1}{v_g}}{\partial \omega} \quad (1.3)$$

$$D = \frac{\partial \beta_1}{\partial \lambda} = -\frac{2\pi c}{\lambda^2} \beta_2 \quad (1.4)$$

The dispersion parameter is called normal when $D < 0$ ($\beta_2 > 0$), and anomalous when $D > 0$. The typical value D is approximately 17 $\text{ps}/(\text{nm}\cdot\text{km})$ for standard fiber at 1550nm.

Likewise, CD can become a cumulative effect along the propagation in all fiber sections and it can be reduced through special fiber sections with an opposite dispersion sign, called dispersion compensating fiber (DCF) or dispersion compensating module (DCM) for

terrestrial system. To compensate the accumulated dispersion, these modules are placed regularly along optical network. Their typical values are [-100; -50] ps/(nm/km) at 1550 nm.

- **Modal dispersion**

Modal or intermodal dispersion is produced in MMF as a result of the differences in the linear properties of the modes. Since the modes are generally not excited equally and they have different effective indices (n_{eff}), they can travel at different velocities producing a differential mode group delay (DMGD). Note that the modal dispersion can be quantified as the DMGD and it depends on the refractive index profile of the fiber. For instance, the modal dispersion can be minimized by using an optimum parabolic profile.

In the context of MM transmission, this effect could introduce a distortion of the signal that results in transmission errors. However, if the transmission distance is short, the modal dispersion effects could be almost negligible. In long haul transmission, the modal dispersion limits the transmission rate and it is all the more significant when the time symbol (T_s) is smaller than the propagation time difference between the fast and slow mode (τ_r). According to equation (1.5), the delay is proportional to the fiber transmission length. Here, $n_{g,max}$ is the group index which corresponds to the group velocity of the propagating mode.

$$\tau_r = \frac{L}{c} \cdot \Delta n_{g,max} = L \cdot DMGD \quad (1.5)$$

$$n_{g,mode} = \frac{c}{v_{g,mode}} = n_{eff,mode} + \omega \cdot \frac{\partial n_{eff,mode}}{\partial \omega} \quad (1.6)$$

Multimode dispersion does not occur if the waveguide allows only one mode to propagate ($\Delta n_{g,max}=0$).

- **Polarization mode dispersion (PMD)**

The speed of propagation of the light depends on the index of refraction of the optical fiber in the direction of oscillation of the electric field. For instance, if we consider a short

length of SMF and an index difference between the x and y directions, a wave that travel in the z direction can be decomposed into two waves having x and y electric fields. These waves propagate at slightly different speeds which lead to an accumulation of the optical phase shift and differential delay as a function of the distance. The optical fiber that presents this optical phase shift can be called birefringent.

Birefringence in the optical fiber can be produced by geometric imperfections (lack of symmetry) that lead to a core deformation making its form elliptical. Likewise, the differential group delay (DGD) is due to the dependence of the birefringence with the wavelength. PMD is defined as the average value of DGD and maybe responsible of output pulse broadening. In figure 1.14, Note that the optical fiber birefringence can cause a difference in the propagation time as a result of the different optical axes due to one polarization mode tending to travel faster than the other.

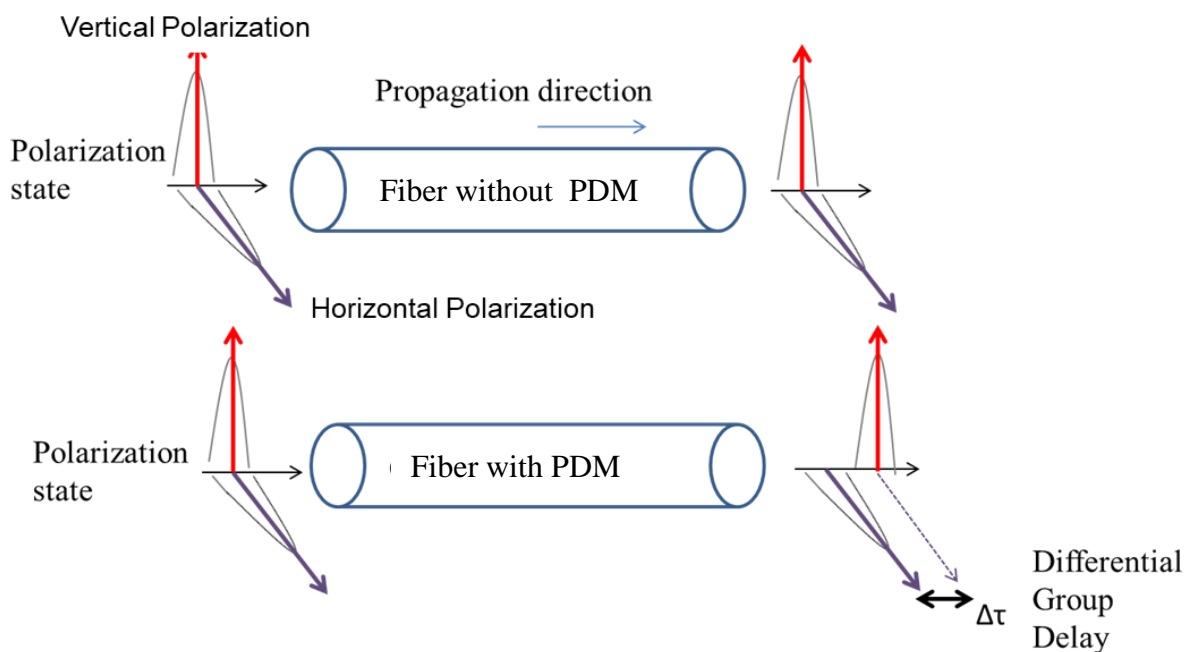


Figure 1-14: PMD impact on the transmitted pulse.

Birefringence can be modeled by dividing the optical fiber in several pieces, each piece having a random orientation axis whose evolution is time dependent. The propagation time differences between both polarization states are known as Differential Group Delay (DGD). The DGD is different along the fiber and has a stochastic nature, following a Maxwellian

distribution [Poole, 1991] for an instantaneous DGD. The PMD is the mean value of the DGD [Frignac, 2003].

$$PMD = \langle DGD \rangle \quad (1.7)$$

By coupling the polarization modes the mean DGD can be increased with the square root of the transmission length (\sqrt{L}).

$$PMD = PMD_{coeff} \cdot \sqrt{L} \quad (1.8)$$

The accumulated PMD is given in ps and its coefficient in ps/km^{0.5}. Typical PMD of a transmission fiber is today between 0.1 to 0.04 ps/km^{0.5}. Thereby, PMD limits the transmission distance to 10000 km (at 10Gb/s) and to 600km (at 40Gb/s). PMD is difficult to reduce, it is generally necessary to introduce an automatic feedback system in the context of direct detection receiver or a digital signal processing after coherent detection.

- **Polarization dependent loss (PDL) and polarization dependent gain (PDG)**

In PDL and PDG, the attenuation (or gain) depends on the polarization state. The difference between them is that PDL comes from the passive components and the PDG comes from saturated amplifier (EDFA) gain anisotropy. The combination of these effects produces time varying degradations. We can express PDL or PDG as the ratio between the maximum and the minimum losses (or gain) depending on the input polarization state. These effects cause OSNR variations, due to the power instabilities.

1.3.2 Nonlinear effects

The nonlinear optical effects are produced because all materials behave nonlinearly at high intensities and their refractive indices change with intensity [Friesem, 1989]. The nonlinear phenomena most relevant for optical system are summarized in Fig. 1.15.

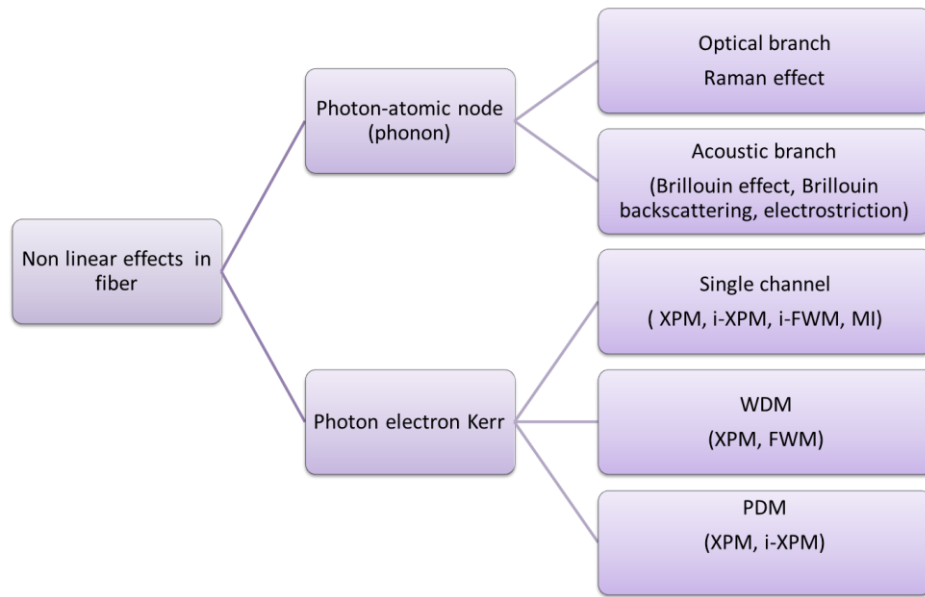


Figure 1-15: Nonlinear Effect in the optical fiber. Stimulated Light Scattering, Stimulated Brillouin Scattering, Stimulated Raman Scattering, Nonlinear Phase Modulation (Self-Phase Modulation, Cross-Phase Modulation), and Four-Wave Mixing.

However, we will not describe the Raman and Brillouin effects.

Instead, we will focus in particular on the Kerr effect distortions, because the capacity in an optical fiber is strongly affected by this effect. Kerr effect produces a change of refractive index of the medium (n) in proportion to the intensity (I). n_o and n_2 are linear and nonlinear refractive indices, whose typical values in the silica are $n_o \approx 1.5$ and $n_2 \approx 2.7 \cdot 10^{-20} \text{ m}^2/\text{W}$.

$$n = n_o + n_2 \cdot I \quad (1.9)$$

As a consequence the accumulated phase shift in the fiber can increase after a transmission distance L .

$$\phi = k n_o L + \phi_{NL} \quad (1.10)$$

Here, k is the free space wavenumber and ϕ_{NL} is a nonlinear phase shift. This phase shift depends on the optical signal power and the fiber nonlinear coefficient.

Kerr effect is usually decomposed into the Self-Phase Modulation (SPM), Cross-Phase Modulation (XPM) and Four-Wave Mixing (FWM). SPM leads to the frequency chirping of optical pulses as a consequence of the nonlinear phase shift accumulated in the fiber. The SPM-induced chirp affects the pulse shape and often generates additional pulse broadening. As a consequence it may aggravate the problems produced by the chromatic dispersion.

XPM is produced when two optical signals with different carrier wavelengths are propagated in the same fiber and one signal affects the phase of the others. This effect can be two times stronger than the SPM. XPM also affects the communication system that uses wavelength division multiplexing (WDM) technique to increase the capacity, because it mixes different optical signals modulated around different carrier wavelengths. Hence, if two or more optical channels have close wavelength and they are transmitted simultaneously, the intensity variations of a particular channel can produce a phase fluctuation over another channel. The nonlinear phase shift for a specific channel depends not only on the power of that channel but also on the power of other channels which implies that each WDM channel must have an adequate equalization.

Another effect is the four-wave mixing (FWM) which is considered as an inter-modulation phenomenon. FWM appears as result of the interactions between two wavelengths that produce two extra wavelengths in the signal. FWM can be generated, for example, between Raman pumps.

One way to mitigate the nonlinear effect is by dispersion management [Bigo, 2006], or DSP after coherent receiver.

1.4 How to increase capacity in optical communications systems

To increase the spectral efficiency, we can combine the multilevel modulation formats and the multiplexing technique. Higher order modulations with $M=2^n$ bits per symbol (QPSK, M-QAM) can increase significantly the transmission rate, but also limit the transmission performance due to the lower robustness to signals impairment or noise addition.

Some of the most typical multiplexing techniques are detailed hereafter.

1.4.1 Wavelength division multiplexing (WDM)

In WDM, each channel is modulated with a particular carrier wavelength (see Fig. 1.16) and then all channels are combined by optical multiplexer. The channels may have different phase or time shift before combination. By this technique, all channel bit rates are usually identical; hence the total throughput is the sum of the individual channel bit rates.

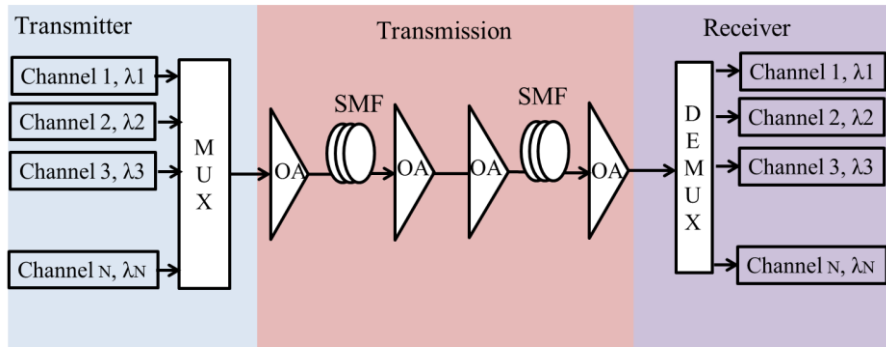


Figure 1-16: Optical transmission system with WDM.

Dense-WDM is used for long distance and is approximately limited to 80 wavelengths using 50GHz ITU-Grid in the C-band of EDFA, since the physical realization of DWDM networks requires accuracy for the wavelength selective devices. Incidentally, some non-linear effects can appear due to the wavelength proximity on certain channels, or by the use of the optical amplifiers to provide long transmission distances.

1.4.2 Polarization division multiplexing (PDM)

As we discussed in section 1.3.1, guided modes in SMF can exhibit degeneration in polarization, which allows to have two orthogonal polarization modes and to use them as independent channels with an effective half-symbolrate, maintaining the bit rate. Thereby, two independent signals can be sent on two orthogonal transverse polarization states and be recovered by separations of these polarizations. However, SMF can exhibit an unwanted birefringence which implies a time delay between the polarization components of the signal or a modification in the polarization state. This rotation of the polarization state should be corrected at the reception as well as the impact of the temporal translation of the symbols.

After the polarization recovery, the signals are treated in order to compensate the dispersion effect in the polarization by using MIMO (Multiple Input Multiple Output), presented in more details in section 1.4.3 and Appendix.

PDM can be exploited in combination with WDM to increase the capacity. It is also known as dual polarization (DP).

1.4.3 Compensation of linear impairments

The digital equalization for a dually polarized system is shown in Fig. 1.17. Note that a PBS divides the signal into two arbitrary and orthogonal signals with x-y polarization. Therefore, the incoming signals are first detected with phase and polarization diversity coherent receiver to obtain the full information of the optical signal and then are recovered in baseband modulated signal by using the dual-polarization optoelectronic downconverter. The outputs of polarization DEMUX and dual downconverters are connected to an anti-aliasing filters with impulse responses $p(t)$ correctly synchronized [Meyr, 1997]. Since the dual-polarization downconverters linearly recover the electric field, CD and PMD can be compensated in the electronic domain after photo-detection by using tunable analog filters. However, they are difficult to make adaptive, so the digital equalization is more advisable.

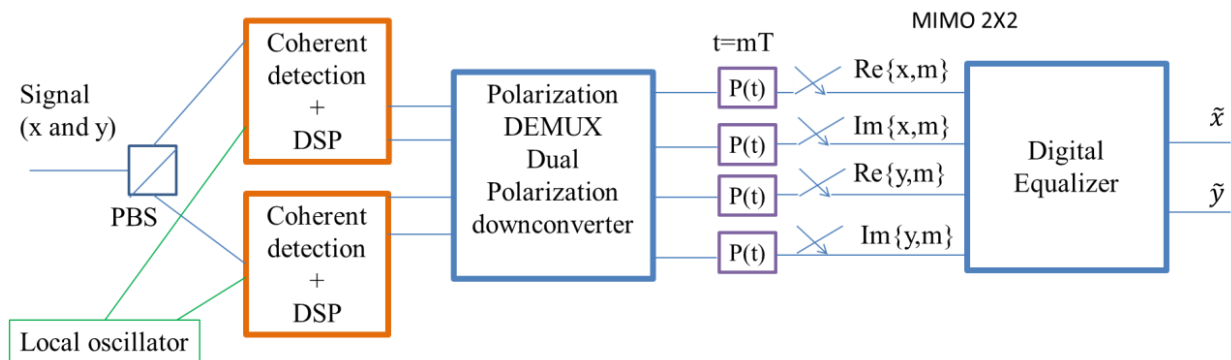


Figure 1-17: Digital equalization with dual polarization.

As discussed above, CD and PMD can be compensated in the electronic domain after detection by using digital equalization. At the output of the dual polarization receivers, it is possible to obtain information on the received electrical field, which permits compensation of distortion by linear filter. The two most known linear filters are infinite impulse response filter (IIR) and finite impulse response filter (FIR). IIR filter allows CD compensation [Goldfarb, 2007] and it has less cell numbers or taps, the taps number being associated to the impulse response system, but it can require very complex receiver due to the need to use the time-reversal filters. Thus, the equalization by FIR is more appropriate under DP coherent system.

In the digital equalizer phase are taken N samples to compute the minimum-mean-square error (MMSE) estimates. Later, the error is obtained in the absence of other channel effects, and this value is used in the mean-square error (MSE) matrix associated with equalizer in order to find the optimized equalizer matrix by using one of the two algorithms: the least mean square (LMS) or recursive least squares (RLS) [Widrow, 1985].

This block is also called MIMO 2x2, the number 2 is associated to two input data series and two output data series. In this case each FIR has $2n$ taps for symbol, because the impulse response is measured as $n.T_s$, where T_s is symbol duration. This technique is also used in MMF.

1.5 Toward spatial division multiplexing (SDM)

Capacity demand in the optical communication is ever growing owing to the increase in the number of customers and new services [Essiambre 2009]. As we have seen in the section 1.4, despite the effort to overcome the limits in the single-mode fiber, the SE maximum and capacity seem to be insufficient to cover the new requirements of optical networks. As we described above, the design of SMF did not evolve and their main problems are the nonlinearity effects (as Kerr effect), which have prevented a greater capacity, regardless of the efforts in reducing the losses, in finding an appropriate modulation format of higher order, in increasing the OSNR, in increasing the WDM channels number or by combination of all the above. To date, the highest SE reported is 15.3bit/s/Hz [Beppu, 2014] by using the combination of a high modulations format 2048-QAM (2^{11} or 11(bit/s/Hz)) and Polarization Division Multiplexing (PDM), but over a distance of 150 km.

Independently of the metric used, the SMF communication systems may not be sufficient to satisfy the future demands (See Fig. 1.18), as it has been demonstrated in several experiments [Sano, 2012], [Qian, 2011]. One of the solutions could be to install additional optical fibers, but the installation cost will also involve the cost of the optical system communication equipment, resulting in a deployment without decreasing the cost per bit transmitted that is prohibitive for the current market, because this cost per bit has declined and continue to do so. Research, laboratories and industries are finding new strategies to increase the capacity by considering a reduction of cost and consumption per bit. One of the proposals consists in using fibers based on Space Division Multiplexing (SDM).

Generalities of the optical communication transmission

SDM can be technically viable due to advances in accurate fabrication methods and design of the optical fiber. SDM is another technique of multiplexing and it uses a multiplicity of space channels to increase the capacity at the expense of a change in the conventional infrastructure that could increase the cost of the installation but with the advantage of covering future capacity demands on the long term without adding new optical fibers (SMF) and elements to the system. The SDM communication system has been made possible by the coherent detection technologies supported by digital signal processing because they can enable multiple inputs and multiple outputs processing (MIMO). Thus, the capacity increase given by SDM system has been demonstrated in laboratory and commercial environment.

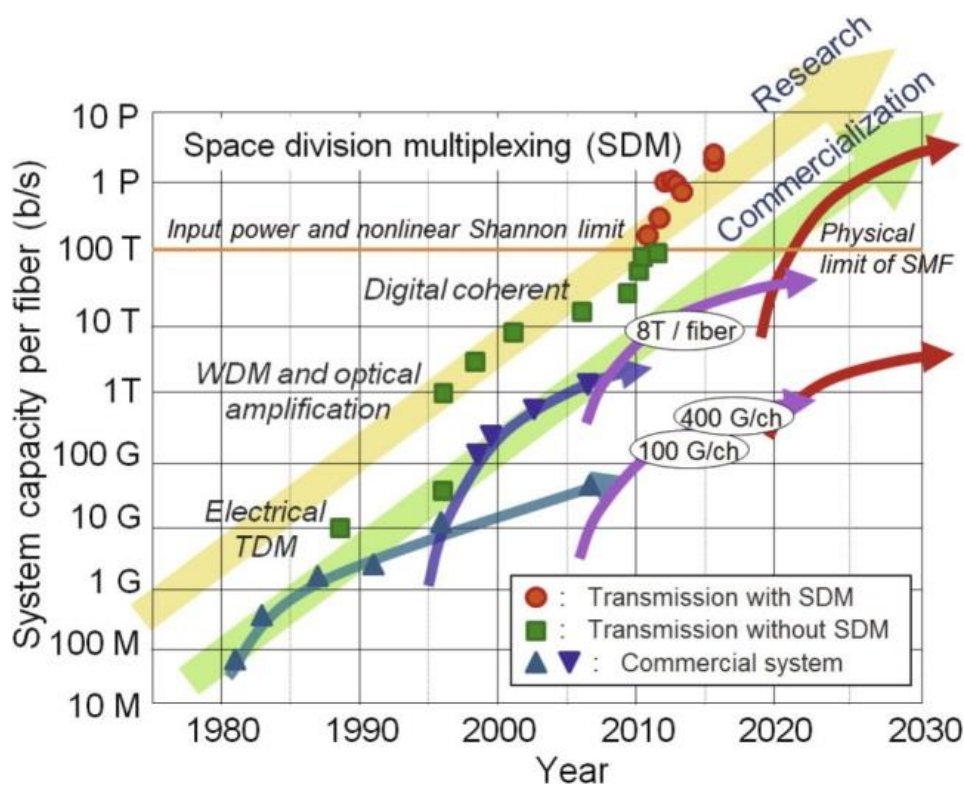


Figure 1-18: Capacity limit for single mode fiber [Mizuno, 2017].

In SDM, many fibers have been proposed to support SDM transmission in optical networks [Richardson, 2013][Zhu, 2013][Bai, 2013], but the most typical fibers to reach high spectral efficiency are multi-core fiber (MCF) and Few-mode fibers (FMF) or the combination of both (see Fig. 1.19). In this section, we will concentrate mainly on FMF.

In the following, we use the term core multiplexing for MCF and mode division multiplexing (MDM) for FMF.

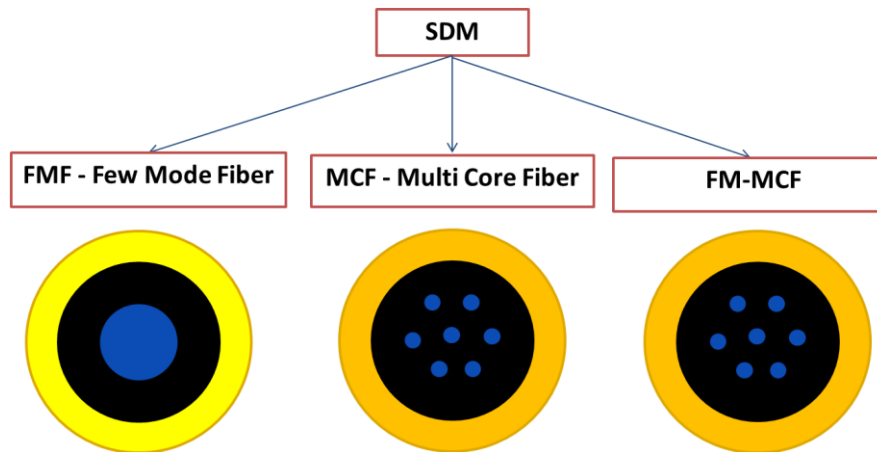


Figure 1-19: Fibers proposals based on SDM to achieve high spectral efficiency (HSE).

1.5.1 Components used in core multiplexing and MDM.

The commercial implementation of SDM could be a challenge, especially in the amplification phase and digital signal processing.

In the first case, the conventional optical amplifiers can hardly ensure similar gain between each spatial mode (FMF) or each core (MCF) and therefore we need to take into account each mode or core separately, and then amplify each of them individually. In the case of FMF, multimode amplifiers have received broad acceptance by the scientific community by using and adapting the conventional methods of amplification based on Erbium doped fiber (FM-EDFA [Bai, 2011], [Le Coq, 2012], [Ono, 2015] and FM-Raman [Weng, 2016]). Likewise, the MCF amplifiers have been studied on the EDFA and Raman amplification: MCF-EDFA and MCF-Raman [Krummrich, 2012].

In both cases, the signal can deteriorate because of crosstalk from the inter-channel coupling, the distortion caused by CD and the accumulated differential mode group delay (DMGD). To compensate them, the frequency domain equalizers are used (MIMO-Multiple Input Multiple Output) and the DSP [van Uden, 2013] [Arik, 2014]. MIMO-DSP uses algorithms that allow tracking fast changes of the channel, even though it can become difficult over large accumulated DMGD, since a large accumulated DMGD requires a large number of training blocks and taps which increases the equalizer complexity. MIMO also depends on the number of the modes or core [Inan, 2012]. In FMF, these equalizers are well-known as uncoupled-MIMO or coupled DSP-MIMO.

For a DSP-MDM with N modes, the MIMO would need to be scaled to $2N \times 2N$, or $2N^2$ adaptive filters (FIR), and $4N$ adaptive filters (FIR) for uncoupled-MIMO. Although the uncoupled-MIMO seems less complex, scalability could be compromised by the increased of the number of modes and by the use of PDM. Uncoupled-MIMO is not able to compensate the DMGD and mode crosstalk completely. In other words, the propagation speed difference between each polarization state would generate a progressive delay that will allow the coupling of information, this phenomenon is generally compensated by the equalization. Thus, DSP-MIMO even if more complex is suitable to compensate DMGD and mode crosstalk, by taking into account the length of the impulse response spread since it must be shorter than the equalization filter length. In both cases, each propagation mode is seen as an independent transmission channel.

Besides, we need to consider the design of the passive components to ensure the transmission by core multiplexing or MDM. Here, we will mention the multiplexer and de-multiplexer, called MUX. However, regardless of the passive components, they must be designed to ensure low insertion loss, low core or mode dependent loss, low crosstalk among modes or cores and wide bandwidth to authorize wavelength division multiplexing techniques on SDM signals.

Many multiplexer and de-multiplexer for FMF and MCF have been proposed: bulk free-space (FMF and MCF), optical photonic lanterns (FMF), photonic integration technology (FMF), 3-dimensional waveguide (3DW) (FMF and MCF), multi-core fiber coupler and fiber-based couplers (FMF and MCF).

The bulk free-space optics use thin glass plates or phase plates with prescribed spatial distributions of phase to generate a spatial modulation and excite a given mode of the FMF [Igarashi, 2014]. To multiplex N spatial modes, it is necessary to have $N-1$ lossy beam combiners (See Fig. 1.20), which leads to high insertion loss. It occupies more space and it could present problems inherent to the manufacturing defects of the phase plates. However, it has been used in seven cores of an MCF [Tottori, 2012].

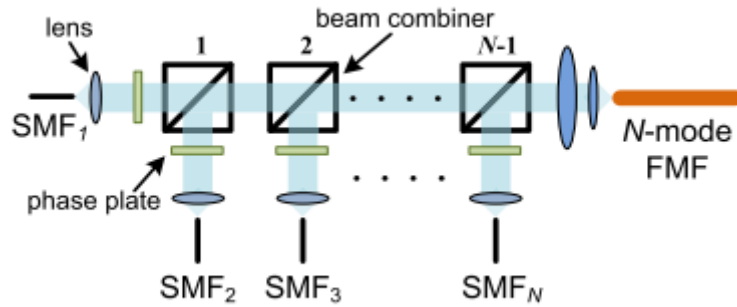


Figure 1-20: Phase-plate based SMUX

Besides, some multiplexer and de-multiplexer for MCF use the fan-in/fan-out components. Basically, they are composed of different SMF, whose core is fused and tapered, and spliced to an MCF [Zhu, 2011] (See Fig. 1.21). The limitation is in the end of the fan-in/fan-out of the MCF, since the arrangement of the SMF has to be as similar as possible to that of the line MCF. There is also MUX fan-in/fan-out which uses free space optics [Tottori, 2014].

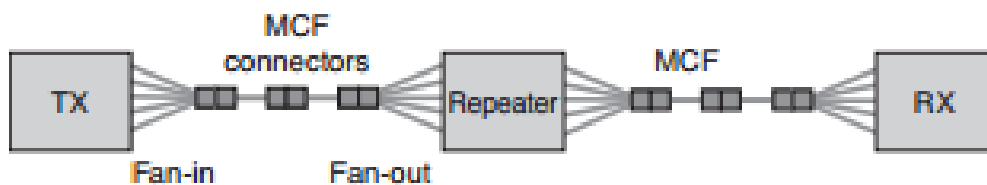


Figure 1-21: Multiplexer for MCF.

One of the most promising proposals for SMUX is the photonic lantern. They are fibers that use the adiabatic conversion from a multimode fiber to a series of single-mode fibers or vice versa (See Fig. 1.22). Photonic lantern can be all-fiber technology manufactured [Leon-Saval, 2014] and 3D waveguide technology [Gross, 2014]. To date, [Ryf, 2014] has demonstrated experimentally the use of the SMUX with 3 modes FMF.

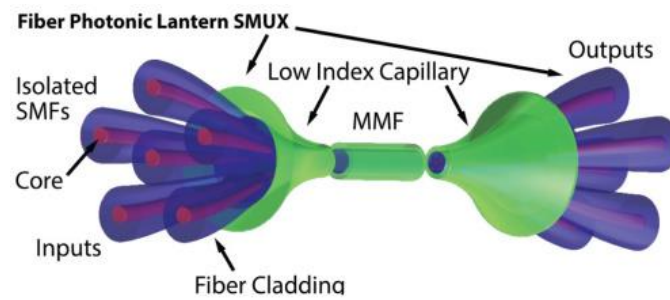


Figure 1-22: Photonic lanterns

The cheapest and most compact MUX solutions are based on the photonic integration technology [Koonen, 2012]. The silicon-on-insulator (SOI) [Heck, 2013] and indium phosphide (InP) [Soares, 2011] are the most known. The principle is to integrate the optical functionalities on a single chip. However, the photonic lantern presents a lower MDL.

The fiber-based couplers use the mode conversion by coupling the fundamental mode of an SMF to a higher-order mode of an adjacent FMF, where the propagation constant of the higher-order mode is the same as that of the SMF. The limitation is that fiber alignment should be precise to obtain as appropriate performance.

The core and cladding in 3-dimensional waveguide are manufactured by pure fused silica on the use of femto-second laser pulses that are focused inside a fused silica substrate (See Fig. 1.23). The waveguides in 3D are created by locally modifying the refractive index of glass (See Fig. 1.24). This provides a solution to modify the refractive index of glass locally and generate waveguides in 3D.

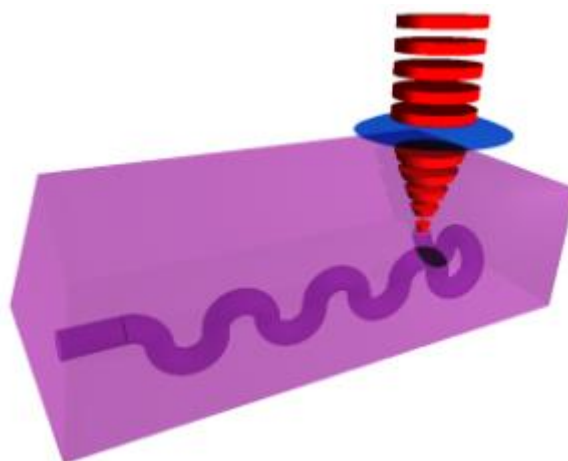


Figure 1-23: The waveguide is inscribed in 3-dimensional by a femto second laser.

In 3-dimensional waveguide, the difference of the refractive index between core and cladding is important, therefore it must be low for MCF coupling because each core is single mode, and large for FMF because the modes share the same core and become more sensitive to the coupling, even more so if we have a large number of modes. A spatial-multiplexer based on this technique has been demonstrated for 6 modes FMF [Chen, 2014].

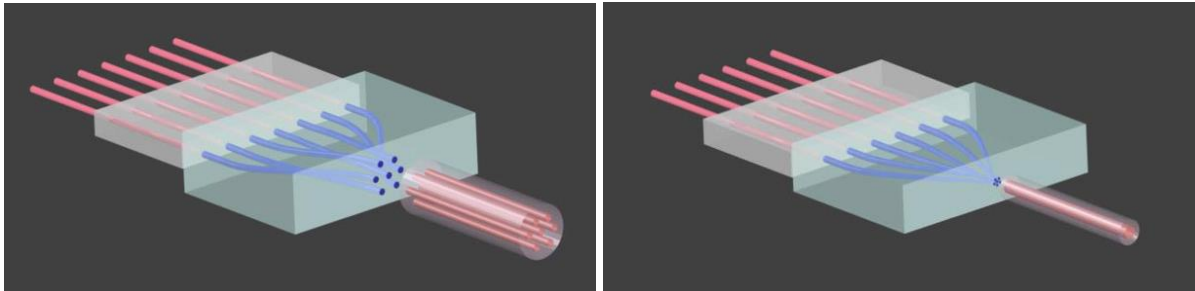


Figure 1-24: 3-dimensional waveguide a) Left: SMUX for 7-core MCF and b) Right: SMUX for 6-mode FMF [Chen, 2014].

Another promising spatial MUX/DEMUX with very low intrinsic loss and high modal selectivity are those based on the Multi-Plane Light Conversion (MPLC). They consist of a series of phase masks separated by a Fourier transform or free-space propagation. In practice, they use a multi-pass cavity where the successive phase profiles are all printed on a single reflective phase plate. This cavity is formed by a mirror and the reflective phase plate, and performs the successive phase profiles and optical transforms. One of the advantages is its scalability to the high number of modes [Morizur, 2015] [Barré, 2017].

1.5.2 Few modes fiber (FMF) and Multicore fiber on transmission

The Few modes fiber (FMF) have only one core that supports multiple modes (fewer modes than an MMF) of propagation and each mode can carry different information. This strategy allows to increase “N modes” times the unitary transmission rate of an SMF. As all modes share the same physical space, the inter-modal crosstalk and the coupling are inevitable. As we will see later, in some cases the coupling may be beneficial (chapter 3).

Increasing the number of spatial modes for FMF is not difficult, but it could complicate the multiplexing and de-multiplexing process. By the same token, the bending loss of the higher-order modes will be larger than the lower-order modes. However, the manufacturing process of the FMF is similar to the conventional fiber which makes them families promising candidates to overcome the capacity crunch.

The FMF can be divided into weakly-coupled and low DGD (strong-coupled). FMF with weakly-coupling could be more adapted to short-distance applications [Sillard, 2016], because the transmission distance is limited by the highest loss and coupling between the modes. FMF with low DGD with DSP-MIMO could be used in long-haul transmission. To decrease the group delay spread (GDS) is equivalent to reduce the DGD. To do so, we can apply one of two strategies (See Fig. 1.25). The first one consists in reducing the DMGD by compensation techniques, such as MIMO-DSP or insertion of DMGD compensation spans by designing fiber with a DMGD as small as possible; generally these fibers have a graded index profile. The characteristic of this method is that group delay spread (GDS) increases linearly with the distance. The second one consists in increasing the coupling by fiber design or by intentional perturbation. Thereby, we expect that the GDS only depends on the square root of the distance. We will study in details these two strategies in the chapter 3.

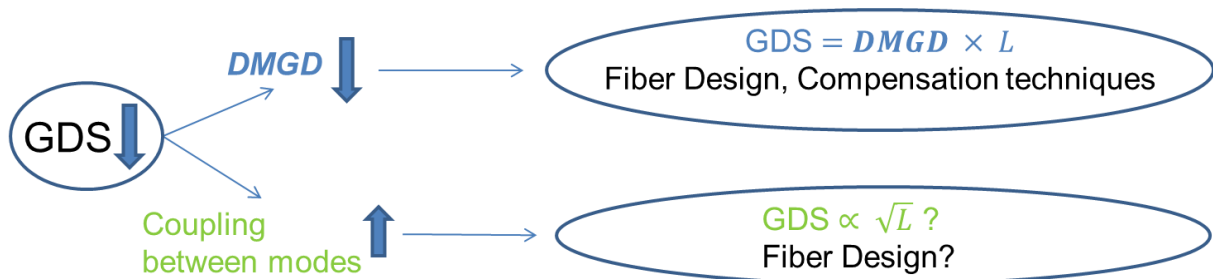


Figure 1-25: Decreasing the DGD

To date, the highest SE for FMF (low-DGD) has been reached with 6 SDM channels [Rif, 2013].

The MCF [Inao, 1979] comprises several independent cores in one fiber core, thus the capacity is increased in N cores times the unitary transmission rate of an SMF. It can be also divided into weakly-coupled and low DGD. The most common are the weakly-coupled, because the MCF with very low DGD needs experimental validation. The weakly-coupled technology is considered as the simplest technology in MCF, because it is not necessary to recover the signal by complex equalization. These fibers have a high spatial density larger than FMF, regardless of the crosstalk between any cores. The crosstalk can be reduced by using a trench assisted inner cladding [Takenaga, 2011], lower-index inner-cladding, or the inter-core crosstalk management and multicarrier nonlinear compensation [Kobayashi, 2013].

Generalities of the optical communication transmission

To date, an MCF weakly-coupled can reach a transmission capacity of 2.15 Pb/s over 31 km, using 22 SDM channels and a spectral efficiency of 214 b/s/Hz [Puttnam, 2015], exceeding the FMF capacity (See Fig. 1.26). The physical implementation with other devices and the non-standard manufacturing could limit its use in the telecommunication business.

Another interesting fiber candidate to improve the spectral efficiency is the FM-MCF fiber that is the combination between few mode and multicore fibers. One of the challenges is to determine the distance between the neighboring cores by considering a similar crosstalk to the conventional MCF and taking into account the transmission distance and the modulation format. To date, 114 SDM channels (19 cores and 4 LP modes) with a spectral efficiency of 456 bit/s/Hz have been reported by [Soma, 2015].

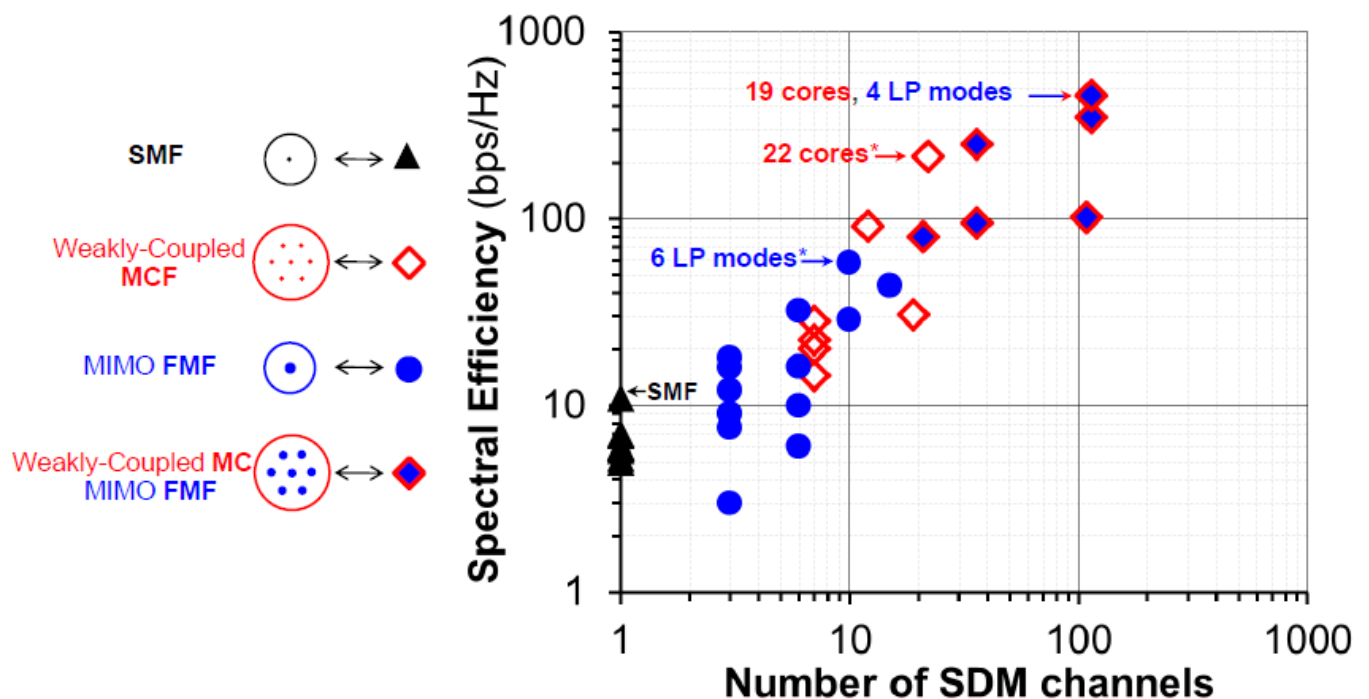


Figure 1-26: Spectral efficiency between different technologies [Sillard, 2016]

A comparison between SDM technologies (MCF and FMF) with the SMF is shown in table 1. The comparison is based on the fiber characteristics, the elements of the communication system, complexity and applications. These parameters give us an idea about the limitations and advantages of each communication system. For example, we can say that the FMF modes share the same core which brings about the undesired intermodal crosstalk between two spatial or polarization modes, similar to that MCF due to the proximity of their

Generalities of the optical communication transmission

cores. If the space density increases, the effective area of FMF and MCF should increase in comparison to the SMF. Therefore, the large core FMF could be advantageous to limit the nonlinearity effect, but these fibers have more modes which could produce more crosstalk and other negative parameters (intermodal four wave mixing, for example). The index profile is also important in the design of the optical fiber to reduce the crosstalk (Step-Index) or DGD (Graded-Index).

Table 1: Evaluation between SMF, MCF and FMF.

Parameter	SMF	MCF	FMF
Fiber loss	<0.2dB/km	Low (~SMF)	Low (~SMF)
Fusion splicing	Easy	Special fusion, medium to high loss	Easy, low loss
Effective area (μm^2)	From 18.8 to 76.3	~72 to 116	Large (depend mode number)
Intra-mode nonlinearity	~SMF	Standard to high	Low
Inter-mode nonlinearity	No	Low	Low to medium
Crosstalk	Very low (< -20dB)	Medium	Low to High (~ -25dB)
Dispersion (ps/nm.km)	From -162 to 17		
Amplifiers EDFA	yes	yes	yes
Amplifiers number	N	N	1
Number of ROADM	N	N	1
DSP complexity	Low	Medium	Medium to high
Multiplexation cost Theoretical	SE_{SMF}	$N_{core} * SE_{SMF}$	$N_{modes} * SE_{SMF}$
Routing	Yes	No	Yes
Index Profile	SI, GI, 3-clad to 4-clad	SI, GI with trench	SI, GI with trench
Application	Little to high reach	Medium to high reach	Little to high reach

1.6 Summary

We have introduced the fundamentals of SMF optical transmission systems and the main physical effects that reduce the transmission distance and capacity. We discussed that the optical fibers are affected by loss, dispersion, non-linear effects, macro bend and micro bend and other drawbacks, needing the recovery of signal at the communication end. Under this approach, the fibers and the communication system must be carefully designed.

We have described the different optical fibers based on SDM and the conventional SMF. Indeed, figure 1.27 summarized the different SDM technologies that offer greater spectral efficiency and they are compared with the SMF [Sillard, 2016]. In any of these cases, the SMF spectral efficiency ($\sim 15.3\text{b/s/Hz}$ [Beppu, 2014]) is lower than the SDM technologies. Thereby, the research points to three SDM strategies: weakly coupled MCF, FMF-MIMO (strong coupled) and weakly coupled.

The maximum SE is reached with weakly coupled MCF+MIMO FMF or weakly coupled MCF. Yet, many are betting on FMF, because it has an easier manufacturing method. Thereby, the interest of this research is focused in FMFs. As was commented above, there is still much to be improved from these emerging fibers and the elements that make up the communications system.

Later, we will describe the FMF propagations and its constraint, specifically the mode coupling.

2 Propagation in the Few Modes Fiber (FMF)

Optical fibers are mainly composed of silicon dioxide (SiO_2) and small amounts of other chemicals are often added. The purity and chemical composition of the glass used in optical fibers as well as the fiber opto-geometrical parameters determine their characteristics, such as the attenuation and chromatic dispersion. These parameters are crucial in the design of an optical fiber, because they could modify the performances of the fiber, such as absorption and scattering. In this study, we will not focus on the manufacturing process, nor on the chemical composition of the optical fiber, but rather on the propagation process of the optical fiber.

The propagation of light inside an optical fiber follows distinct patterns called modes. A mode is fundamentally a path that drives light through of the fiber. Therefore, the optical fiber can be categorized into: single mode (SMF) and multimode (MMF). In this study, we will focus on special type of MMF called FMF for Few Modes Fiber, as introduced in the chapter 1.

The basic structure of an optical fiber consists of two areas: the core and the cladding (See Fig. 2.1a). The core area has a refractive index, denoted $n(x, y)$, which can vary. In variable-refractive-index, the maximum value (n_1) is found at the fiber core axis $r = 0$ (See Fig. 2.1). Whereas the cladding area has a smaller refractive index (n_2) which is usually lower than n to guarantee the total internal reflection inside the core.

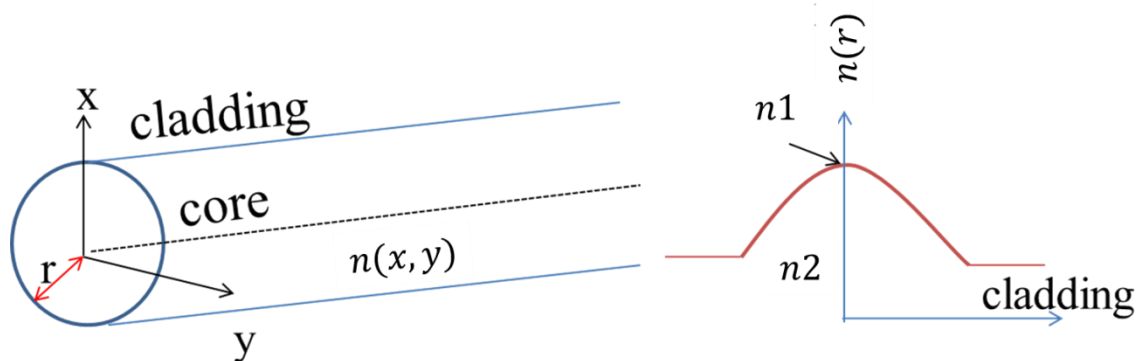


Figure 2-1: Graded index profile $n(x,y)$ with variations only over the core.

In addition, the variation in refractive index over the cross section of the waveguide is given by the profile $n(x, y)$, which can also be represented as a function of the fiber radius $n(r)$. In this study, a general description of the refractive-index profile can rely on the alpha

or power-law profiles (cf. equation 2.1) from [Gloge, 1973] that are mainly used to describe parabolic fiber profiles.

$$n^2(r) = n_1^2 [1 - 2 \Delta f(r)]; \quad f(r) = \left(\frac{r}{a}\right)^\alpha \quad r < a \quad (2.1)$$

Here, r is the radial coordinate, α is the power-law exponent, a is the core radius. Δ is the relative refractive index difference between the maximum index of the core n_1 and the cladding refractive index n_2 .

$$\Delta \approx \frac{n_1^2 - n_2^2}{2n_1^2} \quad (2.2)$$

As discussed in the section 1.2.4, the most well-known refractive index profiles are the step index profile and the parabolic index profile. By equation 2.1, we can account for them by changing the power of the exponent α in $f(r)$. $f(r)$ describes the shape of the profile, and so we can obtain a Heaviside-step for $\alpha=\infty$ (step index profile) or a parabolic profile for $\alpha=2$.

Besides, the propagating modes calculation methods must be adapted to the refractive index profile. The following is a sum-up of the 2 main propagating modes calculation methods:

a) For fibers with step index profiles, the modes can be resolved analytically using the full set of Maxwell's equations. In this case, full vectorial modes are obtained. However, in some cases (low index contrast hypothesis), approximations can be made to simplify the equations and scalar modes can be obtained (known as Linearly Polarized (LP)). These LP modes are useful approximations to understand the modal cutoff and temporal propagation characteristics of the fiber.

b) For fibers with parabolic or graded index profiles, the full or exact solutions are impossible to obtain analytically, because the refractive index varies along to the core. When we use this profile some approximations are needed to obtain the analytical solutions. The approximate solutions can be obtained in the framework of the weakly guiding approximation by considering that the refractive index difference between the core and the cladding tends to zero.

In this research, we will consider a graded index FMF. Consequently, we will use an approximation of the Maxwell's equations which admits analytical solutions under the form of either Laguerre-Gauss [Masaki, 1978] or Hermite-Gauss [Shemirani, 2009]

Propagation in the Few Modes Fiber (FMF)

polynomials considering only an infinite square law profile (refractive index infinite, see Fig. 2.2). The Laguerre-Gauss will be used throughout the entire thesis.

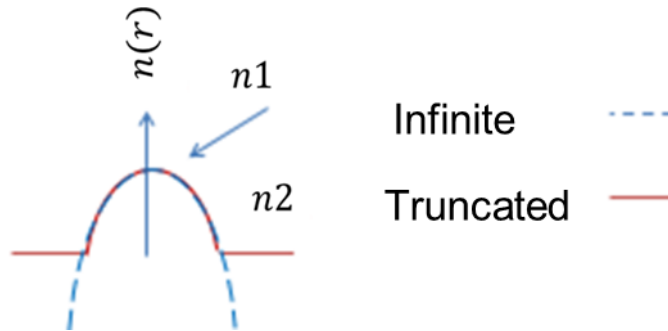


Figure 2-2: Exemplary refractive graded index profile $n(x,y)$. The infinite parabolic profile used by the Laguerre-Gauss method.

The definitions and derivations follow the outline of Bures's book [Bures, 2009].

In this chapter, our aim is to study the characteristics of bound and radiated modes for a set of graded-index profile fibers by numerical means. The calculation of the guided modes will use a homemade tool developed by researchers from Prysmian group. The validation of this method has been proven in cases of guided and leaky modes by [Molin, 2016].

Therefore, the goals of this chapter are to understand:

- How to obtain the different modes (guided, leaky and radiation) of an FMF
- How to improve the performances of an FMF
- The effect of the number of modes over different parameters of the FMF

2.1 Propagation in Optical fiber

Wave propagation in FMFs is similar to conventional MMFs, the main difference lies in a reduced number of modes and the fact that each mode can potentially be used to transmit information. Therefore, we will start with the main definition without making any distinction on fiber type. In a simplistic view, light is reflected on the core-cladding boundary and the wave can interfere with itself giving rise to complex interference patterns, called transverse modes. These modes are the solutions of the propagating equations which result from the Maxwell equations applied on the waveguide. To analyze the optical fiber, we consider the light as an electromagnetic and monochromatic wave with a propagation constant β and an angular frequency ω . Thus, the electric \vec{E} and magnetic fields \vec{H} of this electromagnetic and monochromatic wave can be written as:

$$\vec{E}(\vec{r}, t) = \vec{E}_{(x,y,z)} e^{i(\omega t)} \quad (2.3a)$$

$$\vec{H}(\vec{r}, t) = \vec{H}_{(x,y,z)} e^{i(\omega t)} \quad (2.3b)$$

The following set of Maxwell's equations describes the electric and magnetic fields arising from distributions of electric charges and currents, and the variation of those fields change in time and space.

$$\vec{\nabla} \cdot \vec{D} = \rho \quad (2.4a)$$

$$\vec{\nabla} \cdot \vec{B} = 0 \quad (2.4b)$$

$$\vec{\nabla} \times \vec{E} = -\frac{\partial \vec{B}}{\partial t} = -\mu_0 \frac{\partial \vec{H}}{\partial t} = -\mu_0 i\omega \vec{H} \quad (2.4c)$$

$$\vec{\nabla} \times \vec{H} = \vec{j} + \frac{\partial \vec{D}}{\partial t} \quad (2.4d)$$

Here, vectors \vec{D} , \vec{B} , \vec{E} and \vec{H} : are the electric displacement field, the magnetic induction field, the electric field and the magnetic field respectively.

Let us consider that the monochromatic wave propagates in an isotropic, homogenous medium, non-magnetic material and without charge. As a result, \vec{j} (free current density vector) and ρ (free charge density) are null, and thus the Maxwell's equations can be expressed as:

$$\vec{D} = \epsilon \vec{E} = \epsilon_0 (1 + \chi_e) \vec{E} \quad (2.5a)$$

$$\vec{B} = \mu_0 \vec{H} \quad (2.5b)$$

Here, ϵ , ϵ_0 , μ_0 and χ_e are the permittivity, the vacuum permittivity, the vacuum permeability, the electric susceptibility. These parameters are related to the material. Likewise, we can associate the refractive index of the medium with the relative permittivity or dielectric constant, ϵ_r , by the following expression $n = \sqrt{\epsilon_r}$ to rewrite the equations in term of n .

By using the constitutive relations (2.5a and 2.5b) and (2.3a) and (2.3b), the Maxwell's equation (2.4a, 2.4b, 2.4c and 2.4d) can also be written in terms of E and H vectors as follows:

$$\vec{\nabla} \cdot (\epsilon_r \vec{E}) = 0 \quad (2.6a)$$

$$\vec{\nabla} \cdot (\mu_0 \vec{H}) = 0 \quad (2.6b)$$

$$\vec{\nabla} \times \vec{E} = -i\omega\mu_0 \vec{H} \quad (2.6c)$$

$$\vec{\nabla} \times \vec{H} = i\omega\epsilon_0 n^2 \vec{E} \quad (2.6d)$$

These equations allow finding the homogeneous vector wave equations.

2.1.1 Homogeneous vector wave equations

Because the vector wave equations are current density free, these equations will be homogeneous. They are obtained from equations 2.6c and 2.6d only in terms of \vec{E} or \vec{H} , applying the curl operator ($\vec{\nabla} \times$) to the equation 2.6c, and substituting the equation 2.6d to the result of the previous procedure.

Therefore, we get the equation 2.7a for the electric field by also considering the following vectorial identities: $\vec{\nabla} \times (\vec{\nabla} \times \vec{E}) = \vec{\nabla}(\vec{\nabla} \cdot \vec{E}) - \Delta \vec{E}$ and $\vec{\nabla} \cdot (\vec{\nabla} \times \vec{E}) = 0$.

$$\vec{\nabla} \times (\vec{\nabla} \times \vec{E}) = \vec{\nabla}(\vec{\nabla} \cdot \vec{E}) - \Delta \vec{E} = n^2 k_o^2 \vec{E} \quad (2.7a)$$

Following the same procedure, we can get the equation 2.7b for the magnetic field. Note that in this case we apply the curl operator to the equation 2.6d, and later we substitute the equation 2.6c in the previous result.

$$\vec{\nabla} \times (\vec{\nabla} \times \vec{H}) = \vec{\nabla}(\vec{\nabla} \cdot \vec{H}) - \Delta \vec{H} = i \frac{k_o}{\eta_0} (n^2 \vec{\nabla} \times \vec{E} + \vec{\nabla}(n^2) \times \vec{E}) = k_o^2 n^2 \vec{H} + i \frac{k_o}{\eta_0} \vec{\nabla}(n^2) \times \vec{E} \quad (2.7b)$$

Here, η_0 is the electromagnetic impedance of free space ($\sim 377 \Omega$).

By combining the two curl identities (2.7a and 2.7b) and the above relations:

$$\vec{\nabla} \cdot (n^2 \vec{E}) = 0 = n^2 \vec{\nabla} \cdot \vec{E} + \vec{E} \cdot \vec{\nabla} n^2 \text{ leading to } \vec{\nabla} \cdot \vec{E} = -\vec{\nabla}(\ln n^2) \cdot \vec{E}$$

We obtain the two homogeneous vector wave equations:

$$(\Delta + n^2 k_o^2) \vec{E} = -\vec{\nabla} (\vec{E} \cdot \vec{\nabla} \ln(n^2)) \quad (2.8a)$$

$$(\Delta + n^2 k_o^2) \vec{H} = (\vec{\nabla} \times \vec{H}) \times \vec{\nabla} \ln(n^2) \quad (2.8b)$$

Note that the equation 2.8a and 2.8b are expressed only by the terms \vec{E} , \vec{H} and n^2 .

2.1.2 Translation-invariant optical fiber

Considering the propagation along the z-axis, the transversal and longitudinal components of the \vec{E} , \vec{H} fields can be written as:

$$\vec{E}(\vec{r}, t) = \vec{E}_{(x,y)} e^{i(\omega t)} e^{-i(\beta z)} \quad (2.9a)$$

$$\vec{H}(\vec{r}, t) = \vec{H}_{(x,y)} e^{i(\omega t)} e^{-i(\beta z)} \quad (2.9b)$$

Equations 2.9a and 2.9b become 2.10a and 2.10b, by taking into account a fiber with a refractive index profile invariant along the z-axis. Note that the electric and magnetic field are expressed as a superposition of fields written in separated form (we have omitted the time dependence, $e^{i(\omega t)}$).

$$\vec{E}(x, y, z) = \vec{E}(x, y) e^{-i(\beta z)} = (\vec{E}_t + \hat{z} \cdot E_z) e^{-i(\beta z)} \quad (2.10a)$$

$$\vec{H}(x, y, z) = \vec{H}(x, y) e^{-i(\beta z)} = (\vec{H}_t + \hat{z} \cdot H_z) e^{-i(\beta z)} \quad (2.10b)$$

$\vec{E}_t, \vec{H}_t, E_z$ and H_z correspond to the transversal and longitudinal components of the electrical and magnetic field. In the same way, we can express the gradient operator and Laplacian vector as equations 2.11a and 2.11b, because the electrical and magnetic fields are only x and y dependent.

$$\vec{\nabla} = \vec{\nabla}_t + \hat{z} \frac{\partial}{\partial z} = \vec{\nabla}_t - i\beta\hat{z} \quad (2.11a)$$

$$\vec{\Delta}\vec{E} = \vec{\nabla}_t^2 \vec{E} + \frac{\partial^2 E}{\partial z^2} = \vec{\nabla}_t^2 \vec{E} - \beta^2 \vec{E} \quad (2.11b)$$

Now, we rewrite the homogeneous equation (2.8a and 2.8b) [Bures, 2009], by applying 2.11a, 2.11b and reducing $\vec{\nabla} \ln(n^2)$ to $\vec{\nabla}_t \ln(n^2)$, $\vec{E} \cdot \vec{\nabla} \ln(n^2)$ to $\vec{E}_t \cdot \vec{\nabla}_t \ln(n^2)$.

$$(\vec{\nabla}_t^2 + n^2 k_o^2 - \beta^2) \vec{E} = -(\vec{\nabla}_t - i\beta\hat{z}) (\vec{E}_t \cdot \vec{\nabla}_t \ln(n^2)) \quad (2.12a)$$

$$\beta^2 \vec{E} = (\vec{\nabla}_t - i\beta\hat{z}) (\vec{E}_t \cdot \vec{\nabla}_t \ln(n^2)) + \vec{\nabla}_t^2 \vec{E} + n^2 k_o^2 \vec{E}$$

$$(\vec{\nabla}_t^2 + n^2 k_o^2 - \beta^2) \vec{H} = ((\vec{\nabla}_t - i\beta\hat{z}) \times \vec{H}) \times \vec{\nabla}_t \ln(n^2) \quad (2.12b)$$

$$\beta^2 \vec{H} = -((\vec{\nabla}_t - i\beta\hat{z}) \times \vec{H}) \times \vec{\nabla}_t \ln(n^2) + \vec{\nabla}_t^2 \vec{H} + n^2 k_o^2 \vec{H}$$

The solutions of the equations 2.12a and 2.12b are eigenvectors, eigenmodes or modes of the linear operators that are associated to the eigenvalue β^2 . β can be related to an effective index as in 2.13. This effective index represents the ratio of the propagation constant in the waveguide to the free space propagation constant.

$$\beta = \frac{2\pi}{\lambda} n_{eff} = k_o n_{eff} \quad (2.13)$$

The eigenmodes or modes can be divided into two groups of guided-modes and radiation modes. In general, each mode has its own effective index. To distinguish the modes, we must consider the inferior and superior limit of β . Thus, the guided modes have a real and discrete β and are typically restricted to the range $(k_o \cdot n_1 > \beta > k_o \cdot n_2)$. Where n_1 is the maximum refractive index in the core, n_2 is the refractive index of the cladding.

The radiation modes can be subdivided into: leaky modes and a continuous set of modes with real propagation constants or purely imaginary propagation constants (See Fig. 2.3).

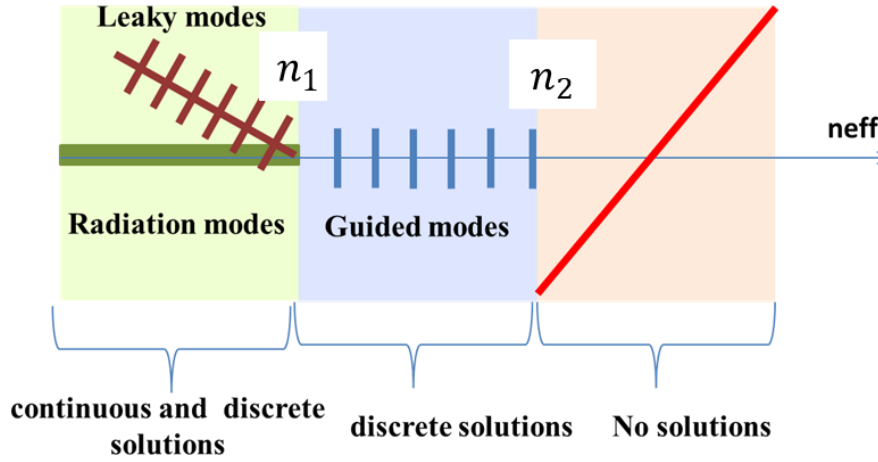


Figure 2-3: Modes inside an optical fiber.

- The leaky modes ($k_o \cdot n_2 > \beta$) have complex and discrete β 's. They propagate like guided modes but with leakage losses due to the imaginary part of their propagation constant. (as, is the case, for example, in photonic crystal fibers)
- The radiated modes ($k_o \cdot n_1 > k_o \cdot n_2 > \beta$) can have a real and continuous β , they propagate like refracted rays and their energy is located outside of the core. These modes attenuate quickly compared to leaky modes and their propagation constants are typically smaller than those of guided-modes.

2.1.3 Modal vector equation

From the Maxwell equation (2.6c and 2.6d), we can express the transverse components (\vec{E}_t and \vec{H}_t) by the longitudinal components (E_z and H_z).

$$\vec{E}_t = \frac{i}{k_o^2 n^2 - \beta^2} (\beta \vec{\nabla}_t E_z - \left(\frac{\mu_o}{\epsilon_o}\right)^{\frac{1}{2}} k_o \hat{z} \times \vec{\nabla}_t H_z) \quad (2.13a)$$

$$\vec{H}_t = \frac{i}{k k_o^2 n^2 - \beta^2} (\beta \vec{\nabla}_t H_z + \left(\frac{\epsilon_o}{\mu_o}\right)^{\frac{1}{2}} k_o n^2 \hat{z} \times \vec{\nabla}_t E_z) \quad (2.13b)$$

Thereby, the transverse component is obtained only in terms of derivatives of the longitudinal components in Cartesian coordinates [as in Bures, 2009].

$$E_x = \frac{1}{k_o^2 n^2 - \beta^2} \left(\beta \frac{\partial iE_z}{\partial x} + \left(\frac{\mu_o}{\epsilon_o} \right)^{1/2} k_o \frac{\partial iH_z}{\partial y} \right) \quad (2.14a)$$

$$E_y = \frac{1}{k_o^2 n^2 - \beta^2} \left(\beta \frac{\partial iE_z}{\partial y} - \left(\frac{\mu_o}{\epsilon_o} \right)^{1/2} k_o \frac{\partial iH_z}{\partial x} \right) \quad (2.14b)$$

$$H_x = \frac{1}{k^2 n^2 - \beta^2} \left(\beta \frac{\partial iH_z}{\partial x} - \left(\frac{\epsilon_o}{\mu_o} \right)^{1/2} k_o n^2 \frac{\partial iE_z}{\partial y} \right) \quad (2.14c)$$

$$H_y = \frac{1}{k_o^2 n^2 - \beta^2} \left(\beta \frac{\partial iH_z}{\partial y} + \left(\frac{\epsilon_o}{\mu_o} \right)^{1/2} k_o n^2 \frac{\partial iE_z}{\partial x} \right) \quad (2.14d)$$

By substituting 2.14a, 2.14b, 2.14c and 2.14d in 2.12a and 2.12b, we obtain the coupled equation for E_z and H_z .

$$\nabla_t^2 E_z + (k_o^2 n^2 - \beta^2) E_z - \frac{\beta}{k_o^2 n^2 - \beta^2} \left\{ \frac{\partial \ln(n^2)}{\partial x} \left(\beta \frac{\partial E_z}{\partial x} + \left(\frac{\mu_o}{\epsilon_o} \right)^{1/2} k_o \frac{\partial H_z}{\partial y} \right) + \frac{\partial \ln(n^2)}{\partial y} \left(\beta \frac{\partial E_z}{\partial y} - \left(\frac{\mu_o}{\epsilon_o} \right)^{1/2} k_o \frac{\partial H_z}{\partial x} \right) \right\} = 0 \quad (2.15a)$$

$$\nabla_t^2 H_z + (k_o^2 n^2 - \beta^2) H_z - \frac{k^2 n^2}{k_o^2 n^2 - \beta^2} \left\{ \frac{\partial \ln(n^2)}{\partial y} \left(\beta \frac{\partial H_z}{\partial y} + \left(\frac{\epsilon_o}{\mu_o} \right)^{1/2} k_o n^2 \frac{\partial E_z}{\partial x} \right) + \frac{\partial \ln(n^2)}{\partial x} \left(\beta \frac{\partial H_z}{\partial x} - \left(\frac{\epsilon_o}{\mu_o} \right)^{1/2} k_o n^2 \frac{\partial E_z}{\partial y} \right) \right\} = 0 \quad (2.15b)$$

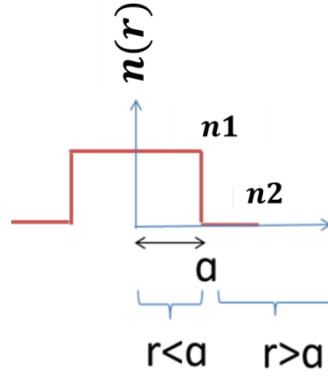
The resolution of the z-component of the fields (2.15a and 2.15b) is the basis to calculate the exact modes or vector modes of the fiber as introduced in the next example.

2.1.3.1 Example: vector modes of a step-index profile

This example which will provide the simplest analytical form of vector modes, is obtained with a circular step-index fiber because its refractive index is constant in the core and the cladding. The propagation in the core is ensured according to $n_1 > n_2$ and $k_o \cdot n_1 > \beta > k_o \cdot n_2$. Thereby, the coupled equations 2.15a and 2.15b are simplified by making the term $\nabla_t \ln(n^2)$ equal to zero, except at the core-cladding interface. At the core-cladding interface, $\nabla_t \ln(n^2)$ can be omitted and replaced by continuity conditions of radial and azimuthal components of the fields.

$$\nabla_t^2 E_z + (k_o^2 n^2 - \beta^2) E_z = 0 \quad (2.16a)$$

$$\nabla_t^2 H_z + (k_o^2 n^2 - \beta^2) H_z = 0 \quad (2.16b)$$



By replacing \vec{E} or \vec{H} by $\psi(r, \theta)$, the same equation accounts for E_z and H_z

$$\nabla_t^2 \psi + (k_o^2 n^2 - \beta^2) \psi = 0.$$

As the fiber has a circular symmetry, the transverse scalar Laplacian of this equation can be represented in cylindrical polar coordinate, by:

$$\Delta_t = \nabla_t^2 = \frac{\partial^2}{\partial r^2} + \frac{1}{r} \frac{\partial}{\partial r} + \frac{1}{r^2} \frac{\partial^2}{\partial \theta^2},$$

Thereby, the two following differential equations from the scalar equation above can also be written in cylindrical polar coordinates. Here, the different regions of optical fiber are considered.

$$\left\{ \frac{\partial^2}{\partial r^2} + \frac{1}{r} \frac{\partial}{\partial r} + \frac{1}{r^2} \frac{\partial^2}{\partial \theta^2} + \frac{U^2}{a^2} \right\} \psi(r, \theta) = 0 \quad 0 < r < a \quad (2.17a)$$

$$\left\{ \frac{\partial^2}{\partial r^2} + \frac{1}{r} \frac{\partial}{\partial r} + \frac{1}{r^2} \frac{\partial^2}{\partial \theta^2} - \frac{W^2}{a^2} \right\} \psi(r, \theta) = 0 \quad r > a \quad (2.17b)$$

These equations (2.17a and 2.17b) contain the modal parameters U (expressed in equation 2.18a), W (expressed in equation 2.18b) and the field $\psi(r, \theta)$. U and W are related with the normalized frequency (V) by equation 2.18c. V depends on the index profile and the wavelength and it is widely used to determine the number of modes. $\psi(r, \theta)$ is the field and by definition it is invariant after a 2π rotation around the z -axis that is why it can be written as:

$$\psi(r, \theta) = F(r) \cdot \begin{cases} \cos(v \cdot \theta + \varphi_p) \\ \sin(v \cdot \theta + \varphi_p) \end{cases}$$

where v is the integer modal azimuthal number and $F(r)$ is the amplitude of the field.

$$U^2 = a^2(n_1^2 k_o^2 - \beta^2) \quad r < a \quad (2.18a)$$

$$W^2 = a^2(\beta^2 - n_2^2 k_o^2) \quad r > a \quad (2.18b)$$

$$V^2 = U^2 + W^2 = (k_o \cdot a \sqrt{n_1^2 - n_2^2})^2 \quad (2.18c)$$

To solve equations 2.17a and 2.17b, we must have noted that the field in each guided mode must be finite in the core in $r \rightarrow 0$ and the field in the cladding must tend to zero when $r \rightarrow \infty$ (the cladding expressions are monotonically decreasing). The appropriate solutions can be expressed with Bessel functions of the first kind J_v in the core ($0 < r < a$) and modified Bessel functions of the second kind K_v in the cladding ($r \geq a$) (a is the radius of the core). From these solutions we can find the longitudinal components E_z and H_z (equations 2.19a, 2.19b, 2.19c and 2.19d) and later, the transversal components (whose mathematic steps are not shown here).

$$E_z(r) = A J_v(U \frac{r}{a}) \cos(v\theta + \phi_p) \quad 0 < r < a \quad (2.19a)$$

$$H_z(r) = B J_v(U \frac{r}{a}) \sin(v\theta + \phi_p) \quad 0 < r < a \quad (2.19b)$$

$$E_z(r) = C K_v(U \frac{r}{a}) \cos(v\theta + \phi_p) \quad r \geq a \quad (2.19c)$$

$$H_z(r) = D K_v(U \frac{r}{a}) \sin(v\theta + \phi_p) \quad r \geq a \quad (2.19d)$$

ϕ_p is the arbitrary phase and v is the angular quantization that must be an integer.

To find the exact mode field expression and the eigenvalue equation, we consider the boundary condition between the core and cladding. That is, this condition must allow continuity of the magnetic field and the electric field tangential and azimuthal components at the interface between the core and cladding. Thereby, we can obtain the equation fulfilled by the propagation constant (2.20).

$$\left[\frac{J'_v(U)}{U J_v(U)} + \frac{K'_v(W)}{W K_v(W)} \right] \left[\frac{n_1^2}{n_2^2} \frac{J'_v(U)}{U J_v(U)} + \frac{K'_v(W)}{W K_v(W)} \right] = v^2 \left[\frac{1}{U^2} + \frac{1}{W^2} \right] \left[\frac{n_1^2}{n_2^2} \frac{1}{U^2} + \frac{1}{W^2} \right] \quad (2.20)$$

Through equation 2.20, we can find three kinds of solutions. These solutions correspond to three classes of modes:

Propagation in the Few Modes Fiber (FMF)

- Transverse electric modes ($TE_{0\mu}$) $\nu=0$:

In such modes, z and radial components of the electric field and the azimuthal component of the magnetic field are equal to zero. The mode corresponding to the μ th root of equation 2.21 is noted $TE_{0\mu}$. The first mode is called TE_{01} (one ring on the intensity field, see Fig. 2.4a), the next one TE_{02} (double ring on the intensity field, see Fig. 2.4b), and etcetera. Eigen modes of such modes are discussed below:

$$\frac{J_1(U)}{UJ_0(U)} = -\frac{K_1(W)}{WK_0(W)} \quad (2.21)$$

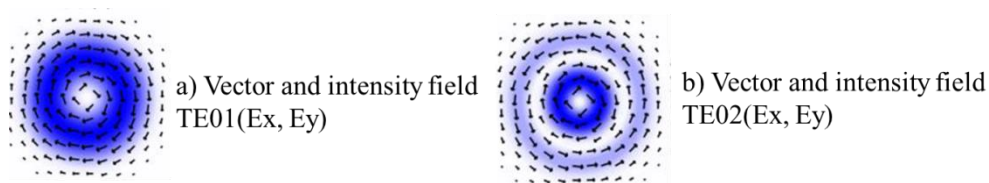


Figure 2-4: The intensity is represented by the shadow and direction of the vector field by the arrows (TE_{01} and TE_{02}).

- Transverse magnetic modes ($TM_{0\mu}$) $\nu=0$:

In such modes, z and radial components of the magnetic field and the azimuthal component of the electric field are equal to zero. Here μ is the index of the U solution of the equation 2.22. The first mode is called TM_{01} (See Fig. 2.5a), the next one TM_{02} (See Fig. 2.5b), and etcetera. Eigen modes of such modes are discussed below:

$$\frac{n_1^2 J_1(U)}{n_2^2 UJ_0(U)} = -\frac{K_1(W)}{WK_0(W)} \quad (2.22)$$

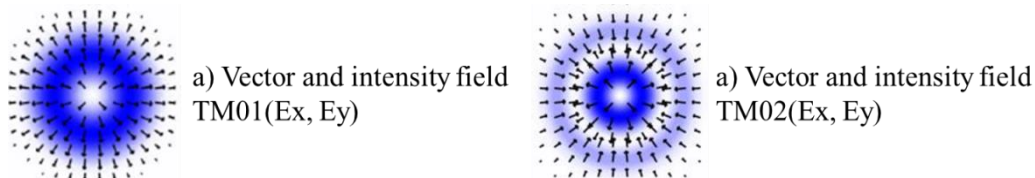


Figure 2-5: The intensity is represented by the shadow and direction of the vector field by the arrows (TM_{01} and TM_{02}).

- Hybrid modes ($HE_{v\mu}$ and $EH_{v\mu}$) $v \neq 0$:

For $v > 1$, the z components of their electromagnetic fields are different to zero. We can find two types of modes: $HE_{v\mu}$ (where $H_z > E_z$) and $EH_{v\mu}$ (where $H_z < E_z$) (See Fig. 2.6).

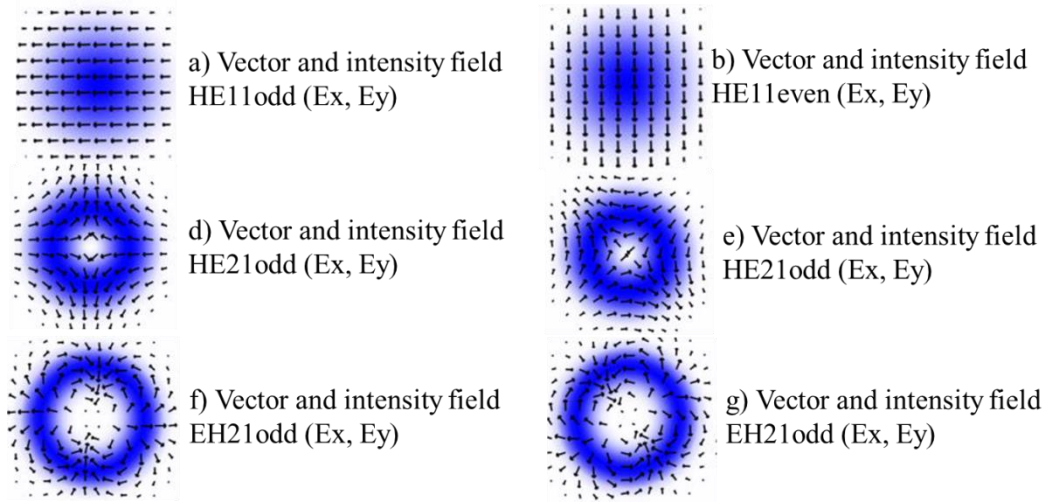


Figure 2-6: The intensity is represented by the shadow and direction of the vector field by the arrows. To be noted that HE_{11} odd and HE_{11} even are linearly polarized.

Likewise, by using the relationship between Bessel functions of consecutive orders, we can find modes that share the almost same propagation constant (for example $EH_{v\mu}$ and $HE_{v+2\mu}$, as well as $HE_{2\mu}$, $TE_{0\mu}$ and $TM_{0\mu}$). These kinds of modes are degenerated with each other. Hence, we can combine them to get other type of modes, such as the linear polarized LP modes (see section 2.1.4).

2.1.4 Scalar modes

If the refractive index difference between the core and the cladding is very small compared to the index value of the core, we can assume that the refractive index in the fiber is homogeneous ($\nabla_t \ln(n^2) \approx 0$), such as in free space case with uniform refractive index. As a consequence the vector wave equations are reduced to the left-hand side and the modes can be considered Transverse Electric and Magnetic (TEM) with $E \approx E_t$ and $H \approx H_t$ and the longitudinal components are equal to zero ($E_z \approx H_z \approx 0$).

Considering $\vec{E}_t = E_x \hat{x} + E_y \hat{y}$, with \hat{x} and \hat{y} as unit vectors parallel to the Cartesian axes, equation 2.12a becomes:

$$\nabla_t^2 E_x + (k_o^2 n^2 - \beta^2) E_x \approx 0 \quad (2.23a)$$

$$\nabla_t^2 E_y + (k_o^2 n^2 - \beta^2) E_y \approx 0 \quad (2.23b)$$

Here, the vectors (\hat{x} and \hat{y}) determine two polarization directions which will define the linear polarized mode with their electrical components along x or y.

Note that equations 2.23a and 2.23b are scalar and can be rewritten as equation 2.24 with $F_\nu(r, \theta)$ being either \vec{E}_x or \vec{E}_y . $F_\nu(r, \theta)$ is the distribution of mode, ν .

$$(\nabla_t^2 + k_o^2 n^2 - \beta^2)F_\nu(r, \theta) = 0 \quad (2.24)$$

The solutions of this scalar wave equation (2.24) are known as linearly polarized modes (LP modes). These modes can be regarded as the proper linear combination of vectorial eigenmodes guided of the fiber. It is usually represented as $LP_{\nu\mu}$, where ν subscript is the angular quantization or the azimuthal number, and represents half the number of minima (or maxima) that occurs in the pattern of intensity, whereas μ subscript is the radial quantization and indicates the number of maxima in the intensity pattern that occur in a radial line between zero and infinity.

These LP modes can be found in fibers whose core is circular and not perfectly circular. However, its study can be simplified by considering radial periodic and symmetric core with respect to the z-axis. In this case $F_\nu(r, \theta)$ must be represented as:

$$F_\nu(r, \theta) = \psi_\nu(r) \cdot \begin{cases} \cos(\nu \cdot \theta) \\ \sin(\nu \cdot \theta) \end{cases} \quad (2.25)$$

Now, the equation 2.24a has two solutions, one for each allowed values of β (cf. paragraph 1.1.2). The first solution produces the even modes $\psi_\nu(r)\{\cos(\nu\theta)\}$ and the second one, the odd modes $\psi_\nu(r)\{\sin(\nu\theta)\}$.

We must also consider two different cases depending on ν :

- For $\nu = 0$, we can have two modes for each allowed values of β . $LP_{0\mu}$ is degenerated two fold (two possible polarization states) and it is obtained assuming (2.26a and 2.26b).

$$\vec{E}_x = \psi_{0\mu}(r) \hat{x} \quad (2.26a)$$

$$\vec{E}_y = \psi_{0\mu}(r) \hat{y} \quad (2.26b)$$

- For $\nu \neq 0$, $LP_{\nu\mu}$ has 4 possible degenerated states (two polarization states and two intensity patterns).

$$\overrightarrow{E}_{x,e} = \psi_{v\mu}(r)\{\cos(v\theta)\} \hat{x} \quad (2.27a)$$

$$\overrightarrow{E}_{y,e} = \psi_{v\mu}(r)\{\sin(v\theta)\} \hat{y} \quad (2.27b)$$

$$\overrightarrow{E}_{x,o} = \psi_{v\mu}(r)\{\cos(v\theta)\} \hat{x} \quad (2.27c)$$

$$\overrightarrow{E}_{y,o} = \psi_{v\mu}(r)\{\sin(v\theta)\} \hat{y} \quad (2.27d)$$

By the following example, we will find the LP modes for a step index.

2.1.4.1 Example: LP modes

To obtain LP modes for a step index, we can express the solution of the scalar equation using the J Bessel function (of the first kind) within the core since field intensity in each guided mode must be finite. For the cladding, we use the K modified Bessel functions of the second kind because the field must monotonically decrease (See equations 2.28a and 2.28b).

$$\Psi_v(r) = A J_v\left(U \frac{r}{a}\right) \begin{cases} \cos(v\theta + \phi_p) \\ \sin(v\theta + \phi_p) \end{cases} \quad 0 < r < a \quad (2.28a)$$

$$\Psi_v(r) = B \frac{J_v(U)}{K_v(U)} K_v\left(W \frac{r}{a}\right) \begin{cases} \cos(v\theta + \phi_p) \\ \sin(v\theta + \phi_p) \end{cases} \quad r \geq a \quad (2.28b)$$

Conversely to the vector mode calculation, LP modes are found by assuming $n_1^2/n_2^2 \approx 1$ from weakly guiding approximation. Thereby, the equation 2.20 becomes:

$$\left[\frac{J'_v(U)}{U J_v(U)} + \frac{K'_v(W)}{W K_v(W)} \right] = \pm v \left[\frac{1}{U^2} + \frac{1}{W^2} \right] \quad (2.29a)$$

From 2.29a, we can obtain three different equations by using the relationship between the Bessel function with their first derivatives. Therefore, one of these equations (2.29b, 2.29c and 2.29d) are used to obtain the finite set of discrete root $U_{v\mu}$, for a given V and v . The root of $U_{v\mu}$ is related to n_{eff} and β .

$$U \frac{J_0(U)}{J_1(U)} = -W \frac{K_0(W)}{K_1(W)} \quad (2.29b)$$

$$U \frac{J_\nu(U)}{J_{\nu-1}(U)} = W \frac{K_\nu(W)}{K_{\nu-1}(W)} \quad (2.29c)$$

$$U \frac{J_\nu(U)}{J_{\nu+1}(U)} = -W \frac{K_\nu(W)}{K_{\nu+1}(W)} \quad (2.29d)$$

As we discussed before U (equation 2.18a) and W (equation 2.18b) are the modal parameters and are related to the normalized frequency (V) by equation 2.18c. V contains all the parameters of the optical fiber (index, wavelength and radius) and the ν value, that is a positive and an integer root number.

The modal solutions of $U_{\nu\mu}$ of a guided mode $LP_{\nu\mu}$ are comprised between the cut-off value of U where the mode can exist, and U values far away of the cut-off. Note that U values are important to determine the solutions. Each $U_{\nu\mu}$ solution represents a guided mode and their values are localized between $U \rightarrow V$ and $U (V \rightarrow \infty)$.

V is commonly used to define the number of modes of an optical fiber. Thereby, we ensure only one mode for a step index, if $V \leq 2.405$ and several modes, if $V > 2.405$. The first mode of an optical fiber is commonly known as the fundamental mode, LP_{01} , Note that there will always be a mode at which $\nu=0$. This mode is the only one present in an SMF.

Contrarily, in a step-index MMF ($V > 2.4$) other LP modes can appear. For instance, we can find 2 LP modes (LP_{01} and LP_{11}) in a step-index fiber with $V < 3.7$. LP_{01} has two possible polarization states and LP_{11} two polarization states and two intensity patterns, as in the Fig. 2.7.

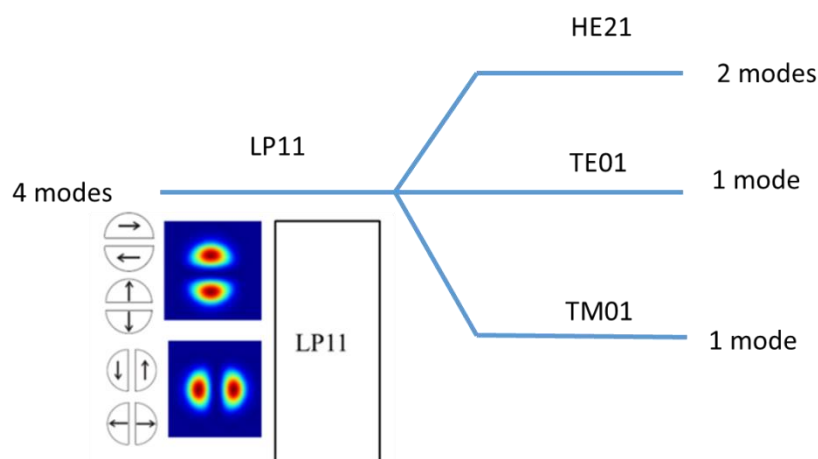


Figure 2-7: Step index fiber with 2 LP modes (LP_{01} and spatial degenerate LP_{11}). LP_{11} mode is obtained by superimposing the vector mode pairs (TE_{01} , HE_{21}) or (TM_{01} , HE_{21}).

Propagation in the Few Modes Fiber (FMF)

To define the modal characteristics (or number of modes) of the fiber, the normalized propagation constant figure are used. In the figures 2.8a and 2.8b, two examples are used to compare the conventional fibers (step-index profile and graded-index profiles) in terms of modal characteristics.

The number of modes with the normalized frequency can also be determined by the following relation:

$$\text{Number of modes} = \frac{\alpha}{\alpha+2} \frac{V^2}{2}$$

However, this relation for a graded-index fiber applies only when the number of modes is a large number.

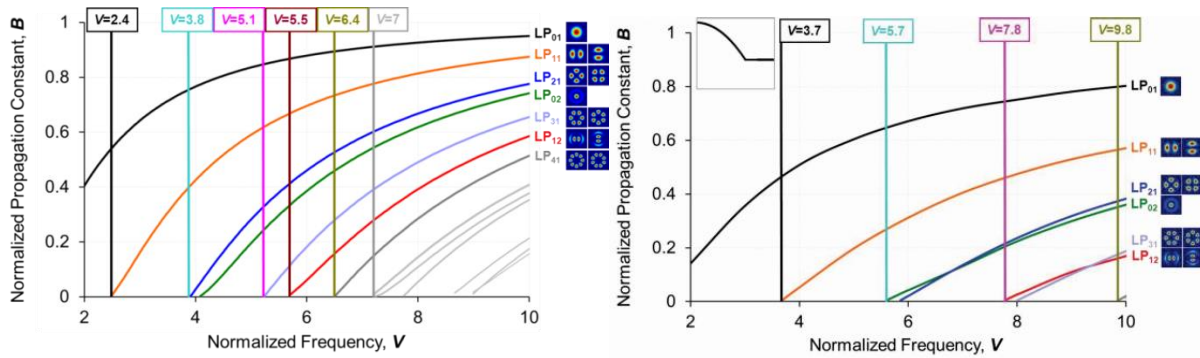


Figure 2-8: Normalized propagation constant vs normalized frequency for a) a step index. b) a graded index ($\alpha=2$) obtained by numerical tools. The x-axis corresponds to the normalized frequency and the y-axis corresponds to the normalized propagation constant, $B=(n_{\text{eff}}^2 - n_2^2)/(n_1^2 - n_2^2)$ [Sillard, 2016]

It should be noted that we ensure only one mode for this graded-index, if $V \leq 3.7$ and several modes, for $V > 3.7$. Comparing with step-index, V is greater in this profile because V depends on the numerical aperture (N.A) that is greater in this profile.

N.A is the ability of an optical fiber to capture light.

In the next section, we shall briefly detail the calculation of the modes in graded-index fiber. In this fiber, the Bessel functions are no longer valid to calculate the modes, since the refractive index in the core is not constant. One of the ways is to solve the wave equation in the core and cladding separately and to match those solutions at the core-cladding boundary. The typically used approach is based on the asymptotic WKB approximation (Wentzel–Kramers–Brillouin), but they are not accurate enough for the practical study of optical fibers [Liu, 1995]. Hence, there are other more appropriate methods which use an analytical expression as Laguerre-Gauss [Masaki, 1978] or Hermite-Gauss [Shemirani, 2009]. These methods allow to calculate the modes from the scalar modes equation.

2.1.5 Laguerre and Hermite modes (graded index profile)

To obtain the analytical expression of the scalar modes for a graded-index profile, we need to assume $\alpha = 2$ and an outer cladding of refractive index invariant extended to infinity (Equations 2.30a-b). For $\alpha \neq 2$, the scalar wave can be solved by the method of approximation known as the Wentel-Kramers-Brillouin-Jeffreys (WKBJ).

$$n^2(r) = n_1^2 \cdot \left[1 - 2 \cdot \Delta \cdot \left(\frac{r}{a} \right)^2 \right] \quad (2.30a)$$

$$n^2(x, y) = n_1^2 \cdot \left[1 - 2 \cdot \Delta \cdot \left(\frac{x}{a} \right)^2 - 2 \cdot \Delta \cdot \left(\frac{y}{b} \right)^2 \right] \quad (2.30b)$$

In this particular case, solutions of the scalar wave equation are expressed below and correspond to the Laguerre-Gauss (in cylindrical coordinator) or Hermite-Gauss Gauss (in cartesian coordinator). That is, the equations 2.31a-b are the exact solution of the scalar wave.

$$\Psi_{mn}(x, y) = \left(\sqrt{\frac{\xi}{2\pi}} \cdot \frac{1}{\sqrt{2^{m+n}}} \cdot e^{-\frac{\xi \cdot (x^2 + y^2)}{4}} \right) \cdot H_m \left(\sqrt{\frac{\xi}{2}} \cdot x \right) \cdot H_n \left(\sqrt{\frac{\xi}{2}} \cdot y \right) \quad (2.31a)$$

$$\Psi_{lq}(r) = \left(\frac{\xi}{\pi} \cdot \frac{q!}{(q+l)!} \cdot e^{-\frac{\xi \cdot (r^2)}{2}} \right) \cdot (\xi \cdot r^2)^{l/2} \cdot L_q^l(\xi \cdot r^2) \quad (2.31b)$$

These equations use the Laguerre (L) and Hermite (H) polynomials, whose sub index mn or lq are the mode indices. Thereby, H_m and H_n are the Hermite polynomial of order m and n and L_q^l is Laguerre polynomial of order l and q.

$$\xi = \frac{k \cdot n_1 \sqrt{2 \cdot \Delta}}{a} \quad (2.32)$$

The effective index of a mode mn is given by the equation 2.33a-b. From these equations, we can find the propagation constant β by the relation 2.13.

$$n_{eff\ mn}^2 = n_1^2 \cdot \left[1 - \frac{(2 \cdot m + 1) \cdot \sqrt{2 \cdot \Delta}}{k \cdot a \cdot n_1} + \frac{(2 \cdot n + 1) \cdot \sqrt{2 \cdot \Delta}}{k \cdot b \cdot n_1} \right] = n_1^2 \cdot \left[1 - \frac{2 \sqrt{2 \cdot \Delta}}{k \cdot a \cdot n_1} \cdot (n + m + 1) \right] \quad (2.33a)$$

$$n_{eff\ lq}^2 = n_1^2 \cdot \left[1 - \frac{2\sqrt{2}\Delta}{k.a.n_1} \cdot (2q + l - 1) \right] \quad (2.33b)$$

It can be noted that the combination of the sub-index ($n+m+1$ or $2q+l-1$) of certain modes can lead to the same effective index or propagation constant. These modes group are known as principal mode number and use the mode group (MG) order $n+m+1$ or $2q+l-1$.

The total mode group numbers of GI, M_{nt} can be calculated by the equation 2.34 and the total modes, M by the equation 2.35. (See Fig. 2.9). M_{nt} should be rounded to the next smaller integer. Indeed this approximation is valid in graded index fibers supporting a lot of modes (with a huge core).

$$M_{nt} = \left\lfloor k \cdot a \cdot n_2 \sqrt{\frac{\Delta \cdot \alpha}{\alpha + 2}} \right\rfloor \quad (2.34)$$

$$M = M_{nt}^2 + M_{nt} \quad (2.35)$$

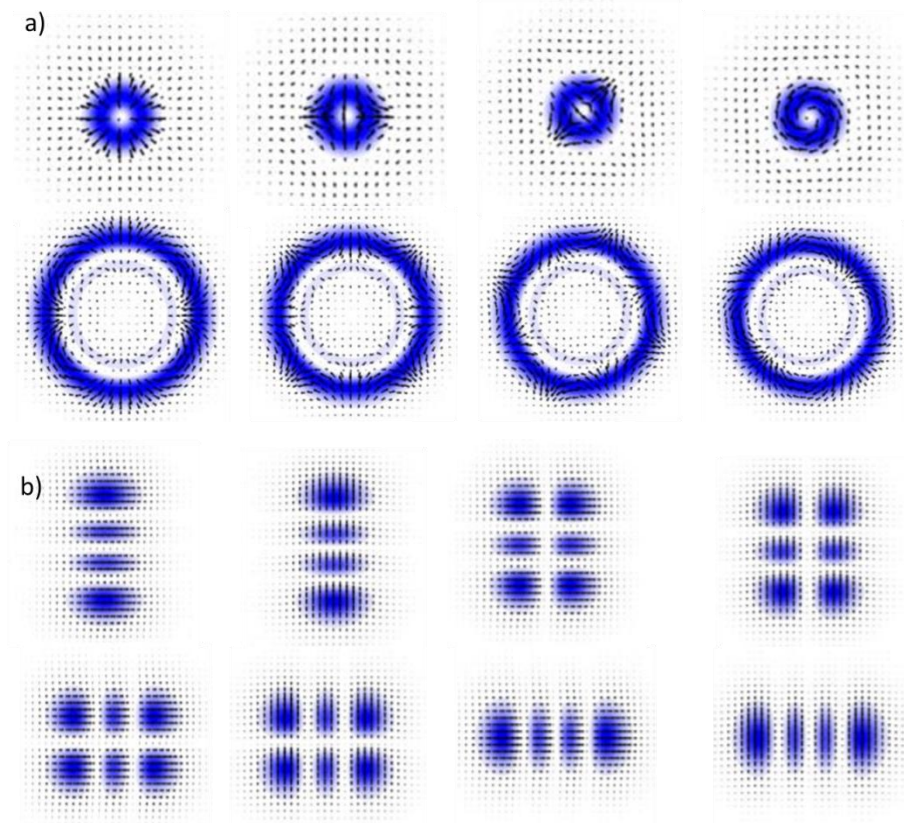


**Figure 2-9: a) Laguerre-Gaussian modes of 4th mode group (=850nm, =1%, a=25μm)
b) Hermite-Gaussian modes of 4th mode group (=850nm, =1%, a=25μm), [Molin, 2016].**

The normalized propagation constant vs normalized frequency for a graded-index is shown in the Fig. 10. Here, the normalized propagation constant is determined by

$$B = 1 - \frac{\sqrt{2n_1}}{v} (2q + l - 1).$$

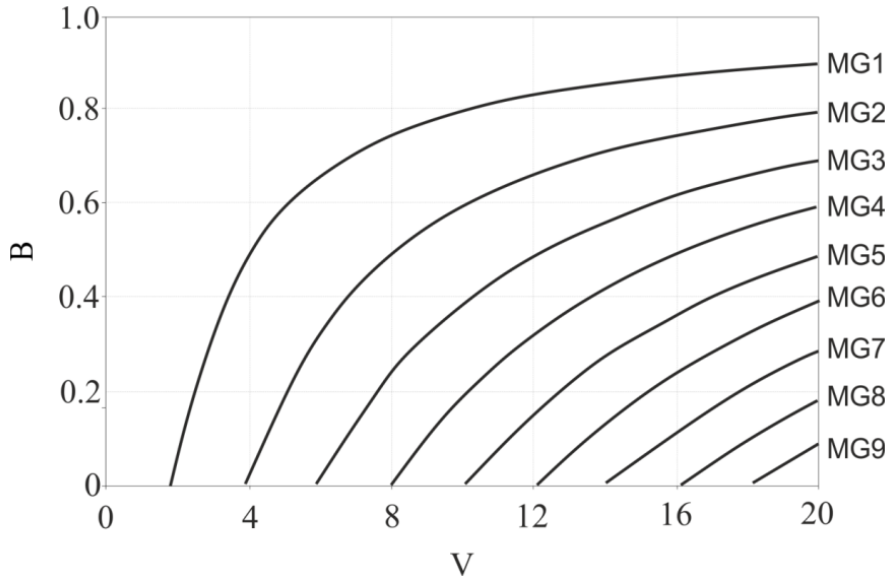


Figure 2-10: Normalized propagation constant vs normalized frequency for a graded index with 9 multi-group (MG) [Molin, 2016].

2.2 Group velocities

The group delay per unit length (fiber length) can be introduced from the group velocity (equation 1.2). It is given by the first order derivative of the propagation constant with respect to the angular frequency.

$$\tau_{\ell q} = \frac{L}{v_g} \quad (2.36)$$

Here, each ℓ, q mode or mode group propagates with its own group delay.

For a graded-index profile, the time delay can be obtained by solving the scalar wave equation or by WKBJ method [Gloge, 1973] (equation 2.37):

$$\tau_{\ell q} = L \frac{n_g}{c} \left(1 - \frac{1}{2} \frac{\left(\alpha - 2 + \frac{2\lambda n_1 \frac{d\Delta}{d\lambda}}{n_g \Delta} \right) \left(\frac{\beta_{\ell q}^2}{n_1^2 k^2} - 1 \right)}{\alpha + 2} + \frac{1}{8} \frac{\left(3\alpha - 2 + \frac{4\lambda n_1 \frac{d\Delta}{d\lambda}}{n_g \Delta} \right) \left(\frac{\beta_{\ell q}^2}{n_1^2 k^2} - 1 \right)^2}{\alpha + 2} \right) + O(\Delta^3) \quad (2.37)$$

$$n_g = n_1 - \lambda \frac{dn_1}{d\lambda} \quad (2.38)$$

In Prysmian's tool the time delays are obtained by solving the scalar wave equation with the Galerkin's method (Appendix D).

2.3 Numerical method

As mentioned before, only in a few types of fibers analytical expression of the eigenvectors can be found (that is step index for vectorial modes, and graded index using approximations). Numerical methods are then important to develop.

Several numerical methods can solve the scalar wave equations. In the current section, we will use the shooting method by using Runge-Kutta 4 procedure to obtain the radiation modes fields (Appendix C). Runge-Kutta 4 is a method for finding numerical solutions of differential equations that combines adaptive step-size routine. As it is well known, numerical methods usually solve systems of first order equations and therefore we must transform the second order equation to first order before applying the numerical method.

Even if we can use this method to find the guided modes, we discard it due to the instability attributable to the fact that the Runge-Kutta's instability does not allow to solve the equation at $x=y=0$. Thus, for guided modes field calculation, the Galerkin method (Appendix D) is one of the best choices, since the shooting method is not appropriate to the large core fibers, because the lower order modes can be miscalculated.

These methods have been developed in MATLAB, and they have been included in the homemade software used by Prysmian. The validations of the guided and leaky modes were assessed by [Molin, 2016].

It is now of interest to introduce the external losses in FMF fiber.

2.4 Few modes fibers

In chapter 1 the FMF based communication system has been discussed briefly. This system uses a class of multimode fibers, well known as FMF that takes few guided modes as a carrier.

To date numerous improvements in the optical properties of FMF have been achieved, such as lower attenuation and modal dispersion control that were inherited from MMF. Despite these improvements, transmission in optical fiber (even FMF) communication system is not 100% effective, chiefly owing to the losses inherent to optical fiber (as Rayleigh scattering) and the external losses produced by fiber mismatches, microbending and macrobending, which will be mainly discussed in 1.2.1, 1.2.3 and 1.2.4.

2.4.1 Rayleigh scattering losses

Rayleigh scattering is the dominant losses mechanism in silica based fibers and it depends on the chemical composition of the fiber. For instance, the higher the dopant concentration, the higher the losses. This parameter varies as $1/\lambda^4$. Rayleigh scattering has been studied in SMF and MMF. Even if our interest is the Rayleigh scattering applied to FMF [Wang, 2016], we will use the Rayleigh scattering losses definition as in [Tsujikawa, (2007)].

$$\alpha_{\beta} = \frac{\int R(r) \cdot |\Psi(r)|^2 r dr}{\lambda^4 \int |\Psi(r)|^2 r dr} \quad (2.39)$$

Here $R(r)$ is the local Rayleigh scattering coefficient and it depends on the fabrication process. $R(r) = R_{si} \cdot (1 + a \cdot c_{Ge}(r) + b \cdot c_F(r))$. Where, a and b are constants, $c_{Ge}(r)$ and $c_F(r)$ are the radial concentration of dopant over the radius expressed in weight percent, in the case of fiber doped with germanium or fluoride.

2.4.2 Microbending losses

Microbending is the loss produced by random bends in the fiber axis and it is mainly dependent on mechanical properties (namely the mechanical stress) of the coating around the fiber. Microbending will be studied in Chapter 3.

2.4.3 Macrobending losses

Macrobending is the loss mechanism associated with bending which produces light leakage in the fiber and it is strongly dependent on the optical properties. Macrobending losses increase logarithmically as the bend radius decreases [Jay, 2010] and it is usually expressed in dB/turn or dB/m for SMF. However, for MMF and SMF, it should be treated differently, especially in MMF, since each mode can have different bend sensitivities on account that the highest order modes are weakly guided compared to the lowest order modes and thus more sensitive to bending. In MMF, the bend loss is expressed in dB by specifying the number of turn and the launching conditions. The launching conditions can influence the bend losses, since a launching condition that predominantly excites the highest order modes produces higher bend loss than a launching condition that excites the lowest order modes.

Hence, the most appropriate launching condition is when the modes are equally excited, such as was developed in the Prysmian's homemade tool [Molin, 2016].

In this tool, the macrobending loss was calculated by considering the semi-analytical approach that is an extension of Marcuse's model [Marcuse, 1976]. Here, all the modes are assumed to be leaky modes, since the external cladding index always surpasses that of the core somewhere. That is, under bending conditions there are no more guided modes and so the propagation constant of all eigenmodes are complex and the macrobending losses calculation only considers the imaginary part of the propagation constant. The optical power outside of the fiber core can be calculated by the expansion of the mode field onto a superposition of cylindrical outgoing waves, thereby we can approximate the bend losses for the bend radius of each guided mode as [Molin, 2016].

One strategy to control the macrobending will be presented in the next paragraph.

2.4.4 Design of trench on refractive index of FMF

It is well known that the bending behavior of FMF fibers is usually different from that of SMF fibers, because the different modes of the FMF can have different bend sensitivities and in addition coupling between modes can occur, which is not the case in SMF. Generally, the highest order modes (HOM) are more sensitive to bending than the lowest order modes since they are weaker guided (n_{eff} close to the cladding). To minimize this macro bending effect, the index profile of the fibers includes a trench in the outer cladding [Molin, 2010]. Using the trench, the macrobending losses can be decreased, without changing the N.A. It should be noted that the trench mainly affects the highest order mode groups.

To obtain an appropriate trench effect, we must carefully design the fiber and therefore locate appropriately the trench. Macrobending losses can be reduced by larger trench volume but it requires improved guidance of undesirable leaky modes, if the trench volume is too large.

Figure 2.11 shows a GI fiber with a trench. To mitigate the presence of the external modes and their negative effects, especially losses and high delay, we must find a compromise on the position of the trench with respect to the core, thus:

- The trench should be close (but not too close) from the core to reduce the losses produced by the external modes (cf. Fig. 2.11, w_1)
- The space between the core and trench should be optimal to minimize differential delay between guided and leaky modes.

Propagation in the Few Modes Fiber (FMF)

These modes can be confined within the core because the trench is too close to the core, resulting in an increase of differential mode group delay, because the highest order modes tend to be slower than the others owing to their excessively high time delay, whose major influence is in the bandwidth.

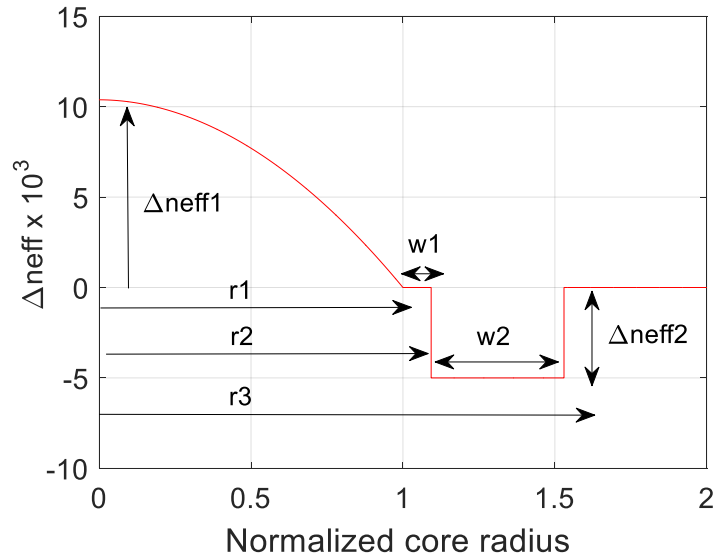


Figure 2-11: Refractive index with trench. r_1 is the length between $R=0$ and the end of the parabolic shape, r_2 is the length between $R=0$ and the beginning of the trench, r_3 is the radius distance between $R=0$ and the end of the trench. Δn_{eff1} is the differential refractive index of the parabolic shape, and Δn_{eff2} is the differential refractive index of the trench. w_1 is width after parabolic shape and before trench. w_2 is width of the trench.

As this profile index promises a low differential mode group delay, low mode coupling and low loss, we will be using the optical fiber with 6-LP modes as in [Sillard, 2014] that is optimized by the trench-assisted fiber design [Molin, 2010]. To obtain the optimized 6-LP mode, firstly, we establish the normalized frequency to support six LP modes, then the trench volume should be adjusted to ensure bend losses less than 10dB/turn at 10mm. It must be mentioned, however, that the optimal α in the parabolic profile does not depend on the trench design.

To find an optimal profile, one of the solutions is to introduce a small cladding between the parabolic index core and the trench. The refractive index inside the cladding (inner ring) is used to equalize the time delay (TD) between the HOM and the other modes.

To manage the time delays of the HOM, we can optimize the position of the trench in the external cladding or implementing the trench far of the core and limits the trench depth.

Prysmian uses a tool based on like pattern search or genetic algorithms to optimize multi-parameters, like exponent of the gradient, the core-cladding interface and volume, position of trench.

2.5 Example GI FMF with trench

Six different profiles fibers keeping 6 LP-modes with varying effective refractive-index differences (see table 2.1) have been designed by numerical method. The effective refractive-index differences are calculated by the difference between the maximal effective refractive index of each mode and the refractive index of the cladding at 1550 nm

$$\Delta n_{eff} = n_{eff}(\text{group of modes } N) - n_{eff}(\text{group of modes } N - 1).$$

Likewise, the trenches of these profiles are optimized by using the optimization algorithms from MATLAB to manage the highest order mode effect and obtain the minimal macro-bending losses.

Two profiles of these fibers will be studied, which correspond to those that can be manufactured with the current manufacturing techniques, $\Delta n_{eff} = 2.1 \times 10^{-3}$ with a core radius of $14\mu\text{m}$ and $\Delta n_{eff} = 3.3 \times 10^{-3}$ with a core radius of $11\mu\text{m}$ (see Fig. 2.12) in term of guided and radiation modes. Indeed, the purpose of this section is to analyze the behavior of these two extreme designs of fibers with regard to the Δn_{eff} effect on the time delay and losses.

It is important to note that the procedure to obtain the propagation constant, field, profile, Δn_{eff} , and so on was discussed in the previous sections of this chapter.

These profiles will also be used in the coupling analysis of the next chapter.

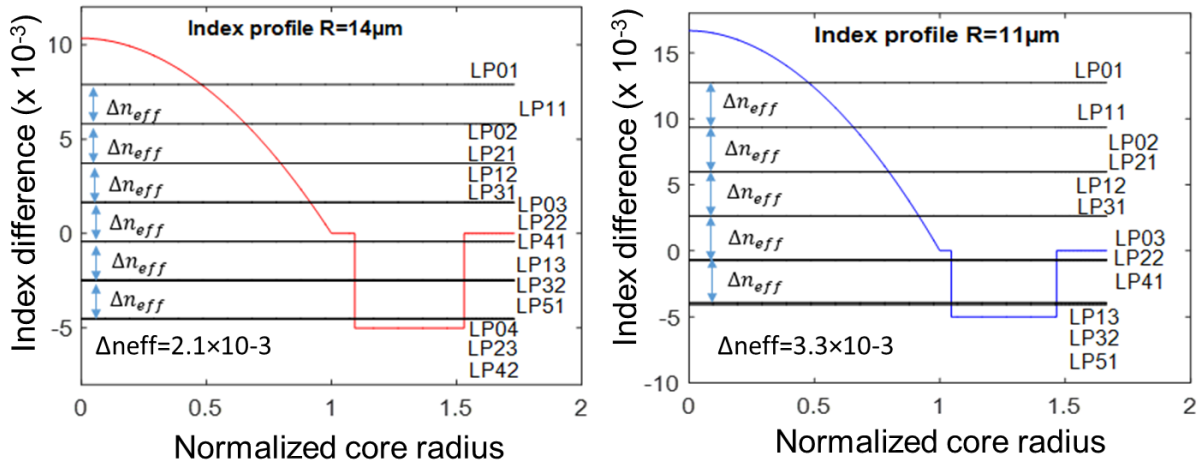


Figure 2-12: Index profile difference for both profiles. Here, LP01, LP11, LP02, LP21, LP12 and LP31 correspond to six guided modes groups, the rest of the modes correspond to the leaky modes. It should be noted that the amount of leaky modes is different between both profiles. Note that the leaky modes appear at $\Delta n_{eff} < 0$, whereas the guided modes exist for $\Delta n_{eff} > 0$. Right: core radius=11µm ($\Delta n_{eff}=3.3 \times 10^{-3}$), Left: core radius=14µm ($\Delta n_{eff}=2.1 \times 10^{-3}$).

2.5.1 Study of trench depth

We study the variation of the differential time delay as a consequence of the variation of the trench depth for two different profiles (See Fig. 2.12). Here, width w_1 and w_2 (cf. Fig. 2.11) and the trench position are fixed taking into account the recommendation of the section 2.4.4

Time delay (TD) (details in the chapter 1, equation 2.37) is obtained from wave equation, and therefore the differential TD by the maximum and minimum value of TD. Figure 2.13 a) and b) show how the TD difference depends on the depth of the trench.

Figure 2.13a and 2.13b also show that the lower macrobending can be achieved for greater depths of the trench, however with a trench deeper than 5µm, the manufacturing process can become complex. The optimal depth of the trench is around -5 µm since at this location the differential time delay is minimized and thus the bandwidth [Molin, 2016].

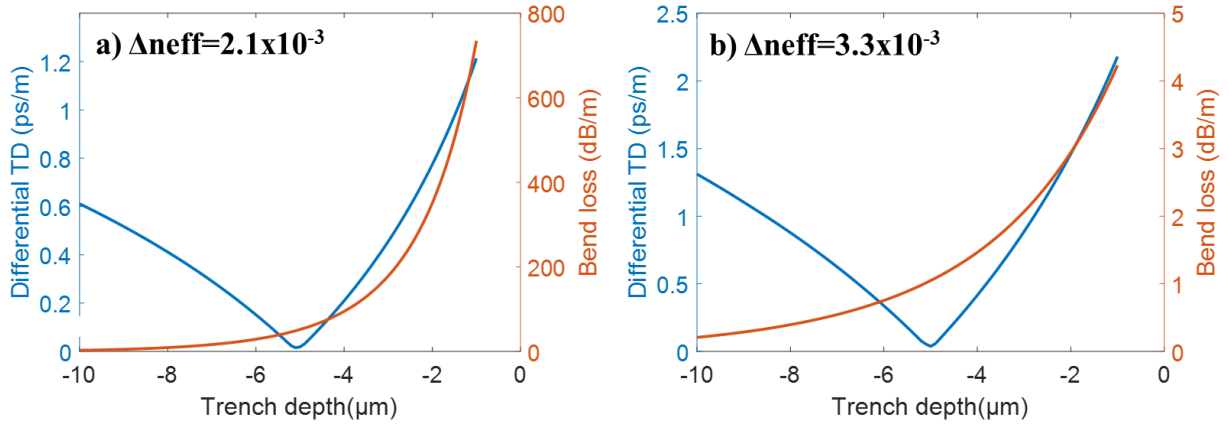


Figure 2-13: Modeling of differential time delay as a function of trench depth for: a) $\Delta n_{eff}=2.1 \times 10^{-3}$ and b) $\Delta n_{eff}=3.3 \times 10^{-3}$.

2.5.2 Impact of differential TD by the modification of the Δn_{eff}

To study the impact of the parameters of the FMF on Δn_{eff} , we have used six FMF fibers with trench-assisted graded-index-core profiles and different Δn_{eff} . These FMF were designed for supporting 6 modes (normalized frequency of $V=9.65$). Besides, they were optimized to get the smallest differential TD possible, low bend losses (<10 dB/turn at 10mm radius) for all the guided modes and high losses (>19.34 dB on a 22m sample) for the higher-order leaky modes to guarantee effective cut-off. That is, the width, depth and position of the trench and the refractive index profile between the end of the gradient and the interior trench radius were carefully adjusted to obtain the best performance in term of macrobending.

Later, we obtain the time delay by the wave equation and we compare all the profiles in terms of differential TD. These profiles will also be used to study the coupling.

Table 2.1: Fiber parameters for the six FMF fibers with trench-assisted graded-index-core profiles. Δn_{eff} varies between 1.8×10^{-3} and 4.4×10^{-3} . Here, we will focus only on $R=11\mu\text{m}$ and $R=14\mu\text{m}$. The calculations of the other profiles follow the same procedure.

Rcore (μm)	10	11	12	13	14	15
$\Delta_{core} \times 10^{-3}$	19.4	16.1	13.5	11.5	10	8.7
$\Delta n_{eff} \times 10^{-3}$	4.4	3.3	2.8	2.4	2.1	1.8
MaxTD - MinTD (ps/km)	312	35.9	26	21.6	18.8	16.1

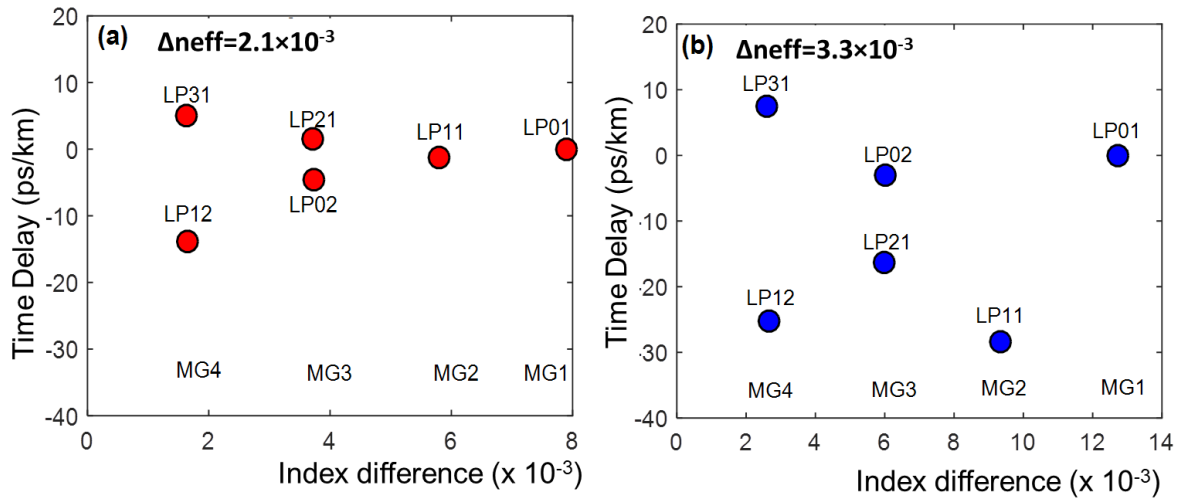


Figure 2-14: Time delay for each modes a) core radius= $14\mu\text{m}$ ($\Delta n_{eff}=2.1 \times 10^{-3}$) b) core radius= $11\mu\text{m}$ ($\Delta n_{eff}=3.3 \times 10^{-3}$). Here, we have grouped into 4 multi-group (MG) taking into account almost the same Δn_{eff} . Thus, LP01(MG1), LP11(MG2), LP02(MG3), LP21(MG3), LP12(MG4). The index difference is the difference between the effective refractive index and the refractive index from cladding.

Using the figure 2.14 is also possible to find the difference between the maximum value and the minimum value of TD, for example for $\Delta n_{eff} = 3.3 \times 10^{-3}$, the maximal value is given by LP₃₁ (8.3 ps/km) and the minimum value by LP₁₁ (-27.6 ps/km), hence the differential TD is (8.3 ps/km - (-27.6 ps/km)) = 35.9 ps/km. Note that TD is considered with reference to LP₀₁.

In figure 2.15, note that as Δn_{eff} decreases the difference time delay decreases, because the difference of propagation constant between the different modes tends to be smaller. This is evident when we compare the difference in time delay between LP₃₁ and LP₁₂ (M4) of the Fig. 2.14a and 2.14b. Likewise, as the modes number increases, time delay increases within a given mode group.

We have demonstrated that for a given V number, the lower difference time delay is reached with a bigger core radius. However, a greater radius in FMF with GI trench can increase the amount of leaky modes that is one of the main causes of the losses under certain conditions. As we will see, Δn_{eff} is used in the design of FMF to control the time delay between modes and so the coupling.

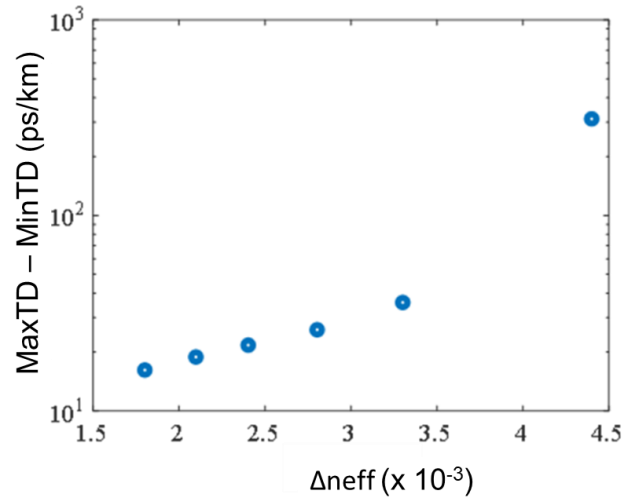


Figure 2-15: Maximum time delay for the different profiles of the table 2.1.

2.5.3 Guided modes

The field intensity of two 6-LP-mode for fibers with different core radius ($R=14 \mu\text{m}$ and $R=11 \mu\text{m}$) are simulated by the LP basis function. These field intensities are normalized to unit with respect to the core radius, such that their maximum value is one. Note that figures 2.16c-d are plotted in absolute values and these figures show the 6 LP modes: LP_{01} , LP_{02} , LP_{11} , LP_{12} , LP_{21} and LP_{31} . All guided modes are essentially restricted to the core region and the fundamental mode, LP_{01} tends to follow the index profile shape in the core region.

Figure 2.16 shows that as the number of modes increases, the amplitude of the field $F(R)$ is increasingly elongated to the cladding, because part of the energy goes away from the core. Besides, the number of times the radial function, $F(R)$ crosses zero for a $LP_{\nu\mu}$ mode corresponds to the radial term (μ) minus 1. Thus, For LP_{11} , LP_{21} and LP_{31} , $\mu=1$, there are no zeros.

Propagation in the Few Modes Fiber (FMF)

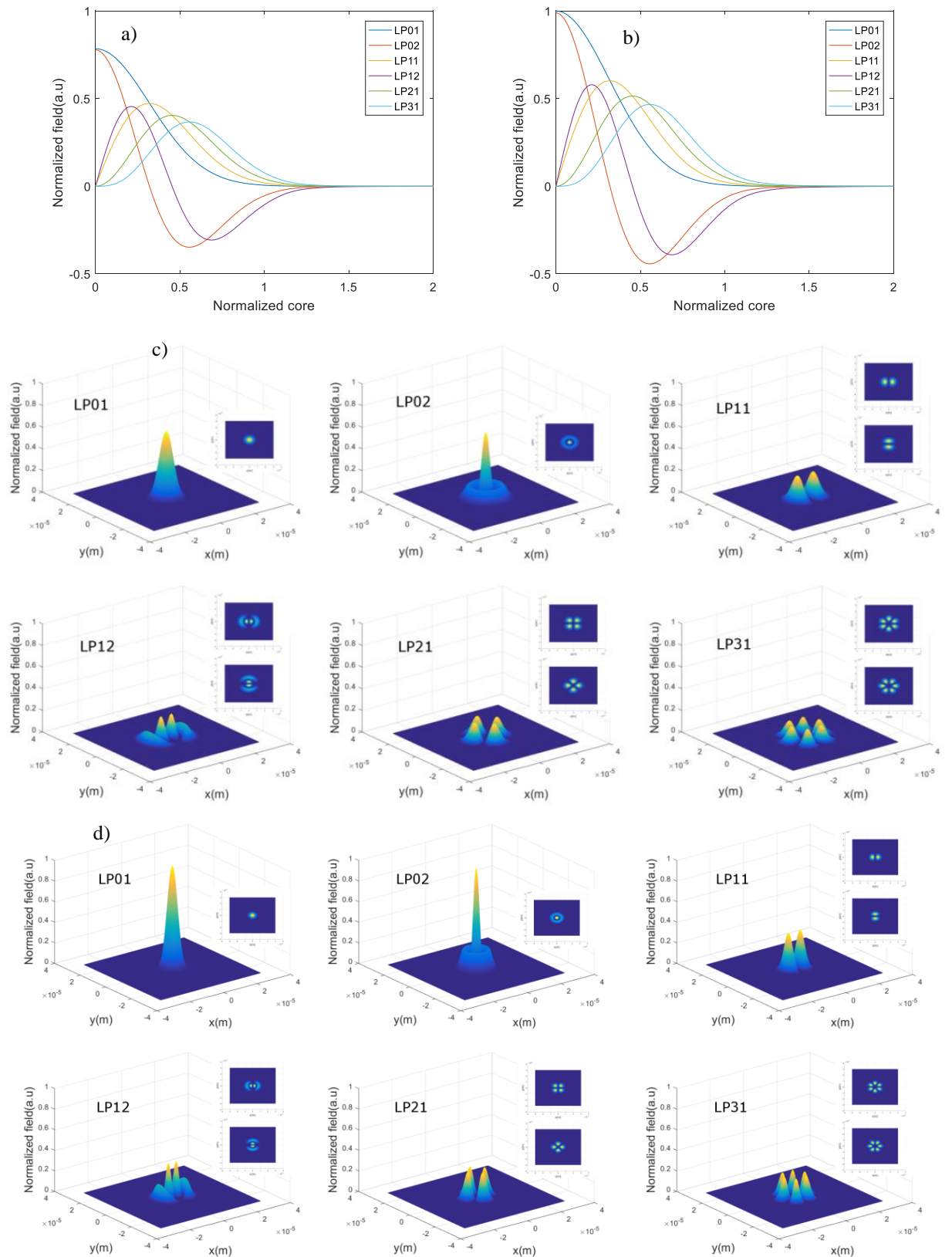


Figure 2-16: F(R) of the 6-LP modes with a-c) $R=14\mu\text{m}$ ($\Delta n_{\text{eff}}=2.1 \times 10^{-3}$) and b-d) $R=11\mu\text{m}$ ($\Delta n_{\text{eff}}=3.3 \times 10^{-3}$).

As we have discussed, there are two polarizations, two for each fundamental mode with $v=0$ and 2 modes and 2 polarizations when $v>0$. In this example, we have 20 guided modes.

For both profiles, we evaluate the losses for all the modes considering an injection on only one mode i of fiber ($i=1,2,\dots,N$) at $z=0$. That is, we calculate the total power section after section, or the sum of the power of all modes. In this calculation, we have only included the Rayleigh scattering (section 2.4.1) for all modes, because β in the guided-modes are real and therefore their leakage losses are null.

Figure 2.17 shows the Rayleigh losses for the two fibers profiles (2.1@ $R=14\ \mu\text{m}$ and 3.3@ $R=11\ \mu\text{m}$). Both profiles keep the same concentration of fluoride (cFl), however they have different concentration of germanium (cGe), so that the fiber profile with a small Δn_{eff} exhibits smaller losses which can be attributed to the lower concentration of germanium (cGe) [Zhi, 2003].

Δn_{eff} decreases, because Δn decreases, which reduces the diffusion.

Note also that for a large Δ (refractive index contrast of an optical fiber) we can find the maximum losses. The information of Δ at 633 nm for each profile is given below:

- Δ @633 nm at 1% 0.705 for $\Delta n_{eff} (\times 10^{-3}) = 2.1$.
- Δ @633 nm at 1% 1.132 for $\Delta n_{eff} (\times 10^{-3}) = 3.3$.

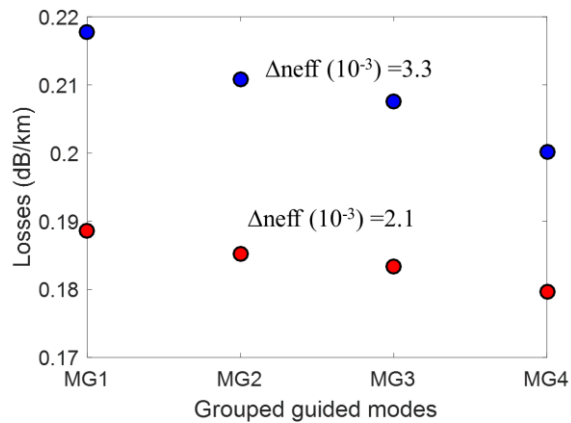


Figure 2-17: Rayleigh losses in guided modes for the profile of the Fig. 2.12.

2.5.4 Leaky modes

The Leaky modes propagate as guided modes but can have leakage losses due to the imaginary part of their propagation constant. This leakage loss could also affect the guided

Propagation in the Few Modes Fiber (FMF)

modes, because leaky modes are capable of being reflected at the core-cladding interface and at the boundary between the inner cladding and the trench. Therefore, it would be far better if we could avoid them.

The Leaky modes correspond to the discrete set of eigenmodes with complex propagation constant. Likewise, they satisfy the propagation equation by considering a complex propagation constant β . The β limits where the leaky modes can appear are:

($k \cdot n_2 > \text{real}(\beta) > k \cdot n_{\text{trench}}$), Here, n_{trench} is the refractive index of the trench.

To obtain the leaky modes, the shooting method (Appendix B) which has been studied in conventional fibers and special fiber profiles with a trench, can be used. In this part the derivations follow the outline of [Molin, 2016].

Let us see the following example that corresponds to the two fibers studied for guided modes:

- For $\Delta n_{\text{eff}} = 2.1 \times 10^{-3}$, the limits of β correspond to $k \cdot (1.457) > \text{real}(\beta) > k \cdot (1.452)$
- For $\Delta n_{\text{eff}} = 3.3 \times 10^{-3}$, the limits of β correspond to $k \cdot (1.457) > \text{real}(\beta) > k \cdot (1.452)$

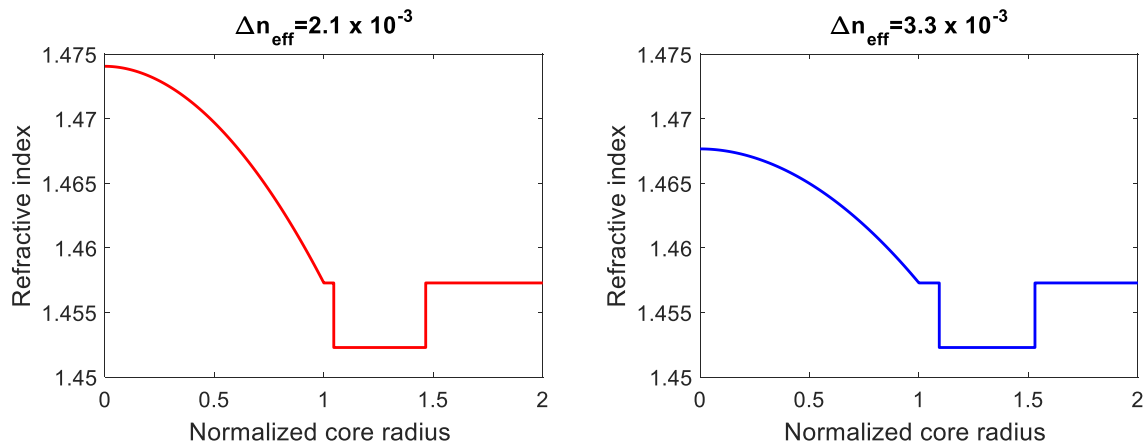


Figure 2-18: Refractive index profile for a) $\Delta n_{\text{eff}}=2.1 \times 10^{-3}$ and b) $\Delta n_{\text{eff}}=3.3 \times 10^{-3}$.

It should be noted that the maximum core radius between both profiles is found for $\Delta n_{\text{eff}} = 2.1 \times 10^{-3}$, which could allow the appearance of more leaky modes. In these examples, the first leaky mode is LP_{41} and the last leaky modes are LP_{13} and LP_{04} for $\Delta n_{\text{eff}} = 2.1 \times 10^{-3}$ and $\Delta n_{\text{eff}} = 3.3 \times 10^{-3}$ respectively. It means that the $\Delta n_{\text{eff}} = 2.1 \times 10^{-3}$ profile presents three more leaky modes. Besides, the leakage+Rayleigh losses and time delay on the leaky modes of these fibers will be taken into account, to be later studied on the effect of the coupling between the leaky and guided modes (Chapter 3).

Propagation in the Few Modes Fiber (FMF)

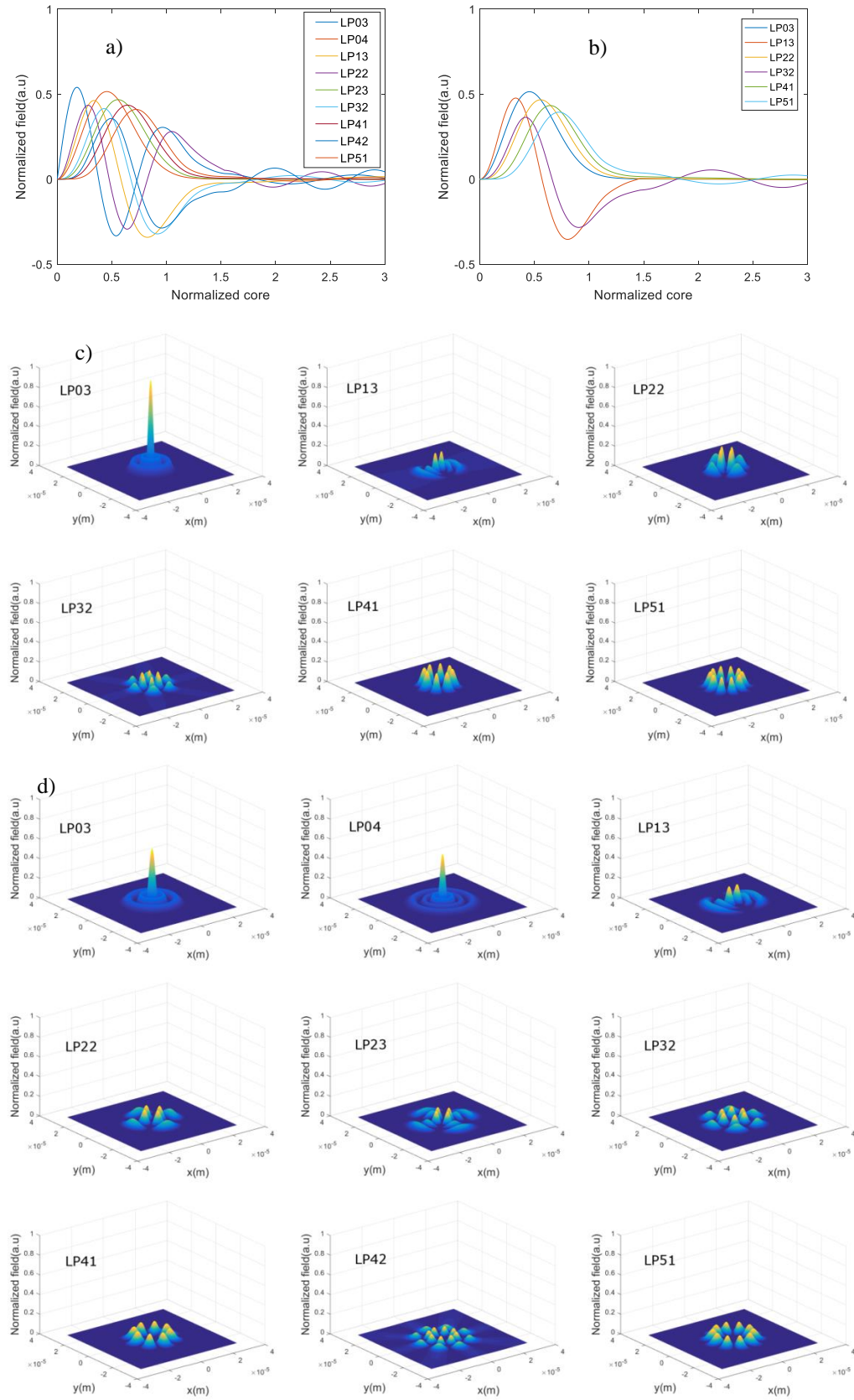


Figure 2-19: a-b) Intensity field of leaky modes for a) $R=14\mu\text{m}$ ($\Delta n_{\text{eff}}=2.1 \times 10^{-3}$) and b) $R=11\mu\text{m}$ ($\Delta n_{\text{eff}}=3.3 \times 10^{-3}$). c-d) Field Intensity of leaky modes for a) $R=14\mu\text{m}$ ($\Delta n_{\text{eff}}=2.1 \times 10^{-3}$) and b) $R=11\mu\text{m}$ ($\Delta n_{\text{eff}}=3.3 \times 10^{-3}$).

Figure 2.20 illustrates the time delay for each leaky modes in the two fibers studied. As one can see, the leaky modes exhibit a very much larger delay than the guided modes (Fig. 2.14). More precisely speaking, the larger delays are found over the leaky modes that are the furthest away from the core since they reach the end of the fiber later than lower order modes.

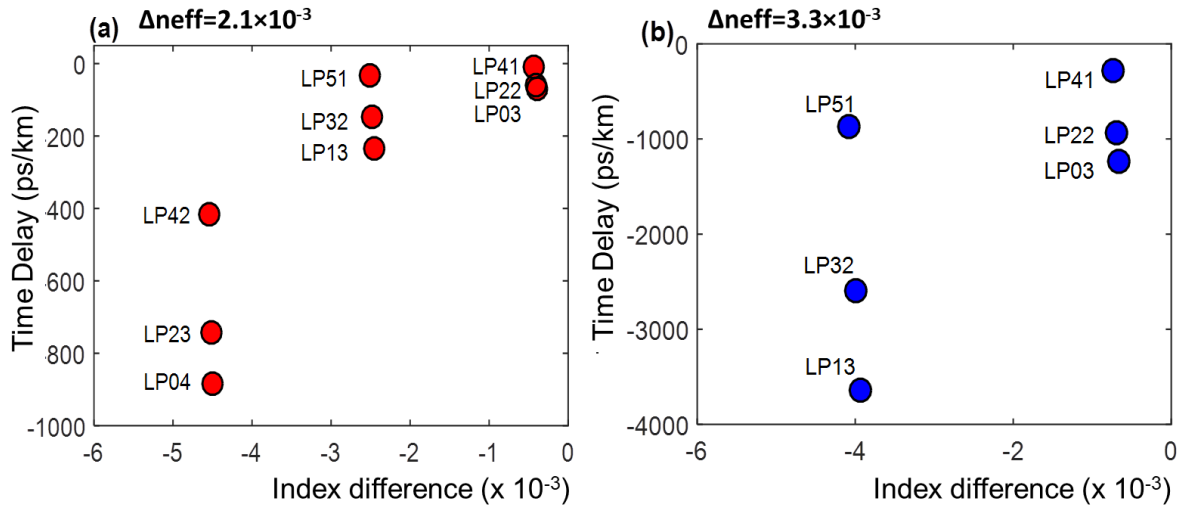


Figure 2-20: Time delay for each leaky modes a) core radius= $11\mu\text{m}$ ($\Delta n_{\text{eff}}=3.3 \times 10^{-3}$), b) core radius= $14\mu\text{m}$ ($\Delta n_{\text{eff}}=2.1 \times 10^{-3}$). The index difference is the difference between the effective refractive index and the refractive index from cladding.

Figure 2.21 represents the leakage + Rayleigh losses for both profiles studied. Here, the Rayleigh loss is calculated by equation 2.39, while the leakage loss is defined by the imaginary part of the propagation constant as:

$$(\text{dB/m}) \text{ loss} = \frac{20}{\ln(10)} \cdot \text{Imaginary}(\beta).$$

Note that leakage + Rayleigh losses increase exponentially and more quickly than the Rayleigh losses of the guided modes (see Fig. 2.17 and 2.21a-c). If we compare both profile, losses are larger in the fiber with lower radius ($\Delta n_{\text{eff}} = 3.3 \times 10^{-3}$) because it presents more leakage losses than the other profile (see Fig. 2.21a-b). Note also that the leakage loss is extremely high, which make that some of these leaky modes disappear along the propagation (especially at several kilometers).

Besides, by varying the position, the depth and thickness of the trench, the leakage losses can be managed. Thus, a wider trench without changing the radius will produce the same amount of leaky modes with lower leakage losses. Now if the trench tends to be infinitely wide, the leaky modes become guided without significant leakage losses.

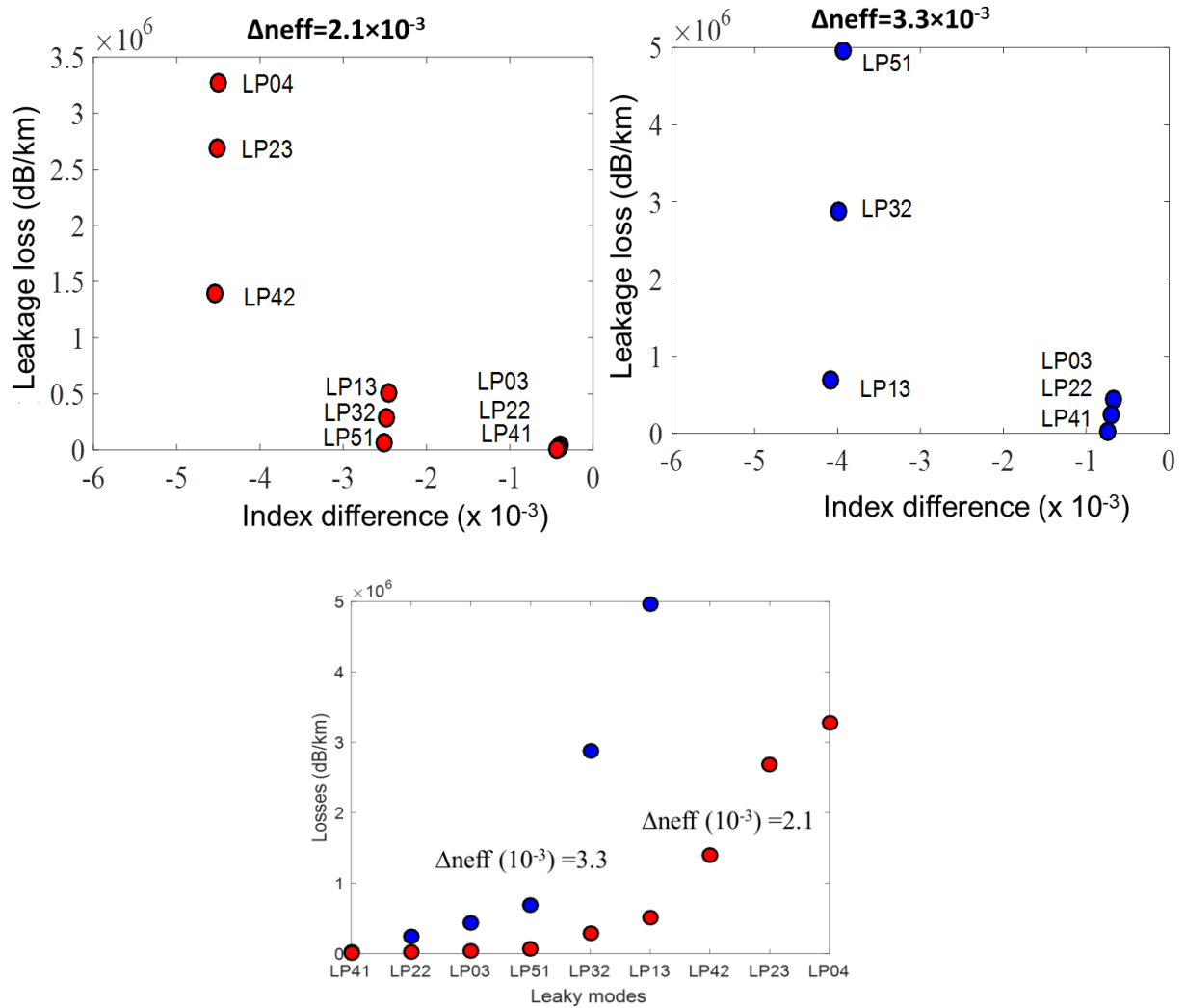


Figure 2-21: a-b) Leakage loss in leaky modes for both studied profile. c) (Rayleigh + Leakage) in leaky modes for the profile of the Fig. 2.12.

2.6 Summary

In this chapter we have studied the notion of the guided mode by solving Maxwell's equations and more importantly, by placing ourselves in the context of the weakly guiding approximation. As discussed this approximation simplifies the solutions of Maxwell's equation under the condition that the normalized refractive index difference is much smaller than unity. Here, the longitudinal components can be neglected, because the fields are transverse which gives rise to the linearly polarized modes (LP), widely used in the study of the optical fiber.

We have demonstrated that a complete analytical set of solutions can be easily obtained in a step index fiber. Conversely, for a graded index it is impossible to obtain these exact equations, which leads to use an approximation whose solutions can be obtained by semi-analytical methods, such as Laguerre-Gauss and Hermite-gauss. Note that the exact or approximated solution is dependent on the specific refractive index profile. In this chapter several fibers with a graded index optimized in order to minimize the macrobending losses and to manage the time delay difference and Δn_{eff} were studied.

The modes of higher order are mostly affected by the cladding profile, making them more sensitive to the leaky modes effect. These effects (losses) can be reduced by avoiding the appearance of these modes by a careful design of the optical fiber. Here, we have also obtained the radiation modes, but it was impossible to make an extensive study of their effects in the guided modes.

In the next chapter, we will study the coupling on the fibers used in the example GI FMF with trench.

3 Coupled mode in the emerging MDM communication systems

A mode division multiplexing system using an FMF with N spatial mode as data channels to transmit N independent information is a potential candidate to the new generation of optical communication systems because it can increase the optical transmission capacity around N-times of an SMF communication system. Many spatial bases of mode, such as LP modes (chapter 2), Principal Modes (PM) (see section 1.4) or modes with an orbital angular momentum (OAM) [Wang, 2014] [Djordjevic, 2016] can be used in MDM systems. However, regardless of the spatial modes used, MDM systems could be affected by mode coupling which produces crosstalk. OAM will not be treated within this study.

Crosstalk can be defined as the mixing of different data channels due to optical power coupling (optical mixing). This power distribution can be written as:

$$\text{Crosstalk (dB)}=10.\log(P_{1\rightarrow 2}/ P_1)$$

Note that the distributed power from channel 1 to channel 2 ($P_{1\rightarrow 2}$) is compared with the total power of channel 1.

The presence of optical crosstalk will affect communications system performance, limiting capacity per unit distance. To explain this phenomenon on communication systems, the following two optical architectures will be used:

- MDM system using an FMF (Fig. 3.1a and 3.2a)
- WDM using an SMF (Fig. 3.1b and 3.2b).

In Figure 3.1a-b are shown these communication systems in the absence of crosstalk. Here, both schemes use multiplexer and demultiplexer elements in order to combine and separate each spatial mode (MDM) or each signal as a function of wavelength (WDM). Note that at the end of the transmission process, in the absence of crosstalk, the signals are affected only by the attenuation in the channel (Optical fiber). The maximal throughput achieved is mainly limited by the FMF bandwidth.

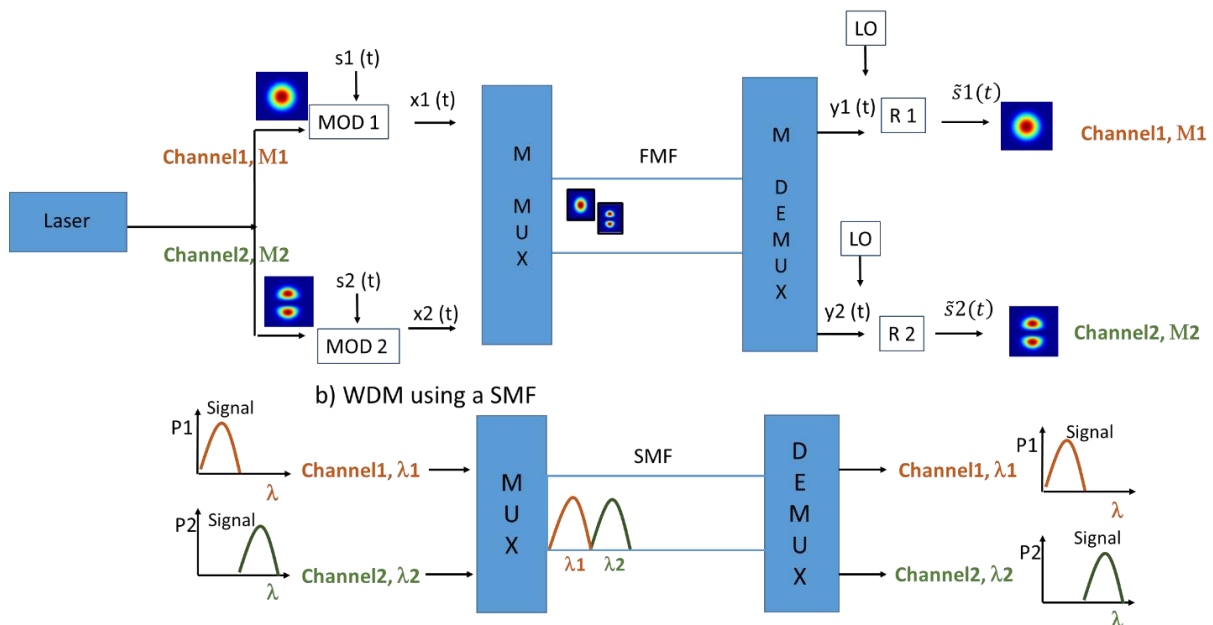


Figure 3-1: General scheme of a) MDM using an FMF with 2 LP modes. b) WDM using an SMF with 2 wavelengths (it was discussed in chapter 1). Here, a laser is used as transmitter divided into N number of modulators. Modulator encodes different data to obtain a modulated optical signal. A basis LP for example is multiplexed (M-MUX) and transmitted on FMF. At the end of the transmission, each mode is de-multiplexed (M-DEMUX) and detected by the photodiodes

Figure 3.2a-b shows the communication system in the presence of crosstalk. The crosstalk in MDM system can be defined as modal crosstalk, because it appears as a consequence of the energy exchange between modes which share the same physical space. Hence, the power of one mode can be transferred to another mode, producing the mode coupling. This effect can only occur in the presence of a perturbation of the waveguide. A perturbation can be created by fiber irregularities (intentional - tapering - or not - random fluctuations), stress, twist, macro or micro-bending. In WDM, it can occur between neighboring channels (out-of-band crosstalk) or signals with same wavelength (in-band crosstalk). Contrary to MDM systems, it finds its origin in nonlinear interactions between the different wavelength channels.

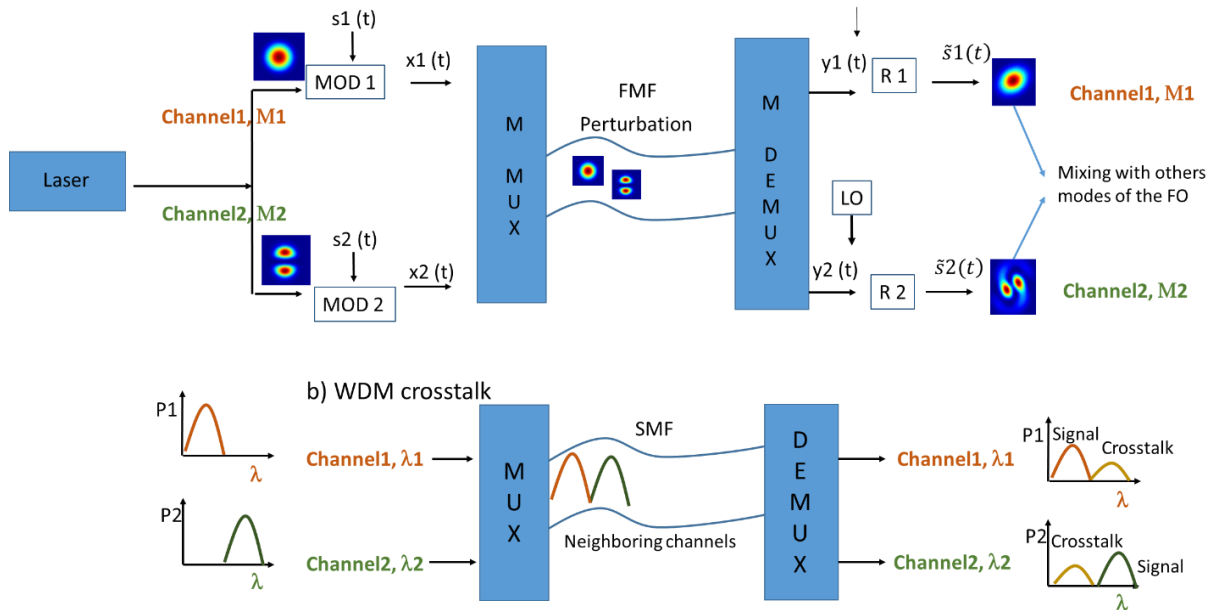


Figure 3-2: Crosstalk in a) MDM using an FMF with 2 LP modes and b) WDM using an SMF with 2 wavelengths.

We usually use the MIMO-DSP (Chapter 1) to mitigate the crosstalk in a communication system. Concerning MDM, the MIMO-DSP is designed in regards of the coupling regime.

As discussed above, crosstalk in long fiber span is mainly produced by coupling. Therefore, in this chapter we will focus on mode coupling only in the optical fiber, and not that produced in each element of the communications system. To describe the coupling in an optical fiber, coupled equations are used. These equations can be obtained by many different ways, but one of most known approaches is through the theories of coupled modes from [Marcuse 1984].

Since mode coupling is mainly generated by a perturbation, the coupling model must take into account this geometrical modification. In an optical fiber, three typical perturbations can occur, such as described in Fig. 3.3. The first one corresponds to a displacement of the core because of a non-centered splice, the second one corresponds to a displacement of the core due to variation that could be produced by the manufacturing process or an applied tension. The last one corresponds to the variation of the core size along the propagation axis (tapered core) that could be produced during the fabrication of the fiber.

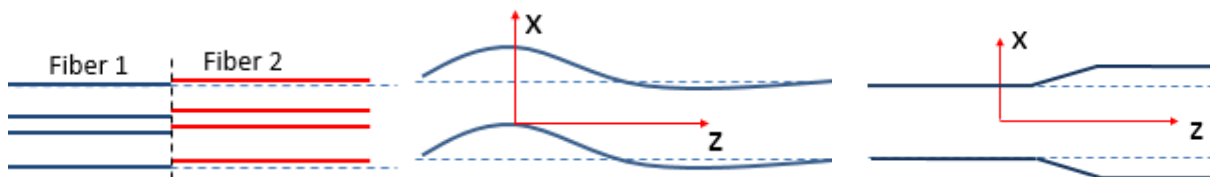


Figure 3-3: Perturbation in the optical fiber. The dotted line corresponds to the unperturbed fiber, whereas the continuous corresponds to the perturbation. a) Splices b) perturbed core, c) tapered core.

It should be noted that the biggest challenge in modeling the coupling effect in the fiber comes from the variety of phenomena that must be taken into account and the random aspect of the birefringence and perturbations in the fiber that makes the coupling localization and quantification difficult to foresee.

As we will discuss later, we must adapt the model according to the treatment of the perturbation.

3.1 State of the art

The coupling studies in FMF date back from the coupling studies in MMF. Therefore, a power coupling theory [Olshansky, 1975] [Gloge, 1972] was developed and used for the first generation of MMF and it is still relevant for MMF laser systems. However, power-coupling theory is unable to take into account the polarization mode dispersion and the existence of main state of polarization. These latest effects are widely used to describe the polarization mode dispersion in SMF [Poole, 1986] and the modal dispersion in MMF [Fan, 2005].

Furthermore, in power coupling, the power distribution always becomes uniform, even in the presence of the perturbation. In practice it has been demonstrated that one uniform perturbation can present random fluctuation on time and space, particularly in terms of phase. This phase variation can be modeled using the field coupling model [Shemirani, 2009] by dividing the optical fiber into several regular sections and model an ensemble of different random phase shifts between the uniform perturbed sections. This model can reproduce the ensemble-average result obtained using the power coupling model.

The field coupling theory can also describe statistically the coupled group delay (GDs) and the mode dependent loss [Juarez, 2014], which has allowed it to gain ground in the coupling studies of the MMF

Following the above studies, theory of mode coupling has also contributed to the design of devices manufactured from FMF. For example, the passive components do not require an external source of energy and many all-fiber passive components are designed by using technologies such as fusion-tapering and grating descriptions. Similarly, the splitter and combiners are based on couplers (FMF modal couplers [Jung, 2013], [Ismaeel, 2013], [Jung, 2014]). Indeed, several components can be concatenated or mixed to have a behavior, which may become more interesting. Moreover, many of these devices use fibers designed to enhance the coupling between modes, as Bragg grating [Wu, 2012] [Fang, 2014] [Ali, 2015] and long period gratings [Erdogan, 1997] [Lee, 2000]. They use small and periodic perturbations to generate the coupling.

If we look at active devices such as the laser, coupled mode has been tested to represent an important mechanism for mode locking based in nonlinear mode coupling [Proctor, 2005] and to realize tunable laser based in tapered fiber [Huang, 2016], or based in two-mode fiber [Yun, 1996]. Other contributions are found in the amplifiers [Jung, 2014] [Trinel, 2017].

Independently of the domain, coupling is relevant in the design of optical fibers especially with new characteristics, either for the emerging communications systems (as we will see in the next section) or for the development of all-fiber devices.

Emerging communication systems use space division multiplexing to increase the transmission rate and to overcome the optical network capacity crunch (as seen in chapter 1). They are based on excitation and detection of a modes group (MG) which are formed by one or several guided modes with almost the same propagation constant, and therefore information is encoded on each of these modes.

One of the advantages of using fiber designed for weak coupling is that a simple MIMO is sufficient to detect the different signals at the end of transmission. Nevertheless, by a simple MIMO, the performance of the signal cannot be improved because, generally, the signal processing is non-existent but it could exist. Note that this approach is interesting for short transmission, including those that use direct detection [Nazarathy, 2013]. However, for long-haul transmission the accumulation of FMF random phenomenon should be compensated by treating the signal at the end of reception, by a MIMO combined with a digital signal processing, called MIMO-DSP. Therefore, the emerging long-haul transmission uses coherent detection and MIMO-DSP to manage the impairments present in the FMF.

Besides, MIMO-DSP could become complex as a consequence of the number of modes and the long differential group delays (DGDs). The latter can be minimized by optical fibers able to reach a strong coupling, in order to accelerate the combination of modes, allowing also

a reduction of the group delay (GDs). This reduction is one of the key properties to decrease the differential groups delay (DGD), and consequently potentially reduce the number of taps required for MIMO processing, and consequently the DSP complexity of MIMO-DSP.

The group delay (GD) description as a function of coupling will allow to evaluate the factors that benefit the reduction of the GD. Thus, [Shemirani, 2009] used the group operator eigenvalue to obtain the GD of the multi-group on different coupling regimes, demonstrating that the minimal GD can be found in the strong coupling regime. Later, a variation of this model was applied by [Juarez, 2013] and [Juarez, 2014] to study the coupling in FMF. The first model considers a circular bend and makes a polarization study by using Principal State of Polarization (PSP). The second one takes into account the losses through a fiber mismatch model using two fields coupling model approaches. Both use a parabolic profile index that restricts the study of trench profile commonly admitted to control the macro bend.

As was noted earlier, most of the signal recovery responsibility lies on the equalizer, and indirectly on the FMF design. In an FMF, all modes share the same core, inducing an intermodal crosstalk created by the energy exchange between modes (mode coupling). In summary, the differences between the group velocities of modes, which could result in a high DGD, can generate difficulties in the propagation of these modes in an FMF. In the end, the mode coupling in addition with a large accumulated DGD could produce Inter-symbol Interference (ISI) on each spatial mode during the transmission and make the detection difficult. Furthermore, the digital processing (MIMO) system can suffer from a very large DGD (Appendix D) making its structure complex.

Whatever the design applied, we must study modal coupling to define its tolerance requirements for each mode but also to globally generate or minimize it. Therefore, depending on the design of the desired FMF system, mode coupling could be enhanced or not. We will study the different regimes of coupling in FMF in order to adapt it to the transmission system.

After this review of previous works dealing with coupling regime in few mode fibers, we will now focus on the emerging mode division multiplexing (MDM) communication systems.

3.2 Coupled mode theory applied to FMF

In this study, we describe the coupled mode theory applied to an FMF. The FMF is modeled as a concatenation of several curved segments (See Fig. 3.4). Each piece is associated with a random bending radius, R . In this model, coupling between back scattered and propagating waves is not considered, neither polarization effect.

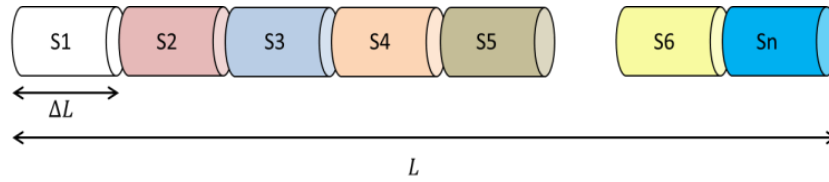


Figure 3-4: Coupling model for FMF. b) Microbending in FMF can be modeled as a set of very small random radius (bends) in the fiber core.

The distribution of the inverse of the bending (the radius of curvature) is chosen to be a normal distribution with a mean value of 0 m^{-1} and a standard deviation of $\sigma_{1/R}$. Here, the normal distribution is a function of the standard deviation of the curvature. For instance, with an array of 10000 random variables for 5 different standard deviations of curvature $\sigma_{1/R}=0.1$, $\sigma_{1/R}=1$, $\sigma_{1/R}=10$, $\sigma_{1/R}=20$ and $\sigma_{1/R}=100$, we obtain Fig. 3.5 which compares the influence of the standard deviation in normal distributions.

Note that the perturbation tends to be smaller when the radii of curvature are big or the standard deviation is small, and vice versa. For example if $\sigma_{1/R}=0.1$, 95% of random values of radii of curvature will be in the range $5 \leq R < \infty$.

Each segment can be associated to an individual matrix of propagation, M_n and calculated with the basis of the ideal mode [Marcuse, 1984] of an unperturbed fiber (as we will detail in the next section). To obtain an entire description of modal propagation of the FMF, we multiply each in individual matrix by using equation 3.1.

$$M_N = \prod_{n=1}^N M_n(\Delta L, \omega) \quad (3.1)$$

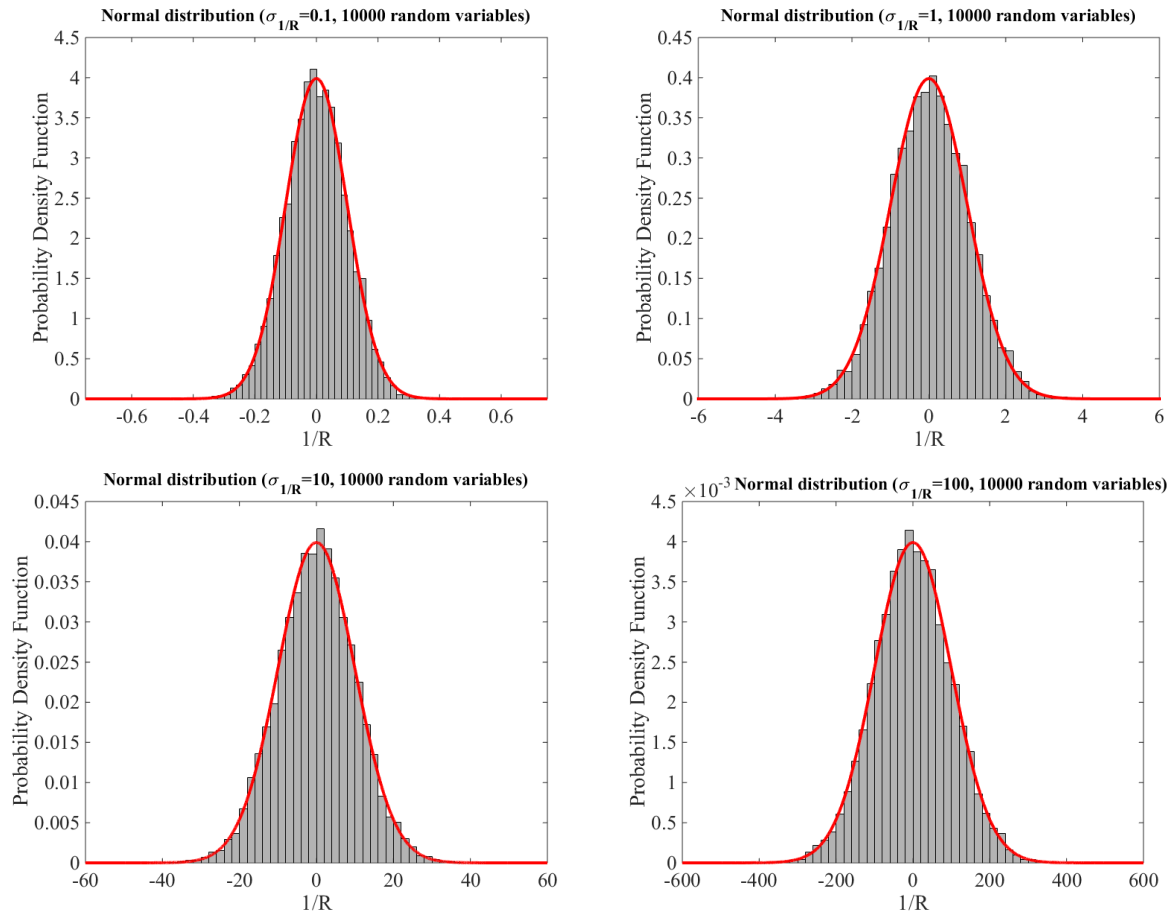


Figure 3-5: Gaussian distribution related with the inverse of bending for different standard deviation of curvature $\sigma_{1/R}$. The x-axis is the inverse of the bending ($1/R$) and the y-axis is the amplitude of the distribution.

We have modeled the perturbation in each segment by considering the theory of perturbation that uses a straight fiber to model a bent fiber [Pettermann, 1976].

A perturbation can have different forms (periodic wave, random behavior), that usually depend on the effect that produces it. For instance, we can model the perturbation as a function of a periodic wave (widely used for Bragg fiber) or a splice (that is the easiest form of which to find the coupling coefficients). Also a random perturbation can be considered and used when we do not have exact knowledge of when and in which part of the fiber it is produced. Hence, statistical tools can model it.

To study the coupling in MDM system, we will focus on the perturbation model based on the refractive index transformation by using statistical tools. It can be adapted to almost all type of perturbation that we will study. The model is based on the changes of the refractive index due to the perturbation (see equation 3.2 a-b). Therefore, a perturbed fiber can be represented by an equivalent straight fiber by considering the transverse wavenumber of the bent and equivalent fiber (k_t and k_{te}):

$$k_t^2 = k^2 \cdot n_o^2(x, y) - \beta^2(x, y)$$

$$k_{te}^2 = n_e^2 \cdot k^2 - n_p^2(x, y) \cdot k^2 - \beta_o^2(x, y)$$

Here, β_o is the fundamental propagation constant.

Consequently, a trigonometric function on Fig. 3.6 is applied to derive the following relation

$$\lambda/(y+R) = \lambda_o/y,$$

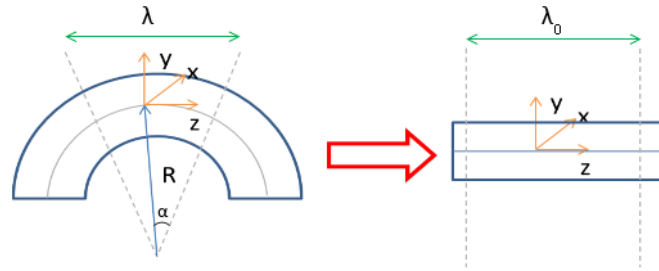


Figure 3-6: Equivalence of a perturbed fiber. It describes the equivalent model of a bend fiber. In a bent fiber, the optical path followed by light is longer at the outside of the concavity than at the inside, meaning that the equivalent wavelength in the material is modified through the cross-section.

However, for convenience, this relation is represented in terms of the propagation constant (β), by substituting the wavelength λ for $\beta=2.\pi/\lambda$. Thus, we can use it over the transverse wavenumber equation. We can say that $\beta = \beta_o$ for the straight fiber since propagation constant is considered invariant over all the cross section. By the assumption that the refractive index difference is small, β_o can be approximated to $k.n_1$.

Later, we find the propagation constant in one of the perturbed axis, extending this study for both axis (See details in Appendix E). Finally, the perturbed refractive index of an equivalent straight fiber can be written as:

$$n_e^2(x, y) = n_o^2(x, y) + n_p^2(x, y) \tag{3.2a}$$

$$n_p^2(x, y) \approx \left(\frac{2.x}{R_x} + \frac{2.y}{R_y} \right) \cdot n_1^2 \tag{3.2b}$$

Here, n_1 is the maximum value of the refractive index of the core on the fiber axis and $n_o(x, y)$ is the refractive index without perturbations. $n_e^2(x, y)$ and $n_p^2(x, y)$ represent the equivalent and perturbed refractive index. Specifically, the equivalent refractive index (equation 3.2a) will be taken into account in the coupling equation (equation 3.36a), because it represents the equivalent of the perturbation in the optical fiber. Since $n_e^2(x, y)$ and $n_p^2(x, y)$

are independent of the z -axis, the numerical modeling of the coupling will be easier. Note also that the influence of the curvature is represented by the radius of curvature in the two axis R_x and R_y .

In order to evaluate the mode coupling caused by this random perturbation, we will study the ideal modes.

3.2.1 Coupled modes theory

To evaluate the modal coupling caused by the perturbation, we expand the mode fields in terms of ideal or local normal modes. In these methods and only in real modes, the wave equation can be solved at each z along the fiber, where the refractive index can be dependent or non-dependent of z . These two main approaches will be briefly presented:

- Method 1 also known as ideal mode coupling method. It is based on approximating the perturbed fiber by using only one set of modes for the whole fiber. These particular modes are the eigenmodes of the ideal fiber. It is recommended if the perturbation is a slight deviation from a z -invariant fiber [Marcuse, 1984].
- Method 2 also known as local mode coupling method. It uses the eigenmodes of the corresponding ideal fiber at a given z , that is, each section is described by a local coordinate system and the eigenmodes are calculated in a fictitious fiber. This method is more appropriate, especially if the waveguide varies slowly along z or if we can describe, in each z cross-section plane, a fiber that locally coincides with the perturbed fiber (Appendix F).

Both approaches are field coupling models, i.e. they describe the coupling by complex coefficients, extending the study of the phase dependent coupling modes [Marcuse, 1984], [Shemirani, 2009]. Coupled power theory can also be used to describe the modes coupling, but using nonnegative real coefficients. Here, we will review the ideal mode theory (method 1), because this method will be used to study the effects of strong and weak coupling in different FMFs.

3.2.1.1 Expansion in terms of ideal normal modes

In uncoupled regimes or in the absence of perturbation, the modes do not couple together. Indeed they are eigenmodes of the ideal fiber. Coupling between modes can be caused by the radius variation dR/dz of the core arising from a perturbation. Bounded or unbounded electromagnetic fields in this perturbed structure can be expressed as an expansion of ideal modes or local normal modes. However, expansion in terms of ideal modes or local normal modes must be adapted to the problem of establishing coupling equations of modes with numerically usable coefficients that allow using the perturbation description in terms of the refractive index variation as a function of z , or $\partial n^2 / \partial z$. To simplify $\partial n^2 / \partial z$, we will use the perturbation model based on refractive index transformation [Pettermann, 1976] (see equation 3.2a), so we need to use the expansion of ideal normal modes. In the following analysis, we will use a development similar to [Marcuse, 1973]

An ideal normal mode is based on approximating the perturbed fiber by using only one set of modes for the whole fiber. These particular modes are the eigenmodes of the ideal fiber. The ideal normal modes of a waveguide can be expressed by a z dependence of the fields.

$$e^{-i.\beta_m z}$$

Where m represents a particular guided mode or a radiation mode, thus the expression of the electric field can be written as: $\vec{E} = \vec{e}_m e^{i.(\omega.t - \beta_m z)} = \widetilde{\vec{E}}_m . e^{i.\omega.t}$.

Here, Maxwell's equations hold, but the refractive index of the optical fiber is $n_o(x, y)$ instead of $n(x, y, z)$, because we assume an ideal optical fiber whose refractive index $n_o(x, y)$ is independent of z .

That is, $\frac{\partial}{\partial z} = -i.\beta_m$.

Now the modes satisfy the Maxwell equations and these equations for the ideal modes can be expressed as:

$$\vec{\nabla}_t \times (\vec{\nabla}_t \times \vec{\tilde{E}}_{mt}) - \mu_o \omega . (\beta_m) \hat{z} \times \vec{\tilde{H}}_{mt} = n_o^2 . k^2 . \vec{\tilde{E}}_{mt} \quad (3.3a)$$

$$\vec{\nabla}_t \times \left(\frac{1}{n_o^2} . \vec{\nabla}_t \times \vec{\tilde{H}}_{mt} \right) + \epsilon_o \omega . (\beta_m) \hat{z} \times \vec{\tilde{E}}_{mt} = k^2 . \vec{\tilde{H}}_{mt} \quad (3.3b)$$

In this case, we will use \overline{e}_m instead of $\tilde{\mathbf{E}}_m$ in equations 3.3a and 3.3b since $e^{-i\beta_m z}$ vanishes.

The total transverse fields $\vec{\mathbf{E}}_t$ and $\vec{\mathbf{H}}_t$ in the perturbed waveguide can be expressed as a sum of the eigenmodes of the ideal waveguide \overline{e}_t and \overline{h}_t , whose solutions are found by the series expansions of these fields (See equations 3.4a and 3.4b).

$$\vec{\mathbf{E}}_t = \sum_{m=1}^{N_m} a_m \vec{e}_{mt} = \sum_{m=1}^{N_m} (A_m^+ \cdot e^{-i\beta_m z} + A_m^- \cdot e^{+i\beta_m z}) \cdot \vec{e}_{mt} \quad (3.4a)$$

$$\vec{\mathbf{H}}_t = \sum_{m=1}^{N_m} b_m \vec{h}_{mt} = \sum_{m=1}^{N_m} (B_m^+ \cdot e^{-i\beta_m z} - B_m^- \cdot e^{+i\beta_m z}) \cdot \vec{h}_{mt} \quad (3.4b)$$

Note that z-dependence is reported in the a_m and b_m coefficients, and is not in the vectorial amplitude of transverse field.

Here, A_m^+ and A_m^- correspond to the amplitude of the progressive and regressive wave.

By assuming a refractive index distribution as $(n_e^2 - n_o^2)$, where n_o is the refractive index without perturbations of and n_e is the equivalent refractive index of the perturbed fiber, we can obtain the equations 3.5a and 3.5b whose solutions are the ideal mode fields.

$$\sum_{m=1}^{N_m} \left\{ \left[\left(\frac{db_m}{dz} \right) + i\beta_m a_m \right] i\mu_o \omega \cdot \hat{z} \times \vec{h}_{mt} + k^2 (n_e^2 - n_o^2) a_m \vec{e}_{mt} \right\} = 0 \quad (3.5a)$$

$$\sum_{m=1}^{N_m} \left\{ b_m \left(\vec{\nabla}_t \times \left[\left(\frac{1}{n_e^2} - \frac{1}{n_o^2} \right) \vec{\nabla}_t \times \vec{h}_{mt} \right] \right) + \left[\left(\frac{da_m}{dz} \right) + i\beta_m b_m \right] i\mu_o \omega \cdot \hat{z} \times \vec{e}_{mt} \right\} = 0 \quad (3.5b)$$

Here, N_m is the number of modes.

It should be noted that the amplitudes of the modes in the coupled-waveguide system are governed by the coupled-mode equations. The solutions of the coupled-mode equations describe wave propagation and coupling in the perturbed waveguide. The coupling coefficients are calculated based on the optical fiber characteristics and using the coupled mode equation system.

3.2.1.2 Differential equations for the coupled mode theory

Using the cross product properties $(\vec{A} \times \vec{B}) \cdot \vec{C} = \vec{A} \cdot (\vec{C} \times \vec{B})$ and multiplying the equation 3.5a with \vec{e}_{mt}^* and 3.5b with \vec{h}_{mt}^* and later the integration over the infinite cross section of the optical fiber, we obtain the following integro-differential equation sets:

$$\left(\frac{da_m}{dz}\right) + i\beta_m b_m - 2 \sum_{n=1}^N [k'_{mn} \cdot b_n] = 0 \quad (3.6a)$$

$$\left(\frac{db_m}{dz}\right) + i\beta_m a_m - 2 \sum_{n=1}^N [K'_{mn} \cdot a_n] = 0 \quad (3.6b)$$

Here, a_m is the wave amplitude and β_m propagation coefficient for each m-th mode. β_m is developed until 2nd-order to consider both modal and chromatic dispersions, as: $\beta_n \approx \beta_0^{(n)} + \beta_1^{(n)}(\omega - \omega_0) + \frac{1}{2}\beta_2^{(n)}(\omega - \omega_0)^2$. Besides, K'_{mn} and k'_{mn} are the coupling coefficients of the transverse part:

$$K'_{mn} = \frac{\omega \cdot \epsilon_0}{4iP_z} \cdot \iint_{A_\infty} (n_e^2 - n_o^2) \cdot (\vec{e}_{mt}^* \cdot \vec{e}_{nt}) dS \quad (3.7a)$$

$$k'_{mn} = \frac{-1}{4 \cdot P_z i \cdot \omega \cdot \epsilon_0} \cdot \iint_{A_\infty} \vec{h}_{mt}^* \cdot \nabla_t \times \left[\left(\frac{1}{n_e^2} - \frac{1}{n_o^2} \right) (\nabla_t \times \vec{h}_{nt}) \right] dS \quad (3.7b)$$

Note that in the absence of coupling (see equations 3.6a-b and 3.7a-b), all coupling coefficients are equal to zero, because in a unperturbed fiber, the equivalent refractive index which represent the perturbation is equal to the refractive index of the fiber $n_e = n_o$, which makes $K'_{mn} = 0$.

$$\left(\frac{da_m}{dz}\right) + i\beta_m b_m = 0 \quad (3.8a)$$

$$\left(\frac{db_m}{dz}\right) + i\beta_m a_m = 0 \quad (3.8b)$$

Besides, the coupling coefficient can be expressed as a function of the longitudinal part of the fields (See equation 3.9a and 3.9b), by using the following relations:

$$\vec{e}_{mz} \hat{z} = \frac{-i}{\epsilon_0 \omega n_o^2} \vec{\nabla}_t \times \vec{h}_{mt} \quad \text{and} \quad \vec{h}_{mz} \hat{z} = \frac{i}{\epsilon_0 \omega} \vec{\nabla}_t \times \vec{e}_{mt}$$

$$k'_{mn} = \frac{1}{4P_z} \cdot \iint_{A_\infty} \vec{h}_{mz}^* \cdot \vec{\nabla}_t \times \left[\frac{1}{n^2} (n_e^2 - n_o^2) \cdot \vec{e}_{nz} \right] dS \quad (3.9a)$$

$$K'_{mn} = \frac{\omega \cdot \epsilon_0}{4iP_z} \cdot \iint_{A_\infty} \left[\frac{n_o^2}{n_e^2} (n_e^2 - n_o^2) \cdot \vec{e}_{mz}^* \cdot \vec{e}_{nz} \right] dS \quad (3.9b)$$

As an example, we will use this method to study the steady state and the slowly varying amplitude of an optical fiber with 2 modes.

- **Example: Two-modes fiber**

In the absence of coupling and considering two modes, the coupling equations become:

$$\left(\frac{da_m}{dz}\right) + i\beta_m b_m = 0$$

$$\left(\frac{db_m}{dz}\right) + i\beta_m a_m = 0$$

By differentiating equation 3.8b, the second-order differential equations (3.10a and 3.10b) are obtained.

$$\left(\frac{d^2 a_m}{dz^2}\right) + \beta_m^2 a_m = 0 \quad (3.10a)$$

$$b_m = \frac{i}{\beta_m} \left(\frac{da_m}{dz}\right) \quad (3.10b)$$

In this case, equation 3.10a is a simple differential equation that admits two sets of solutions: $a_m^+ = A_m^+ e^{-i\beta_m z}$ and $a_m^- = A_m^- e^{i\beta_m z}$. Likewise, using equation 3.10b, we obtain the coefficient for the magnetic field,

$$b_m^+ = A_m^+ e^{-i\beta_m z} \text{ and } b_m^- = -A_m^- e^{i\beta_m z}$$

These solutions correspond to the guided modes in steady state of the waveguide, since they have a $e^{-i\beta_m z}$ dependency. That is, the amplitude depends on the propagation constant and z, while A_m is constant.

- **Example: Slowly varying mode amplitudes**

For solutions to perturbations of the coupled wave equations it is convenient to introduce slowly varying mode amplitude approximation. We will take into account the progressive and regressive modes. The amplitude can be rearranged as: $a_m = a_m^+ + a_m^-$ and $b_m = b_m^+ - b_m^-$.

Under this condition, the set of coupled mode equations are:

$$\left(\frac{da_m^+}{dz}\right) + i\beta_m a_m^+ - \sum_{m=1}^N [K_{mn}^{++} \cdot a_m^+] = 0 \quad (3.11a)$$

$$\left(\frac{da_m^-}{dz}\right) - i\beta_m a_m^- - \sum_{m=1}^N [K_{mn}^{-+} \cdot a_m^+] = 0 \quad (3.11b)$$

With the coupling coefficients:

$$K_{mn}^{pq} = pK'_{mn} + qk'_{mn}$$

$$K_{mn}^{pq} = \frac{\omega \cdot \epsilon_0}{4iP_z} \cdot \iint_{A_\infty} (n_e^2 - n_o^2) \left[p \cdot \vec{e}_{mt}^* \cdot \vec{e}_{nt} + \frac{n_o^2}{n_e^2} \cdot \vec{e}_{mz}^* \cdot \vec{e}_{nz} \right] dS \quad (3.12)$$

Rewriting the equations 3.11a and 3.11b by using A instead of a_m , we obtain:

$$\left(\frac{dA_m^+}{dz}\right) + i\beta_m A_m^+ - \sum_{m=1}^N [K_{mn}^{++} \cdot A_m^+ + K_{mn}^{+-} \cdot A_m^-] = 0 \quad (3.13a)$$

$$\left(\frac{dA_m^-}{dz}\right) - i\beta_m A_m^- - \sum_{m=1}^N [K_{mn}^{-+} \cdot A_m^+ + K_{mn}^{--} \cdot A_m^-] = 0 \quad (3.13b)$$

The matrix form of set of equations above is written as:

$$\begin{pmatrix} \frac{dA_m^+}{dz} \\ \frac{dA_m^-}{dz} \end{pmatrix} = \sum_{m=1}^N \begin{bmatrix} K_{mn}^{++} e^{i(\beta_m - \beta_n)z} & K_{mn}^{+-} e^{i(\beta_m + \beta_n)z} \\ K_{mn}^{-+} e^{-i(\beta_m + \beta_n)z} & K_{mn}^{--} e^{-i(\beta_m - \beta_n)z} \end{bmatrix} \begin{pmatrix} A_m^+ \\ A_m^- \end{pmatrix} \quad (3.13c)$$

These solutions correspond to the guided modes in slowly varying mode coupling. Here, the amplitude depends on the propagation constant sum of two modes, z and coupling coefficient.

3.2.2 Ideal mode propagation applied to an FMF

The couple mode theory is applied to model an FMF by using an expansion in terms of one set of orthogonal modes that describe the fiber as unperturbable or invariant with respect to z (ideal modes). The perturbation is modeled as in the equation 3.2a [Pettermann,1976]. The undistorted FMF and its eigenmodes follow the homogeneous scalar wave equation defined in Chapter 2. Depending on the fiber profile, the eigenmode can be described by the Bessel function for step index or by a good approximation as: Laguerre-Gauss mode basis for graded-index.

In the presence of perturbation, the modes couple and their propagation can be expressed by equation 3.14.

Coupling and propagation description is calculated in each segment by using a matrix notation of the equations 3.11a-b to simplify the calculation in the numerical tool (equation 3.14).

The equation 3.14 represent the coupling equation for a particular segment of the fiber. Later, this equations will be extended for entire of the fiber.

$$\left[\frac{d\mathbf{a}(z)}{dz} \right] = (-i[\mathbf{B}(\omega)] - i[\mathbf{K}])[\mathbf{a}(z)] \quad (3.14)$$

Here, $[\mathbf{a}(z)]$ corresponds to the column matrix which contains the wave amplitudes: $[\mathbf{a}(z)] = (\mathbf{a}_0(0), \mathbf{a}_1(z), \dots \dots \dots \mathbf{a}_N(z))^T$, where N is number of modes.

Note also that equation 3.14 is a transmission matrix having two terms: the first term defines the uncoupled propagation matrix and contains the propagations matrix of a degenerate mode group, $[\mathbf{B}(\omega)]$ and the second describes the coupling between modes, by the matrix, $[\mathbf{K}]$. This linear ordinary differential equations can be solved by its matrix solution, where the matrix exponential function is used.

$$[\mathbf{K}] = \begin{bmatrix} \mathbf{K}_{11} & \cdots & \mathbf{K}_{1N} \\ \vdots & \ddots & \vdots \\ \mathbf{K}_{N1} & \cdots & \mathbf{K}_{NN} \end{bmatrix} \text{ and } [\mathbf{B}(\omega)] = \begin{bmatrix} \mathbf{B}_1(\omega) & \cdots & 0 \\ \vdots & \mathbf{B}_2(\omega) & \vdots \\ 0 & \cdots & \mathbf{B}_N(\omega) \end{bmatrix}$$

To calculate the terms of $[\mathbf{K}]$, we use equation 3.15a which represents the coupling coefficient between the m-th and n-th modes. Here, \mathbf{K}_{mn} is written by assuming longitudinal components of the fields negligible or low index difference.

In the case of a lossless system, $\mathbf{K}_{mn}=\mathbf{K}_{nm}$ and the matrix, \mathbf{K} is Hermitian. In the absence of coupling $[\mathbf{K}]$ is a null matrix.

$$K_{mn} = \frac{\omega \cdot \epsilon_0}{4iP_z} \iint_{A_\infty} (n_e^2 - n_o^2) \cdot (\vec{e}_{x,m}^* \vec{e}_{x,n} + \vec{e}_{y,m}^* \vec{e}_{y,n}) dS \quad (3.15a)$$

It should be noted that $\vec{e}_{x,n}$ and $\vec{e}_{y,n}$ are the x and y components of the normalized electric field for both polarization.

Using the relation $n_p^2(x, y) = n_e^2(x, y) - n_o^2(x, y)$ and equation 3.15a, the coupling coefficient becomes:

$$K_{mn} = \frac{\omega \cdot \epsilon_0}{4iP_z} n_1 \iint_{A_\infty} \left(\frac{2 \cdot x}{R_x} + \frac{2 \cdot y}{R_y} \right) \cdot (\vec{e}_{x,m}^* \vec{e}_{x,n} + \vec{e}_{y,m}^* \vec{e}_{y,n}) dS \quad (3.15b)$$

Likewise, the coupling coefficient can be expressed by considering the perturbation in only one axis, as in the following equation:

$$K_{mn} = \frac{\omega \cdot \epsilon_0 n_1}{2iP_z \cdot R_x} \iint_{A_\infty} (x) \cdot (\vec{e}_{x,m}^* \vec{e}_{x,n} + \vec{e}_{y,m}^* \vec{e}_{y,n}) dS$$

To be more generic, we can include the propagation losses in the coupling model, by the matrix, $[\alpha]$

$$[\alpha] = \begin{bmatrix} \alpha_1 & & 0 \\ & \alpha_2 & \\ 0 & & \alpha_N \end{bmatrix}$$

This new term is also added in the differential equation 3.14, so that:

$$[\mathbf{a}(z)] = (-[\alpha] - i[\mathbf{B}(\omega)] - i[\mathbf{K}])[\mathbf{a}(0)] \quad (3.16a)$$

Since matrices $[\alpha]$, $[\mathbf{B}(\omega)]$ and $[\mathbf{K}]$ are independent of z at a given segment, the resolution of the equation 3.16 can be given by:

$$\left[\frac{d\mathbf{a}(z)}{dz} \right] = e^{-([\alpha] + i[\mathbf{B}(\omega)] + i[\mathbf{K}]) \cdot z} [\mathbf{a}(0)] \quad (3.16b)$$

$$[\mathbf{a}(\Delta L)] = [\mathbf{M}(\omega)] [\mathbf{a}(0)] \quad (3.16c)$$

ΔL is the segment length, $[\mathbf{a}(\Delta L)]$ describes the evolution $[\mathbf{a}(\mathbf{0})]$ after a segment of the fiber. $[\mathbf{M}(\omega)]$ is the propagation matrix, generally associated to the lossless propagation $[\mathbf{U}(\omega)]$ by the following relationship:

$$[\mathbf{M}(\omega)] = e^{-i\Phi_1(\omega)}[\mathbf{U}(\omega)] = e^{-([\alpha]+i[B(\omega)]+i[K]).\Delta L} \quad (3.17a)$$

$[\mathbf{M}(\omega)]$ can be written, as a diagonal block matrix for a single section of ΔL length. Where, x, y sub-indices correspond to the x and y polarizations within a section.

$$[\mathbf{M}_t(\omega)] = \begin{bmatrix} e^{M_{N_x}\Delta L} & 0 \\ 0 & e^{M_{N_y}\Delta L} \end{bmatrix} \begin{bmatrix} e^{M_{N-1_x}\Delta L} & 0 \\ 0 & e^{M_{N-1_y}\Delta L} \end{bmatrix} \dots \begin{bmatrix} e^{M_{1_x}\Delta L} & 0 \\ 0 & e^{M_{1_y}\Delta L} \end{bmatrix} \quad (3.17b)$$

To obtain the total propagation matrix, $[\mathbf{M}_t(\omega)]$, the individual propagation matrices of each segment are concatenated. This total propagation matrix describes the modal propagation on the whole optical fiber.

Besides, we can additionally obtain a new expression of $[\mathbf{M}(\omega)]$, from the following relationship:

$$[\mathbf{U}(\omega)] = e^{i\Phi_1(\omega)}[\mathbf{M}] \quad (3.18)$$

$\Phi_1(\omega)$ is arbitrarily chosen to be the phase of the fundamental mode with a propagation constant, $\beta_1(\omega)$.

$$\Phi_1(\omega) = i(-\alpha - i.\beta_1(\omega))z \quad (3.19a)$$

By expanding $\beta_1(\omega)$ through Taylor series $(\beta_{1,0} + \beta_{1,1}(\omega - \omega_0) + 0(\omega - \omega_0)^2)$ and making $\beta_{1,1}(\omega - \omega_0) \approx \tau_1(\omega - \omega_0)$, equation 3.19a can also be rewritten as:

$$\Phi_1(\omega) \approx (\beta_{1,0} + \tau_1(\omega - \omega_0) - i\alpha) . \Delta L \quad (3.19b)$$

Where, τ_1 is the group delay of mode 1 per unit of length.

z is replaced by a length segment ΔL .

Here, $\Phi_1(\omega)$ represents the scalar variation of propagation constant as a function of the deviation of the angular center frequency by the transmission length.

Now, $[\mathbf{U}(\omega)]$ can be written

$$\begin{aligned} [\mathbf{U}(\omega)] &= e^{\alpha_1 \Delta L} e^{i\beta_1 \Delta L} e^{-([\alpha] + i[\mathbf{B}(\omega)] + i[\mathbf{K}]) \Delta L} \\ [\mathbf{U}(\omega)] &= \left(e^{[\Delta\alpha] \Delta L + i[\Delta\mathbf{B}(\omega)] \Delta L - i[\mathbf{K}] \Delta L} \right) \end{aligned} \quad (3.20)$$

where,

$$\begin{aligned} [e^{-[\Delta\alpha] \Delta L}] &= \begin{bmatrix} 1 & & & 0 \\ & \dots & & \\ 0 & e^{(\alpha_1 - \alpha_2) \Delta L} = e^{\Delta\alpha_2 \Delta L} & & \\ & & \dots & \\ & & & e^{(\alpha_1 - \alpha_N) \Delta L} = e^{\Delta\alpha_N \Delta L} \end{bmatrix} \\ [e^{-i[\Delta\beta] \Delta L}] &= \begin{bmatrix} 1 & & & 0 \\ & \dots & & \\ 0 & e^{(\beta_1 - \beta_2) \Delta L} = e^{\Delta\beta_2 \Delta L} & & \\ & & \dots & \\ & & & e^{(\beta_1 - \beta_N) \Delta L} = e^{\Delta\beta_N \Delta L} \end{bmatrix} \end{aligned}$$

Here, $\Delta\alpha_N = (\alpha_1 - \alpha_N)$ and $\Delta\beta_N = (\beta_1 - \beta_N)$ are the attenuation coefficients and propagation constant relative to those of the fundamental mode.

- **Example: For three modes, only one segment**

To illustrate the impact of bending on the fiber modes, we have simulated a step-index fiber that supports three modes, namely LP_{01} , LP_{11e} and LP_{11o} . The e-o sub index is used to differentiate between even or odd mode orientations, respectively, in the vertical direction normal to the plane of the bend. Figures 3.7a-c show the coupling matrices and electric field in response to perturbation for different radii of curvature in each axis of the fiber. That is, a straight fiber is represented by making R_x and R_y infinite, whereas a perturbed fiber the radius of curvature on one or both axis must be varied.

It should be noted that coupling matrix is an null matrix in the absence of perturbation and the electric fields correspond to the LP modes. As bending increases, the non-diagonal elements of the coupling matrix become different to zero, evidencing the coupling effect. Note also that intensity of the electrical field is affected by two factors: the coupling regime and the direction of the perturbation.

Coupled mode in the emerging MDM communication systems

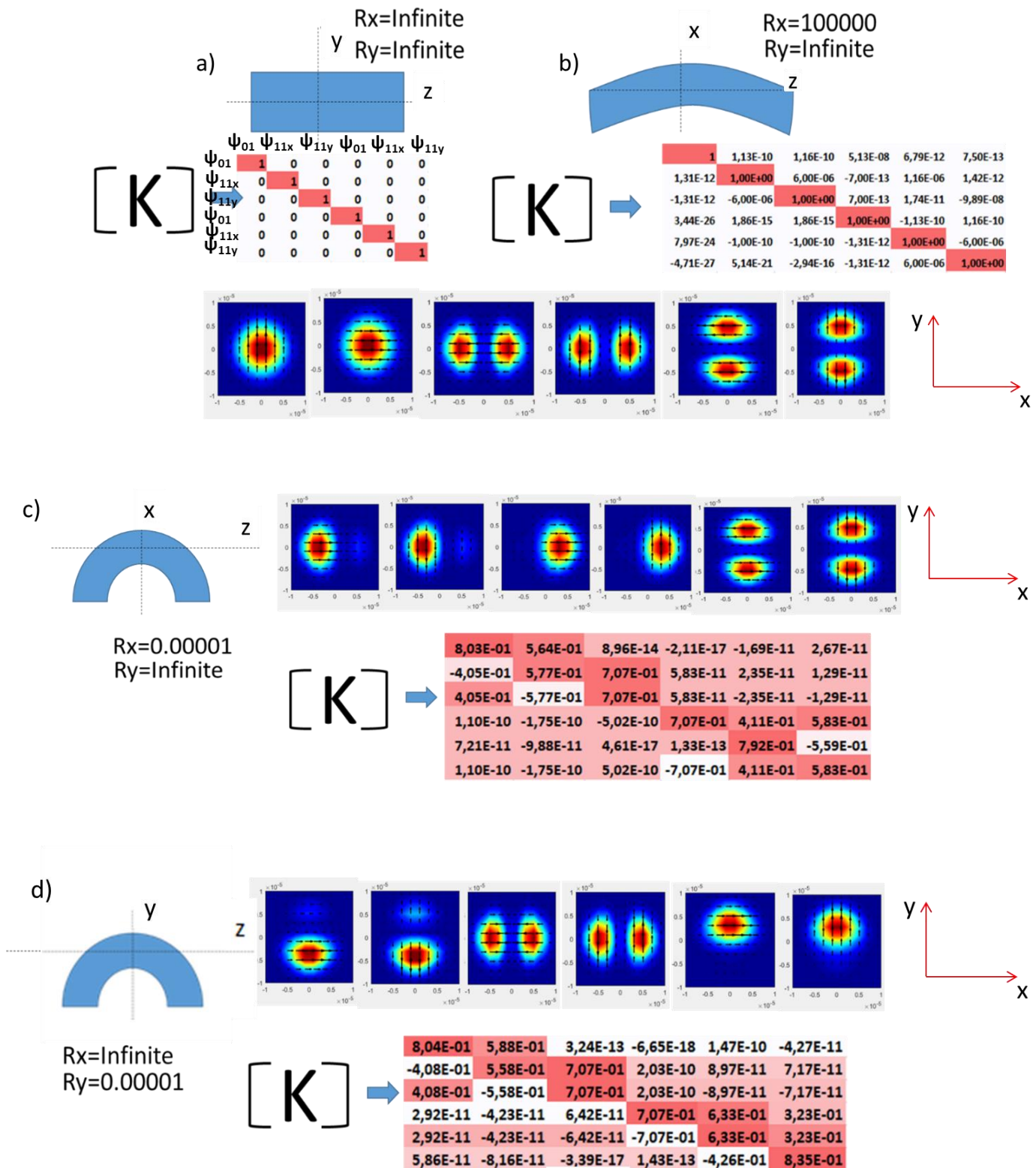


Figure 3-7: a-b) Coupling matrices and intensity of the electric field for a) straight fiber b) slightly perturbed fiber. c) Coupling matrices and intensity of the electric field for a perturbed fiber in x-axis. d) Coupling matrices and intensity of the electric field for a perturbed fiber in y-axis.

3.3 Group delay operator

Principal modes (PM) are one of the possible candidates for long haul optical transmission that use FMF because they are free of group delay dispersion to first order in frequency. The term first order denotes the fact that this description arises from the first-order term in a series expansion of matrix, $[\mathbf{M}(\omega)]$ (around the center frequency), in the absence of polarization-dependent loss.

Principal modes is originally based on the concept of principal states of polarization (PSPs) developed to describe the dispersion in SMF. [Shemirani, 2009] and [Juarez, 2015] adapted this study on MMFs. Thereby, the eigenvectors of the group delay operator are the PMs. To obtain the group delay operator, we consider a narrowband optical signal at a given frequency, ω_0 and an FMF that supports N guided modes.

Later, the group delay operator will be compared to group delay (GD) under certain conditions. So, we consider relevant to give a review of GD. GD for m-th mode after propagation through a segment of length z of fiber is given by:

$$T_m = \frac{z}{v_g} = z \frac{d\beta_m}{d\omega} = z d_\omega \beta_m \quad (3.21)$$

GDs of an optical fiber can be defined by a vector $[\mathbf{T}(\omega)]$ as:

$$[\mathbf{T}(\omega)] = L \cdot \partial_\omega [\mathbf{B}(\omega)] \quad (3.22)$$

Equation 3.22 can also be written as equation 3.23, by using the group delay per unit of length, τ .

$$[\boldsymbol{\tau}] = \partial_\omega [\mathbf{B}(\omega)] \quad (3.23)$$

To obtain the group delay operator, we will use the equation 3.16c

$$[\mathbf{a}(z)] = [\mathbf{M}(\omega)] [\mathbf{a}(0)]$$

As we have seen earlier, $[\mathbf{a}(0)]$ describes the excitation of the modes at the input end of the fiber ($z=0$), and it is constant. To simplify, we change for the following notation:

$$|a\rangle = [\mathbf{a}(0)] \text{ and } |b\rangle = [\mathbf{a}(z)]$$

The output field after propagation in the optical fiber can be written as follows by using relation 3.18:

$$|b\rangle_{\omega} = e^{-i\Phi_1(\omega)}[\mathbf{U}(\omega)] |a\rangle \quad (3.24)$$

Note that $|b\rangle$ depends on pulsation, ω on the carrier. To evaluate the frequency dependence equation 3.24 will be derived on both sides. For this case, the information carried occupies a bandwidth leading to the frequency dependence of the output, $|b\rangle$, excepting in the input field pattern, because it can have slow variation with respect to ω .

$$\partial_{\omega} |b\rangle = (-i \partial_{\omega} \Phi_1(\omega)[\mathbf{U}(\omega)] + \partial_{\omega}[\mathbf{U}(\omega)])e^{-i\Phi_1(\omega)}|a\rangle$$

By using equation 3.24, the last expression can be written as:

$$\partial_{\omega} |b\rangle = (-i [\mathbf{U}(\omega)]\partial_{\omega} \Phi_1(\omega) + \partial_{\omega}[\mathbf{U}(\omega)] [\mathbf{U}(\omega)]^{-1})|b\rangle$$

By differentiating equation 3.19b, we can obtain:

$$\partial_{\omega} \Phi_1(\omega) = \partial_{\omega}(\beta_{1,0} + \tau_1(\omega - \omega_0) - i\alpha) \cdot z = \tau_1 \cdot z - iz\partial_{\omega} \alpha$$

This equation can be rearranged by neglecting frequency variation of α

$$\partial_{\omega} |b\rangle = (-i(\tau_1 \cdot z - iz\partial_{\omega} \alpha)[\mathbf{I}] + \partial_{\omega}[\mathbf{U}(\omega)] [\mathbf{U}(\omega)]^{-1})|b\rangle$$

Here, $[\mathbf{I}]$ is identity matrix. The output field depends on the frequency due to the group delay operator $G(\omega)$, which is identified as $\partial_{\omega}[\mathbf{U}(\omega)] [\mathbf{U}(\omega)]^{-1}$.

$$\partial_{\omega} |b\rangle = (-i(\tau_1 \cdot z - iz\partial_{\omega} \alpha)[\mathbf{I}] + [\mathbf{G}(\omega)])|b\rangle \quad (3.25)$$

Note that equation 3.25 describes the frequency evolution of the output fields at the end of the fiber.

3.3.1.1 Uncoupled and lossless fiber

In this case, the coupling and loss matrices are negligible, thus matrix, $[\mathbf{U}(\omega)]$ becomes:

$$[\mathbf{U}(\omega)] = e^{i[\Delta\mathbf{B}(\omega)].z}$$

This equation will be evaluated for each mode, m

$$\partial_{\omega}(e^{-i.\Delta\beta_m.z}) = iz\partial_{\omega}(\Delta\beta_m)e^{i.\Delta\beta_m.z}$$

$\Delta\beta_m$ is the difference between the propagation constants of the fundamental mode and mode, m.

Then, we write $\Delta\beta_m$ in terms of the group delay, by expanding each β in Taylor series, and substituting $\beta_1(\omega-\omega_0)$ by $\tau.\omega$, which is the term related to the inverse of the group velocity or group delay.

$$\Delta\beta_m = \left((\beta_{1,0} + \tau_1(\omega - \omega_0) - (\beta_m + \tau_m(\omega - \omega_0)) \right), \text{ whose derivative is equal to:}$$

$$\partial_{\omega}(\Delta\beta_m) = \Delta.\tau_m$$

It should be noted that the derivative of $\Delta\beta_m$ corresponds to the difference in group delay per unit of length of mode, m compared with the fundamental mode.

For this case, group delay operator $[\mathbf{G}(\omega)]$ can be written as:

$$[\mathbf{G}(\omega)] = iz [\Delta\boldsymbol{\tau}]$$

$[\Delta\boldsymbol{\tau}]$ is a diagonal matrix whose element corresponds to $\Delta.\tau_m$. The eigenvectors of $[\Delta\boldsymbol{\tau}]$ are the normal mode of the fiber, while eigenvalue are group delays differences between each mode.

3.3.1.2 Slowly varying envelop

Assuming a slowly varying envelop and only one segment of the fiber and considering the modes at the output end of the fiber as:

$$|b\rangle_{\omega} = e^{-i\Phi_1(\omega)}[\mathbf{U}(\omega)] |a\rangle = [\mathbf{M}(\omega)] |a\rangle$$

We can write matrix, $[\mathbf{M}(\omega)]$ of an uncoupled and lossless fiber, as follows:

$$[\mathbf{M}(\omega)] = e^{-i[\mathbf{B}(\omega)].z}$$

Normal modes of this diagonal matrix $e^{-i[\mathbf{B}(\omega)].z}$ propagate without changing.

For instance, by considering the fundamental mode of the fiber with a propagation constant β_1 in one only segment, the output end of the fiber can be expressed as:

$$|b\rangle_\omega = e^{-i[\mathbf{B}(\omega)].z} |1\rangle \text{ which means that } \mathbf{a}_1(z) = e^{-i\beta_1 z} (\mathbf{a}_0(0))$$

Note that the matrix coefficients can exhibit rapid oscillation for numerical considerations. We can avoid the previous condition by defining a slowly varying envelope $|B\rangle$ for the fields after the propagation in the fiber.

$$|b\rangle_\omega = e^{-i[\mathbf{B}(\omega)].z} |B\rangle$$

By differentiating, we obtain

$$|b\rangle'_\omega = -i[\mathbf{B}(\omega)]e^{-i[\mathbf{B}(\omega)].z} |B\rangle + e^{-i[\mathbf{B}(\omega)].z} |B\rangle'$$

And thus:

$$|B\rangle = -ie^{i[\mathbf{B}(\omega)].z} [\mathbf{K}]e^{-i[\mathbf{B}(\omega)].z} |B\rangle' \quad (3.26)$$

- **Example: For three modes, only one segment**

Figures 3.8 a-c exhibit the group delays (GDs) under different conditions of bending for a 3-LP step-index fiber (same fiber used in Figs. 3.7 a-c). The GDs have been calculated from the wave equation and eigenvalues of $[\mathbf{G}(\omega)]$ respectively. Note that in uncoupled regime, the calculated GDs by both methods are similar, since $[\mathbf{U}(\omega)]$ is a unitary matrix, so that $[\mathbf{G}(\omega)] = \partial_\omega[\mathbf{U}(\omega)] [\mathbf{U}(\omega)]^{-1}$ and the diagonal matrix becomes the time delay of each mode.

$$\partial_\omega |b\rangle = (-i(\tau_1.z - iz\partial_\omega \alpha)[\mathbf{I}]) |b\rangle$$

In very weak coupling, the calculated GDs are also similar, because $[\mathbf{U}(\omega)]$ matrix depends almost exclusively on the propagation constant matrix, $[\mathbf{U}(\omega)]$ is Hermitian, and the variation of the diagonal matrix from group operator $[\mathbf{G}(\omega)]$ are tiny. In a strong coupling, the calculated GDs by both methods are different, because $[\mathbf{U}(\omega)]$ depends additionally of the coupling matrix and there are more significant variations of $[\mathbf{G}(\omega)]$.

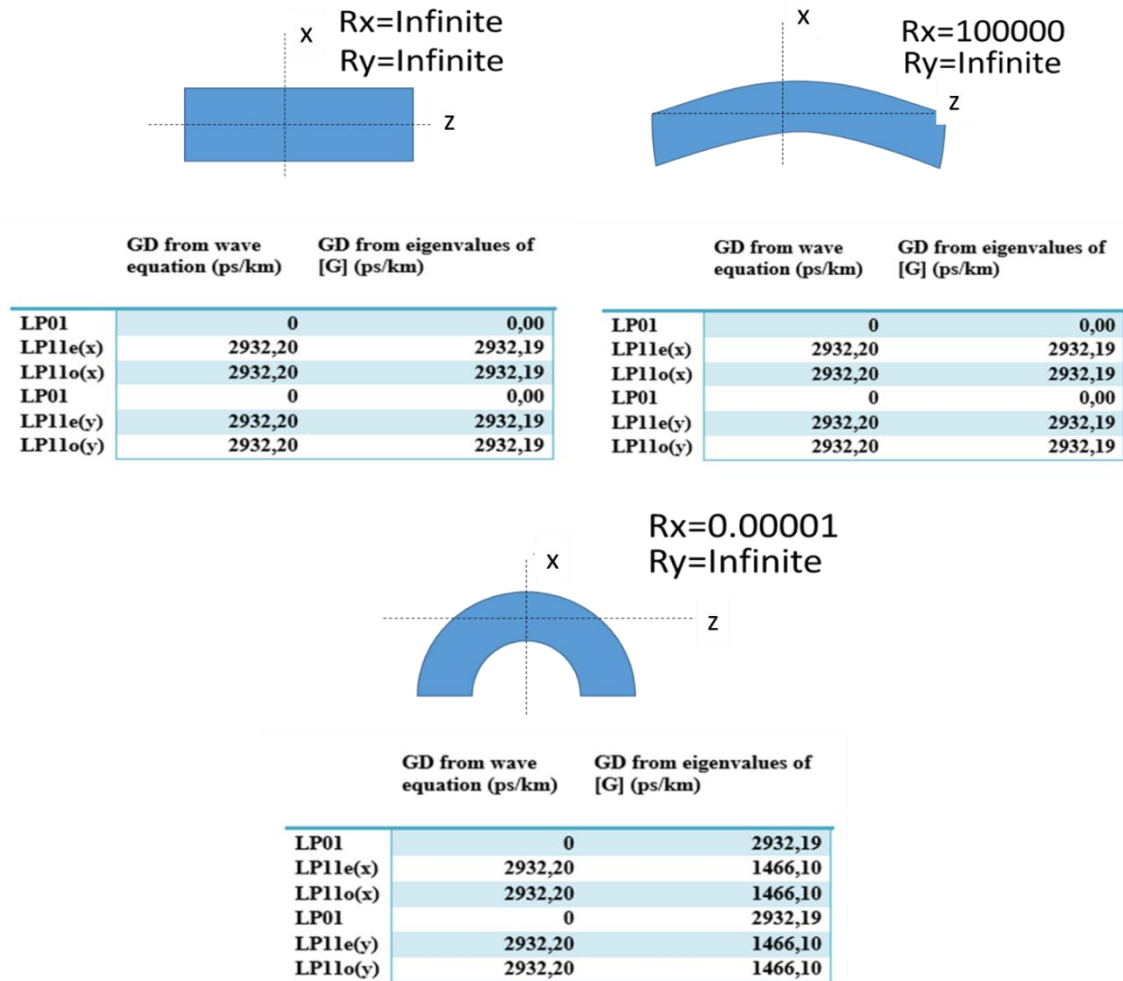


Figure 3-8: Group delay for a) straight fiber b) slightly perturbed fiber and c) perturbed fiber.

3.4 Principal modes (PM)

As discussed above (by equation 3.25), the output pattern after propagation at the end of the fiber (length z) depends on the frequency due to $[G(\omega)]$ and initial composition of modes injected at the input of the fiber. However, we can find an output pattern independent from the frequency change to the first order by the following equation:

$$[G(\omega)] |b_p\rangle = \gamma_p |b_p\rangle$$

Therefore, the eigenmodes from this equation correspond to the Principal Modes (PM) and the eigenvalues to the group delay of principal modes. The eigenvalues can be complex if we consider the losses.

Assuming invariant losses in ω

$$\partial_{\omega}|b_P\rangle = \{-i\tau_1.z + Y_P\}|b_P\rangle$$

We can find also PM at the input end of the fiber

$$\{-i\tau_1.z[\mathbf{I}] + \partial_{\omega}[\mathbf{U}(\omega)][\mathbf{U}(\omega)]^{-1}\}|a\rangle = 0 \quad (3.27)$$

Here, $[\mathbf{U}(\omega)][\mathbf{U}(\omega)]^{-1}$ can be also $[\mathbf{I}]$, since $[\mathbf{U}(\omega)]$ is a Hermitian matrix.

That is, $\partial_{\omega}[\mathbf{U}(\omega)][\mathbf{U}(\omega)]^{-1}$ can be written as $-[\mathbf{U}(\omega)]^{-1}\partial_{\omega}[\mathbf{U}(\omega)]$.

For simplicity, we can define $[\mathbf{F}(\omega)]$ as $[\mathbf{U}(\omega)]^{-1}\partial_{\omega}[\mathbf{U}(\omega)]$, thus equation (3.27) becomes:

$$(-i\tau_1.z[\mathbf{I}] + [\mathbf{F}])|a\rangle = 0$$

By solving the eigenvalue equation 3.28, the PM at the input end of the fiber can be found.

$$(-i\tau_P[\mathbf{I}] + [\mathbf{F}])|a_P\rangle = 0 \quad (3.28)$$

PMs at the input end of the fiber are generally different from the PMs at the output end of the fiber since operators $[\mathbf{U}(\omega)]^{-1}[\mathbf{U}(\omega)]$ do not commute.

It should be noted that τ_P is a scalar value, and a_P does not depend on frequency.

PMs does not satisfy the orthogonal condition since the losses in each PM could be different.

In order to know the advantages of PMs on other bases (LP, OAM), a theoretical study of the PM in different coupling regime will be done. The PM are studied in terms of the variation of DGD with the fiber length for weak and strong coupling.

However, if we take into account the losses, the set of output PMs becomes a non-orthogonal basis. PM can be used to expand any electromagnetic field pattern and provide an appropriate basis that describes dispersion in FMM.

- **Example: For six modes**

Six 6-LP graded-index fibers with trench are used to study the PM (table 3.2). Such fibers support 10 spatial-modes organized into 4 nearly-degenerate mode groups (PMs) at 1550 nm (Fig. 3.9). To obtain the PMs, equation 3.28 is used by adapting the frequency by considering each fiber and number of segments.

PMs have been studied in terms of the evolution of the differential mode group delay ($\max|\text{DMGD}|$) as a function of the standard deviation of curvature. Therefore, $\max|\text{DMGD}|$ has been defined as the difference between the maximum and minimum value of the GD ($\text{MaxGD} - \text{MinGD}$). Later $\max|\text{DMGD}|$ of the PMs will be used for comparison with the $\max|\text{DMGD}|$ between the LP modes derived from the wave equation, as is summarized in Table 3.2.

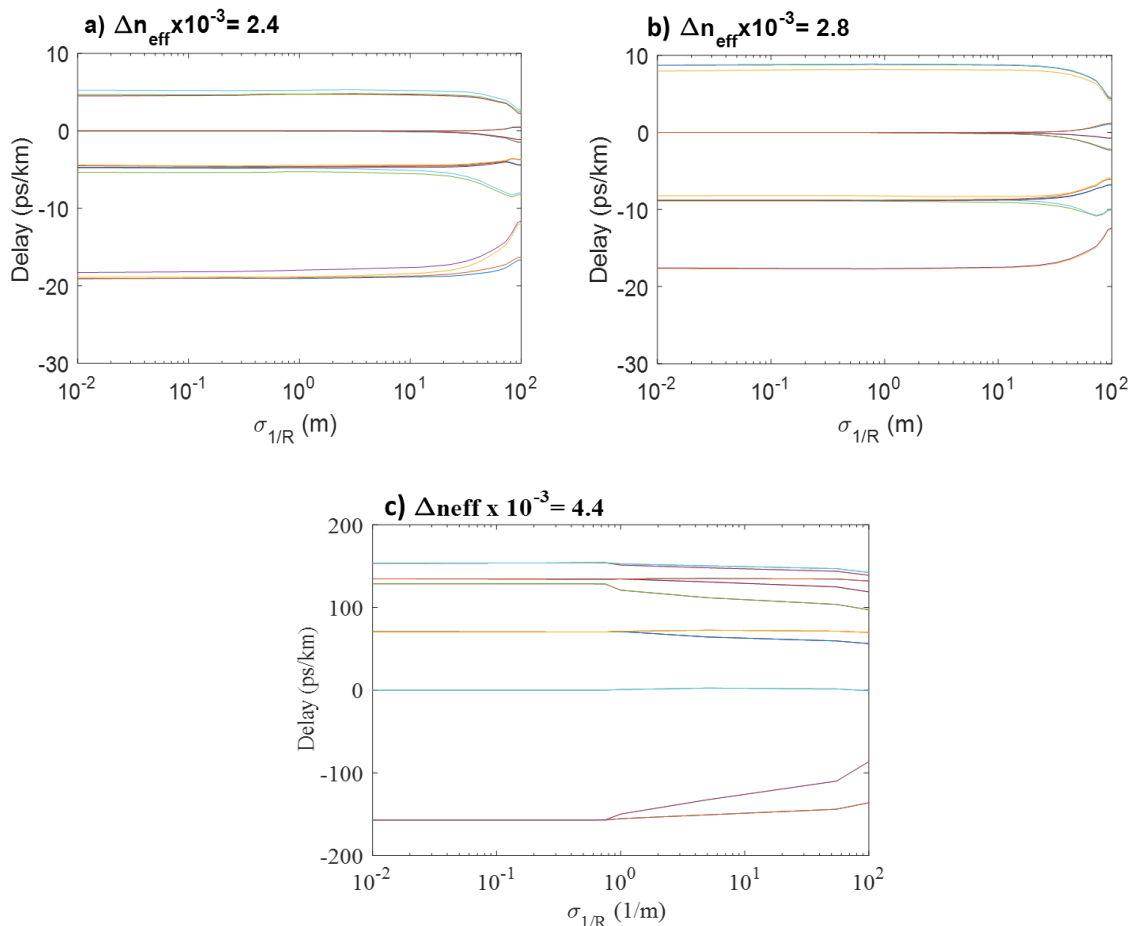


Figure 3-9: Evolution of group delay (delay) of the PMs as a function of standard deviation of the curvature for a trench-assisted 6-LP graded-index fiber of a) 13 μm core radius. b) 12 μm core radius c) 10 μm core radius. Here, a coupling model using ideal mode was considered. The bending radius follows a Gaussian distribution with the given standard deviation of the curvature. GD of PMs over 100 segments.

More precisely, we vary the standard deviation of curvature on a range of 10^{-2} to 10^2 to study the group delay (GDs) evolutions of the PMs (Fig. 3.9 a-c). For this coupling regime (weak coupling, $1/R < 0.01$), the PMs are well differentiated, without mixing with each other. Note that for the profiles $\Delta n_{eff} = 2.4 \times 10^{-3}$ and 2.8×10^{-3} (even for $\Delta n_{eff} = 1.8 \times 10^{-3}$, 2.1×10^{-3}), LP modes are grouped into 4 keeping almost the same $\max|DMGD|$ after reaching the coupling. However, for the fiber of radius = $10 \mu\text{m}$ ($\Delta n_{eff} = 4.4 \times 10^{-3}$), the modes are grouped into 5. This result can be attributed to the larger Δn_{eff} (design of the fiber).

At weak coupling, the crosstalk tends to increase when Δn_{eff} increases. As coupling increases and strong coupling is achieved, the PM's are no longer the real modes of the fiber.

3.5 Coupling regime

The coupling regime is a key in the design phase of optical fibers and to choose the MIMO-DSP. The coupling regime can be divided into two categories: weak and strong. In weak-coupling, there is a slight mode coupling, allowing each LP mode and their group delay value to be properly defined. Likewise, the GDs are not degenerated and the difference of group delay (DGD) grows linearly with the fiber length, L . In strong-coupling, there is a high mode coupling which reduces the DGD because the GDs tend to merge. Usually, DGD is proportional to the square root of the fiber length [Shemirani, 2009].

These regimes can be estimated by finding the correlation or coupling length (L_C), over which the local eigenvector can be assumed constant [Kahn, 2012]. Therefore, a weak coupling has a fiber length much smaller than L_C . Over this regime, we can find a coupling between degenerated modes, forming multi-group (MG), or PM due to their similar propagation constant, but the rest of the modes have a restricted coupling. A strong coupling has a fiber length much bigger than L_C . Here, we can find a significant coupling between all modes; allowing the Group Delay (GD) or delays tending to merge.

3.6 Study of 10-spatial-mode fibers with trench-assisted graded-index-core profiles

We have studied six 10-spatial-mode fibers with trench-assisted graded-index-core profiles. The 10 spatial modes are divided into 4 mode groups also equally spaced with

respect to the effective index n_{eff} (see Fig. 3.10). These fibers were optimized to get the smallest possible DMGDs, low bend losses ($<10\text{dB/turn}$ at 10mm radius) for all the guided modes and high losses for the higher-order leaky modes to guarantee effective cut-off. They have different core-cladding index differences (Δn_{core}) and different core radii (R_{core}), but the same normalized frequency, leading to different DMGDs and Δn_{eff} . As previously reported [Sillard, 2014], DMGDs and Δn_{eff} increase when R_{core} decreases and n_{core} increases, evidencing the resilience of the perturbation (coupling). The main fiber parameters are summarized in Table 3.2.

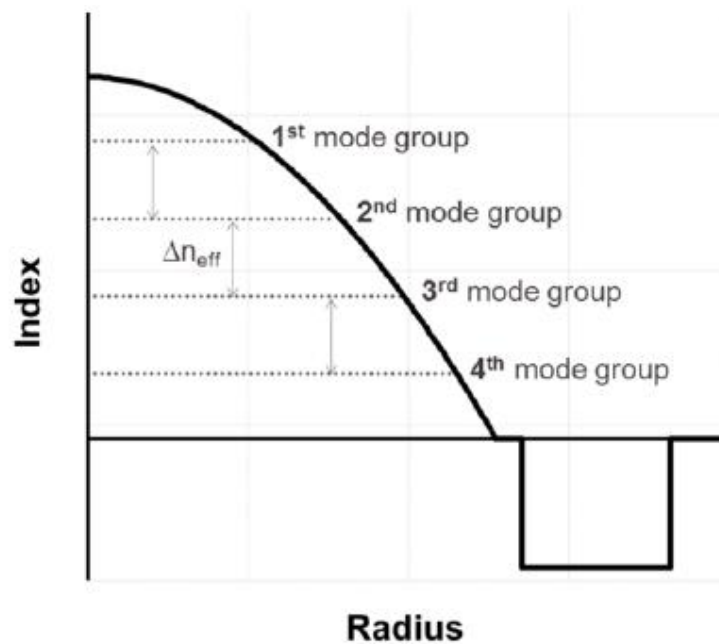


Figure 3-10: Group delay operator calculation

The coupling can influence the reduction of the overall DMGD of the FMF. An optical signal can travel on different modes at different times, which leads to an exchange of energy between modes randomly during the transmission [Shemirani, 2009]. By considering only one FMF type as the entire system without any devices (such as amplifiers, connectors, switches, etc.), it is possible to observe the change in the group delay of LP modes and PM.

3.6.1 Validation of the tools

We have validated the PM model for 10-spatial-mode fibers with calculations, obtained by solving the scalar wave equation (Equation 2.37) in the weakly-coupled regime ($\sigma_{1/R} = 10^{-20}$). We compared the differences between the maximum and the minimum GDs of the PMs, divided by the distance, with the $\max|\text{DMGD}|$ between the LP modes derived from the wave equation. As shown in Table 3.2, results are in very good agreement for these two different calculations. Note that in the absence of coupling the $\max|\text{DMGD}|$ is almost similar for both calculations methods. As Δn_{eff} increases, the $\max|\text{DMGD}|$ calculated by PM method tend to be less accurate. The $\max|\text{DMGD}|$ calculation by the group operator (equation 3.28) uses derivatives that are calculated by approximate methods (as numerical differentiation) in the numerical tools. A similar PM approach has been validated with experimental results obtained with a multi-core fiber in the strongly-coupled regime ($\sigma_{1/R} = 10^{-2}$) [Fujisawa, 2015].

Besides, we have studied the group delay as a function of the curvature and the group delay variation as a function of the width trench on the profiles presented in Table 3.2. Note that different Δn_{eff} lead to different coupling behaviors, so that the higher the Δn_{eff} , the more resistant to coupling. In other words, a large Δn_{eff} (small core) produces a high DMGD and vice versa.

Table 3.2: Fiber parameters. It contains different radii of the core from 10 μm to 15 μm keeping the same the normalized frequency and bend losses to ensure minimal macrobending losses (as defined in chapter 2).

Rcore (μm)	10	11	12	13	14	15
$\Delta\text{core} (\times 10^{-3})$	19.4	16.1	13.5	11.5	10	8.7
Normalized Frequency	9.65	9.65	9.65	9.65	9.65	9.65
$\Delta n_{eff} (\times 10^{-3})$	4.4	3.3	2.8	2.4	2.1	1.8
Bend Losses (dB/turn)	<10	<10	<10	<10	<10	<10
Max DMGD [wave Eq.] (ps/km)	312	35.9	26	21.6	18.8	16.1
Max DMGD [PM analysis] (ps/km)	308	34.7	25.6	21.4	18.7	16.0

3.6.2 Group delay as a function of the curvature

We have computed numerically the group delay as a function of the standard deviation of curvature on a range of 10^{-20} to 10^3 based on the coupling model described previously for different segment number (100 and 1000) with a fixed fiber length of 1km. We used the fiber profiles of table 3.2 to study the coupling regime at different Δn_{eff} .

To study the GDs evolution as a function of the curvature, we use the PM modes. They are obtained by the PM analysis modifying the frequency range. Figure 3.11 a-f) shows GDs of a fiber for different segments and two profiles: radius =14 μm ($\Delta n_{eff} = 2.1 \times 10^{-3}$) and radius =11 μm ($\Delta n_{eff} = 3.3 \times 10^{-3}$). Note that one of the main influences of the mode coupling is the reduction of the DMGD as the standard deviation (std) increases. This variation (in the DMGD) allows to determine different coupling regimes. Through these graphs, it is possible to describe three different coupling regimes $\text{std} \sim 10 \text{ m}^{-1}$ (very weak coupling), $10 < \text{std} < 10^2 \text{ m}^{-1}$ (intermediate coupling) and $\text{std} > 10^2$ (strong coupling). At very weak coupling, the vector modes with a very similar propagation constant are grouped in MG, demonstrating their degenerescence. For an intermediate coupling, all the modes reduce their delay, leading to reductions in the DMGD. At strong coupling, the tendency is that all modes merge tending to have similar delay, further reducing the DMGD. It should be noted that the minimal spread between the maximum and minimum values of GDs is reached as the number of segments is increased.

To study the leaky mode effect in the guided modes, we have considered two cases, without and with leaky modes (See Figs. 3.12a-b and Fig. 3.13a-b). To compare we have analyzed the attenuation (Rayleigh+leakage) as a function of the standard deviation of curvature on a range of 10^{-10} to 10^3 based on the attenuation calculation described previously in chapter 2 for 1000 segments with a fixed fiber length of 1000 m. Note that, in the absence of leaky modes and in the strong coupling regime, the tendency is that all modes merge, losses are higher for some modes and lower for others. Here, the curvature losses are not considered.

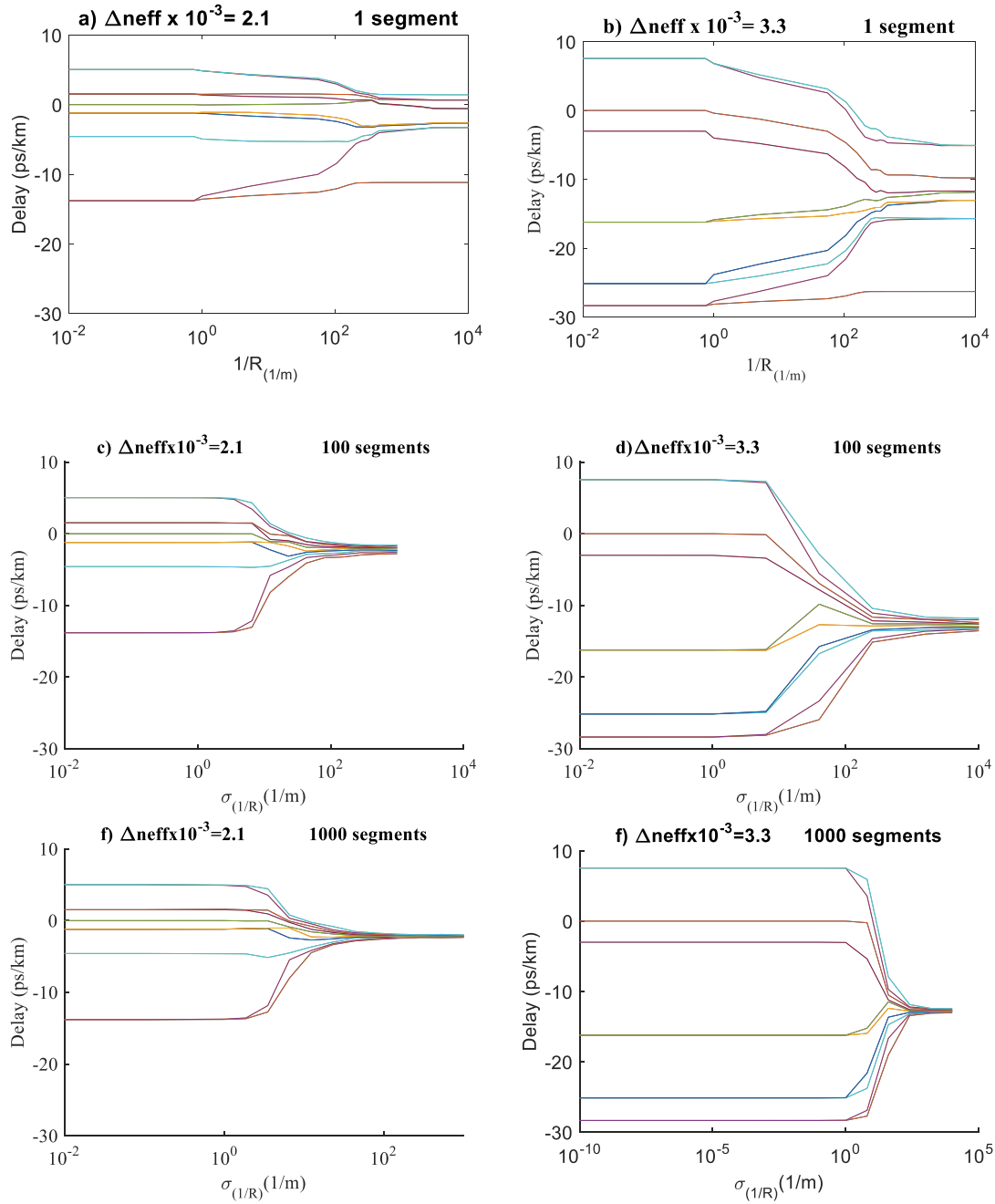


Figure 3-11: a-b) Evolution of group delay of the PM modes as a function of curvature (1/R). c-f) Evolution of group delay of the PMs as a function of the standard deviation of curvature.

In the presence of leaky modes and intermediary coupling, we have expected that the leaky effect impacts over the guided modes. However, the leaky effect or attenuation presented an abrupt increase at 10^{-3} (close to the end of weak coupling) for the profile with a $\Delta n_{eff} = 2.1 \times 10^{-3}$ and at 10^{-2} for the profile with a $\Delta n_{eff} = 3.3 \times 10^{-3}$ (Fig. 3.13 a-b). That is, the leaky effect occurs faster on $\Delta n_{eff} = 2.1 \times 10^{-3}$ because some of their leaky

modes have a Δn_{eff} closer to the guided modes, with a difference from the other profile (Section 2.8, chapter 2).

For $\text{std} > 10^{-3}$, $\Delta n_{eff} = 2.1 \times 10^{-3}$ (143 dB/km) presents higher losses than $\Delta n_{eff} = 3.3 \times 10^{-3}$ (30 dB/km) because the first profile has a greater amount of leaky modes and some of them undergo higher losses than the second profile which favors the losses during the coupling.

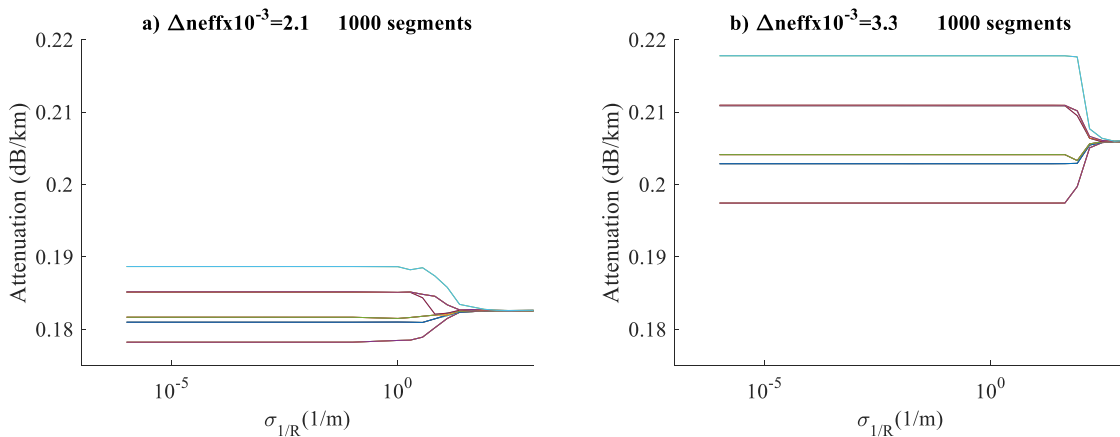


Figure 3-12: a-b) Evolution of attenuation (guided PMs modes without leaky modes) as a function of curvature.

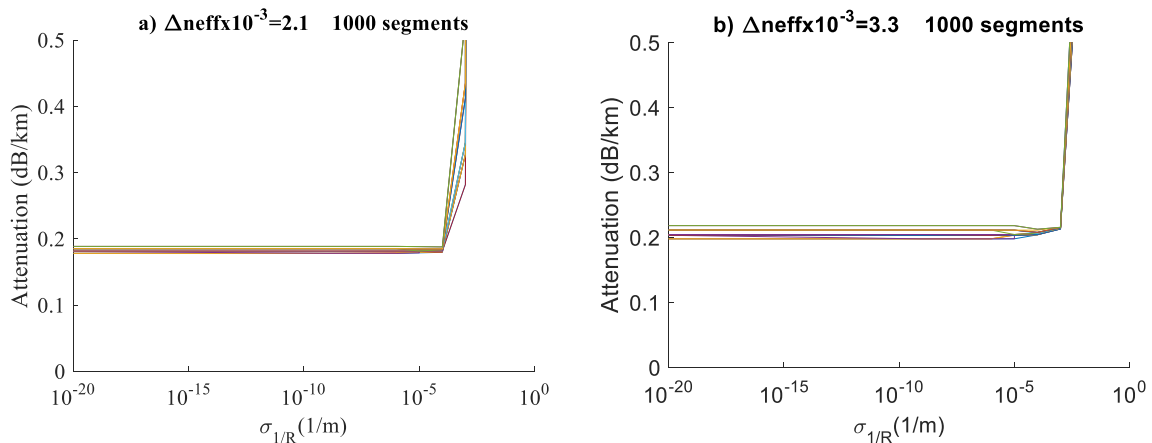


Figure 3-13: a-b) Evolution of attenuation (guided modes with leaky modes) as a function of curvature. To make the graph, a linear interpolation between the calculated points was realized.

Note that when the leaky modes are considered on these fibers profiles, the guided modes can exhibit high losses before to reach the strong coupling.

3.6.3 Study of the group delay variation as a function of the distance

To study the group delay evolution, we varied the propagation length keeping the same segment length for different coupling regime. Thereby, the number of segments can change with the distance. We study the linear and square root behaviors of the GDS as a function of the propagation length. These linear and square root behavior can also be studied by equations 3.29a and 3.29b which permits to find the standard deviation, σ_{GD} of the coupled modes in weak and strong coupling, through of the standard deviation of only one segment $\sigma_{GD,s}$ and the segment number used, N [Ferreira, 2015]. These equations are valid if all FMF segments have identical statistical properties.

$$\sigma_{GD} = N \cdot \sigma_{GD,s} \quad (3.29a)$$

$$\sigma_{GD} = \sqrt{N} \cdot \sigma_{GD,s} \quad (3.29b)$$

These behaviors are obtained by multiplying the number of segments by the MaxGD-MinGD value of an uncoupled mode.

Likewise, by evolution of group delay (delay) figure, the linear and square root behavior can be well differentiated as in Figure 3.14.

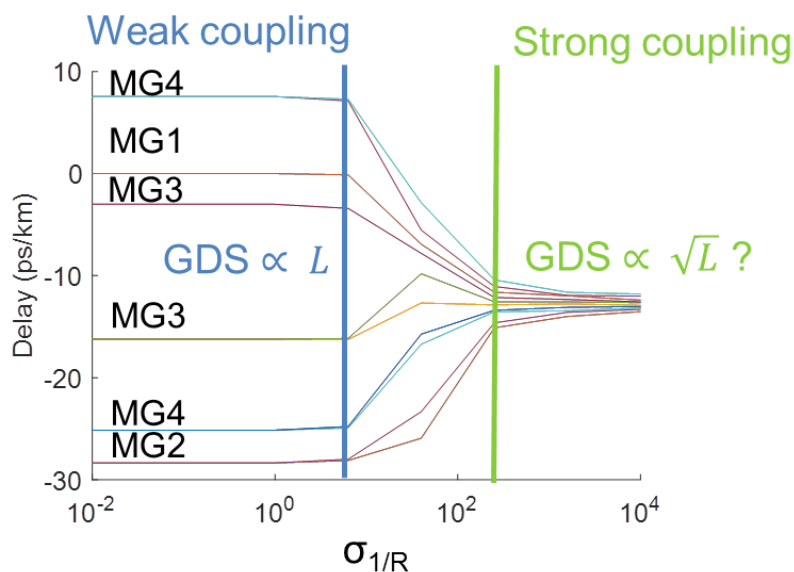


Figure 3-14: The linear and square root behaviors in the coupling regime curve.

Figure 3.15 and 3.16 show the results up to a distance of 10000 km for fibers with $\Delta n_{eff} = 4.4 \times 10^{-3}$, and with $\Delta n_{eff} = 2.4 \times 10^{-3}$. The upper solid line and the lower solid line represent the linear and square root behavior of the GDS respectively, and the dotted lines are the MaxGD-MinGD simulated values for $\sigma_{1/R} = 10^{-20}, 10^{-2}, 10^0, 10^1$ and 10^2 .

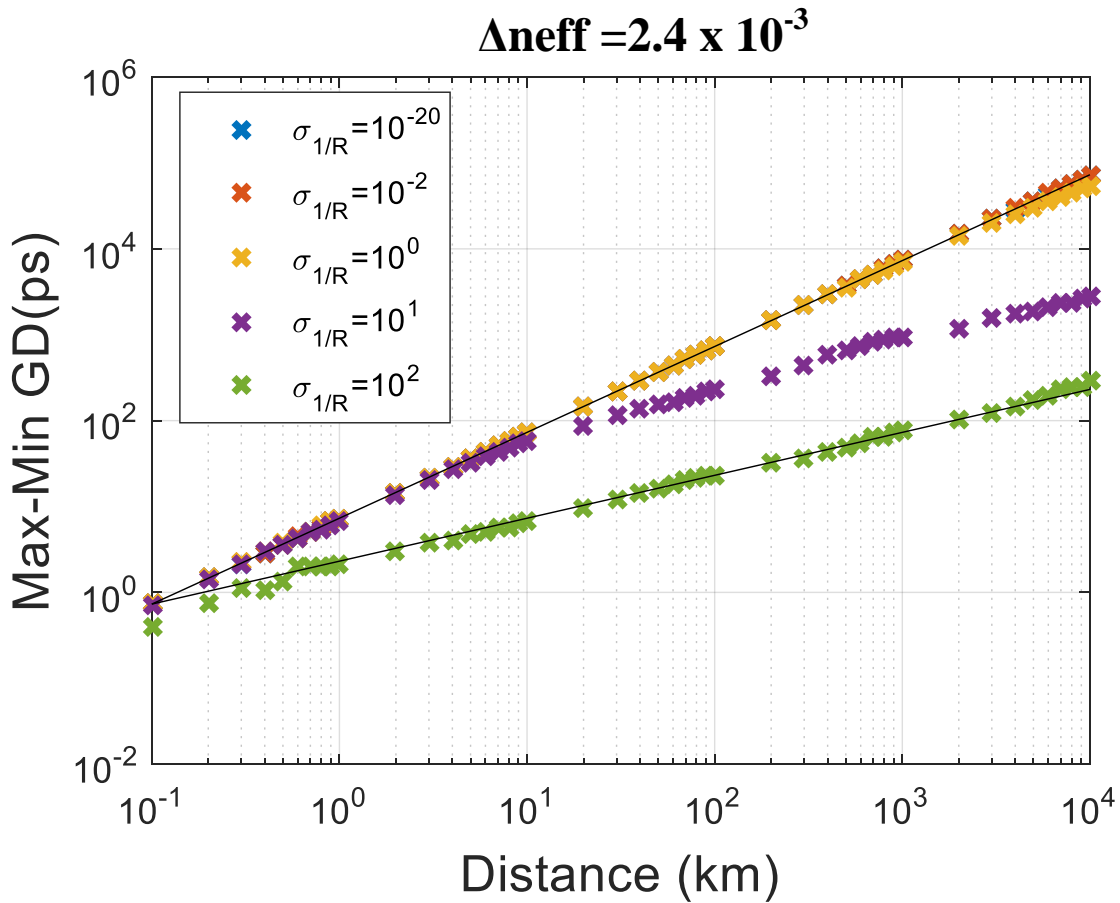


Figure 3-15: Max-Min GD as a function of the propagation distance for different coupling strengths $\sigma_{1/R}$ for 10-spatial-mode fibers with $\Delta n_{eff} = 2.4 \times 10^{-3}$.

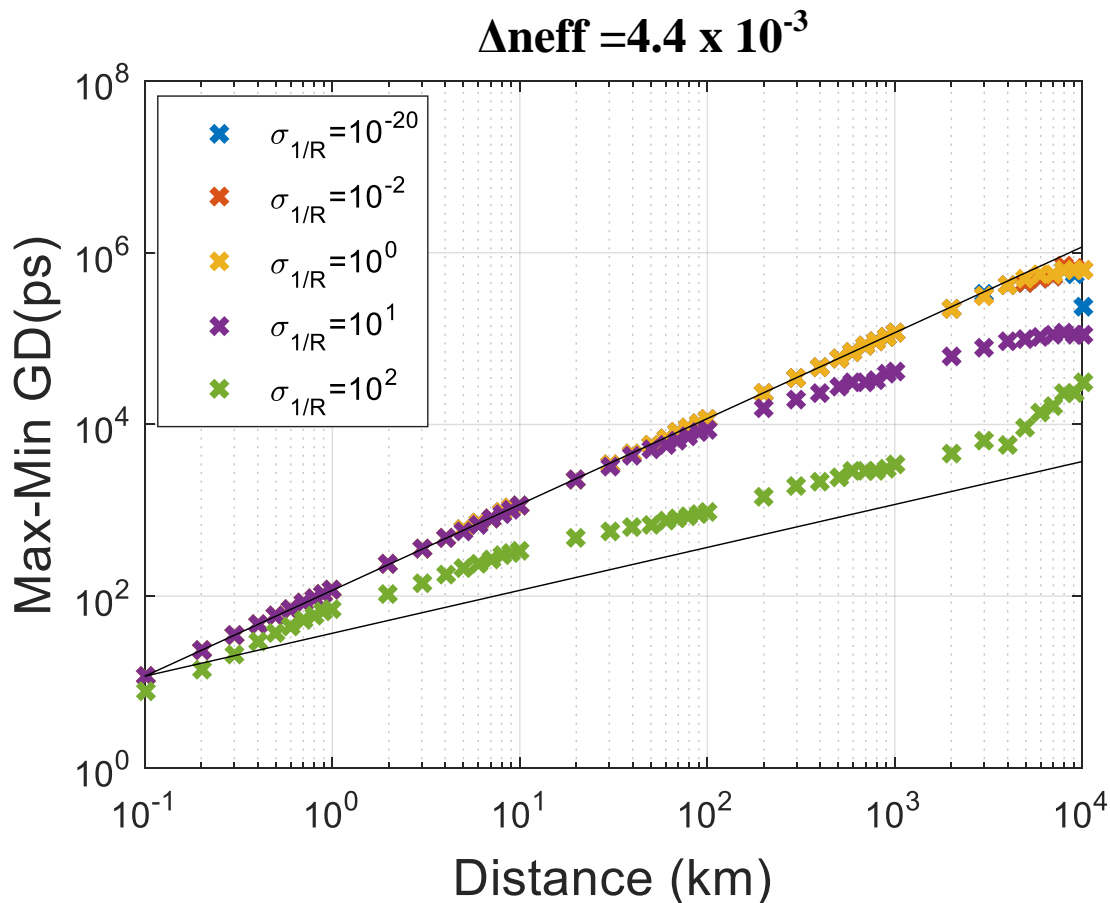


Figure 3-16: Max-Min GD as a function of the propagation distance for different coupling strengths $\sigma_{1/R}$ for 10-spatial-mode fibers with $\Delta n_{eff} = 4.4 \times 10^{-3}$.

As expected (Fig 3.15 and 3.6), in the weakly-coupled regime ($\sigma_{1/R} = 10^{-20}$), the GDSs increase linearly with the distance and perfectly follow the upper line for all 10-spatial-mode fibers. This is in line with experiments made with graded-index 6-spatial-mode fibers where coupling between mode groups does not occur after 100s of km of propagation distance [Ryf, 2013] because of too small perturbations. Once the mode coupling ($\sigma_{1/R}$) increases, the GDS starts to decrease and its dependence with distance becomes weaker. The square root behavior is finally reached for very high perturbations ($\sigma_{1/R} \geq 10^2$) and for Δn_{eff} between 3.3×10^{-3} and 1.8×10^{-3} (see representative results for $\Delta n_{eff} = 2.4 \times 10^{-3}$ in Fig. 3.15). What is remarkable is that this behavior is never attained for distances up to 10000 km for $\Delta n_{eff} = 4.4 \times 10^{-3}$ even for very high perturbations ($\sigma_{1/R} = 10^1$ and $\sigma_{1/R} = 1$ produced quite similar results as those for ($\sigma_{1/R} = 10^{-2}$), as shown in Fig. 3.16. This suggests that there is a Δn_{eff} upper limit, between 3.3×10^{-3} and 4.4×10^{-3} for these fiber profiles, above which coupling becomes constant even for very high perturbations, which prevents them from reaching the strongly-coupled regime and the square root behavior of the GDS. This is in

agreement with recent experiments that evidenced a constant mode-coupling phenomenon for Δn_{eff} above a certain value for several few-mode fibers, including a graded-index 3-spatial-mode fiber [Maruyama, 2015].

To evaluate the root square behavior of the GDS, we take the extreme cases of propagation distances of 1 and 1000 km and $\sigma_{1/R}$ of 10^{-20} and 10^2 . At 1 km and 1000 km for small perturbations ($\sigma_{1/R} = 10^{-20}$) the GDS varies linearly, however the GDS increases once the distance increases, evidencing a GDS cumulative with the distance. For high perturbation and small distances (≤ 1 km), the coupling slightly reduces the GDS.

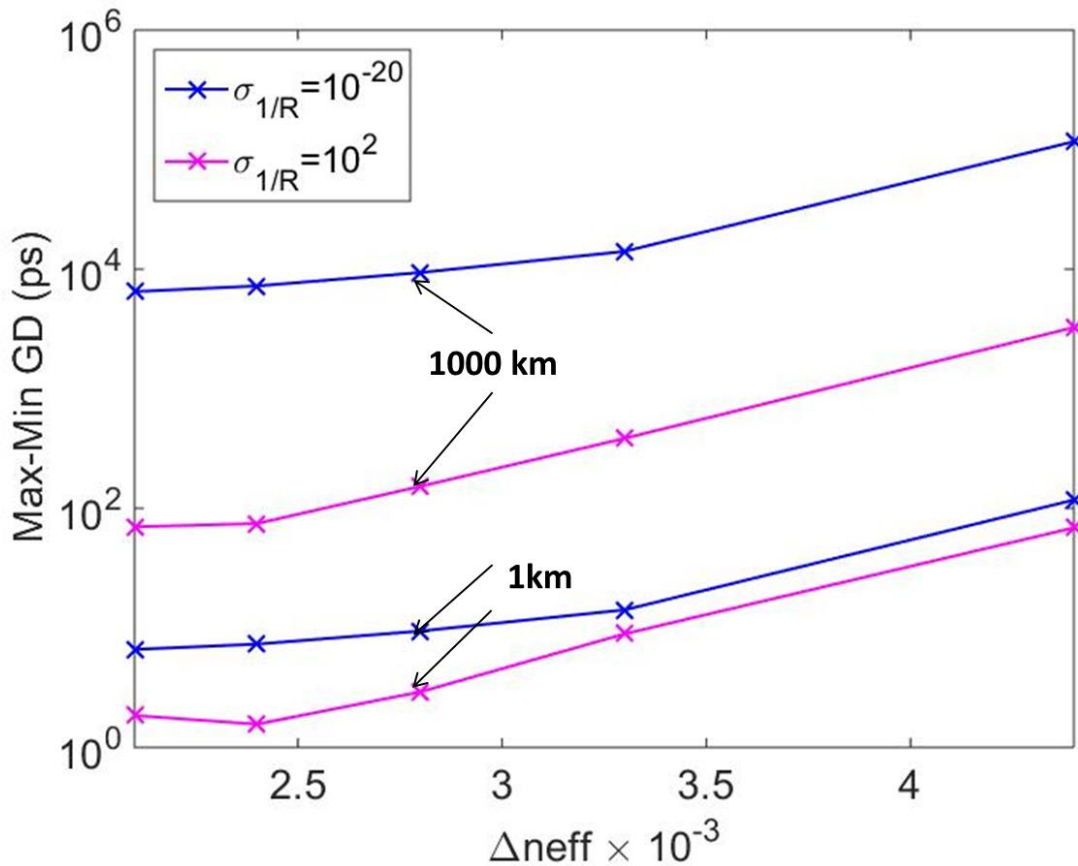


Figure 3-17: Max-Min GD as a function of Δn_{eff} for $\sigma_{1/R} = 10^{-20}$ and 10^2 and propagation distance of 1km and 1000km for 10-spatial-mode fibers.

For $\sigma_{1/R} = 10^2$ (high perturbations) and high distances (≥ 1000 km), the strongly-coupled regime should be reached, and the GDS strongly reduced. Nevertheless, the steep increase of the GDS for Δn_{eff} between 3.3 and 4.4×10^{-3} is clearly visible, showing that in this Δn_{eff} range, the strongly-coupled regime is never reached and probably it is in the intermediary coupling. The reduced GDS obtained when moving from small to high perturbations for distances between 1 and 1000 km is also shown.

Fig. 3.18 shows the square-root behavior of the GDS between the propagation distances of 1 and 1000 km and $\sigma_{1/R}$ of 10^{-20} and 10. At 1 km and 1000 km and for small perturbations the GDS difference between $\sigma_{1/R}$ of 10^{-20} and 10 are lower than in the previous case (Fig. 3.17) demonstrating a slight reduction of GDS or quite same behavior for both of $\sigma_{1/R}$.

However, for high perturbation and small distance (≤ 1 km), the GDS difference is lower than in the Figure 3.17 evidencing that the GDS are leaving the linear zone without reaching the root square behavior.

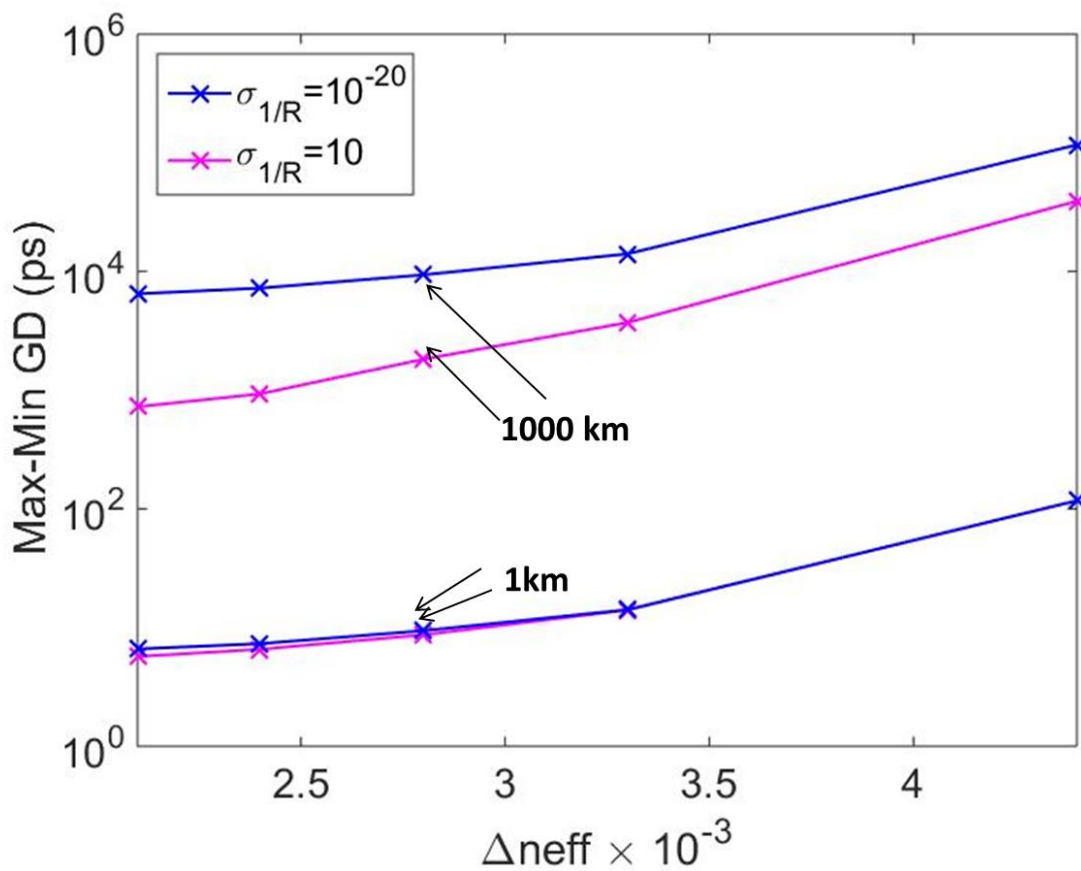


Figure 3-18: Max-Min GD as a function of Δ_{neff} for $\sigma_{1/R} = 10^{-20}$ and 10 and propagation distance of 1km and 1000km for 10-spatial-mode fibers.

3.6.4 Influence of coupling regimes on the electrical field

Figure 3.19 and 3.20 show the electric field vector for different coupling regimes, here we should consider the absolute value of E_x or E_y , multiplied by the real part sign of them. In

the absence of coupling and at very weak coupling, the LP modes are found without deformation. Whereas at strong coupling, these modes start to deform until they cannot be recognized.

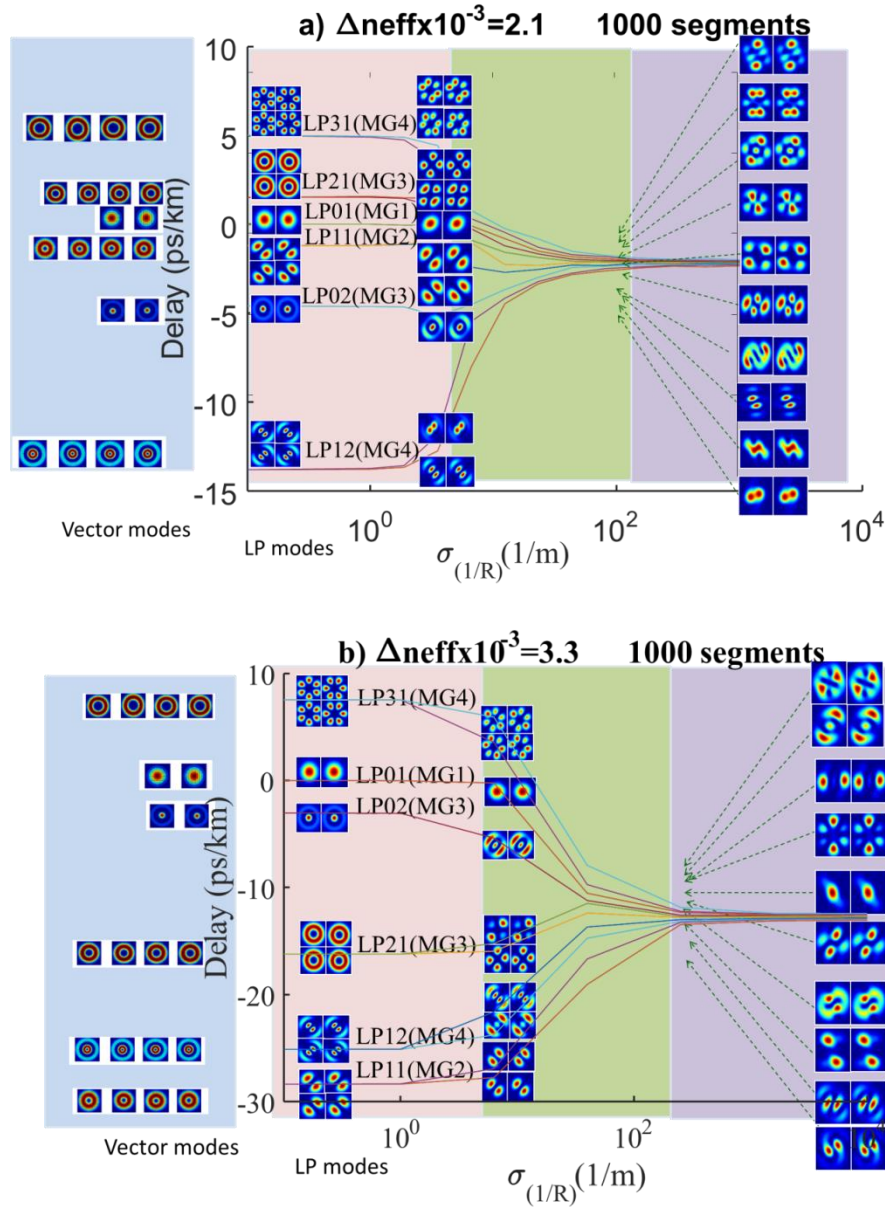


Figure 3-19: Evolution of electric field vector as a function of curvature for a) $\Delta n_{eff}=2.1 \times 10^{-3}$ b) $\Delta n_{eff}=3.3 \times 10^{-3}$.

For weak and intermediary coupling, LP_{01} and LP_{11} seem to be more resilient to the coupling in both profiles.

Taking as example the LP_{01} mode at $\Delta n_{eff} = 2.1 \times 10^{-3}$ profile, the intensity of the electrical field vector $LP_{01}(MG1)$ has more deformation than the $\Delta n_{eff} = 3.3 \times 10^{-3}$ profile

(cf. Fig. 3.19b), possibly because LP_{01} receives more influence from its neighbors (LP_{11} and LP_{21}), due to its low GD separation (See Fig. 2.14).

It should be noted that some vectors of the electrical field in the presence of leaky modes are shifted to the cladding and others have lost their orientation. Probably, this displacement is produced by the reflections from leaky modes between cladding.

3.7 Summary

The strength of coupling between the modes determines the coupling regime and it can be used as a criterion to reduce the MIMO-DSP complexity in FMF communication systems or to design fibers resilient to the coupling. The coupling between modes depends on how close is the modal propagation constant (or Δn_{eff}) from each mode and this parameter is used in the FMF design. As was demonstrated, we can find two well-defined coupling regimes: weakly-coupled and strongly-coupled, and an intermediate coupling [Ferreira, 2015].

To describe the coupling regime, we can use the correlation length (L_C), L_C is found according to the invariability of the eigenvector, as proposed by [Fan 2005]. Once L_C is identified, we compare the fiber length with L_C to determine the coupling regime. A weak coupling has a fiber length much smaller than L_C . Over this regime, we can find an important coupling between non degenerate modes, forming multi-group (MG) or modes which are used in several practical applications.

As we have seen above, the study of the GD as a function of the propagation distance for different coupling strengths allows to evaluate at which distance the square root behavior of GDS as a function of distance can be achieved. Thus, this behavior can be reached in the strongly-coupled regime up to 10 spatial modes, but only for high perturbations and for Δn_{eff} below a threshold value. To minimize the GDS, one has to target fibers with the lowest possible Δn_{eff} while ensuring low bend losses for all modes. The challenge is to introduce high perturbations with low losses to achieve the strong coupling: should we use mode scramblers? Long period gratings?

Instead of using the unperturbed eigenmodes of the FMF, Principal Mode (PM) is a candidate to use with MIMO-DSP, because these modes can minimize the modal dispersion, which is the main cause of the bandwidth limitation. The orthogonal advantage of the PM allows a minimal distortion in modal coupling. Thus, it is easier for MIMO-DSP to treat this mode group or PM, instead of the isolated modes (Eigenmodes). However, it must still be assessed how this could affect the transmission system elements, such as amplifiers, routers, etc.

Strongly-coupled FMF is a promising technology for high-speed long-haul optical systems, while FMF weakly-coupled can be an interesting solution for short distances.

Hence, depending on the coupling strategy, we distinguish two cases:

Coupled mode in the emerging MDM communication systems

- For strongly coupled regimes, reducing the differential group delay (DGD) allows to decrease the complexity (in reception) in FMF systems based on so-called full MIMO DSP.
- For weakly coupled regimes, reducing the coupling among all modes by design of the FMF allows the use of small size MIMO in the communications system, at the price of more stringent specifications for the optical fiber.

4 Localized mode coupling measurement in FMF

As discussed in previous chapters, mode coupling is a stochastic process related to the fiber irregularities and perturbations. Several methods can measure the modal coupling ratio, but in FMF it is convenient to evaluate the modal content, especially so as to characterize crosstalk. Spatially and spectrally resolved imaging (S2 imaging), the correlation filter technique (CFT) and other techniques are experimental methods that allow to measure it.

S2 can be used to retrieve modal content and power distribution in FMF. One can presume that this method could be expanded to characterize mode coupling. It is based on a spectral and spatial imaging technique and relies on Fourier analysis of the inter-modal interferences. However, in some cases, interpretation of the beat profile can be difficult and advanced S2 imaging (A-S2) provides a more robust analysis method [Sevigny, 2014]. We will now study the mode coupling in FMF under localized perturbation, using A-S2.

4.1 A brief review of coupling measurement

4.1.1 Method for measuring the modal content of a fiber

As we have discussed before, FMF over MDM supports multiple spatial modes, thus each mode is seen as an individual communication channel. To be used at its optimum optical level of performance, an MDM system requires advanced characterization methods to evaluate the modal content of the FMF from several aspects: the geometry of the modes, the dispersion of the group index and the distribution of power between the different modes.

Various methods, often interferometric, make it possible to characterize one or the other of these aspects, but only a few techniques are able to properly characterize all of them. The spatially and spectrally resolved imaging (S2) is one of the methods that offers the most simple experimental setup to characterize the modal content. It operates by spatially resolving the interferences that occurs when a coherent beam in an optical fiber is propagated over different modes with different group delays. As we will briefly see in this next section, there are other methods to reconstruct the total or partial information of modal content, for instance, the correlation filters and cross-correlated imaging (C2).

4.1.1.1 Correlated filter and matched filter (CFT)

This method was introduced by [Golub, 1982] and requires a light shaping system in order to reconstruct the phase of the modes by a scanning of wavelength or delay which needs a certain time of acquisition. Thus, on the beam interference at the optical fiber output, a hologram is used which is especially encoded by the phase pattern of each mode. The calculation of this hologram uses the shape of the field envelopes, which are previously calculated or measured elsewhere. Through the successive diffraction of the beam by the holograms, proper to each mode, we get the different figures of intensity. This hologram is produced by a computer and specially masked as phase hologram (spatial light modulator-SLM) [Flamm, 2012] or amplitude hologram (a personalized mask) [Kaiser, 2009].

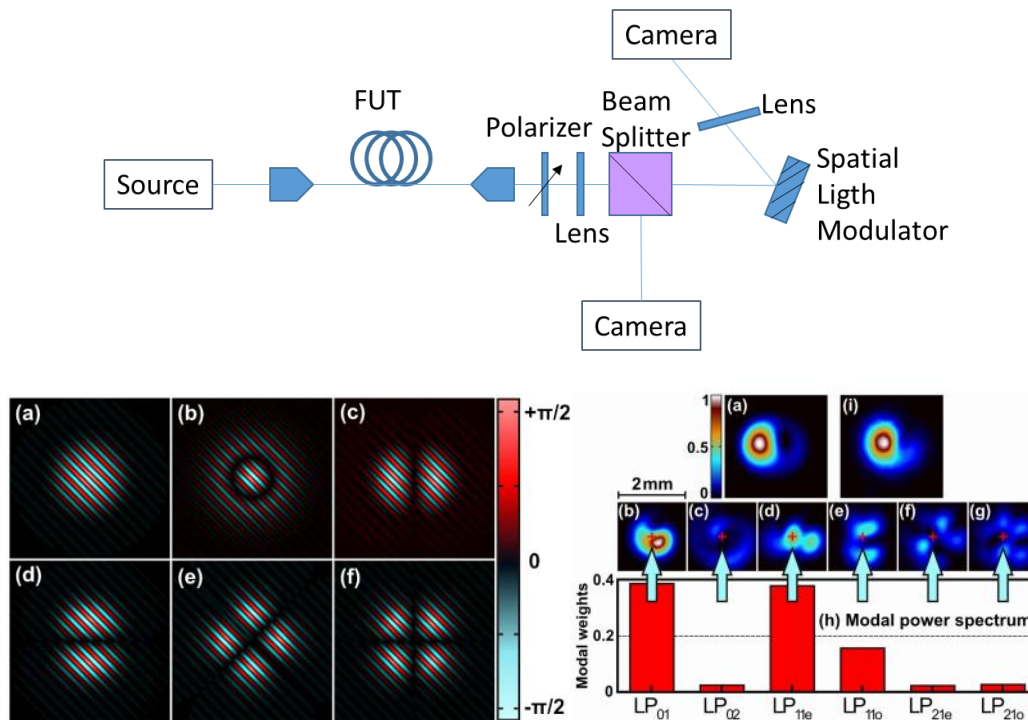


Figure 4-1: a) The correlated filter method scheme to obtain the modal content. [Flamm, 2012]. b Left) Phase-hologram (encoded phase modulation) example for the six first guided modes by using an SLM as correlation filter. Right) Modal analysis with HM content, a) measured near-field intensity by measuring of the power as intensity of the diffracted signal (red cross). b-g) Signal after correlation for the phase-hologram of figure-left. H) Measured modal power spectrum. Here, 60% of the total power is guided by HOM.

SLM allows an amplitude and phase modulation encoded in a digital hologram which makes its use much more interesting than the conventional hologram. Indeed it is able to examine an arbitrary and unknown fiber with a successful modal decomposition by the real-

time switching of the digital hologram. Unfortunately, the quality of the hologram can be affected by the SLM resolution, the modulation functions selected and the scaling factor that requires a priori knowledge of the modes geometry that is a strong limitation. The correlated filter is a very efficient method but does not measure directly the modal dispersion.

As we can see from figure 4.1, the output beam of the fiber is retransmitted through a beam splitter to a near-field camera and an SLM in reflection mode. The diffracted beam from the SLM is followed by a lens and then detected on a second camera (far field). The diffracted far field pattern contains direct information about the mode powers and intermodal phase differences. Thus, it is possible to measure the correlation signals, the amplitude and phase of the modes [Schulze, 2015] and even determine the angular alignment (horizontal or vertical) of the modes by the orientation of the hologram.

This method is appropriate for real time decomposition of multimode fiber beams and its advantage is that the modes power evaluation is obtained directly by measuring the intensity, however measurements accuracy can be affected by the number of modes detected.

4.1.1.2 Cross-correlated imaging C2

C2 is another method that can be applied to obtain information on modal content, intensity distribution of the modes and group delay. The method allows to study the interference between the beam of the fiber and an external reference beam, detecting different modes in the time-domain as consequence of two relative optical paths of the two beams [Schimpf, 2011]. This method can also be performed in the frequency-domain [Demain, 2014].

The C2 scheme is shown in the figure 4.2. The beam from the laser is divided into two beams: the reference and the probe arms here presented in a standard Mach-Zehnder interferometer configuration. The reference arm uses a dispersion compensating SMF, while the probe arm contains the fiber under test. The reference arm has an automated translation stage that scans across the temporal delay of each individual mode of the probe arm. Thereby, by the position variations of the delay stage, the camera takes the image of the interference between the combined beams of both arms. The resolution of the obtained cross correlation trace is sensitive to dispersion. Likewise, the relative weak size of the modes can crop the interference figures or make the intensity of the fundamental mode smaller, restraining the reconstruction of the field amplitudes.

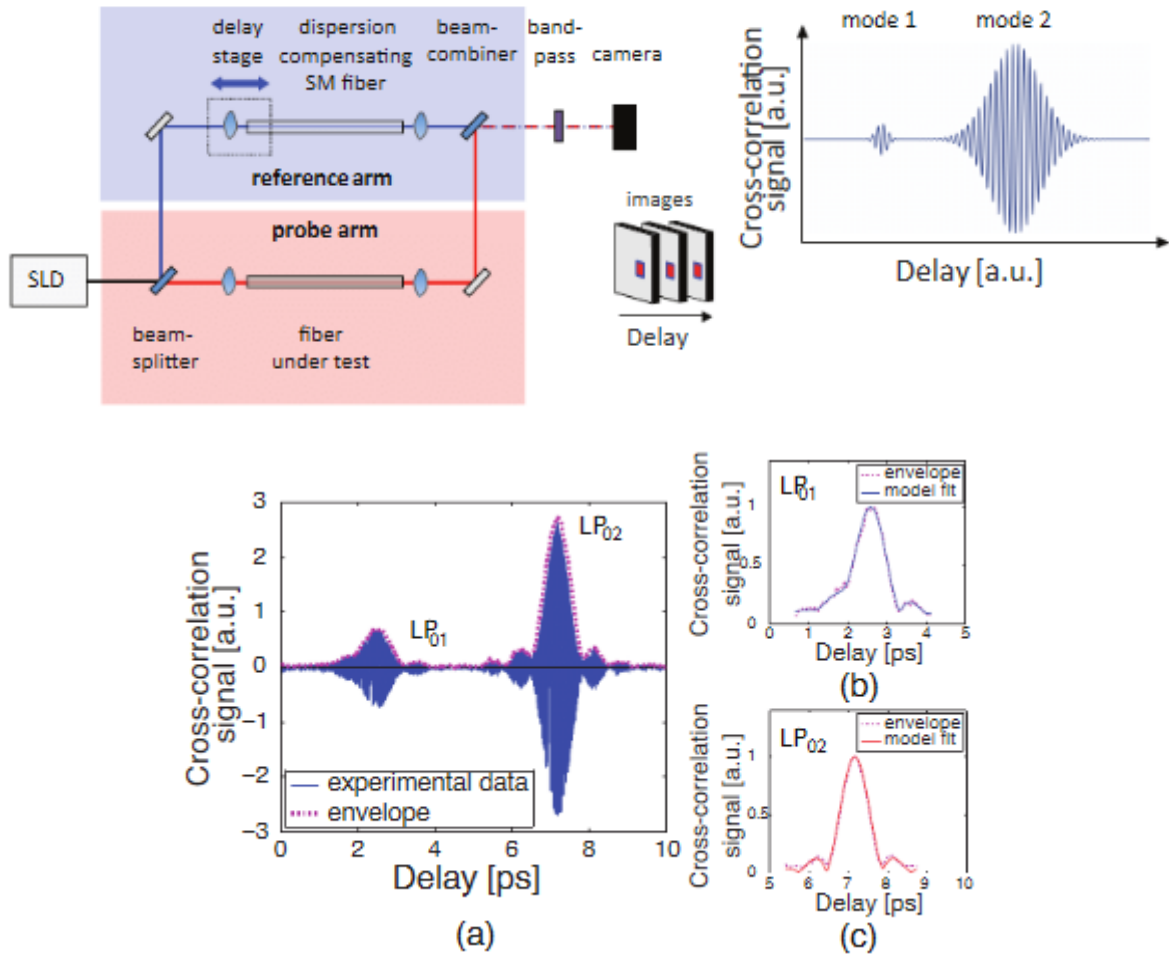


Figure 4-2: a- Left) The C2 imaging scheme to obtain the cross-correlation trace [Schimpf, 2011]. SLD: super luminescent diode. Right) Cross-correlation trace at one pixel of the images group. b- Left) Cross-correlation trace between the reference field and the output of the fiber by integrating over all pixels recorded by the camera. The peaks in the trace correspond to the two different modes (LP_{01} and LP_{02}) in the fiber.

In temporal term, C2 can be considered similar to S2 measurement. Even their data sets can be obtained through mathematically analogous methods. Both methods allow to reconstruct the modes from the stack of images obtained by the data acquisition (Camera). Specifically, C2 captures an intensity image at a given stage position. Thus, the electric field from intensity image is treated mathematically within a certain frequency domain to obtain a superposition of the output and reference fields. This sum describes the superposition of the optical fiber modes. Summarizing, the envelope of the cross-correlation trace is obtained from the stack of images recorded by the camera.

By assuming that all modes have the same spectral excitation, the intensity can be described by the sum of two intensities which is the interference between the reference field

and the individual modes. Thereby, one of the intensity terms is independent from the stage position and the other depends on the phase-mismatch between the two arms of the interferometer. In the end, the difference between these two intensities is used to obtain a signal as a function of the translation stage position used to determine the envelope of the cross-correlation trace.

C2 depends on the group-delay and dispersion. In the absence of dispersion, broad spectra can be used to achieve maximal temporal resolution. However, when the interferometer cannot control the dispersion (unbalanced dispersion), the broadening of cross-correlation signal is dominated by the dispersion. For high bandwidths, C2 requires to control the dispersion to obtain an appropriate measurement, unlike to S2 imaging technique. By this technique, we can measure the group delay, dispersion, polarization, and the modal content.

4.1.1.3 Spectrally resolved imaging (S2)

S2 was introduced by [Nicholson, 2010] and it takes advantage of the fact that each mode propagates with a different propagation constant which leads to a spectral interference pattern in the fiber output. The spectral interference pattern in the near-field images is caused by the group delay difference between modes. This method measures this interference pattern at different wavelengths at any arbitrary point, which allows to obtain the optical spectrum (See Fig. 4.3-Left). The collected data (optical spectrum) is studied by Fourier transform analysis in order to determine several beat frequencies at different group delays or group index differences (See Fig. 4.3-Right), or to reconstruct the amplitude and phase profiles. S2 is similar to C2 except that the reference is not an external beam, but a mode of the fiber.

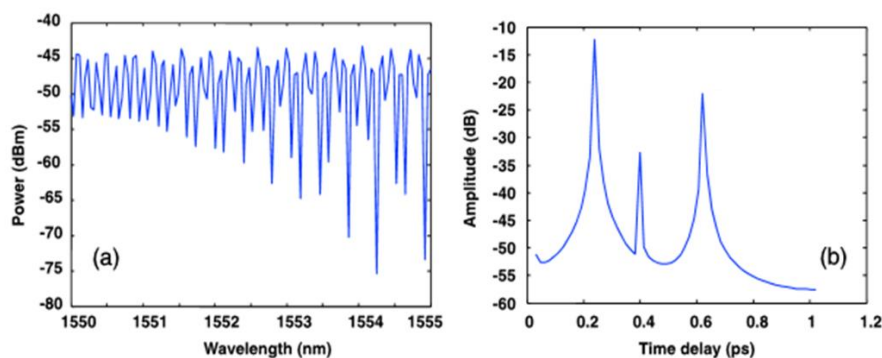


Figure 4-3: Left) Example of an optical spectrum. Right) its Fourier transform with multiple beat frequencies [Nguyen, 2012]. These peaks correspond to each beats between the fundamental modes and each higher order modes.

As we already discussed, conventional S2 allows the characterization of field geometry, the difference of the group index between the modes and the power distribution of the different modes. However, its usefulness is limited by two factors: firstly one mode must clearly dominate the others, its relative power must be greater than 90% of the total power and, secondly, the group index differences of this mode with the others must not be degenerated with others group index difference, in which case the information on these two modes is confused and inseparable.

To understand the method, let us assume linear polarization and uncoupled modes. Thus, the optical near field of the fiber at a given frequency can be written as in the equation 4.1

$$E_{(x,y,\omega)} = \sum_{k=1}^M F_{k(x,y)} \cdot \sqrt{P_k} \cdot (e^{i(\frac{2\pi n_{eff,k}}{\lambda} L - \omega t)} + CC) \quad (4.1)$$

where F_k is the normalized field amplitude of the k th mode, P_k is the power in the k th mode, $n_{eff,k}$ corresponds to its effective index, M is the total number of modes in the optical fiber and CC is the complex conjugate.

The square of this output field allows to retrieve the intensity recorded by the camera. Thereby, from a mathematical point of view, we can obtain the spectral intensity caused by the interference between the propagating modes by the coherent sum of all modes fields of the fiber. Thus, the intensity (Equation 4.2) can be written as a function of the difference between the propagation constant $\Delta\beta_{k\ell} = \beta_k - \beta_\ell$ of the guided modes k and ℓ by considering the following relationship $\beta = 2\pi \cdot n_{eff} / \lambda$.

$$I = \bar{I}_{(x,y)} + \sum_{k=1}^{M-1} \sum_{\ell=k+1}^M 2 \cdot \sqrt{P_k \cdot P_\ell} \cdot F_k(x,y) \cdot F_\ell(x,y) \cdot \cos((\beta_k - \beta_\ell) \cdot L) \quad (4.2)$$

In the equation 4.2, the first term corresponds to the constant intensity $(\sum_{k=1}^M P_k \cdot F_k(x,y)^2)$ and the second term to the interference between the different modes. This interference can be characterized experimentally by the variation of the wavelength (optical frequency). Therefore, the mode propagation constant that is a frequency-dependent term can be expanded to the first order of the Taylor series (Equation 4.3).

$$\beta(\omega) \approx \beta_o(\omega_o) + (\omega - \omega_o) \cdot \beta_1(\omega_o) \quad (4.3)$$

$$\beta_1(\omega_o) = \left. \frac{\partial \beta}{\partial \omega} \right|_{\omega=\omega_o} = \frac{1}{v_g} = \frac{n_g}{c} \quad (4.4)$$

Note that the term β_1 is the inverse of the group velocity (v_g).

Likewise, we write the effective index difference, $\Delta\beta_{k\ell} = \beta_k - \beta_\ell$, using equation 4.3.

$$\Delta\beta_{k\ell} \approx (\beta_{1,k} - \beta_{1,\ell}) \cdot \omega + \left[\frac{(\beta_{o,k} - \beta_{o,\ell})}{\omega_o} - (\beta_{1,k} - \beta_{1,\ell}) \right] \cdot \omega_o = (\beta_{1,\ell} - \beta_{1,k}) \cdot \omega + \frac{\phi_{k\ell}}{L} \quad (4.5)$$

We can also define the propagation constant difference as a function of the group index or the time delay difference by: $\omega = 2\pi c/\lambda$

$$\Delta\beta_{k\ell} = \Delta\beta_o + (\omega - \omega_o)\Delta\beta_1 = \Delta\beta_o + (\omega - \omega_o)\Delta\tau_{k\ell}/L \quad (4.6a)$$

$$\Delta\beta_{k\ell}L = \Delta\beta_oL + (\omega - \omega_o)\Delta\tau_{k\ell} = \phi_{k\ell} + \omega \Delta\tau_{k\ell} \quad (4.6b)$$

c is the speed of light and n_g is the group index.

Besides, $\Delta\tau_{k\ell}$ is the difference of the propagation time between the k and l modes. It is directly related to the group delay difference $\Delta n_{k\ell} \cdot L / c$. Likewise, the propagation time difference is similar to the DMGD. Thus, equation 4.2 becomes:

$$I_{(x,y,\omega)} = \bar{I}_{(x,y)} + \sum_{k=1}^{M-1} \sum_{\ell=k+1}^M 2 \cdot \sqrt{P_k \cdot P_\ell} \cdot F_k \cdot F_\ell \cdot \cos(\Delta\tau_{k\ell} \cdot \omega + \phi_{k\ell}) \quad (4.7a)$$

The spectrum of the signal presents different peaks localized at some determined time delay, ω is the optical angular pulsation and $\phi_{k\ell}$ represents initial phase of the beat.

By using the following notation $\Gamma_g = 2 \cdot \sqrt{P_k \cdot P_\ell}$, $r_g(x, y) = F_k \cdot F_\ell$ (this notation will be also used later) and $\tau_g = \tau_{k\ell}$, equation 4.7a can be written:

$$I_{x,y,\omega} = \bar{I}_{x,y} + \sum_{k\ell=g=1}^N \Gamma_g \cdot r_g(x, y) \cdot \cos(\tau_g \cdot \omega + \phi_g) \quad (4.7b)$$

By assuming an infinite wavelength range, a time delay difference independent of ω (group velocity tends to zero) and the Fourier transform definition $\delta(\tau) = \frac{1}{2\pi} \int_{-\infty}^{\infty} e^{-i\omega\tau} d\omega$, the Fourier transform of Equation 4.7a becomes:

$$J = \bar{I}\delta(\tau) + \sum_{k\ell=g=1}^N \Gamma_g \cdot r_g(x, y) \cdot [\delta(\tau - \tau_g) + \delta(\tau + \tau_g)] \quad (4.8)$$

It has to be noted that the interferences are located at particular τ_g values, whose spatial profile is given by the beat envelopes of the two interfering modes. Likewise, the constant intensity term is located at a null frequency. Let us suppose a fiber with total length

L propagating only 2 LP modes without degeneracies. In bi-mode fibers, only one spectral interference can be found which corresponds to the interaction between the fundamental mode and the higher order mode. In the Fourier domain, it will be represented by one peak (See Fig. 4.4). Thus, if the fiber has N modes, the spectrum can contain $\frac{N^2-N}{2}$ different observable beat frequencies, resulting from the interferences between the fundamental modes and the higher order modes, and the interferences between HOMs themselves.

In detail, Figure 4.4 shows the beat amplitude as a function of Δng . At $\Delta ng=0$ ($\tau=0$), we observe the average intensity term which represents the intensity of the fundamental mode from a nearly single mode excitation. At Δng 01-11, we find the interference of modes LP_{01} and LP_{11} whose amplitude is given by the term $2 \cdot \sqrt{P_k \cdot P_\ell} \cdot F_k \cdot F_\ell$. It should be noted that the position and quantities of peaks, as we already mentioned, depend on number of modes but also to certain physical phenomenon such as splices, constrains, that induce mode coupling, as we already mentioned. Similarly, the peak coming from the two interferences is not infinitely narrow, because the data window is not infinite.

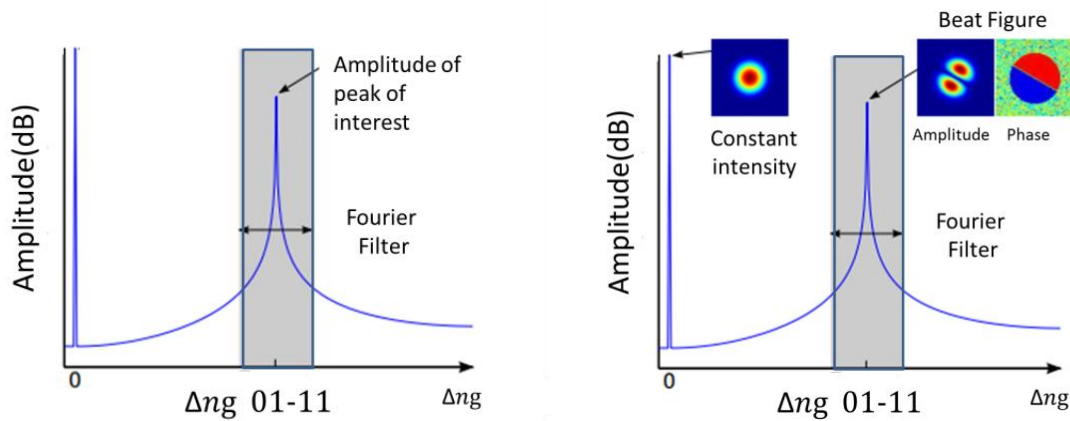


Figure 4-4: Amplitude profile for a bi-mode fiber.

In the end, the spectra is calculated for each pixel and their amplitude are summed, so that the spectral contributions accumulate, which makes it possible to see all the peaks simultaneously. Similarly, some modes have zero intensity in some part of space and so each pixel does not reflect the same interference pattern.

In S2, the conventional algorithm used to recover modes is based on the hypothesis that the fundamental mode supports at least more than 90% of the total power. Thus, the interferences between other modes can be minimized. That is, all the terms related to the interferences between higher order amplitude modes become negligible in comparison to the terms of the fundamental mode.

Besides, the dispersion of the group velocity and the intensity source spectral-distribution can cause an additional enlargement of the peaks which adds complexity to the discrimination between different beat profiles, even more so if the number of modes increases. This problem could be improved by the integration of the power output in the time domain (Fourier filter) or by filter techniques [Jollivet, 2014]. However, it could lead to additional optical elements complicating the setup.

S2 has been used to analyze large mode area fibers [Nicholson, 2009], photonic crystal fiber [Bromage, 2011], all-solid and hollow core band-gap fibers [Fini, 2013], erbium-doped fiber amplifier [Nicholson, 2013]. Even if this method allows the evaluation of the modal content, it requires a modification in the signal processing to achieve the evaluation of degenerated modes. Sévigny et al. uses the intra-data correlation to discriminate the different beat profiles. In the following section, we will provide details about this method [Sévigny, 2015].

- **Summary**

Technique	Source type	Fiber length	Difficulty of experimental setup
Correlated Filter CFT	LED	≈30 cm	
Cross-correlated imaging C2	LED/LASER	≈ 1 m	
Spectrally resolved imaging S2	Laser	> 100m	

4.1.2 Method for measuring the mode coupling

To study fiber properties and mode coupling in standard single-mode fibers, the curvature in the fiber has been experimentally studied in a sensor such as a Bragg fiber, especially in the long period grating configuration [Lee, 2003], [Schulze, 2013]. Likewise, different methods for studying coupling have been used in the telecommunication. Usually, these methods allow to examine the macro-curvature, micro-curvature and splices [Jay, 2010].

Several studies have been made on mode mixing effects in multimode fibers, but most of the experimental methods describe it only qualitatively or consider only LP mode groups without lifting the degeneracies. Thereby, the mode coupling can be obtained by analyzing the mode conversion ratio at splice point using the frequency domain responses [Maruyama 2014], by the relationship between modal crosstalk on optical MIMO transmission [Mori, 2014], or by measuring the loss difference between the modes with a synchronous multichannel OTDR [Nakazawa, 2014].

Further emergent telecommunication fibers (FMF or MMF) are developed taking into account the mode coupling in order to find the appropriated DGD to reduce the complexity at the reception.

Recently, experimental methods have been used to measure mode coupling on degenerated modes. Some of them permits to measure the back-scattered light in each mode with both polarizations by using Brillouin optical time domain reflectometer (BOTDR) [Li, 2014]. This method needs to be combined with an SLM to examine the modal content in x,y polarization with a polarization beam splitter.

There are other more sophisticated methods to evaluate mode coupling in FMF, namely the correlation filter technique (See section 1.1.1.1) and the advanced spatially and spectrally resolved imaging (AS2 imaging), as we will explain in the next section.

In the context of the present work, we will use an improved version of the S2 method to measure localized coupling in an FMF.

4.2 Advanced S2 and principal component analysis

A-S2 has the same data acquisition procedure than S2. This simplicity (See Fig. 4.5) makes S2 and A-S2 imaging significantly easier to implement experimentally than other methods.

As was explained above, the intensity pattern caused by interference between propagating modes can be described by the coherent sum of the intensities of all modes at the fiber output. It was noted that the equations 4.7a or 4.7b have two terms: the constant intensity and the interference between the different modes, this second member being responsible of the appearance of the peaks localized at a well-defined $\tau_{k\ell}$.

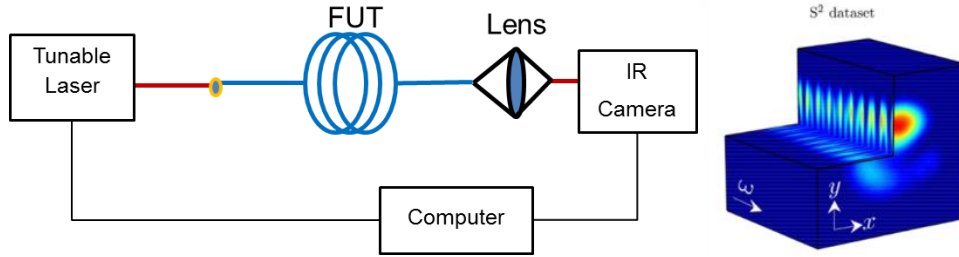


Figure 4-5: Schematic of the S2 imaging setup [Sévigny, 2015].

It was also explained that after processing the data by Fourier analysis, we could recover the mode profiles, power in each modes and DGD. However, when standard method S2 is applied to FMF, it is difficult to discriminate some beating modes even by using filtering techniques, because they can share almost similar differential group delay and energy distribution. One proposal is to use a statistical method to single out the different terms by using the spatial and spectral correlations, known as A-S2 [Sevigny, 2014]. As a result by using the A-S2 method we can obtain the isolated and degenerated beating modes.

The data is treated by A-S2 using the principal component analysis (PCA), which is described hereafter, and independent component analysis (ICA), which will not be described. The PCA uses to process the data obtained from an experiment on FMF, will be described hereafter.

- **Principal component analysis (PCA)**

PCA tries to express the mixture of random variables into completely un-correlated components. Thus, it discriminates correlated and un-correlated components considering the spectral and spatial domain. In this operation, the data is decomposed in principal components of beat and their spectra according to their correlation. Thus, the beats with the same group index differences can be separated in case they do not have spatial correlation. In the end, the uncorrelated interferences of the same nature are separated, excepting the beat mode with high spatial correlation. Let us summarize the PCA procedure details being presented in [Sevigny, 2015].

To begin, we can define the correlation function in the spectral domain by:

$$C_{(x,y,x',y')} = \frac{1}{\Delta\omega} \int (I_{x,y,\omega} - \bar{I}_{x,y})(I_{x',y',\omega} - \bar{I}_{x',y'})d\omega \quad (4.9a)$$

Here, $\Delta\omega = \omega_{max} - \omega_{min}$ is the full spectral width of the measurement, (x,y) and (x',y') corresponds to the correlation points. By substituting 4.7b into 4.9a, the cross-correlation can be studied by the cosines terms, as follows:

$$C_{(x,y,x',y')} = \frac{1}{\Delta\omega} \sum_{g=1}^N \sum_{h=1}^N \Gamma_g \cdot \Gamma_h \cdot r_g(x, y) \cdot r_h(x', y') \int \cos(\tau_g \cdot \omega + \phi_g) \cos(\tau_h \cdot \omega + \phi_h) d\omega \quad (4.9b)$$

As was discussed previously, PCA is based on the verification of the correlation of the spectra between each pixel, to isolate the corresponding beat figures and to get as much information as possible from the dataset. Notice from equation 4.9b that the correlation is a two-dimensional quantity calculated for the spectra of two different pixels.

To begin, the images must be linearized, to form linear vectors for each optical frequency. Therefore, the obtained image from the dataset should be transformed to linear vectors by mapping the two-dimensional indices to a linear index for integration over ω . The concatenation of these vectors will then form a power signal matrix, V , whose each term corresponds to the integral over pixel surface centered in (x, y). For small pixels (pixels square), this value is proportional to the pixel intensity.

$$V = \begin{bmatrix} I(x_1, y_1, \omega_1) & I(x_i, y_i, \omega_1) & I(x_r, y_r, \omega_1) \\ I(x_1, y_1, \omega_j) & I(x_i, y_i, \omega_j) & I(x_r, y_r, \omega_j) \\ I(x_1, y_1, \omega_\eta) & I(x_i, y_i, \omega_\eta) & I(x_r, y_r, \omega_\eta) \end{bmatrix}$$

Here, 1.....i correspond to the position of the pixels and 1.....j is the frequency numbers, η is the points numbers of frequency and r is the number of pixels.

By subtracting to each element the mean value of each column ($I - \bar{I}$), the scalar products of two pixels m, n (Equation 4.10) can then be used to represent the correlation.

$$C_{(x_m, y_m, x_n, y_n)} = \frac{1}{\Delta\omega} \sum_{i=1}^r [I(x_m, y_m, \omega_i) - \bar{I}(x_m, y_m)] [I(x_n, y_n, \omega_i) - \bar{I}(x_n, y_n)] \delta\omega \quad (4.10a)$$

$$C_{(x_m, y_m, x_n, y_n)} = \frac{1}{\eta} v_m^T v_n \quad (4.10b)$$

Here, v_n correspond to the column of \bar{V} that is the signal of the pixel n, $\Delta\omega = \eta \cdot \delta\omega$ is the number of pulsation points and $\delta\omega$ is the pitch of pulsation.

The total correlation matrix and the correlation matrices can then be written as:

$$C = \eta^{-1} \bar{V}^T \cdot \bar{V} \quad (4.11a)$$

$$\mathbf{C}' = \eta^{-1} \overline{\mathbf{V}\mathbf{V}^T} \quad (4.11b)$$

Here “T” denotes the matrix transpose of \mathbf{V} , \mathbf{V}^T is refers to the centered dataset and they contain the spatial and spectral function. η is the sum of the columns and the division of the angular frequency number.

\mathbf{C} and \mathbf{C}' are symmetrical matrices whose dimensions are (m, m) .

The principal components (PCA) are obtained by the diagonalization of the calculated correlation matrix. By this simple diagonalization of \mathbf{C} and \mathbf{C}' , we can reconstruct all the terms of the interferometer, if they are uncorrelated both in space and in the spectrum. The eigenvectors of \mathbf{C} are images and the eigenvectors of \mathbf{C}' are signal or spectra after FFT. If there is not coupling between the solutions, \mathbf{C} and \mathbf{C}' can have the same eigenvalues, Λ (same case for dataset where only one mode is dominant). That is, the eigenvectors can directly be the beat figures of the modes (See diagram of the Fig. 4.4). In this case, the eigenvalues can be represented by:

$$\Lambda_{k,\ell} = 2 \cdot S_{k,\ell} \cdot P_k \cdot P_\ell \quad (4.12)$$

Here $S_{k,\ell}$ is the normalization constant of the beat profile.

$$S_{k,\ell} = \int \int F_k \cdot F_\ell \, dx dy$$

In summary, the principal component analysis aims at expressing a mixture of random variables in components completely uncorrelated with one another, the so-called principal components. It has thus been make possible, by observing the correlation of the spectra between each pixel, to isolate the corresponding beat patterns. Likewise, if all the terms of the equation of the interferometer are spectrally or spatially uncorrelated each other, they can be separated by PCA.

Note also that from the beat figures it is possible to recover the transverse field profile. To recover the intensity field profile of any mode by using the average intensity figure and all the beats involving in this mode as in [Otto, 2013], we can write the average intensity as function of a given mode, ℓ (See equation 4.13a). Later, we multiply the equation 4.13a by $I_\ell = P_\ell |F_{\ell(x,y)}|^2$ to obtain 4.13b

$$\bar{I} = P_\ell F_\ell^2 + \sum_{i,i \neq \ell}^M P_i F_i^2 \quad (4.13a)$$

$$I_\ell = \frac{1}{2} \left[\bar{I} \pm (\bar{I}^2 - 2 \cdot \sum_{i,i \neq \ell}^M P_i \cdot P_i |F_\ell(x,y) F_i(x,y)|^2) \right] \quad (4.13b)$$

Through this method, it is possible, from a known field distribution, to deduce the other field distributions. Later, we can obtain the modal reconstruction by considering the product of radial and azimuth function. The A-S2 method is summarized in the Fig. 4.6. ICA is not considered in this study.

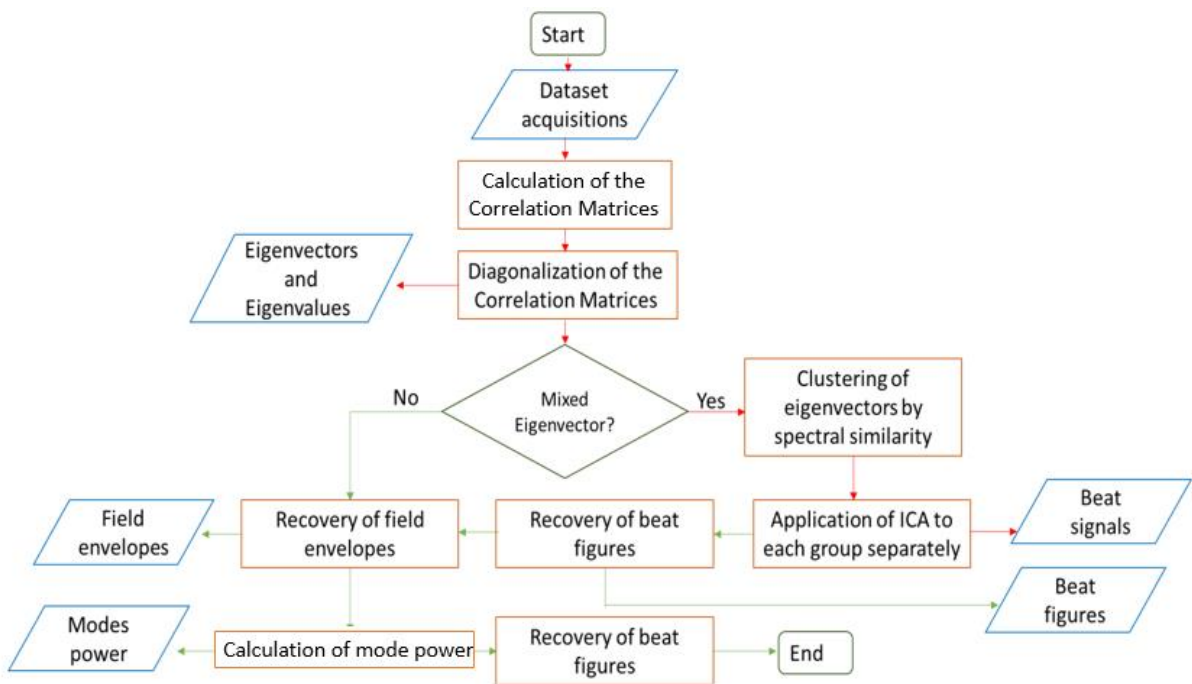


Figure 4-6: Beat resolution by the advanced S2 method

4.3 Schematic representation of the localized coupling in a two-mode fiber

As we have seen above, the intensity patterns caused by interferences between propagating modes can be described by the coherent sum of all the modes of the fiber (See Equation 4.7a). In this equation, the first term corresponds to the constant intensity, the second term is the interference between the different modes and is responsible for the appearance of the peaks localized at a determined value.

Localized mode coupling measurement in FMF

Let us find these peaks by considering a FMF of total length, L , supporting only two modes without degeneracies (LP01 and LP11) and without perturbations. To start this study, we assume that the fiber can be described as an unperturbed system with two input and output ports, as illustrated by Fig. 4.7a. In this figure, P is the fiber input through which the laser power feeds each input port or LP mode. In the practical scheme, an offset splice is used to ensure the excitation of the higher modes and to feed one mode with higher power than the other, usually 90% of the power for one of them [Nicholson, 2009].

In the absence of perturbation, energy is conserved for each port. In this case, we can find only two output ports (LP01 and LP11). The combination of the routes between each input port and each output port is called a path. Following the figure 4.7a we can form two paths between the input and output ports, as follows: LP01-LP01 (path 1) and LP11-LP11 (path 2). At the system output, the beat is the result of a two-paths interference (See Fig. 4.7b), in other words only one peak (α beat) should appear that corresponds to the interaction between both output ports (path 1 and path 2).

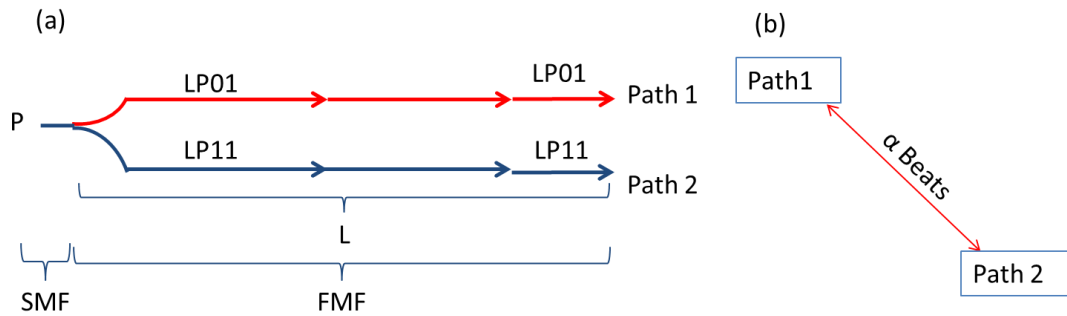


Figure 4-7: a) Diagram of an unperturbed FMF. .b) α beat corresponding to one interference between 2 paths.

The Figure 4.8 shows the beat amplitude as a function of Δn_g . We can generally find two spectral amplitudes, located at $\Delta n_g=0$ and $\Delta n_g=c/L(\Delta \tau_g)$ For $\Delta n_g=0$, we expect to observe the average intensity term. For $\Delta n_g \neq 0$ the interference of modes LP₀₁ (path 1) and LP₁₁ (path 2) is expected. Notice that the position and quantities of peaks depends on the number of modes and physical disturbance such as splices, constrains, etc, that can open new paths.

Moreover, the beat frequency is proportional to the fiber length and to the difference between the group indices of the modes. The number of beats is equal to the possible coupling of modes. Thereby, when N modes are excited inside the FMF, we can have $\frac{1}{2}(N^2-N)$ beats. That is, by a Fourier transform, we can obtain $\frac{1}{2}(N^2-N)$ peaks that are distributed along Δn_g .

The amplitude is related to the power coupled in each mode. We will demonstrate such a coupling effect in the next paragraphs.

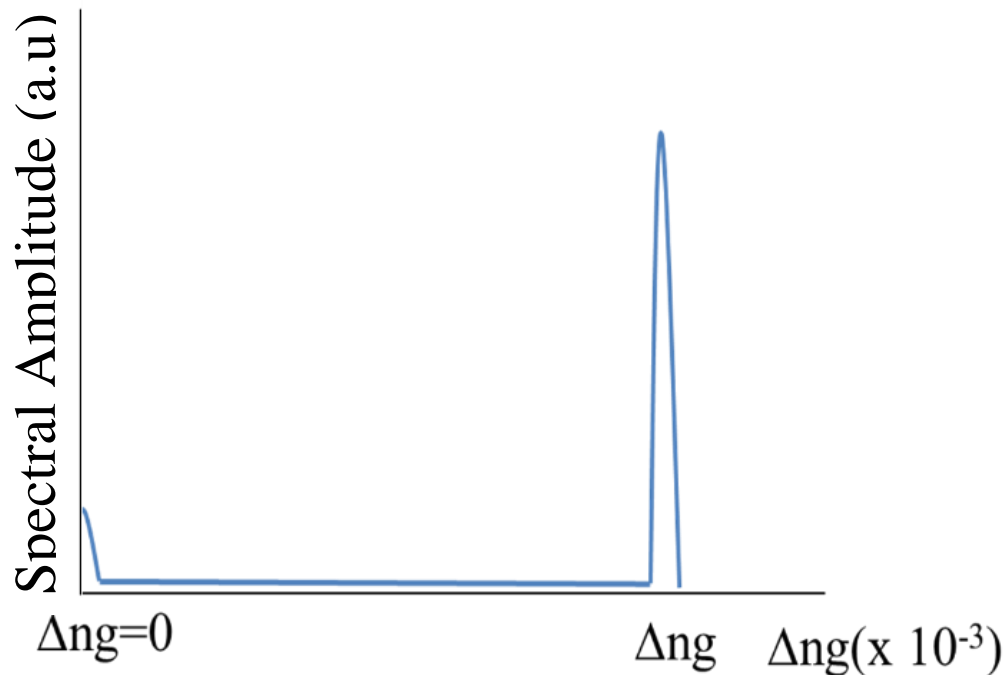


Figure 4-8: Fourier transform of the optical spectra of an unperturbed 2 modes FMF.

Let's assume that we apply a localized perturbation (splice, wire-mesh, etc.) situated approximately at 40% of the total distance to avoid overlap of peaks with others around the spectra. In presence of this perturbation, it can be anticipated that new peaks can appear due to exchange of energy between the modes. Thus, the location of these new peaks will depend on the position of the perturbation.

Let's start the study by the condition of a new system with 2 input ports and 4 output ports. By comparing the figure 4.7a and 4.9a, we can see that the output ports number has doubled due to the coupling, which leads to new paths (path1: LP01-LP01, path 2:LP11-LP11, path3: LP11-LP01 and path4: LP01-LP11). More clearly, path 1 is the route between the input LP01 and output LP01, path 2 is the route between the input LP11 and output LP11, path 3 is the route between the input LP11 and output LP01, and path 4 is the route between the input LP01 and output LP11 (See Fig. 4.9b). From the interaction of these four paths six beats are produced. Thereby, the 6 elementary beats (γ , δ , β , α , μ and ϵ) are the result of the interference between the 4 paths. On figure 4.9a, L is the total length of the 2MF decomposed into L1 (length before perturbation) and L2 (length after perturbation).

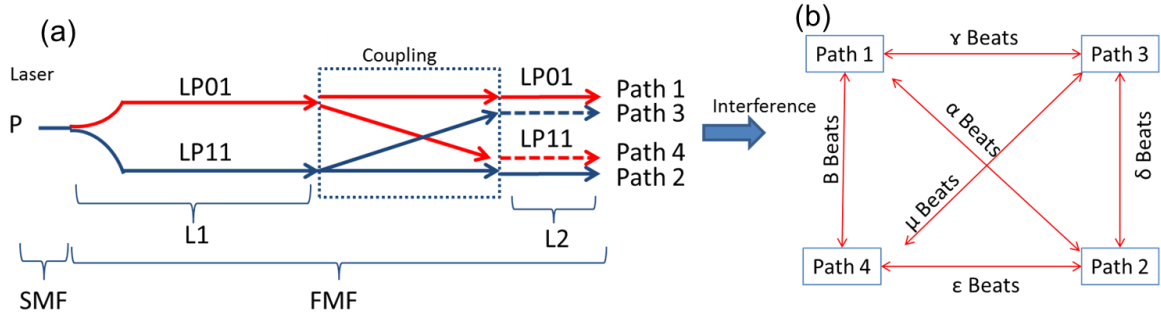


Figure 4-9: a) Coupling diagram of a perturbed FMF. b) beats corresponding to six interferences between 4 paths.

As in the previous system (Fig. 4.9a), the laser power (P) at the fiber entrance can be distributed as $P \cdot \tau$ and $P \cdot (1 - \tau)$ for both guided modes. Here, τ is the percentage of the energy injected in LP01.

$$E = \sum_m A_m \cdot F_m \cdot e^{-i\omega t} \cdot e^{i\beta L} \cdot e^{i\phi_m} \quad (4.14.a)$$

$$\begin{aligned} E &= \sqrt{P \cdot \tau \cdot M_{11}} \cdot F_{01} \cdot e^{-i\omega t} \cdot e^{i\beta_1 \cdot L} \cdot e^{i\phi_1} \Rightarrow \text{Path 1} \\ &+ \sqrt{P \cdot (1 - \tau) \cdot M_{22}} \cdot F_{11} \cdot e^{-i\omega t} \cdot e^{i\beta_2 \cdot L} \cdot e^{i\phi_2} \Rightarrow \text{Path 2} \\ &+ \sqrt{P \cdot (1 - \tau) \cdot M_{21}} \cdot F_{01} \cdot e^{-i\omega t} \cdot e^{i\beta_2 \cdot L_1} \cdot e^{i\beta_1 \cdot L_2} \cdot e^{i\phi_2} \Rightarrow \text{Path 3} \\ &+ \sqrt{P \cdot \tau \cdot M_{12}} \cdot F_{11} \cdot e^{-i\omega t} \cdot e^{i\beta_1 \cdot L_1} \cdot e^{i\beta_2 \cdot L_2} \cdot e^{i\phi_1} \Rightarrow \text{Path 4} \end{aligned} \quad (4.14.b)$$

$$\begin{aligned} E^* &= \sqrt{P \cdot \tau \cdot M_{11}} \cdot F_{01} e^{i\omega t} \cdot e^{-i\beta_1 \cdot L} \cdot e^{-i\phi_1} \Rightarrow \text{Path 1}^* \\ &+ \sqrt{P \cdot (1 - \tau) \cdot M_{22}} \cdot F_{11} e^{i\omega t} \cdot e^{-i\beta_2 \cdot L} \cdot e^{-i\phi_2} \Rightarrow \text{Path 2}^* \\ &+ \sqrt{P \cdot \tau \cdot M_{12}} \cdot F_{11} \cdot e^{i\omega t} \cdot e^{-i\beta_1 \cdot L_1} \cdot e^{-i\beta_2 \cdot L_2} \cdot e^{-i\phi_1} \Rightarrow \text{Path 3}^* \\ &+ \sqrt{P \cdot (1 - \tau) \cdot M_{21}} \cdot F_{01} \cdot e^{i\omega t} \cdot e^{-i\beta_2 \cdot L_1} \cdot e^{-i\beta_1 \cdot L_2} \cdot e^{-i\phi_2} \Rightarrow \text{Path 4}^* \end{aligned}$$

Next, we can calculate the electric field in all the modes by the coherent sum of the electric fields for a 2-mode fiber (2MF) as is done in 4.14.a and 4.14.b. To compute the coupling, we consider the product of $E \cdot E^*$ (for instance, equations 4.14b) and the relation $\Delta\beta = \Delta n_g \cdot L / c \cdot \omega$, where Δn_g is the group index difference.

It should be noted that in 4.14a and 4.14b, coupling can be described by a coupling matrix in intensity, M, each element of this matrix M_{ij} corresponding to the coupling coefficient between the modes i and j. To help understanding the coupling matrix, we have changed the ports notation (See Fig 4.10), so that M_{11} corresponds to the coupling effect

between the LP01-LP01, M_{12} corresponds to the coupling effect between the LP01-LP11, and so on.

In presence of coupling, the coupling coefficients must be considered to deduce the intensity detected on each pixel of the camera.

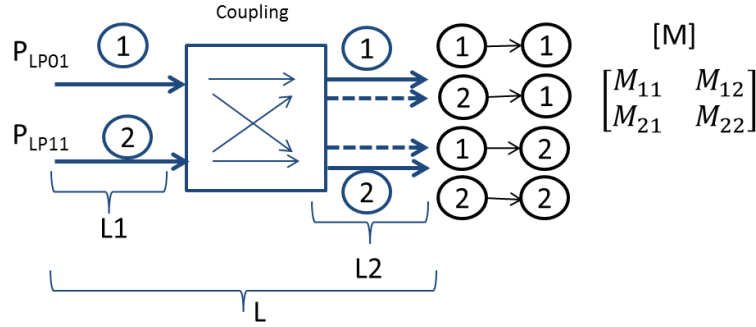


Figure 4-10: Coupling diagram and coupling matrix of a perturbed FMF.

From a mathematical point of view, the intensity detected on each pixel of the camera can be described by two kinds of terms (See equation 4.7a): the first one is the constant intensity (term without interference: $\sum_i \sum_j (P_i \cdot M_{ij} \cdot I_i)$) whereas the second one corresponds to the 6 interferences (or beats) between the 4 paths. Therefore, this intensity can be written as follows:

$$\begin{aligned}
 I = & P \cdot \tau \cdot M_{11} \cdot I_1 + P \cdot (1 - \tau) \cdot M_{22} \cdot I_2 + P \cdot \tau \cdot M_{12} \cdot I_2 + P \cdot (1 - \tau) \cdot M_{21} \cdot I_1 \\
 & + P \cdot \sqrt{\tau \cdot (1 - \tau) \cdot M_{11} \cdot M_{22}} \cdot F_{01} \cdot F_{11} \cdot 2 \cdot \cos \left[\left(\frac{\Delta n_g}{c} \cdot \omega \cdot L \right) + \phi_\alpha \right] \quad \alpha \\
 & + P \cdot (1 - \tau) \cdot \sqrt{M_{22} \cdot M_{21}} \cdot F_{01} \cdot F_{11} \cdot 2 \cdot \cos \left[\frac{\Delta n_g}{c} \cdot \omega \cdot L_2 + \phi_\delta \right] \quad \delta \\
 & + P \cdot \tau \cdot \sqrt{M_{11} \cdot M_{12}} \cdot F_{01} \cdot F_{11} \cdot 2 \cdot \cos \left[\frac{\Delta n_g}{c} \cdot \omega \cdot L_2 + \phi_\beta \right] \quad \beta \\
 & + P \cdot \sqrt{\tau \cdot (1 - \tau) \cdot M_{12} \cdot M_{22}} \cdot I_{11} \cdot 2 \cdot \cos \left[\frac{\Delta n_g}{c} \cdot \omega \cdot L_1 + \phi_\epsilon \right] \quad \epsilon \\
 & + P \cdot \sqrt{\tau \cdot (1 - \tau) \cdot M_{11} \cdot M_{21}} \cdot I_{01} \cdot 2 \cdot \cos \left[\frac{\Delta n_g}{c} \cdot \omega \cdot L_1 + \phi_\gamma \right] \quad \gamma \\
 & + P \cdot \sqrt{\tau \cdot (1 - \tau) \cdot M_{21} \cdot M_{12}} \cdot F_{01} \cdot F_{11} \cdot 2 \cdot \cos \left[\frac{\Delta n_g}{c} \cdot \omega \cdot (L_2 - L_1) + \phi_\mu \right] \quad \mu
 \end{aligned} \tag{4.15}$$

Here, F01 and F11 are the normalized field profiles of the modes (respectively LP01 or LP11), c is the speed of light, ϕ_α is the relative phase of the beat α , ϕ_δ is the relative phase of the beat δ , and so on. I_1 and I_2 stand for $F_{01} \times F_{01}$ and $F_{11} \times F_{11}$. If we consider the cosine

Localized mode coupling measurement in FMF

argument for each term from equation 4.15, some beats have almost similar arguments, such is the case from δ and β or γ and ε . That is they share the same spectral dependence. Similarly, some beats can share the same spatial dependence, for example δ and β , ($F_{01} * F_{11}$). Table 4.1 provides a summary of the spatial and spectral signatures of the 6 elementary beats.

Table 4.1. Correlated and un-correlated beats data in spectral and spatial domain.					
		Spectral domain			
Spatial		$\Delta\eta_g^*(L_2-L_1)/L$	$\Delta\eta_g^*(L_1/L)$	$\Delta\eta_g^*(L_2/L)$	$\Delta\eta_g$
	$F_{01} * F_{11}$	(Beats μ)		(Beats β, δ)	(Beats α)
	$F_{01} * F_{01}$		(Beats γ)		
	$F_{11} * F_{11}$		(Beats ε)		

As shown above, ε , γ and β , δ share the same frequencies and we expect only 4 peaks in the S2 analysis, at the positions $(\Delta\eta_g(L_2-L_1)/L)$, $(\Delta\eta_g L_1/L)$, $(\Delta\eta_g L_2/L)$ and $\Delta\eta_g$ (see Fig. 4.6). Correlations between ε , γ and β , δ beats make it difficult to analyze them. However, we can see that μ and α have particular unshared frequency, and thus, these beats are easy to extract from the experimental dataset, and to analyze.

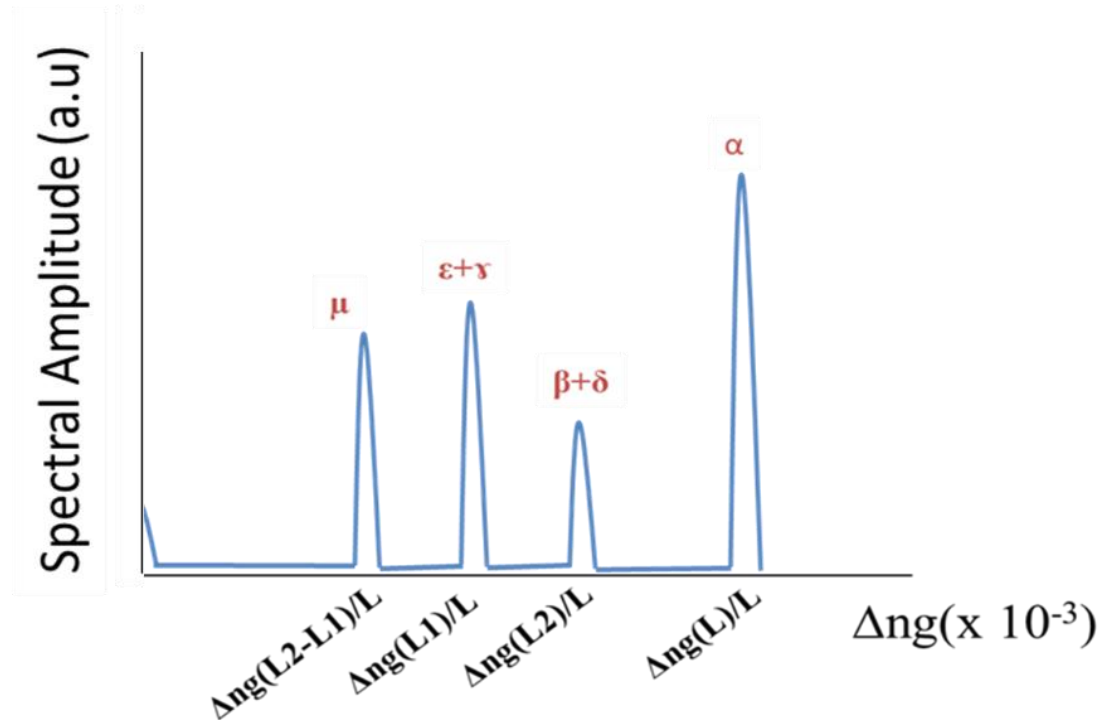


Figure 4-11: Fourier transform of the optical spectra of a perturbed 2 modes FMF.

The amplitude of these peaks are obtained after the Fourier transform of the equation 4.15. Thus, A_μ is the amplitudes of μ beat, A_α is the amplitudes of α beat, $A_{\beta+\delta}$ is the

amplitudes of $\beta+\delta$ beat (See equation 4.16a-c). Notice that A_μ and $A_{\beta+\delta}$ appear only in presence of coupling. Therefore, A_α can be used as a reference since it is the only peak that appears in an uncoupled regime.

$$A_\alpha = \sqrt{\tau \cdot (1 - \tau) \cdot M_{11} \cdot M_{22}} \quad (4.16.a)$$

$$A_{\beta+\delta} = \tau \cdot \sqrt{M_{11} \cdot M_{12}} + (1 - \tau) \cdot \sqrt{M_{22} \cdot M_{21}} \quad (4.16.b)$$

$$A_\mu = \sqrt{\tau \cdot (1 - \tau) \cdot M_{21} \cdot M_{12}} \quad (4.16.c)$$

By considering an ideal symmetric matrix ($M_{12}=M_{21}$), the coupling coefficients M_{12} can be extracted from the ratio of the amplitudes of μ beat (A_μ) and α beat in absence of perturbation (A_α^{init}) (See Equation 4.17b). For A_α^{init} the diagonal matrix is equal to one ($M_{11}=M_{22}=1$) and the other of elements are zero. Therefore the equation 4.16a can be written as 4.17a.

$$A_\alpha^{init} = \sqrt{\tau \cdot (1 - \tau)} \quad (4.17.a)$$

$$A_\mu^{pert} = \sqrt{\tau \cdot (1 - \tau)} \cdot \sqrt{M_{21} \cdot M_{12}} = A_\alpha^{init} \cdot M_{12} \quad (4.17.b)$$

Herein, two methods have been derived to calculate the coupling coefficient M_{12} . We will use the first one.

$$M_{12} = \frac{A_\mu^{pert}}{A_\alpha^{init}} \quad (4.18)$$

By the equation 4.18, we can study the coupling, as we will see.

4.4 Experimental setup

The experimental setup and data acquisition are similar between both methods, S2 and A-S2. The figure 4.5 shows the S2 and A-S2 experimental setup. Through the camera, it is possible to measure the intensity profile $I(x,y,L,\omega)$ at the output cleaved face with a resolution given by pixel size. Likewise, by a spectral scanning produced by a tunable laser source, it is possible to follow the spectral evolution of this intensity profile. However, this implies that

the acquisition of an image for each wavelength can lead to a large number of recorded images, making the acquisition long and the amount of data to be treated quite large.

More precisely, so as to acquire the dataset, we need to adjust three parameters: the total length of the fiber (L), the spectral range ($\Delta\lambda$) and the wavelength step ($\delta\lambda$). $\Delta\lambda$ is the maximal spectral range on which the FFT is made and $\delta\lambda$ determine the resolution of the measurement in term of difference of group indices measurable. The relation between these parameters is given by equation 4.19a.

$$\delta(\Delta n_g) = \frac{\lambda^2}{L \cdot \Delta\lambda} \quad (4.19.a)$$

The main idea is to find the appropriate spectral range by adjusting the fiber length and the step resolution of the wavelength that gives access to the maximum group index difference that can be measured, as is shown by equation 4.19b.

$$\Delta n_{g,\max} = \frac{\lambda^2}{2 \cdot L \cdot \delta\lambda} \quad (4.19.b)$$

Before, we need to calculate Δn_g for both fibers in order to know the position of the peaks without perturbation.

4.5 Experimental setup for studying the localized coupling in a two-mode fiber

So as to investigate the effect of a localized perturbation on mode coupling, we used two step-index fibers of different characteristics (See table 4.2). These fibers present a small and a large core-cladding index difference ($\Delta n \sim 5 \times 10^{-3}$ and $\Delta n \sim 15 \times 10^{-3}$ at 1550 nm) and guide 2 LP mode groups (i.e. three spatial modes, namely LP_{01} , LP_{11e} & LP_{11o}) at 1550 nm. They have been manufacture by MCVD.

The optical properties of these fibers have been deduced from the refractive index profile of the rescaled to the fiber dimension.

Table 4.2- Fiber characteristic		
SI(Step Index)	Fiber A	Fiber B
R1 (μm)	3.9	8
$\Delta n(\times 10^{-3}$ at 1550 nm)	15	5.6
$\Delta n_g(\times 10^{-3}$ at 1550 nm)	1.52	0.92
Length (m)	80	100
Refractive index		

The setup consists of a tunable laser connected to a small piece of single-mode fiber (SMF). This SMF is off-centered spliced to the 2-mode fiber (2MF) under test, ensuring the excitation of both LP_{01} and LP_{11} modes at the fiber input (LP_{01} being more strongly excited than LP_{11}). The 2MF fibers lengths have been set to $L=80\text{m}$ and 100m . Moreover, the perturbation (splice or wire-mesh, see Figs. 4.12a and 4.12b) is localized at $L_1=40\text{ m}$ from the fiber entrance. The output end of the fiber is imaged on an InGaAs camera and near field is recorded as a function of wavelength. The acquisition begins at 1550nm and ends at 1560nm with a resolution of 1pm or $\delta\lambda=0.001\text{nm}$. To fix these values we used the equations 4.19a-b.

Figure 4.12b shows the localized coupling generated by a mesh grid and weights. This wire-mesh and the different weights are used in order to create micro-bends and, thus, initiate mode coupling at a localized point. Thereby, multiple measurements have been made under the same experimental conditions with incremental weights of 500 g , from 0 to 10 kg , as is shown in Fig. 4.13a. By these measurements, we are able to evaluate mode coupling as a function of the intensity of the perturbation. Later, the coupling ratio is obtained by comparing the measurement without and with weights. Besides, the reproducibility was qualitatively tested by detecting the presence of the coupling on the same experiment and under the same conditions at different times.

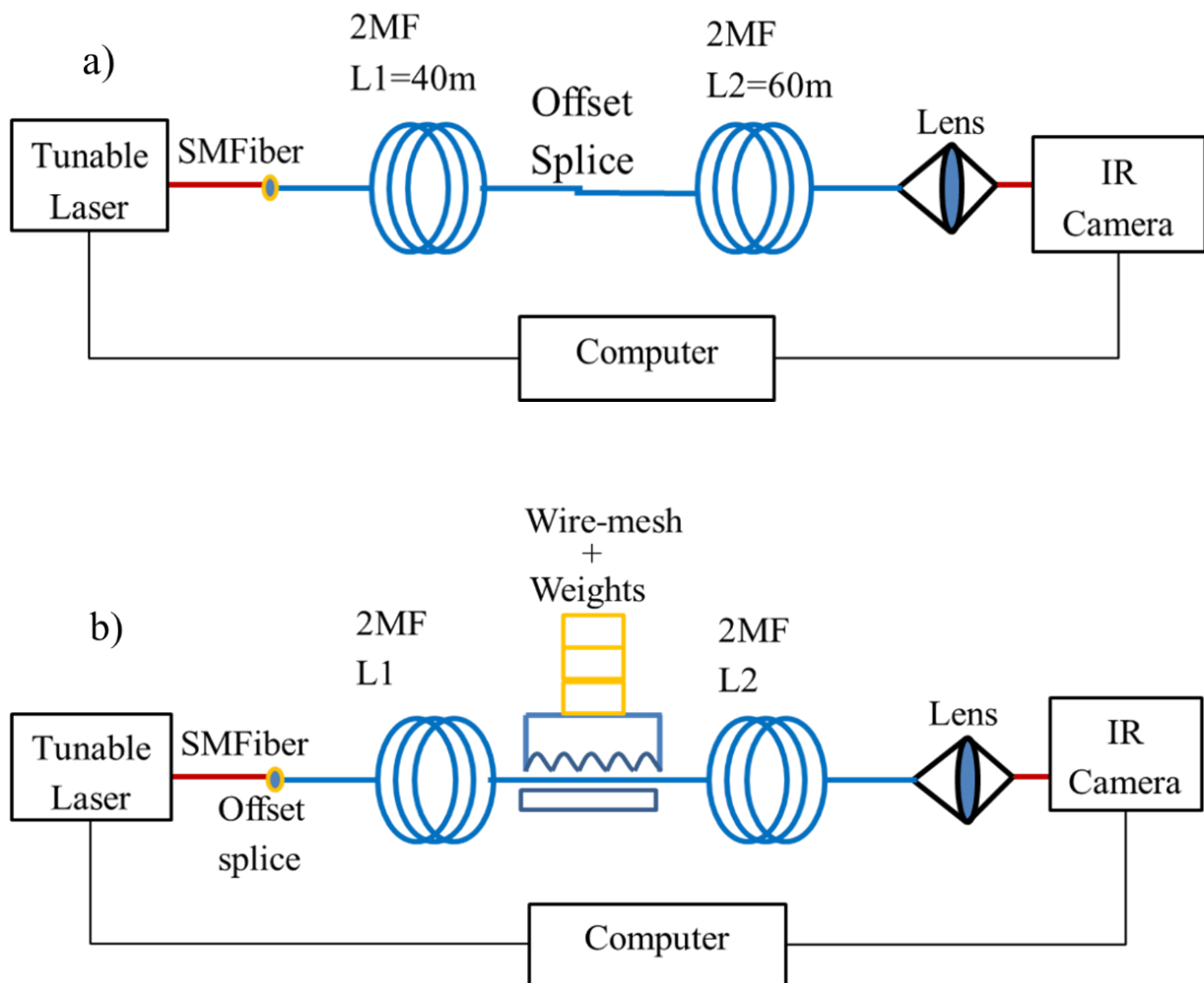


Figure 4-12: a) Experimental setup. a) Localized coupling generated by an offset splice. b) localized coupling generated by a mesh grid and weights

In this experimental setup, the effect of the fiber position inside the wire mesh has been considered by using three different settings, straight fiber, big loop and small loop fiber, as is illustrated on Fig. 4.13b.

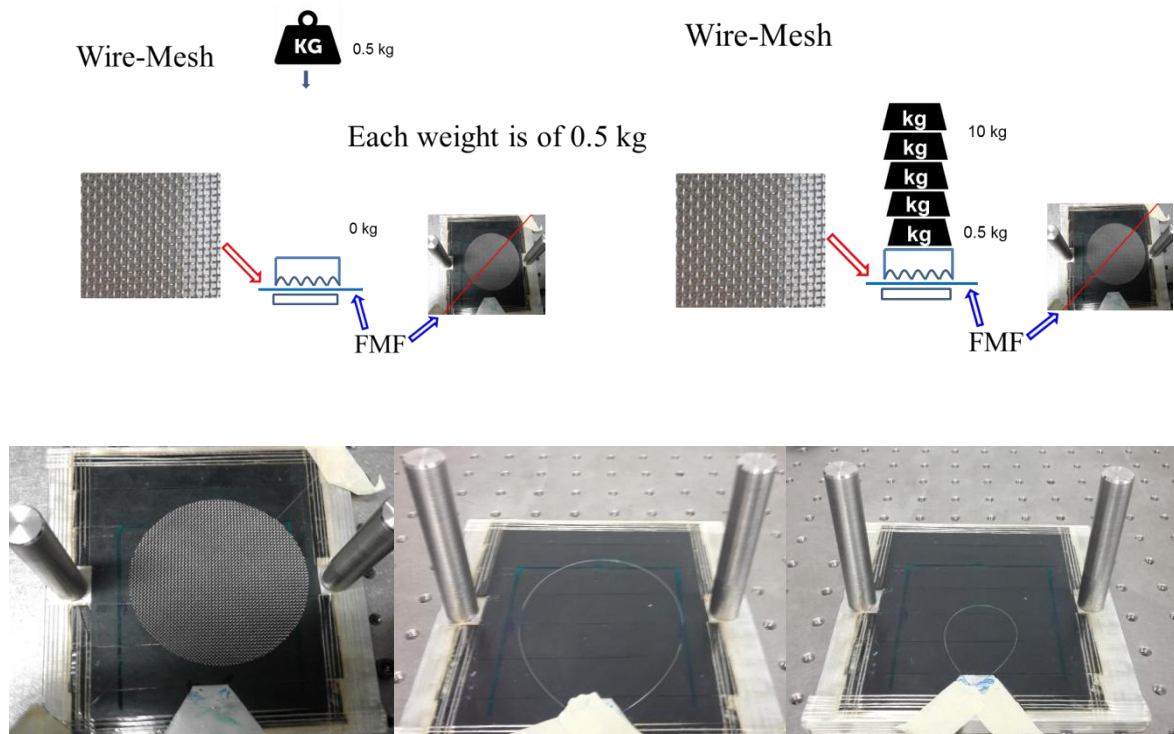


Figure 4-13: a) Wire-mesh system. b) Fibers setting in the wire mesh: straight fiber (9.8cm), big loop (24cm) and small loop (12cm).

In addition, the fibers were exposed to three types of meshes (See table 4.2) to evaluate the effects of the mesh dimensions on the coupling.

Table 4.3- Mesh characteristic	
	Sieve opening(mm)+ Wire(mm)
Mesh 1	1.018
Mesh 2	2
Mesh 3	0.96
Mesh 4	0.3

4.6 Modeling the localized perturbation (wire-mesh)

Thanks to the wire-mesh system (Figs. 4.13a and b), the coupling can be mechanically induced. That is, by pressing the fiber between the wire-mesh and a flat plate, the fiber is slightly deformed itself due to the applied stress, which creates periodic micro-curvatures in the fiber. In the case of a straight fiber, these micro-curvatures act similarly to a long period grating, coupling the fundamental mode of the core with the different modes of the cladding and higher order modes.

The period of the perturbation of a grid can be defined as the period between two wires in the mesh (period Λ). Λ can differently affect mode coupling in the fiber, as well as the wire diameter and gap between the wires. In long period grid, Λ is calculated by the ratio between the vacuum wavelength (1550nm) and the difference of effective index between two modes [Vengsarkar, A., 1996].

$$\Delta n_{eff} = \frac{\lambda}{\Lambda}$$

Note that perturbation periods tends to be big ($\Lambda \rightarrow$ infinite), when Δn_{eff} tends to be small, which means that the degenerated modes are susceptible to couple at any weight.

For fiber under test ($\Delta n \sim 5,6 \cdot 10^{-3}$), Δn_{eff} between LP01 and LP11 is equal to $2 \cdot 10^{-3}$, so we expect that the coupling will occur by using a mesh whose perturbation period is almost similar to $\Lambda \sim 0,775$ (mm).

Now we will try to model the coupling by using the coupled mode theory (chapter 3) for the straight fiber condition and by considering the wire-mesh characteristics. In chapter 3, the coupled mode was modeled by using the following parameters: number of sections, section length and total length. Therefore, we have modeled the wire-mesh perturbation by associating the number of sections with the total number of periods of the grid, the length of the section (L_m) with the period length of the grid, and the total length of the grid with the total length perturbed fiber (See Fig. 4.14). For instance, one section in the theoretical model is one period in the grid.

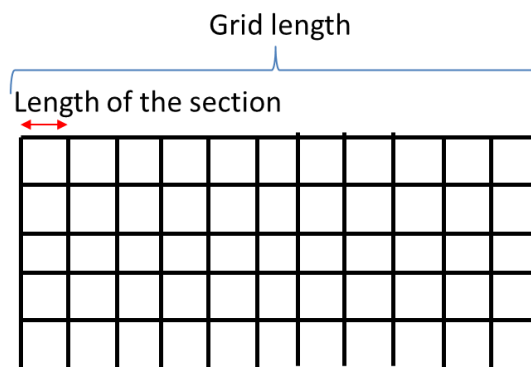


Figure 4-14: Modeling the grid of wire-mesh system.

To evaluate the coupling, we operated with the real profile of the fiber (RIP). Likewise, we have varied the number of sections and the length of perturbed fiber in order to find the appropriated setup for the simulation and experimental results, and thus compare both results. However, the random behavior of the experiment and the sensitivity to the fiber

position inside the wire-mesh as a consequence of the mesh orientation and weight can make these experiments non reproducible, even under same conditions.

Moreover, modeling could be arduous especially because the experimental values do not coincide with those of the model. Since some of their variables can have different physical properties such is the case between the theoretical (chapter 3) and current experimental models, where the coupling is generated by different ways, the first one by the standard deviations of curvature and the second one by the wire-mesh and weight. Herein, we tried to model the experiment by associating the standard deviations to applied weights, because the deformation intensity in the fiber can be statistically modeled by the inverse of the radii of curvature, which induces the same effect as the weight on fiber, even if these two parameters are not of the same physical nature. At the end, the most important is to have an idea of the coefficient coupling variation or the sensitivity of the optical fiber to different perturbation conditions.

Based on the model described in chapter 3, we have performed numerical modeling of FMFs step-index of the table 4.2 with their real profile (RIP of the fiber) modifying one of the radii of curvature (R_x or R_y) of the axis of each section of the FMF to produce the perturbation. The radius of curvature (R_x or/and R_y) of each section is a random variable, whose probability density function is the positive side of a Gaussian distribution with a standard deviation of curvature. Moreover, the section number has been varied among 20, 30, 45, 100, for different lengths of the perturbed fiber (50mm, 70mm and 90mm) with the purpose of modeling the mesh effect (section number) on the coupling. By the relationship between the sections number and the length of the perturbed fiber, we can determine the section length, which is related to the perturbation period (See table 4.4). The simulation parameters have been chosen by taking into account the characteristics of the mesh from table 4.4.

Fiber Length (mm)	Sections number	Section Length (mm)
90	30	3
90	45	2
90	100	0,9
50	20	2,5
70	30	2,33
70	100	0,7
70	60	1,16

Figures 4.15 a-b) show the evolution of the amplitude of the modes as function of the standard deviation of the curvature for different sections number (30 and 45). The perturbed fiber is of 90mm which corresponds approximately to mesh 2. Here, the launched conditions and perturbation are the same for all the modes (LP₀₁& LP₁₁).

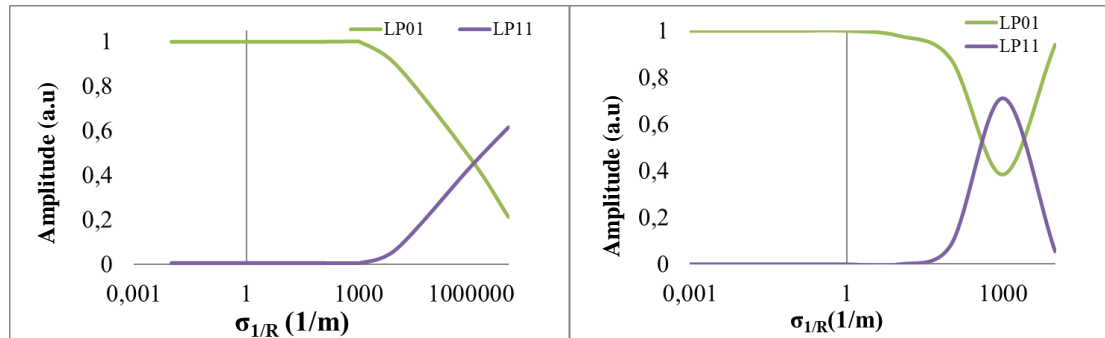


Figure 4-15: Evolution of the amplitude of the modes as a function of standard deviation of curvature for perfect step index profile, and fiber length of 90mm. Perturbation is considered in Rx. a-b) Section number=30 and 45. LP01 and LP11

Figures show that as the number of sections becomes greater, the coupling is achieved at smaller standard deviation (See Fig. 4.15), because an increase in the number of sections must produce more coupling between modes.

In the case of the fiber A, the coupling regime never was reached over the different mesh at large values of curvature. This behavior is qualitatively consistent, because its large core-cladding index difference makes this fiber resilient to the coupling.

The present result provides an idea of the coupling behavior in these fibers. We will now present the experimental result.

4.7 Experimental result for s2 measurement

So as to validate the S2 method, we used the experiment of the Fig. 4.12b with a loop of fiber (24cm) inside the wire mesh used with mesh 3 (table 4.3). Thereby, we compare the theoretical value of group index difference Δn_g calculated by Prysmian tools for these fibers (table 4.2) with the one deduced from the measurement (last peak). For instance, for a fiber with $\Delta n \sim 5 \times 10^{-3}$ (Fiber B), the value obtained experimentally, Δn_g is around 9.2×10^{-4} . Note that Δn_g value calculated (9.2×10^{-4}) is in agreement with the experimental results (See Fig. 4.16 a-b).

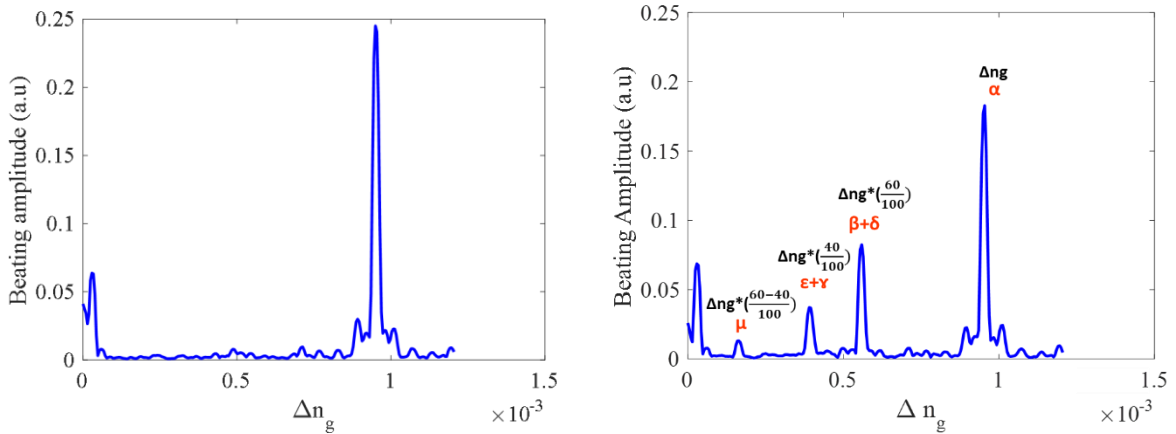


Figure 4-16: Fourier transform of the optical spectra by S2 a) Left: without perturbation (0kg) b) Right: with perturbation (6kg).

As expected, without perturbation, two peaks appear on S2 spectra, the peak at $\Delta n \sim 0$ corresponds to the constant intensity and the peak at $\Delta n_g \sim 9.2 \times 10^{-4}$ is associated to α beat over the whole fiber length (position Δng). In the presence of perturbation generated by the wiremesh, three additional peaks appear at the positions $(\Delta ng(L2-L1)/L)$, $(\Delta ng L1/L)$ and $(\Delta ng L2/L)$ (See Fig. 4.16b).

4.8 A-S2 from S2

As explained early, A-S2 and S2 are based on the same data acquisition, but they are treated differently. Therefore, A-S2 analysis was applied to the dataset in order to retrieve the proper peaks with the corresponding beat profile. As we have seen, A-S2 is based on multivariate statistical analysis method allowing the separation of the interference terms spatially and spectrally correlated. Contrary to S2, A-S2 can separate the spatial beat profiles for LP01-LP11e beats and LP01-LP11o beats, as shown in the figure below.

On figure 4.17a and 4.17d, the first spectrum presents the result obtained with the S2 method (top figure) and then with the A-S2 (bottom figures) to compare the two methods for fiber under the same perturbation.

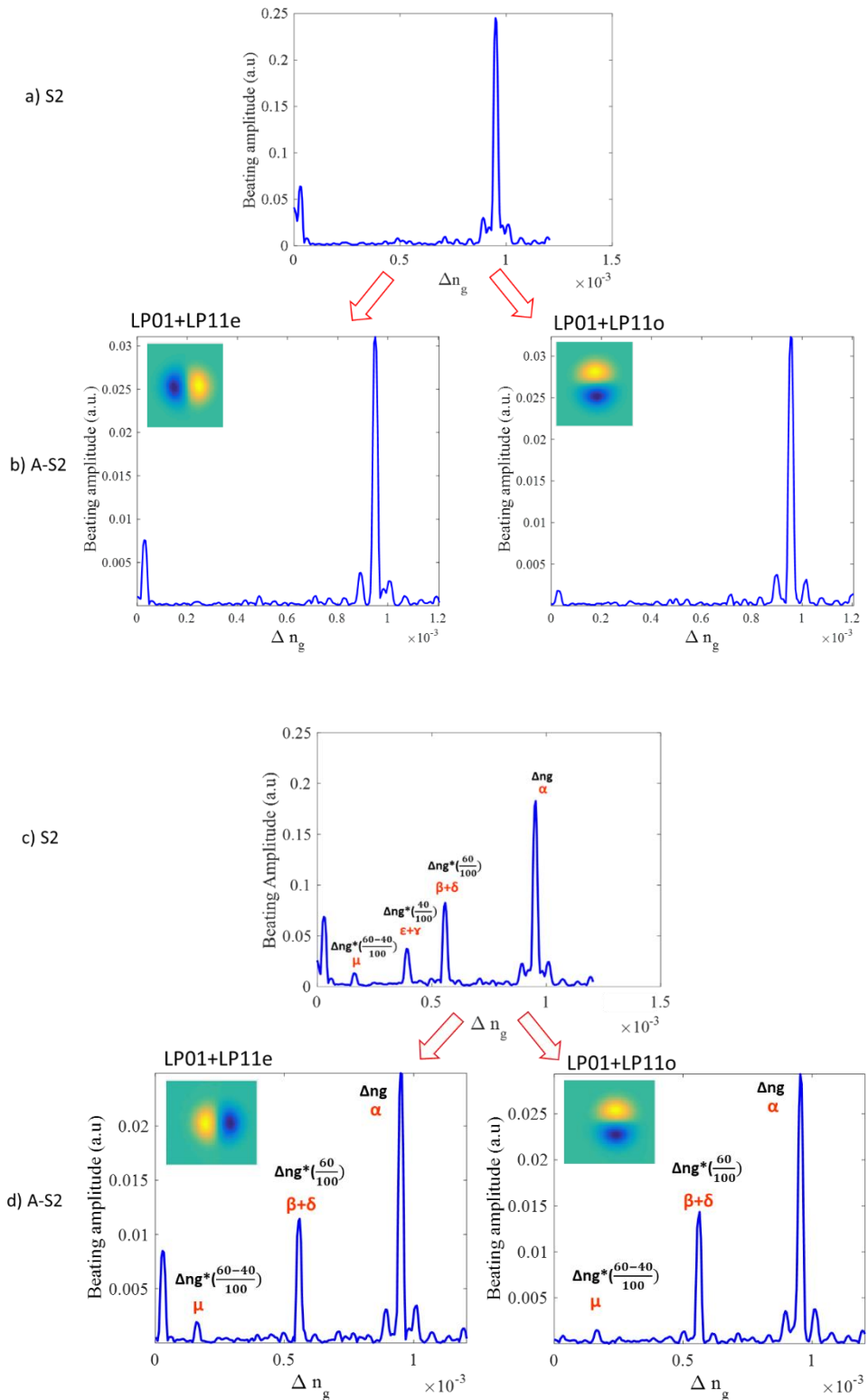


Figure 4-17: a-b) Upper: Spatial and spectral eigenvectors (LP01-LP11 beats) obtained by S2 and A-S2 analysis for uncoupled case. a) Lower-left: LP01+LP11e. b) Lower -right: LP01+LP11o.

c-d) Upper: Spatial and spectral eigenvectors (LP01-LP11 beats) obtained by S2 and A-S2 analysis for coupled case (6kg). c) Lower-left: LP01+LP11e. d) Lower -right: LP01+LP11o.

From figure 4.17 d) noted that the second peak ($\epsilon+\gamma$) disappears on the A-S2 results, since ϵ and γ beats do not correspond to a LP01-LP11 beat (See Table 4.1). That is, $\epsilon+\gamma$ are correlated and unseparated in spatial domain (see section 4.2). However, the coupling between LP01 and LP11o and between LP01 and LP11e can be analyzed by the ratio between the amplitudes of peak μ and α , as in the equation 4.18a.

Besides, we compare the energy of the last peak from S2 and the sum of the energy of each last peak from A-S2. Here, energy was calculated by integrating PSD (power spectrum density) within a frequency range for uncoupled (0 kg) and coupled (6 kg) cases. Commonly the computation of PSD can be obtained directly by the method called FFT (Fast Fourier Transform) spectrum of the signal. The results are shown in the following table 4.3.

Table 4.3

Weight (kg)	Energy of the (α) peak	
	S2	A-S2
0	0.0208	0.0234
6	0.0178	0.0184

Note that as expected the energy of LP01+LP11 calculated by S2 is similar to the sum of energy of LP01+LP11e and LP01+LP11o calculated from A-S2. Moreover, the small difference in this calculation can be attributed to the frequency window of integration.

In the following, the other results will be shown based only on the A-S2 method over different conditions.

4.9 Experimental result for A-s2 measurement

Fiber A (largest core-cladding index difference) was installed at different positions in the wire-mesh and submitted to different entrance conditions (centered and offset splice). One of the results on the coupling condition is shown in the Fig. 4.18 a-b.

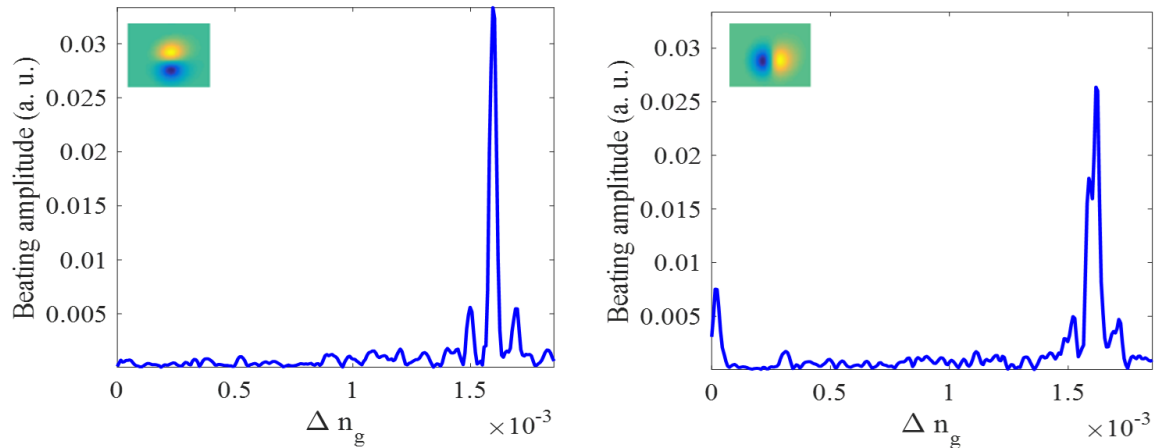


Figure 4-18: Spatial and spectral eigenvectors obtained by S2 and A-S2 analysis for the fiber A ($\Delta n \sim 15 \times 10^{-3}$). We use a wire-mesh with a weight of 8kg and a straight fiber position inside to the mesh. a) Left: LP01+LP11e. b) Right: LP01+LP11o.

It is obvious that, for this fiber, the perturbation is not sufficient to initiate coupling. This explains why, we will only present the result of the fiber with a small core-cladding index difference ($\Delta n \sim 5 \times 10^{-3}$).

4.9.1 Effect of the weight on the optical fiber

Figure 19 shows the evolution of the spatial and frequency spectra as a function of the weight applied to the fiber ($\Delta n \sim 5 \times 10^{-3}$). For this experience, we have used the experimental setup of Fig. 4.12a and a loop of fiber (98cm) positioned below the mesh 3.

The weight and the mesh structure generate perturbation in the fiber, and the coupling between modes. Indeed, the coupling is detected by the appearance and evolution of amplitude between the peaks, as we explained early. Using these results, we can generate the next spectra for different conditions.

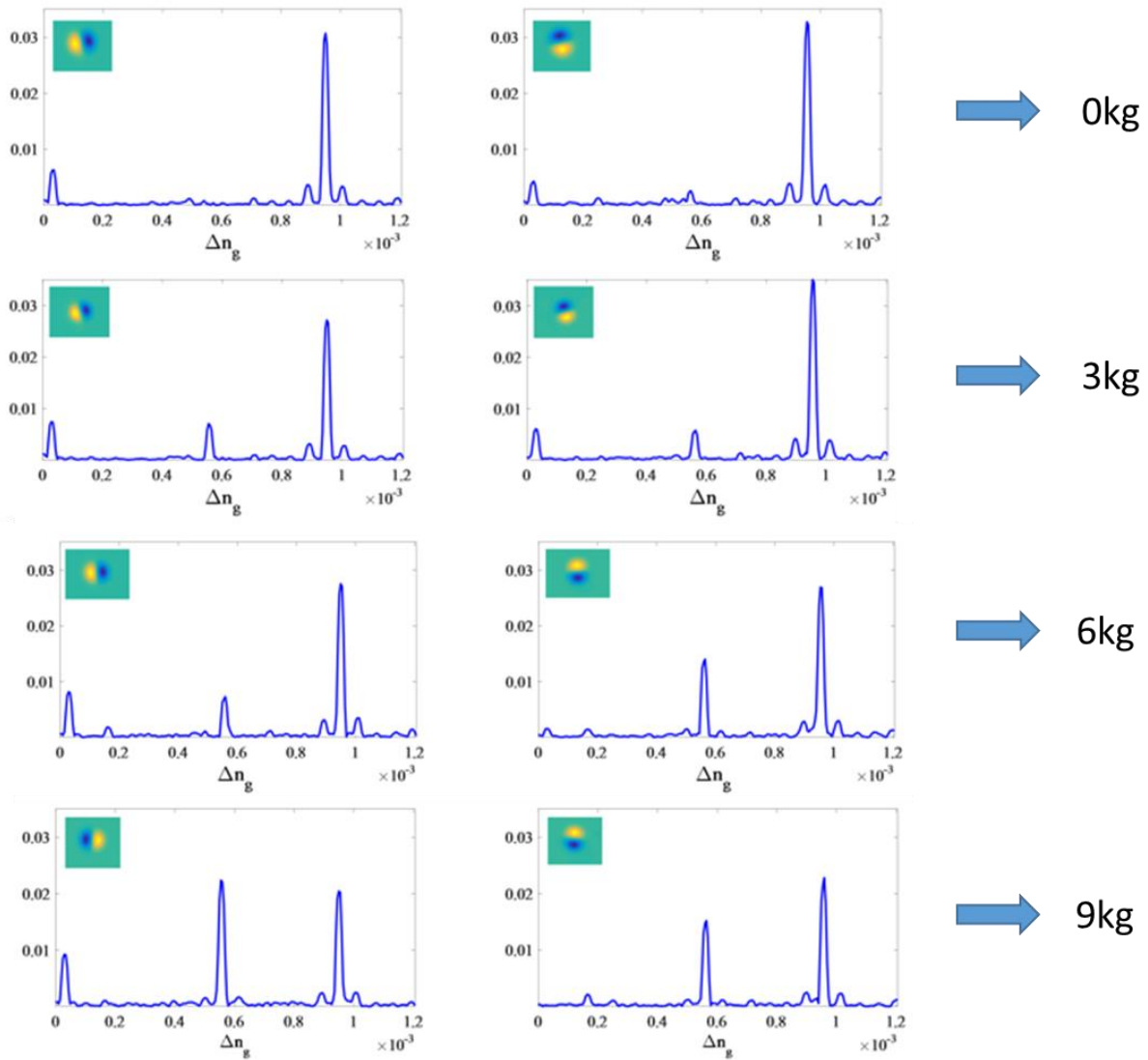


Figure 4-19: Evolution of the beats and frequency spectra (μ , $\beta+\delta$ and α) as a function of the weight applied to fiber B. a) Left: LP01+LP11o. b) Right: LP01+LP11e.

4.9.1.1 Radius of curvature 98mm (fiber length =24cm)

Figures 4.20 and 4.21 show the evolution of the peak amplitudes according to the weight for S2 and A-S2 analysis by using a loop of fiber (98cm) positioned below the mesh 3. As the weight increases from 0kg to 10kg, the energy transfer between the modes is more significant. As can be seen, the evolution of these amplitudes is not linear and follows a trend similar to that of a fiber coupler. Note that as the amplitude α decreases, the amplitude of $\beta+\delta$ increases in almost the same proportion.

The evolution of the amplitude of peaks α , $\beta+\delta$ and μ between the LP01-LP11e and LP01-LP11o analyzed by A-S2 are different (see Fig. 4.21-a-b), as their eigenvalue (see Fig.

4.23-a-b) demonstrating that LP11e and LP11o behave differently as a consequence of the asymmetry of the perturbation applied between the two axis of the fiber. Thus, the core shape of the fiber can be temporarily disturbed owing to the stress field in the core, alike the intensity and phase of the electric field of the modes LP11e and LP11o in a different way. At the end, coupling coefficient M12e and M12o are not necessarily the same.

Figures 4.21 c-d represent the evolution of the μ peaks as a function of weight. These figures exhibit almost the same behavior than the coupling coefficient M12e and M12o (see Fig. 4.22 a-b), evidencing the dependence of μ to M12e and M12o. Notice that LP01+LP11o (lower-right) behaves almost linearly, whereas the LP01+LP11e (lower-left) behaves non-linearly.

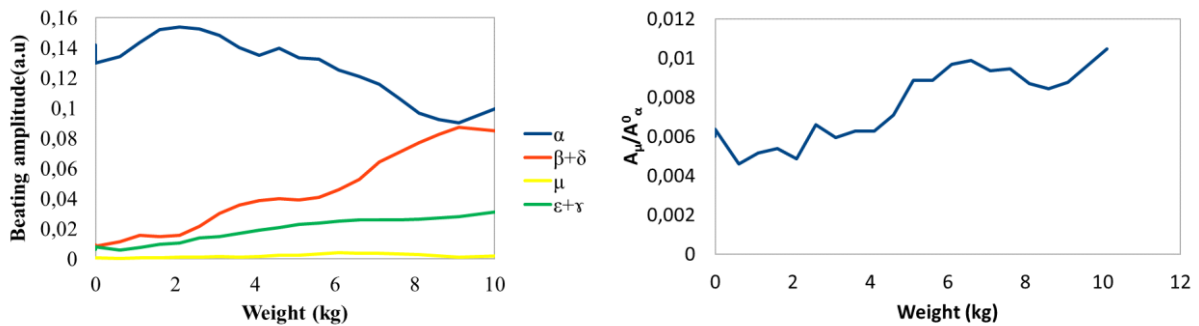


Figure 4-20: a) Evolution of the amplitude of the peaks as a function of weight in S2. b) Evolution of the coupling coefficient as a function of weight.

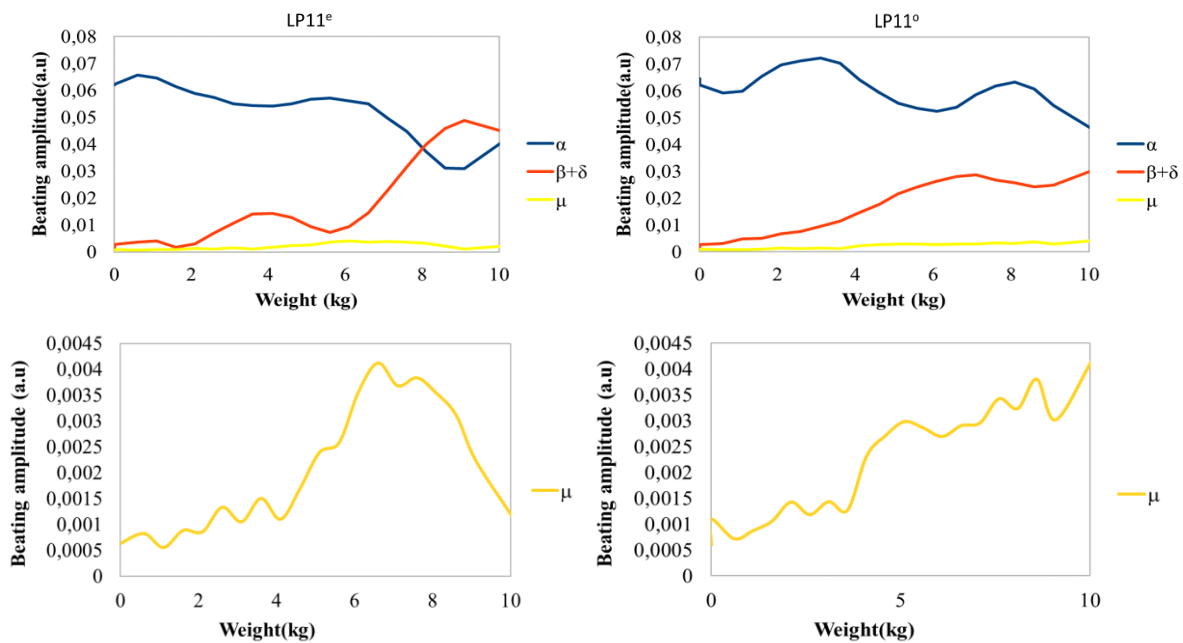


Figure 4-21: a-b) Evolution of the amplitude of the peaks as a function of weight in A-S2 for LP01+LP11e (upper-left) and LP01+LP11o (upper-right). c-d) Evolution of the amplitude of the μ peak as function of weight in A-S2 for LP01+LP11e (lower-left) and LP01+LP11 (lower-right).

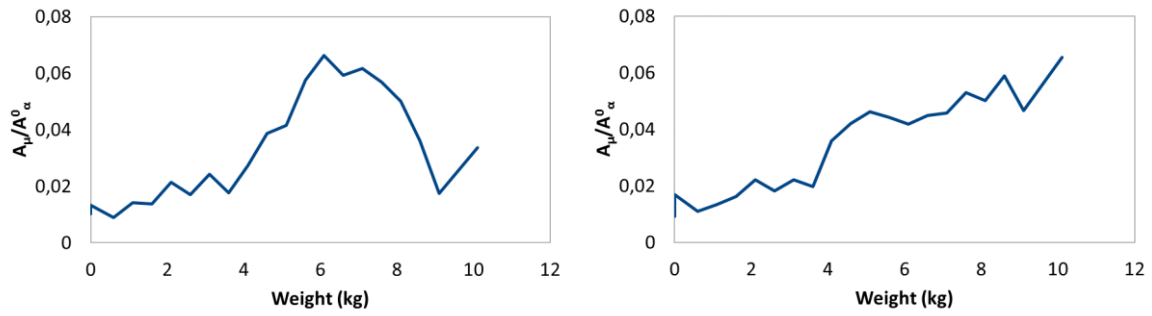


Figure 4-22: a-b) Evolution of the coupling coefficient deduced by equation 4.18 as a function of weight for eigenvectors LP01+LP11e (upper -left) and LP01+LP11o (upper-right).

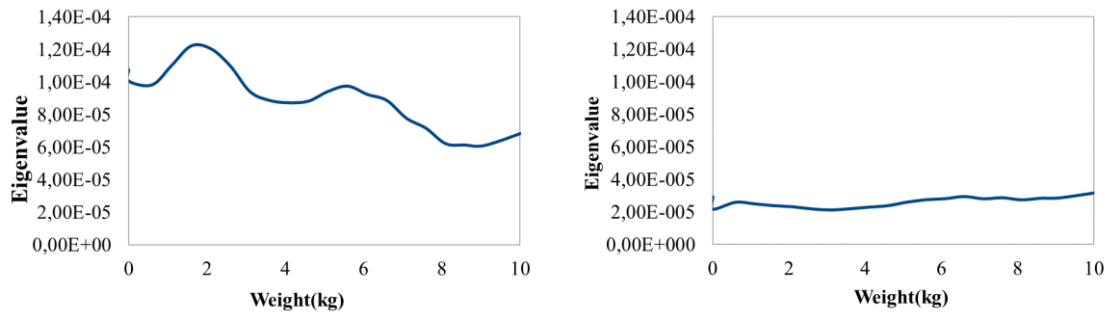


Figure 4-23: a-b) Evolution of the eigenvalue as a function of weight, LP01+LP11e (lower-left) and LP01+LP11o (lower-right).

Figure 4.24 c-d corresponds to the variation of the power in each mode as a function of weight. Each power modes is obtained by the average of square of each intensity over the constant intensity. At 0kg, 94.33% of total power is found in the LP01 mode, while only 4.22% and 1.45% in the LP01e and LP01o respectively. By increasing the weight (coupling), the power of the LP01 mode is slightly modified but stays around 90% of the total power. The variation of each mode power is detailed in the Figs. 4.24 b-d.

Besides, it must be noted that strong coupling occurs when two mixed modes (as the case for LP11e and LP11o for 8kg) have almost equal amount of power (~50%) contained in the core (See Fig. 4.21a).

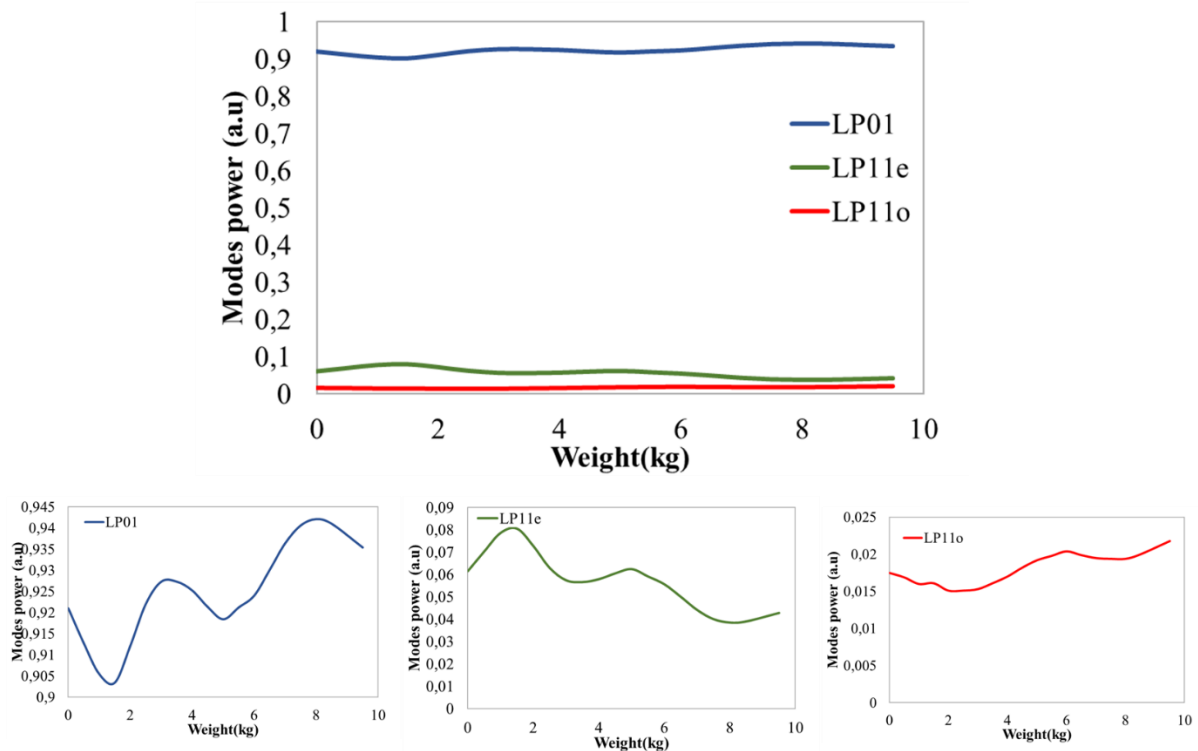


Figure 4-24: a) Evolution of the power in each mode as function of the weight (upper). b)-d) Evolution of the power in LP01 (lower-left), LP11e (lower-middle) and LP11o (lower-right) as function of the weight(mesh 3, radius of curvature of 98 mm)..

Figure 4.21 can be compared with Fig. 4.15, which represents the simulations of the mesh 2. Here, the comparison is qualitative due to the different natures of the variables, one is the applied weight at the perturbation and the other the standard deviation of curvature. Thereby, we compare the oscillatory variation of the shape more than the numerical values.

4.9.1.2 Radius of curvature of 49mm (fiber length =12cm)

Figures 4.25 and 4.26 show the evolution of the peak amplitudes according to the weight for S^2 and A- S^2 analysis by using a different loop of fiber (49cm) positioned below the mesh 3. Unlike the experiment with a radius of curvature of 98mm, the total exchange of the amplitude between α and $(\beta+\delta)$ occurs at 6kg that coincides with the maximum value of μ . As the macro curvature is more pronounced (radii of curvature smaller), LP01+LP11e is probably more sensitive to the coupling under this condition.

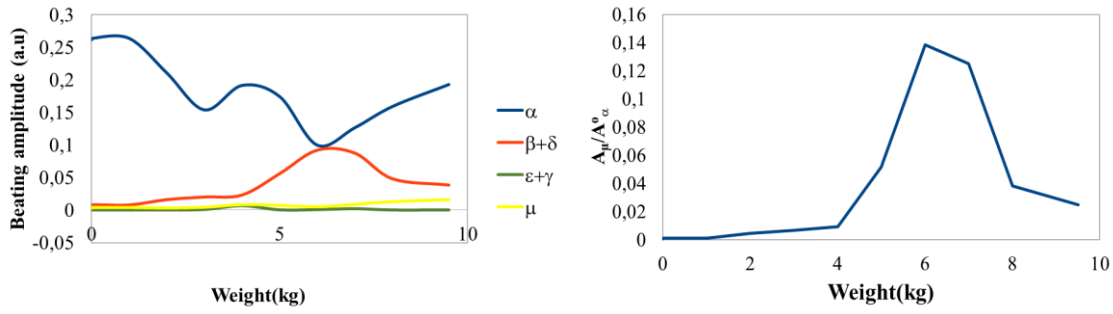


Figure 4-25: a) Evolution of the amplitude of the peaks as a function of weight in S2. b) Evolution of the coupling coefficient as a function of weight.

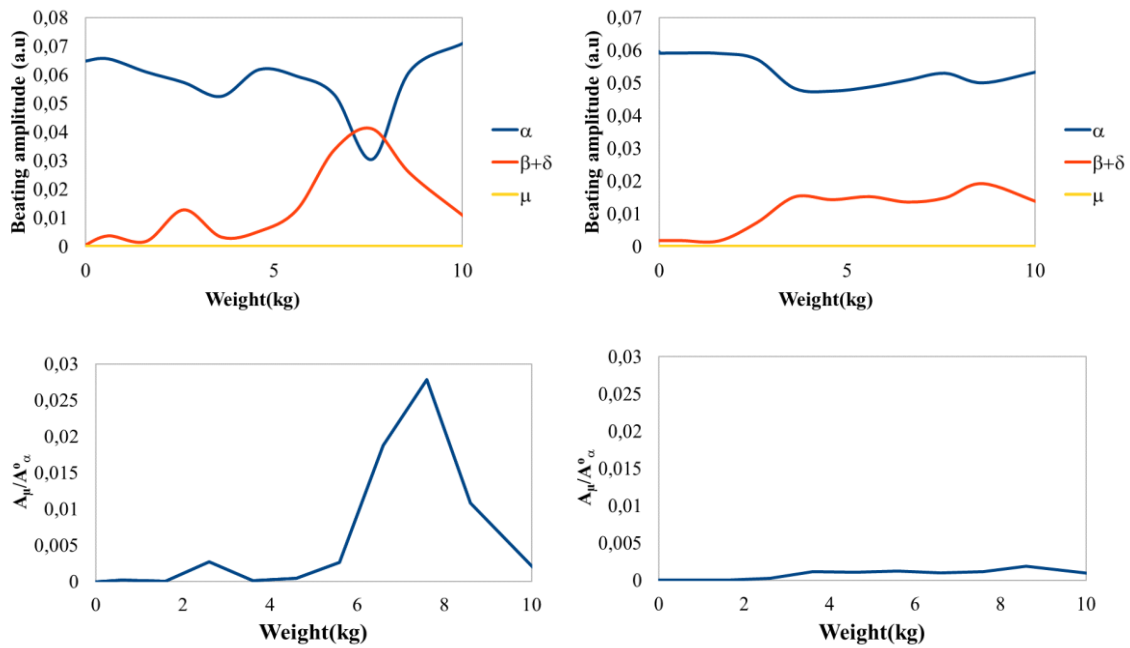


Figure 4-26: a-b) Evolution of the amplitude of the peaks as a function of weight in A-S2 for LP01+LP11e (upper-left) and LP01+LP11o (upper-right). c-d) Evolution of the coupling coefficient as a function of weight for eigenvectors LP01+LP11e (lower-left) and LP01+LP11o (lower-right).

The fact that modes LP11e and LP11o vary in a different way, demonstrates that the applied weight exerts an asymmetric stress on the optical fiber. This behavior is also found in the coupling coefficient (see Fig. 4.26 c-d). We can see that the evolution described by Fig. 4.26c is non-linear, which can be related to the strong coupling whereas the evolution shown on Fig. 4.26d is more linear, which can be related to the weak coupling, (such as in Fig. 4.23 a-b). This behavior can be easily understood by looking at the evolution of amplitudes of μ beat; that is, for a non-linear variation of μ , a non-linear evolution of M12 can be produced, and for a linear variation of μ , a linear evolution of M12 can be obtained.

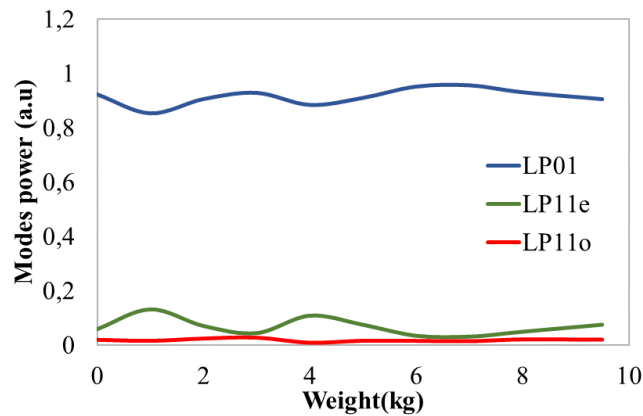


Figure 4-27: Evolution of the power in each mode as function of the weight (mesh 3, radius of curvature of 49mm).

Figure 4.27 presents the evolution of the power in each mode as a function of the weight. As was previously the case, the LP01 mode presents more than 90% of the total power for all the weights.

Using the Fig. 4.15 as an illustration, we could have an idea about the coupling evolution, because it represents the simulations of mesh 3. However, the actual simulations cannot predict the effect of the macro curvature on different coupling regime. Therefore, we will change the settings of the optical fiber in the wire mesh (Section 4.9.1.3)

4.9.1.3 Straight Fiber (fiber length =9.8cm)

For an appropriate comparison between the simulation and the experimental results, we have placed a straight fiber inside the wire-mesh in order to avoid the macro-curvature effect. Even if the simulation of the Fig. 4.15 is close from this experimental setup, we have demonstrated that the simulations cannot reproduce exactly the experimental behavior, but can predict the oscillatory behavior periodicity (compare Fig. 4.29a and Fig. 4.15).

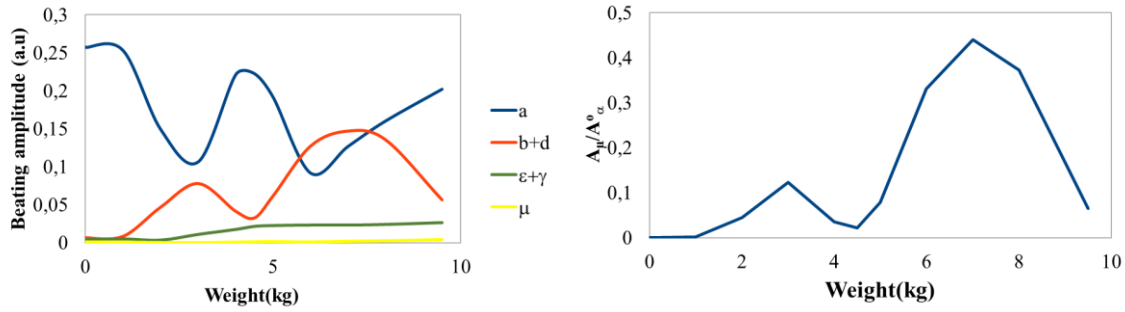


Figure 4-28: a) Evolution of the amplitude of the peaks as a function of weight in S2. b) Evolution of the coupling coefficient as a function of weight.

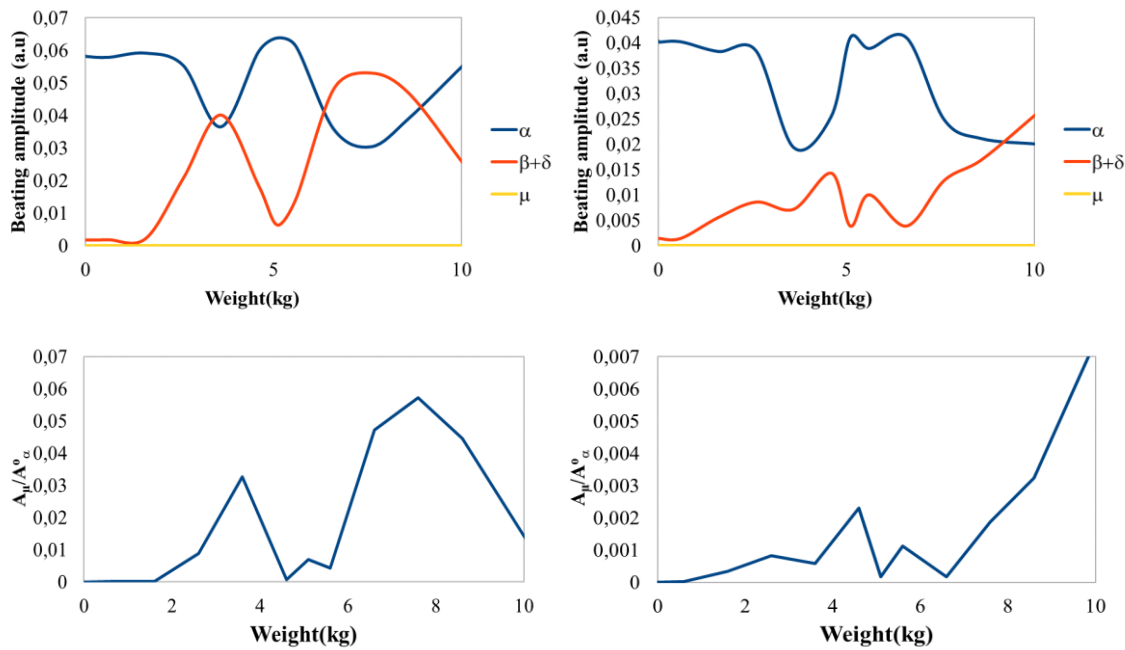


Figure 4-29: a-b) Evolution of the amplitude of the peaks as a function of weight in A-S2 for LP01+LP11e (upper-left) and LP01+LP11o (upper-right). c-d) Evolution of the coupling coefficient as a function of weight for eigenvectors LP01+LP11e (lower-left) and LP01+LP11o (lower-right).

In contrast with the previous experiments, the oscillation occur at 2kg, 6kg and 8kg for LP01+LP11e and at 9kg for LP01+LP11o. For LP01+LP11e, we can see that the first oscillation occur almost each 2kg, this periodic behavior is also found in coupler devices and another experiences [Schulze, 2015].

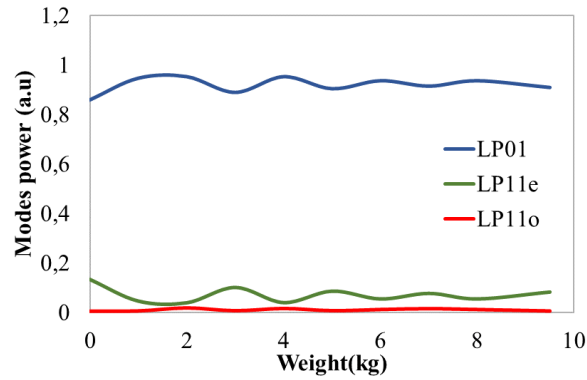


Figure 4-30: Evolution of the power in each mode as a function of weight (mesh 3, straight fiber).

Figure 4.30 shows the variation of power as a function of weight. Here, the maximum value is found in LP01 (more than 85% of the total power), followed by modes LP11e and LP11o, respectively. Notice that the maximum and minimum values of each mode coincide with the total amplitude exchange of the peaks α and $(\beta+\delta)$ from Fig. 4.30a, which means that these graphs could give us an idea about the coupling.

By comparing these results with the previous one, we can deduce that the impact of the position of the fiber inside the wire-mesh together with the macro-curvature value could clearly affect the coupling regime. However, their impact cannot be measured on the present conditions of the experiment.

4.7.2.2- Effect of mesh type

We have studied the mesh effect by using the experimental setup (Fig. 4.12b) with different meshes: mesh 1, mesh 2 and mesh 4 (see table 4.2). Likewise, we have considered a maximum input power on LP01 and the usual coupling test that consider a macro-curvature of diameter of 98cm in the fiber under the mesh.

Localized mode coupling measurement in FMF

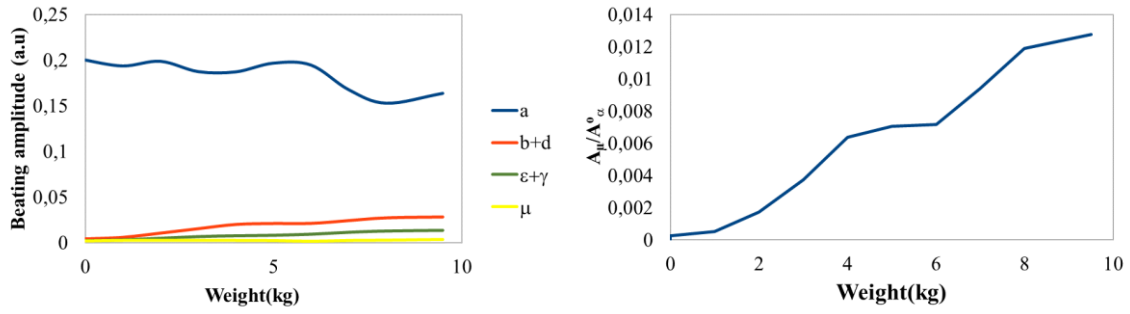


Figure 4-31: a) Evolution of the amplitude of the peaks as a function of weight in S2. b) Evolution of the coupling coefficient as a function of weight. The experimental setup uses mesh 4.

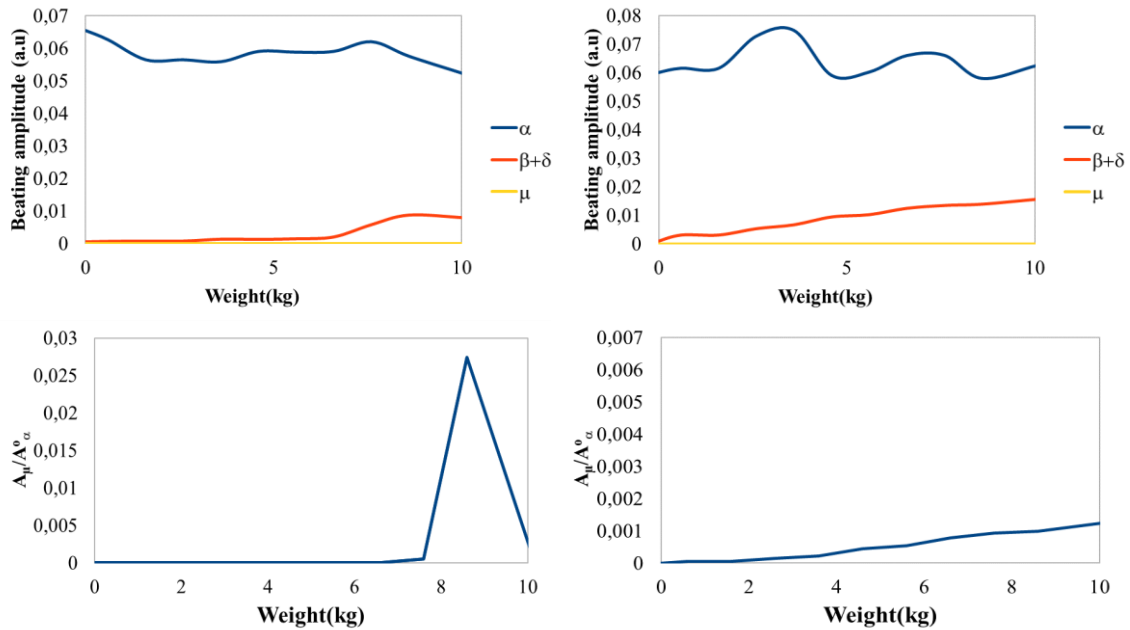


Figure 4-32: a-b) Evolution of the amplitude of the peaks as a function of weight in A-S2 using mesh 4 for LP01+LP11e (upper-left) and LP01+LP11o (upper-right). c-d) Evolution of the coupling coefficient as function of weight for eigenvectors LP01+LP11e (lower-left) and LP01+LP11o (lower-right). The experimental setup uses mesh 4.

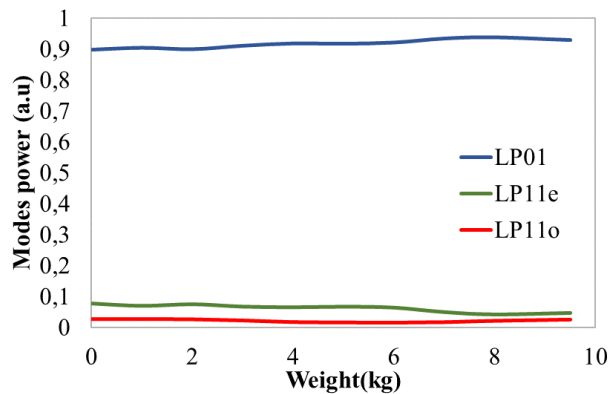


Figure 4-33: Evolution of the power in each mode as a function of weight. The experimental setup uses mesh 4.

Localized mode coupling measurement in FMF

The results from Figs. 4.31, 4.32 and 4.33 are related to the experiment with the finest mesh (mesh 4). Notice that, a very weak coupling is produced on all the applied weight range, which makes this mesh inappropriate for the coupling study. One explanation may be that the wire is so thin that it does not produce a perturbation sufficient to induce the strong coupling, even applying the maximum weight. This experiment was not simulated, because, the wire diameter of the mesh is not considered into the model.

In the next experiments, only the evolution of the amplitude of the peaks α , μ and $(\beta+\delta)$ and the coupling coefficient as a function of the weight in A-S2 will be presented, because it is sufficient for comparing the mesh effect in the coupling.

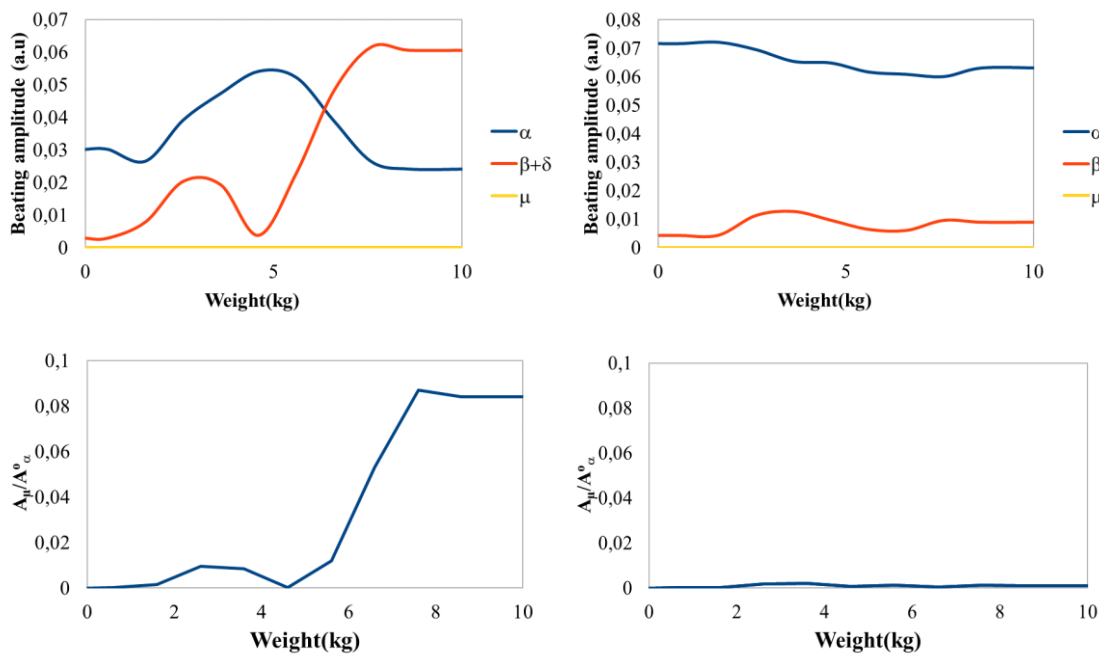


Figure 4-34: a-b) Evolution of the amplitude of the peaks as a function of weight in A-S2 for LP01+LP11e (upper-left) and LP01+LP11o (upper-right). c-d) Evolution of the coupling coefficient as a function of weight for eigenvectors LP01+LP11e (lower-left) and LP01+LP11o (lower-right). The experimental setup uses mesh 1.

Figure 4.34 corresponds to the experiment with mesh 1, as in the experiment with mesh 3, we can see that the oscillation occur at 6kg. Note that, even if these two experiments suggest that coupling occurs almost at the same weight, the shape of Figs. 4.34 are not similar to Figs. 4.22 since initial condition, fiber position and mesh are not the same. Likewise, LP01+LP11e achieves the coupling, while LP01+LP11o never reaches.

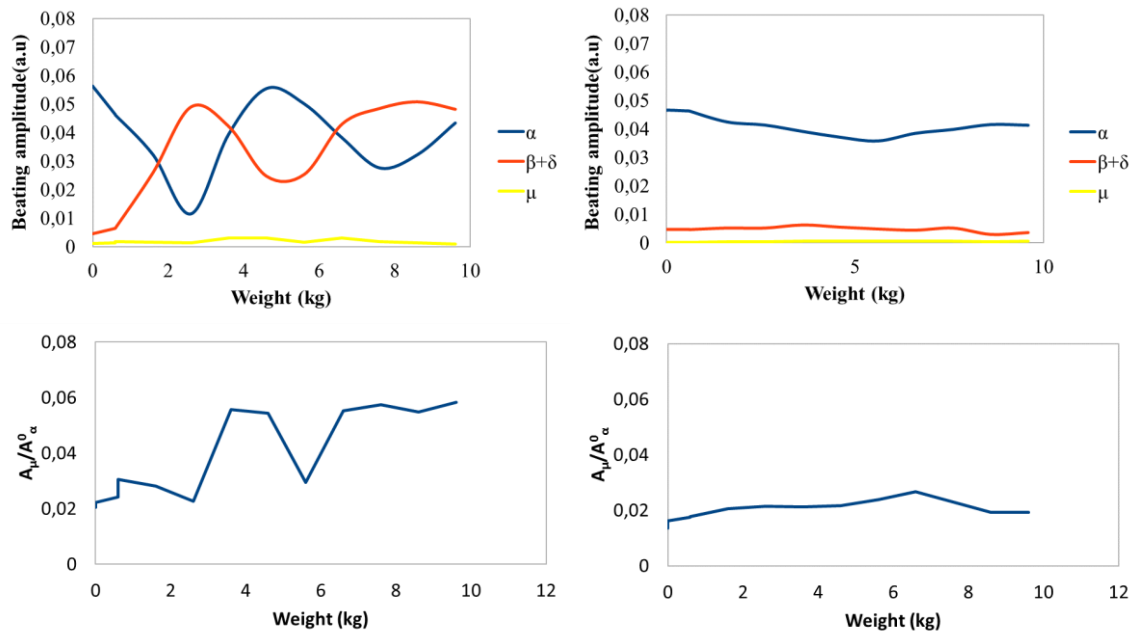


Figure 4-35: a-b) Evolution of the amplitude of the peaks as a function of weight in A-S2 for LP01+LP11e (upper-left) and LP01+LP11o (upper-right). c-d) Evolution of the coupling coefficient as a function of weight for eigenvectors LP01+LP11e (lower-left) and LP01+LP11o (lower-right). The experimental setup uses mesh 2.

The results from figure 4.35 (mesh 2) demonstrates that the coupling is reached around 2kg. Contrary to the other meshes (almost same diameter), mesh 2 possesses the largest wire diameter, making it difficult to predict when the strong coupling could be reached by comparing only with the other meshes. In case that mesh 2 would have had almost the same diameter than the other, under this condition the strong coupling would be reached after 6kg as a consequence of a longer period of the grid. However, the experiment shows that the strong coupling is reached around 2kg, instead of 6kg. One explanation may be that the wire diameter length could generate an additional deformation on the fiber, as is described in Fig. 4.36.

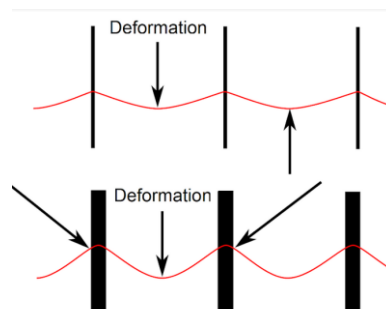


Figure 4-36: Deformation as function of the wire diameter.

It should be noted that each mesh produces different results (as we expected) and it can affect the coupling regime, because the experiment depends on the fiber disposition under the wire-mesh and mesh type.

4.9.2 A splice as localized perturbation

We used the experimental setup of the Fig. 4.12a with three different conditions for the localized perturbation (splice): without splice, centered splice and offset splice (See Fig. 4.37). The coupling is measured through the evolution of the intensity of peaks between the unperturbed and perturbed fiber. Using the method described above, we can deduce the experimental value of coefficient, M_{ij} . From this, we obtain the coupling coefficient to describe the strength of the interaction between the eigenmodes, by using the equation 4.18.

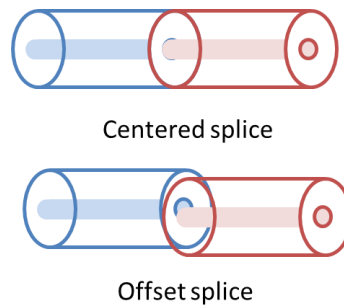


Figure 4-37: Localized perturbation by splice.

The theoretical coupling can be derived by using the amplitude transmission coefficient from one upstream fiber mode to any downstream fiber mode. It is well described by the so-called overlap integral. The theoretical prediction of M_{ij} could be interesting to have the evolution as a function of position to the core (equation 4.20).

$$\Gamma_{i,j} = \iint_{A_\infty} \Psi_i \cdot \Psi_j^* \cdot T \, dS = 0; \quad m \neq n \quad (4.20)$$

. However, in practice, we could not measure the offset between the optical fibers (splice), so the experimental results cannot be compared to the theoretical simulations. Therefore, we will only present the experimental results.

Here ψ_i corresponds to the field profile of an upstream fiber mode whereas ψ_j corresponds to a downstream fiber mode, T is the transmittance of the junction between the two fibers. T depends of the amplitude and the phase. Generally, the different rates of overlap between modes can be written in the form of a matrix or transition matrix of the mode. This matrix is not square, because it depends on the modes number guided in each fiber, excepting in this case (splice with the same fiber). Nevertheless, we can obtain the power transition matrix between the modes by the square module of each term of this matrix $|\Gamma_{ij}|^2$. In the absence of the coupling, the transition matrix is square and the diagonal terms are equal to one, that is, the power of a given mode remains in this mode (the modes in a perfect fiber are identical and orthogonal to each another). However, when two fibers are not perfect, the diagonal terms are less than one and could appear another diagonal terms.

$$\Gamma_{i,j} = \begin{bmatrix} 1 & 0 \\ 0 & 1 \end{bmatrix} \quad \text{ideal case without coupling}$$

$$\Gamma_{i,j} = \begin{bmatrix} 0.7 & 0.3 \\ 0.3 & 0.7 \end{bmatrix} \quad \text{Only coupling effect}$$

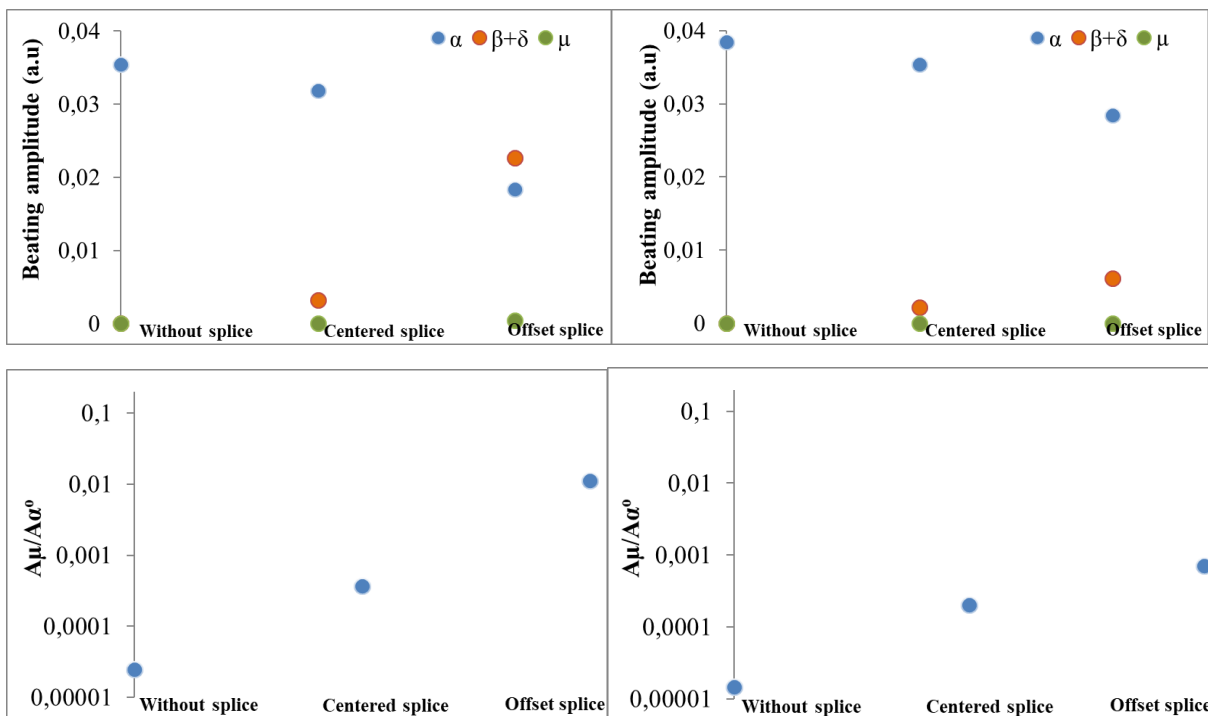


Figure 4-38: a-b) Evolution of the amplitude as function of the splice condition for LP01+LP11e (upper-left) and LP01+LP11o (upper-right). c-d) Evolution of the $A\mu/A$ as function of the splice condition for LP01+LP11e (lower-left) and LP01+LP11o (lower-right).

Figures 4.38c-d show the evolution of the non-diagonal term of the coupling matrix for different splice conditions for the small core-cladding index difference. Notice that these

Localized mode coupling measurement in FMF

figures are deduced from Fig. 4.38a-b. As we expect without perturbation, the non-diagonal terms are very small (tend to be zero) and the values of $\beta+\delta$ and μ are close to zero, but not equal to zero due to the noise. For the centered splice, a weak coupling is reached, indicating the difficulty there exists in realizing a perfectly centered splice, while for the offset splice, a strong coupling can be reached depending to the offset and fiber. This method can be recommended to examine the coupling effect on splices.

4.6- Summary

Advanced S2 allows to measure and to analyze the modal crosstalk and the mode coupling between all modes, including spatially degenerated modes of a particular fiber. The measures of these parameters are crucial to study the fiber susceptibility and their impact on emergent optical communication system based in MDM.

By using A-S2 and a wire-mesh, we have demonstrated the modal coupling of an FMF that LP_{11_e} and LP_{11_o} modes undergo different coupling coefficients as a consequence of the core deformation generated by the applied stress (perturbation).

We determined that the sensitivity of the mesh system depend on the mesh type used and the dimension of the wire. Therefore, it is important to use an appropriate mesh that allows measure the curvature in the fiber.

By using A-S2 and a splice, we have demonstrated qualitatively the mode coupling of a FMF. Therefore, this method can also be applied to the analysis of the effect of other perturbations, such as the splices and tapers.

In order to compare the theoretical microbending model and the experiments, we have modeled the periodic perturbation (wire-mesh) by controlling the following parameters of the model: number of sections, section length and total length. The obtained values from simulation shows the amplitude behavior for different coupling of the degenerates modes, instead of the beat modes, however, these results provide an idea about the behavior of the optical fiber under coupling condition.

5 CONCLUSION AND OUTLOOKS

As the demand for data transmission increases and the optical fiber capacity approaches its limits, the research community is evaluating new ways and technologies to overcome the capacity crunch. To date, it is not yet clear if MCF or FMF, both, or neither will be the next generation of transmission fiber (chapter 1). MCF can minimize crosstalk among spatial channels (inter-core crosstalk), but the communication system would need high hardware complexity (the number of amplifiers, multiplexers, etc.) especially when scaling up to more cores. Besides, the manufacturing methods needed to synthesize these fibers are more complicated compared to the one used to manufacture FMF. However, an FMF-based system requires higher dimension channel equalization in comparison with SMF, and its complexity increases as the number of modes increases. Even if the SDM (MCF or FMF) system could be a possible candidate to overcome the capacity crunch, there are many unknowns such as optical amplifiers, nonlinearity in FMF, cost and power efficiency, etc. In this work, we focused on the passive FMF, particularly on the study of the mode coupling.

In Chapter 3, a coupling model based on an expansion of ideal normal mode was developed for FMF. This model accepts any refractive index profile and an arbitrary number of modes, which extends its validity to the MMFs. Besides, it allows studying the mode coupling induced by random perturbations in the FMF, such as micro-bendings and splices. Mode coupling is modeled by dividing the fiber into numerous segments, each segment possessing a random bending. Therefore, we obtained a propagation matrix, the principal modes and their group delay for each random set of the following input parameters: fiber length, number of sections and standard deviation of the bending radius. To validate the mode coupling model, we compared the differences between the maximum and the minimum group velocity delay of the principal modes divided by the distance, with the maximum differential mode group delay ($\max|\text{DMGD}|$) between the LP modes derived from the wave equation under the condition of weak-coupling. This model has been adopted and adapted by Prysmian group to improve the set of tools they have already developed to model the behavior of numerous optical fibers.

The model has been used to study the evolution of the group delay under different coupling regimes, especially in weak and strong coupling conditions. As we discussed, a

CONCLUSION AND OUTLOOKS

small standard deviation of the curvature and a small fiber length produce weak mode coupling regimes and the group delays of the spatial modes (principal modes) are close to the values of LP modes, in absence of coupling. In this regime, the group delay behaves linearly as a function of distance. As the standard deviation of the curvature and fiber length increases, the group delay tends to merge and a strong coupling is reached, as long as the fiber design allows it. Under these conditions, we obtain a square root behavior of the group delay spread as a function of the propagation length.

The evolution of the group delay as a function of the propagation distance has been studied through a set of FMFs (10 spatial modes) with various effective index differences and for a wide range of coupling strengths. Likewise, the group delay operator has been used to evaluate these evolutions for groups of modes and its spread reduction induced by the mode coupling process. We demonstrated under certain conditions (such as, high perturbations and an effective index difference between modes above a threshold value) that the group delay spread has a square root dependence on the propagation distance. This high perturbation usually allows a strong mode coupling. This regime has been proposed for long-haul MDM systems and imposes the use of coherent detection and full MIMO DSP. However, the MIMO DSP complexity depends on the DMGD. To obtain a low DMGD and a simple MIMO, group delays must be minimized by achieving a strong mode coupling, intentionally perturbing the FMF and considering a design with a small difference of effective index between modes with low bend losses for all modes. Further work in this area must be carried out to study the feasibility of MDM systems using external perturbations.

As said before, long-haul transmission system use coherent detection and working on the basis of the principal modes [Fan, 2005] could be an interesting approach to increase their throughput, especially because these modes undergo a minimal distortion in modal coupling during their propagation. As these modes are robust in terms of the modal dispersion, they are good candidates MIMO-DSP as well. However, the other optical elements of transmission systems (such as optical amplifiers, router...) will have to take into account this basis of modes in their design.

In Chapter 4, we have measured the mode coupling by an advanced-S2 method. This method allows to analyze the mode coupling between all modes, including spatially degenerated modes. By this method and applying either homogeneous or periodic mechanical stress (wire-mesh), we studied the mode coupling for a 2-mode FMF. The coupling between the non-degenerated modes (LP_{01} and LP_{11}) and between degenerated modes (LP_{11e} and LP_{11o}) was indirectly measured.

Our measurements have demonstrated that the coupling coefficients of the LP_{11o} and LP_{11e} modes are sensitive to the mechanical stress, evidencing that the perturbation acts on each axis of the fiber differently. This method can be applied to analyze the effects of other perturbations, including splices. Besides, the conventional coupling model allows to obtain the amplitude values of the degenerated modes and not the beat modes, which allows to compare only the amplitude shape between the experimental and the simulation results.

What are the limitations of our study?

We found it difficult to compute the DMGD and losses when leaky modes are included in the coupling mechanism because the GD and loss values between the guided and leaky mode could vary significantly, especially in strong coupling regime. This made the calculation of these values from numerical method using Matlab, impossible.

Data acquisition in the S2 method is sensitive to light, vibration, connectors, splice and entrance conditions. Therefore, we have tried to control these parameters, especially the influence of the input splice between the source and the fiber under test (FMF) to produce a beat-free result on uncoupled conditions. Here, we have replaced the input splice by several taper sections of the same FMF. However, the different tapers did not produce a beat-free result.

Recommendations for further research

- Since the realistic long-haul-optical transmission systems use amplifiers, fiber connectors, switches..., it would also be helpful to study the impact of these elements on the mode coupling and not only the impact of the transmission fiber.
- It would be necessary to perform an in-depth exploration of how the different spatial-mode-basis (LP, PM, OAM, and so on) influence the performance, latency, cost and complexity of a MDM system, especially of a MIMO–DSP. Likewise, the application of spatial-mode-basis is only thinkable if they can be excited without using costly adaptive systems.
- More measurements and research works are needed on advanced-S2 to validate the method on FMF with more modes.

6 APPENDIX

A. Normalization

We consider $LP_{\nu\mu}$ notation (ν and μ modes) to study the normalization. Modes are eigen vectors of the Maxwell's equation, and thus are orthogonal by definition, meaning that they do not interfere between each other [Snyder, 1983]. We will discuss here the orthonormalization method. An integral overlap allows orthonormalization of modes as defined in Eq. (A.1). Thus, for guided modes, the projection of the mode with itself ensures an integral overlap of one ($Y_{\nu\mu} = 1$), whereas the projection between different modes (ν, μ) produces a null overlap integral ($Y_{\nu\mu} = 0$). Thereby, the overlap integral is equal or less than 1. For radiation modes, the expression on the right side of the equation, will be a function delta due to the continuous characteristic of the radiation modes.

$$\begin{cases} Y_{\nu\mu} = \iint_{A_\infty} \Psi_\nu \Psi_\mu^* dS = 0; & \nu \neq \mu \\ Y_{\nu\mu} = \iint_{A_\infty} \Psi_\nu \Psi_\mu^* dS = 1; & \nu = \mu \end{cases} \quad (\text{A.1})$$

To note that we apply the orthogonality and normalization conditions over the forward-propagating modes. Here, A_∞ is the infinite cross section, Ψ_μ^* correspond to the complex conjugate of Ψ_μ .

B. Shooting method

This method is based on an iterative method, which use Runge Kutta (RK4) to obtain the approximate solutions of ordinary differential equations.

We will explain this method for guided modes by using the following differential equation (2.24):

$$(\nabla_t^2 + k^2 n^2 - \beta^2)F_\nu(r, \theta) = 0$$

Remember that $\psi(x,y)=F(r).G(\theta)$. Thus, firstly we obtain its normalized version in order to adapt it to the numerical method [Stoltz, 1982]. Then, we normalize the refractive index profile and radius as in equations B.2 and B.3.

$$\frac{d^2 f}{dR^2} + \frac{(2\nu+1)}{R} \frac{df}{dR} + V^2(S - B)f = 0 \quad (\text{B.1})$$

$$R = r/a \quad (\text{B.2})$$

$$S(R) = \frac{(n^2(R) - \beta \cdot n_2^2)}{(n_1^2 - n_2^2)} \quad (\text{B.3})$$

Here R is the normalized radius, B is the normalized propagation constant, $S(R)$ is the normalized refractive index profile and $F(R)$ is the field amplitude $F(R) = R_\nu \cdot f(R)$ and $f(R)$ are the solutions over 0 and 1.

To solve the equation, we chose the initial condition. For example, for the guided modes, the boundary condition was set at $R=1$ between the core and the cladding interface to guarantee their continuity. Later, we integrate the equation B.1 by RK4 from $R=0$ to $R=1$ for a trial value of β . As was demonstrated by [Molin, 2016], this method is unstable for guided modes because it is not defined for $R=0$.

B.1. Using the shooting method (Runge kutta 4) to find the radiation modes

Radiation modes have an oscillatory wave form in the cladding and a β that is real and continuous. Radiation modes are derived by considering an infinite cladding. We adapt differential equation 2.27 to the numerical method (see equation B.1).

To differentiate the radiation modes from the guided mode, we change the subindex ν to v .

$$\Psi(r, \theta) = F(r) \begin{cases} \cos(v\theta) \\ \sin(v\theta) \end{cases} \quad (\text{B.4})$$

$Z_\nu(r)_\nu$ in the equation B.5 corresponds to the different function solutions of the differential equation in the core ($r \leq a$) and the cladding ($r > a$). Therefore, the radiation modes can be described in the region $r > a$ as the sum of the Hankel functions of the first kind $H_v^{(1)}$ and Hankel functions of the second kind $H_v^{(2)}$ because the outward and inward propagating cylindrical wave can be represented by these functions whereas in the region $r \leq a$ the radiation modes are represented by parabolic function (F_ν) [Marcuse, 1991]. Note

that to resolve the equation, we must have noted that the power in each radiation mode must be infinite and oscillatory for $0 < r < \infty$.

The function in the core and cladding can be summarized as:

$$Z_\nu(r)_\nu = \begin{cases} A \cdot F_\nu(\sigma \cdot r) & r \leq a \\ B \cdot H_\nu^{(1)}(\rho \cdot r) + C \cdot H_\nu^{(2)}(\rho \cdot r) & r > a \end{cases} \quad (\text{B.5})$$

With $\sigma = \sqrt{n_{co}^2 \cdot k_o^2 - \beta^2}$ for $r < a$ and $\rho = \sqrt{n_{cl}^2 \cdot k_o^2 - \beta^2}$ for $r > a$

To obtain B and C values as in the equation B.5, we have taken into account the boundary conditions for Z_ν and dZ_ν/dr to guarantee the continuity in the region $r=a$.

$$\begin{aligned} \begin{bmatrix} B \\ C \end{bmatrix} &= \frac{1}{\rho \cdot H_\nu^{(1)}(\rho \cdot a) \cdot H_\nu^{(2)'}(\rho \cdot a) - \rho \cdot H_\nu^{(2)}(\rho \cdot a) \cdot H_\nu^{(1)'}(\rho \cdot a)} \\ &\cdot \begin{bmatrix} \rho \cdot H_\nu^{(2)'}(\rho \cdot a) & -H_\nu^{(2)}(\rho \cdot a) \\ -\rho \cdot H_\nu^{(1)'}(\rho \cdot a) & H_\nu^{(1)}(\rho \cdot a) \end{bmatrix} \cdot \begin{bmatrix} F_\nu(1) \\ F_\nu'(1) \\ a \end{bmatrix} \end{aligned} \quad (\text{B.6})$$

To solve the equation B.5 by the numerical method known as shooting method, we must transform the second order equation into a system of first order equations. As a second-order differential equation is equivalent to a system of two first-order differential equations, we applied the same procedure with a very simple change of variable $df/dR = w$. In the end, we obtain the equation B.7 and B.8.

$$\frac{dw}{dR} + \frac{(2\nu+1)}{R}w + V^2(S(R) - B)f = 0 \quad (\text{B.7})$$

$$\frac{d}{dR} \begin{pmatrix} f \\ df/dR \end{pmatrix} = \begin{bmatrix} 0 & 1 \\ -V^2(S - B) & -\frac{2\nu+1}{R} \end{bmatrix} \begin{pmatrix} f_\nu \\ df_\nu/dR \end{pmatrix} \quad (\text{B.8})$$

Now, we can find the value of $f(R)$ and $f'(R)$ for a given R , by fixing a trial value β over the infinite possibilities of the radiation modes ($k_{o,n_{co}} > k_{o,n_{cl}} > \beta$) and the initial conditions of the equation B.9.

$$U_{input}(Ri) \text{ is } \begin{pmatrix} f_v \\ \frac{df_v}{dR} \end{pmatrix} = \begin{pmatrix} 1 \\ 0 \end{pmatrix} \quad (\text{B.9})$$

$$U_{output} = \begin{bmatrix} 0 & 1 \\ -V^2(S - B) & -\frac{2 \cdot v + 1}{R} \end{bmatrix} U_{input} \quad (\text{B.10})$$

Here, $U_{output}(R_{i+1})$ for R_{i+1} is calculated by RK4 algorithm.

B.2. Using the shooting method to find the leaky modes

Leaky modes can be calculated by solving the scalar wave equation B.1 of the shooting method, under an appropriate boundary condition at the core-cladding interface ($R=1$).

The function in the core and cladding can be summarized as:

$$\frac{f'(1)}{f(1)} = \left[\frac{H_{v-1}^{(2)}(V\sqrt{B}) - H_{v+1}^{(2)}(V\sqrt{B})}{H_v^{(2)}(V\sqrt{B})} \cdot V\sqrt{B}n_{eff} - v \right] \quad (\text{B.12})$$

Here, $H_v^{(2)}$ is the Hankel function of the second kind of order. Note that in the cladding the leaky field is defined by the Hankel function of the second kind and in the core leaky field is defined by the modified Bessel function of the second kind.

C. Radiation modes

We can decompose exactly the transverse fields \vec{E}_t and \vec{H}_t on the complete basis of all the transverse fields of the modes of the fiber with the radiation modes. To calculate radiation modes, we have used the method described in the section B.1.

$$\vec{E}_t = \sum_{\beta=1}^N a_{\beta} \cdot \vec{E}_{\beta t} \cdot e^{i(\beta z)} + \sum \int_0^{\infty} a_p \vec{E}_{pt} dp \quad (\text{C.1a})$$

$$\vec{H}_t = \sum_{\beta=1}^N a_{\beta} \cdot \vec{H}_{\beta t} \cdot e^{i(\beta z)} + \sum \int_0^{\infty} a_p \vec{H}_{pt} dp \quad (\text{C.1b})$$

To simulate, we have chosen a $\lambda=1550\text{nm}$, a finite radius of $62.5\mu\text{m}$ as in the MMF standardization and the core radius of $R=11\mu\text{m}$ and $R=14\mu\text{m}$. To obtain the radiation modes, we firstly validate the coefficient B and C ($B=C=0.5$) in the limit of $\sigma=\rho$ from equation B.5. Where:

$$\sigma = \sqrt{n_{co}^2 \cdot k_0^2 - \beta^2} \quad \text{for } r < a \quad \text{and} \quad \rho = \sqrt{n_{cl}^2 \cdot k_0^2 - \beta^2} \quad \text{for } r > a$$

Secondly, we verify the continuity between F_v and $B \cdot H_v^{(1)}(\rho \cdot r) + C \cdot H_v^{(2)}(\rho \cdot r)$

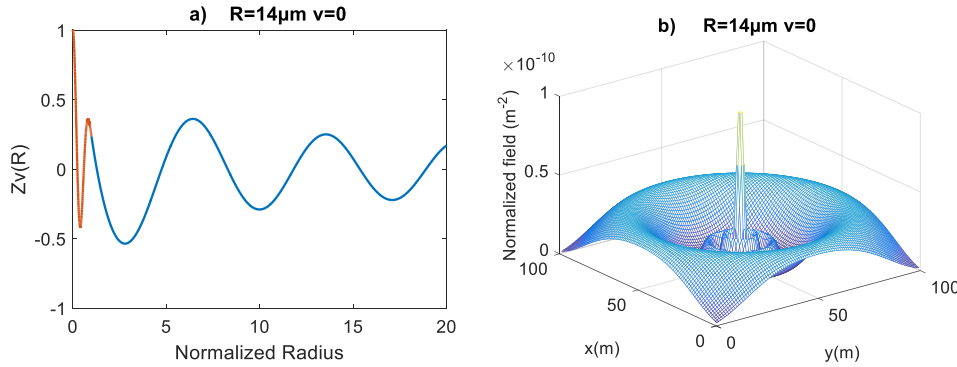


Figure 6-1: $Z_v(R)$ of the 6-LP modes with $R=14\mu\text{m}$ $v=0$ b) field of the 6-LP modes with for $\Delta n_{eff} = -0.084$ for $R=14\mu\text{m}$.

To normalize the radiation modes, we will take into account the eigenmode expansion technique which we would have liked to use them in the coupling study (chapter 3). It should be remembered that the radiation modes have infinite energy and so the normality condition from equation A.1 cannot be expected to apply. Radiation modes (open structure) are continuously oscillating and fields never vanish, thus the normalization integrals are unbounded. However, we can include the Dirac delta function, $\delta(\rho - \rho')$ (it should be a distribution) to normalize these modes [Sammut, 1982]. $\delta_{v\mu}$ is the Kronecker symbol.

$$Y_{v\mu} = \iint_{A_{\infty}} Z_v Z_{\mu}^* dS = \delta_{v\mu} \delta(\rho - \rho') \quad v, \mu = 1, 2 \dots N \quad (C.3)$$

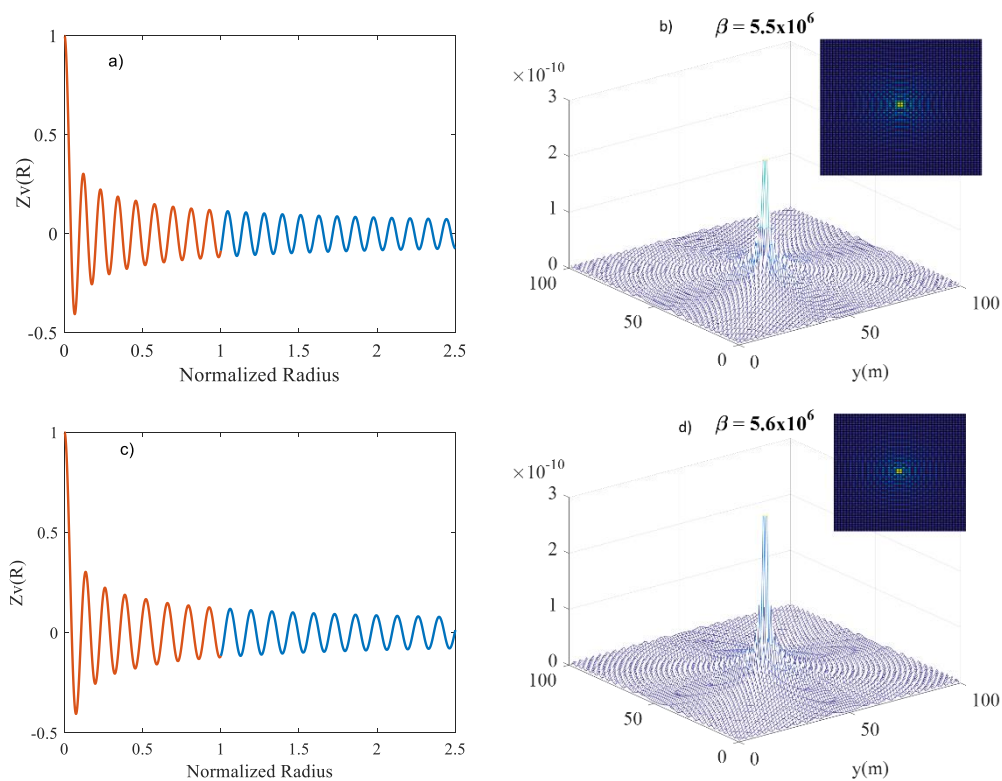
$Z_v(r)$ and $Z_{\mu}(r)$ in the equation C.3 are the different functions solutions for v and μ mode.

The normalization of the radiation modes could be accomplished by direct computation of the normalization integral. However, due to the time limitation of the project, the normalization problem has not been solved and so we cannot use radiation modes to the coupling study in the next chapter.

In order to compare with the guided mode fields (Fig. 2.16), Fig. 5.2a-h illustrates those of the radiation modes at different propagation constants (between 5.5×10^6 and 5.88×10^6) keeping the condition ($k \cdot n_1 > k \cdot n_2 > \beta$) and the modes number to zero (ν or $\mu=0$). Note that in the guided modes, the envelope of the cladding field decays exponentially along the radius direction, that is without losses, whilst the radiation modes exhibit an envelope of cladding field monotonically and slowly decays. As β decreases, the number of oscillations tends to increase.

Figure 5.3a- shows the radiation field at different modes ($\nu=\mu=0, 1, 2, 3$ and 4) with a given $\beta=5.88 \times 10^6$. As ν or μ increases, the oscillation amplitude in the cladding decays and the energy is confined in the core. For $\mu=0$, the amplitude of the oscillations inside the core are greater than those of other radiation modes. Therefore, the impact of this mode on the guided mode can be considerable with respect to the others.

For higher radiation modes $\mu=5, 10, 15, 20, 25$, the energy that was confined in the core starts to move away from the core to the cladding. It shows that the higher order radiation modes have oscillations far away from the core and their energy could be considered negligible for the guided modes.



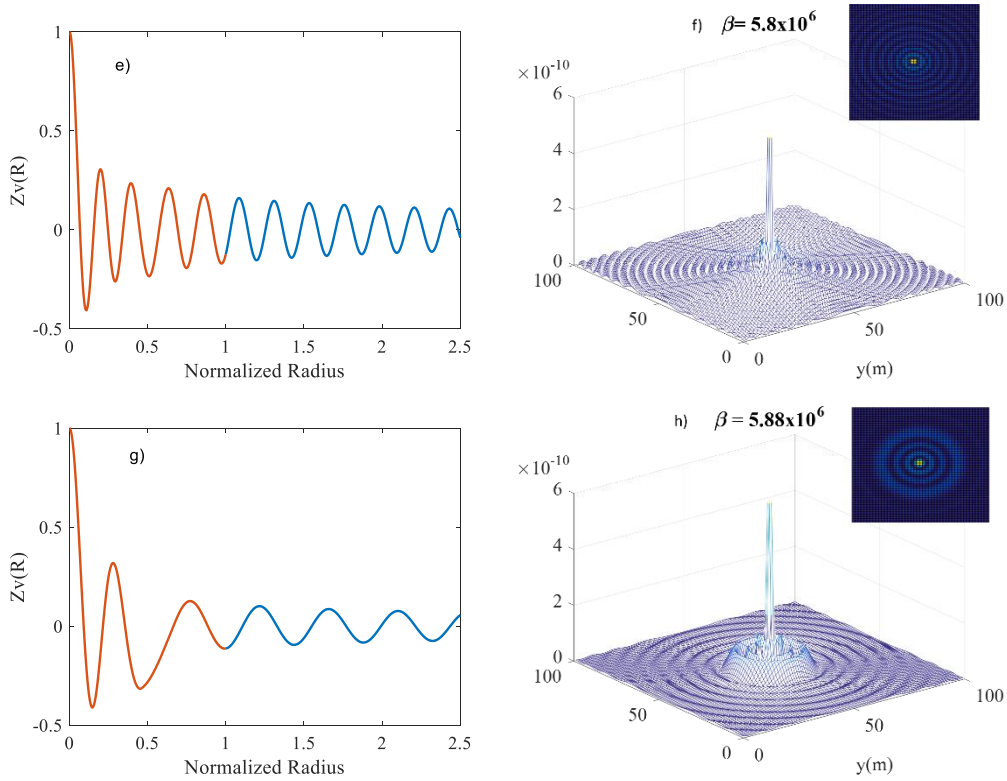


Figure 6-2

Figure 6-3: a-h) $Z_v(R)$ and radiation field of 6-LP modes, $R=14\mu\text{m}$ and $v=0$ for different propagation constants.

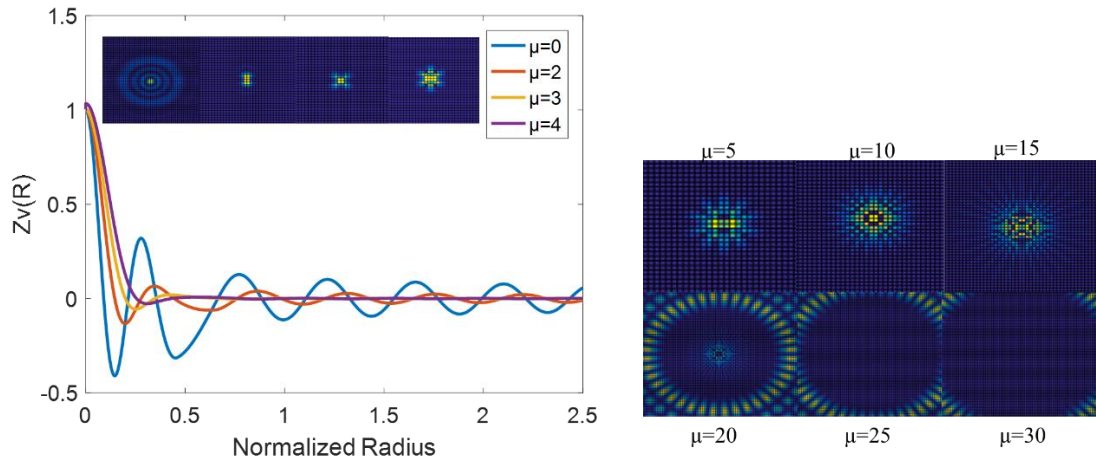


Figure 6-4: a) $Z_\mu(R)$ and radiation field of 6-LP modes, for different radiation modes. B) Radiation field for higher modes.

D. Galerkin method

By the Galerkin method [Gallawa, 1991], we adapt the differential equation into a set of simultaneous linear equation to simplify the numerical method. This method uses the Hermite or Laguerre-Gauss polynomial as solutions, which leads to a transformation of the differential equation from 2.50 to 2.55 through of the transformation parameters D.1 a-b

$$q = V.R^2 \quad (\text{D.1 a})$$

$$f(R) = J(R).e^{-\frac{(V.R)^2}{2}} \quad (\text{D.1 b})$$

$$q \cdot \frac{d^2 J}{dq^2} + (l + 1 - q) \cdot \frac{dJ}{dq} + 0.25[q - 2 \cdot (l - 1) + V \cdot (S(q) - B)] \cdot J = 0 \quad (\text{D.2 a})$$

$$q \cdot \frac{d^2 J}{dq^2} + (l + 1 - q) \cdot \frac{dJ}{dq} + g \cdot J = 0 \quad (\text{D.2 b})$$

Here, $g = 0.25[q - 2 \cdot (l - 1) + V \cdot (S(q) - B)]$ should be an integer to admit the Laguerre polynomial L_g^l as a solution. Hence, this equation is expanded in terms of orthogonal function basis as in [Gallawa, 1991].

$$J_l(q) = \sum_k^N a_k \cdot L_g^l(q) \quad (\text{D.3})$$

Later, equation D.3 will be included into equation D.2a and normalized by the orthogonality of Laguerre polynomials in the interval $(0, \infty)$ with respect to the gamma distribution. In this part the derivations follow the outline of [Molin, 2016].

$$\int_0^\infty e^{-q} \cdot q^{l+1} \cdot L_k^l(q) \cdot L_p^l(q) dq = \begin{cases} (1 + 2 \cdot k + l) \cdot \frac{(k+l)!}{k!} \cdot \delta_{kp} \\ -(1 + k + l) \cdot \frac{(k+l)!}{k!} \cdot \delta_{kp-1} \\ (k + l) \cdot \frac{(k+l-1)!}{(k-1)!} \cdot \delta_{k-1p} \end{cases} \quad (\text{D.4 a})$$

$$\int_0^\infty e^{-q} \cdot q^{l+1} \cdot L_0^l(q) \cdot L_p^l(q) dq = -(1 + l)! \cdot \delta_{0p-1} + (1 + l)! \cdot \delta_{0p} \quad (\text{D.4 b})$$

$$\int_0^\infty e^{-q} \cdot q^{l+1} \cdot L_0^l(q) \cdot L_0^l(q) dq = (1+l)! \quad (\text{D.4 c})$$

The set of simultaneous linear equations are obtained by multiplying $e^{-q} \cdot q^{l+1} \cdot L_p^l(q)$ and integrating from 0 to ∞ :

$$\sum_{k=0}^N \begin{pmatrix} a_k \cdot \frac{(k+l)!}{k!} \cdot \left((1+2k+l) \cdot \delta_{kp} - (1+k+l) \cdot \delta_{k,p-1} - k \cdot \delta_{k-1,p} \right) \\ - a_k \cdot \frac{(k+l)!}{k!} \cdot 2 \cdot (1+2k+l) \cdot \delta_{kp} \\ + a_k \cdot V \cdot \int_0^\infty e^{-q} \cdot q^l \cdot S(q) L_k^l(q) \cdot L_p^l(q) dq = 0, \forall p = 0, \dots, N \end{pmatrix} - V \cdot B \cdot \sum_{k=0}^N a_k \cdot \frac{(k+l)!}{k!} \cdot \delta_{kp} \quad (\text{D.5})$$

The equation D.5 can be written as in D.6

$$[T - I \cdot \lambda] \cdot A = 0 \quad (\text{D.6})$$

Here, matrix T is a square matrix with dimension (N+1), I is the identity matrix and λ corresponds to the eigenvalues. I. λ can be defined equally as the multiplication of a D diagonal matrix by the B constant propagation matrix and represents the eigenvalue of D^{-1} . It should be noted that the equation is easy to compute numerically, because it becomes linear and first order. In the end, the eigenvector a_k are the mode field amplitude.

The Galerkin method is not appropriate to find the leaky mode because the function basis applied there does not take into account the boundary conditions of the leaky modes.

E. MIMO-DSP in MDM transmission system

The Multiple-Input Multiple-Output Digital signal processing (MIMO-DSP) presented in the chapter 1 was analyzed to compensate the signal against the impairments suffered during transmission. Therefore, the effect produced by CD, FMF, mode coupling and mode dispersion must be compensated. In this chapter, we will adapt MIMO-DSP to MDM system transmission. In a simplistic view, we consider a DSP in MDM (SDM). This DSP needs the

contribution of all the other output signals to compensate mode coupling effect that occurred in the FMF during the propagation and thus to recover each mode.

MIMO can be classified into simple MIMO and MIMO-DSP. A simple MIMO use the direct detection, it is low cost, but it does not improve the performance significantly, because the receiver does not have the phase information (Awad, 2009). In opposition to simple MIMO, MIMO-DSP improves the performance, because it uses a coherent receiver which allows obtaining phase and amplitude information at the end of the transmission. Besides, we can use the higher order modulation formats to increase the data rate.

Figure E.1 shows a MIMO digital signal processing [Juarez, 2013]. Note that each basis (LP or PM), carry a different data, which is mode-multiplexed (M-MUX) into the FMF, then transmitted and mode-de-multiplexed (M-DEMUX) by a spatial filter and detected at the receiver. LO is the local oscillator laser which transforms the pass band signal into a baseband signal.

Then, MIMO-DSP is used to recover and to equalize the output information.

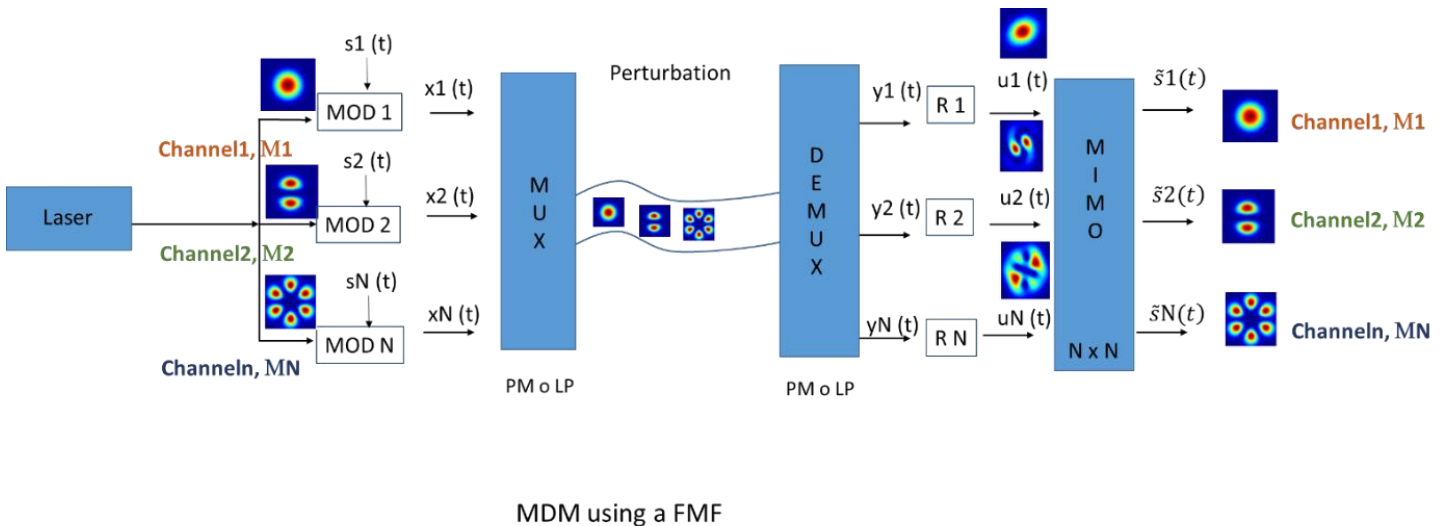


Figure 6-5: MDM system using MIMO-DSP.

In figure 5.4, $x_1(t) \dots x_N(t)$ corresponds to the modulated input signal, $y_1(t) \dots y_N(t)$ are the optical output signal, $u_1(t) \dots u_N(t)$ are the complex envelope of the optical signal, $y_1(t) \dots y_N(t)$ are the pass band signals and $u_1(t) \dots u_N(t)$ are the baseband signals. Hence, $Y_n(t)$ can be defined by considering the complex envelope of the optical signal and ω_o is the optical carrier frequency, as in equation E.1a.

$$y_N(t) = u_N(t) \cdot e^{-i \cdot \omega_o \cdot t} \quad (\text{E.1.a})$$

The signal at the end of the de-multiplexer ($y_N(t)$) can also be written as its inverse Fourier transform (E.1b). Here, the signals are DE-multiplexed from LP-modes.

$$y_N(t) = \mathcal{F}^{-1}(y_N(\omega)) \quad (\text{E.1.b})$$

MIMO-DSP will be studied by assuming an MDM transmission system without noise which uses an ideal coherent receiver without frequency compensation technique, and a MIMO based on the Wiener Filter [Oppenheim, 2010]. Wiener Filter uses a complex filter coefficient, allowing treatment of the signals of the Fig. 5.4 without decomposing the signal in phase and quadrature component. A Wiener filter is an adaptive filter using the Minimum Mean-Squared Error (MMSE, Fig. 5.5) solution of the cost function to equalize the output signal of a distorted but noise free input signal. Thus, the MIMO Wiener filter can equalize the output signal, $s_N(t)$, by minimizing the square error.

$$E\{|e(t)|^2\} = E\{|s_N(t) - \tilde{s}_N(t)|^2\} \approx 0 \quad (\text{E.2})$$

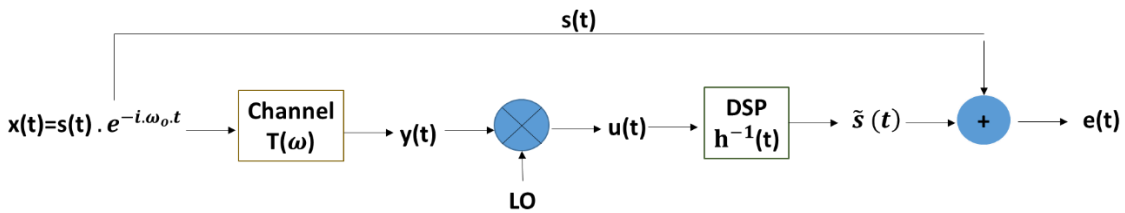


Figure 6-6: A simple MIMO Wiener system. Here, $T(\omega)$ is the transfer function of the propagation channel. $h^{-1}(t)$ represents the estimated inverse channel impulse response and $e(t)$ is the error. [Manolakis, 2005]

In a simplistic view, we consider a simple single-input single-output (SISO) Wiener system. Here, the Wiener filter is studied for SMF and the channel is considered causal and invariant of the signal. Therefore, an input signal, $x(t)$ propagates through an SMF.

By following the Figure E.2, the output signal $y(t)$ can be written as:

$$y_N(t) = \mathcal{F}^{-1}(X(\omega) \cdot T(z, \omega) \cdot a) \quad (\text{E.3})$$

The $u(t)$ is sampled, and then convoluted with the $h^{-1}(t)$ as in the equation E.4

$$\tilde{s}(t) = h^{-1}(t) * u(t) \quad (\text{E.4})$$

Note that, the output signal is an estimate of the input data signal. Thus, the error, $e(t)$ is treated and used to estimate the input signal after its optimization. The optimization from the Wiener filter is obtained when the expectation value of the square error is minimal (Equation E.5).

$$E\{|e(t)^2|\} = E\left\{|sN(t) - \widetilde{sN}(t - T')|^2\right\} = \text{Minimal value} \quad (\text{E.5a})$$

T' is time delay that be omitted for simplicity. The signal must be resampled by considering the Nyquist criterion in order to avoid aliasing. The sampled version of equation E.5 can be written as:

$$E\{|e(nT)^2|\} = E\left\{\left|s(nT) - \sum_{l_{fir}=0}^{L_{fir}-1} c_{l_{fir}}^* u(nT - lT)\right|^2\right\} \quad (\text{E.5b})$$

The length of FIR filter is L_{fir} and the complex filter coefficient are $c_{l_{fir}}^*$. The error signal can be represented as:

$$e(nT) = s(nT) - \sum_{l_{fir}=0}^{L_{fir}-1} c_{l_{fir}}^* u(nT - lT) \quad (\text{E.6})$$

To minimize the square error $|e(nT)^2| = e(nT).e(nT)^*$, the equation E.5b must be derivated with respect to the cf filter coefficients, as:

$$\frac{\partial |e(nT)^2|}{\partial cf} = \frac{\partial e(nT)}{\partial cf} \cdot e(nT)^* + e(nT) \frac{\partial e(nT)^*}{\partial cf} = 0 \quad (\text{E.7})$$

From the previous equations, we can obtain the following equation:

$$E\{u(n-f).s^*(n)\} - \sum_{l_{fir}=0}^{L_{fir}-1} c_{l_{fir}}^* \cdot E\{u(n-f)u^*(n-l_{fir})\} = 0, \text{ where } f \in [0, L_{fir}-1] \quad (\text{E.8a})$$

$$r_f - \sum_{l_{fir}=0}^{L_{fir}-1} c_{l_{fir}}^* \cdot R_{f,l_{fir}} = 0 \quad (\text{E.8b})$$

Equation E.8 can be divided into two parts: the first term, r_f that corresponds to the cross-correlation value between the output and input signal and the second term, $R_{f,l}$ that describes the autocorrelation of the $u(t)$ at different time $f-1$.

E.1. MIMO-DSP complexity

To study the complexity in MIMO-DSP, we will present the following example:

Example: Filter length $L_{\text{fir}}=3$

By the equation E.8b, we can obtain the following set of equation for $L_{\text{fir}}=3$

$$\begin{aligned} r_0 &= c_0 \cdot R_{0,0} + c_1 \cdot R_{0,1} + c_2 \cdot R_{0,2} \\ r_1 &= c_0 \cdot R_{1,0} + c_1 \cdot R_{1,1} + c_2 \cdot R_{1,2} \\ r_2 &= c_0 \cdot R_{2,0} + c_1 \cdot R_{2,1} + c_2 \cdot R_{2,2} \end{aligned} \quad (\text{E.9a})$$

Equation E.9b is the matrix form of Equation E.9a

$$\begin{bmatrix} r_0 \\ r_1 \\ r_2 \end{bmatrix} = \begin{bmatrix} R_{0,0} & R_{0,1} & R_{0,2} \\ R_{1,0} & R_{1,1} & R_{1,2} \\ R_{2,0} & R_{2,1} & R_{2,2} \end{bmatrix} \cdot \begin{bmatrix} c_0 \\ c_1 \\ c_2 \end{bmatrix} \quad (\text{E.9b})$$

$$\vec{r}_{us} = R_{uu} \cdot \vec{c} \quad (\text{E.9c})$$

Note that the vector \vec{c} comprises all the unknown filter coefficients, the vector, \vec{r}_{us} contains the crosscorrelation coefficients and the matrix, R_{uu} contains all components the autocorrelation, whose size is $L_{\text{fir}} \times L_{\text{fir}}$. The coefficient vector can be obtained by equation E.9c.

$$R_{uu}^{-1} \cdot \vec{r}_{us} = \vec{c} \quad (\text{E.9d})$$

Figure 5.6 shows the filter structure for a FIR length of $L_{\text{fir}}=3$. Here, the number of filter coefficient is equal to L_{fir} .

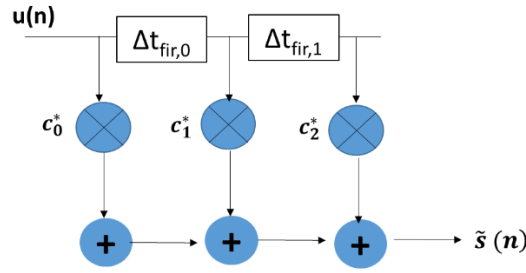


Figure 6-7: FIR filter for signal de-convolution.

The signal passes by the filter bank. Then, $u(n)$ is delayed by Δt_{fir} and multiplied by the complex filter coefficient. In the end, the estimated signal, $\tilde{s}(n)$ is obtained by the sum of all these blocks. As discussed before, the estimation of the cross-correlation vector needs the information of the input signal. It can be acquired for instance by training in real optical transmission systems. Moreover, the output signal $u(n-T_d)$ suffers from the delay (T_d) which should also be taken into account. Here, the length of the delay is an important parameter to obtain an appropriate detection, so that:

- If the delay is too small, there is no correlation and the filter coefficients could be estimated incorrect, which leads a higher error.
- If the delay is large, more than one filter tap necessary to minimize the square error, which leads to increase the complexity of the system.

Assuming $1 \dots i^{\text{th}}$ input signals and D is the total output signals, the expectation value of the square error can be described by:

$$E\{|e_i(nT)|^2\} = E\left\{\left|s_i(nT) - \sum_{d=1}^D \sum_{l=0}^{l_{fir}-1} c_{l_{fir}}^* u_d(nT - l_{fir}T)\right|^2\right\} \quad (\text{E.10})$$

Note that the number of taps and equation change to $D \times L_{fir}$

$$\vec{r}_{us_i} = R_{uu} \cdot \vec{c}_i \quad (\text{E.11a})$$

R_{uu} is a matrix and its diagonal describes the autocorrelation of the output signal, the non-diagonal values describe the correlation between the different output signals. The cross-correlation vector, \vec{r}_{us_i} comprises the correlation values between the input signal and all the output

signals. Besides, equation E.11 describes a receiver structure with multiple input single output (MISO), which can be adapted to the Multiple Input Multiple Output (MIMO) receiver by considering $D \times D$ number of equation (cf. Fig. 5.7).

In Figure 5.7 shows a MISO assembly FIR to produce a MIMO. Here the output signals are combined to obtain the $1, 2, \dots, i$ input signal estimation.

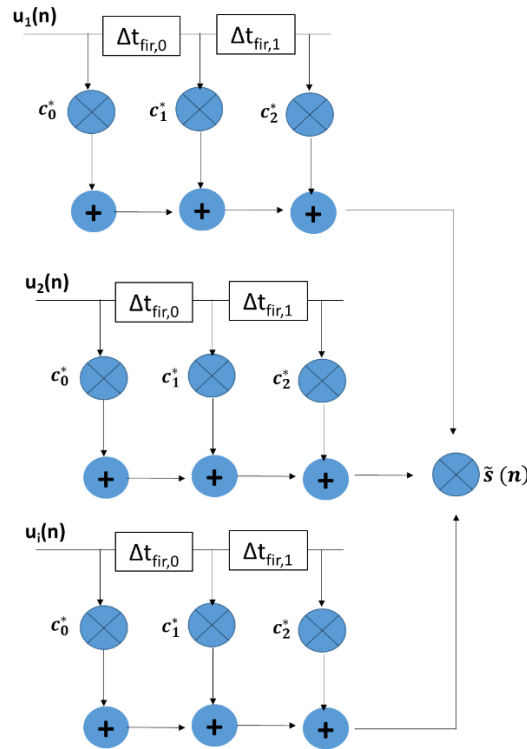


Figure 6-8: FIR filter for signal de-convolution.

These MIMO are used in MDM transmission system with FMF. We can classify MIMO in two groups depending on digital filtering technique: MIMO Time-Domain Equalization (TDE) and MIMO Frequency-Domain Equalization (FDE).

- In MIMO-TDE, the digital filtering is commonly implemented by direct time domain convolution and its complexity increase with the temporal memory length
- In MIMO-FDE, we used a Fast Fourier Transform algorithm and the overlap-save or overlap-add method (Arik, 2013). For this MIMO, the complexity is related to the FFT block length which can also produce high processing latency.

In this section, the Digital filtering and adaptation algorithm are not analyzed. However, the approaches to reduce MIMO equalizer complexity will be mentioned:

- The first approach is to design all the system components, de-multiplexers, FMF, amplifiers and switches to minimize mode coupling crosstalk.
- The second approach is to design the transmission system with low group delay (GD) spread, whose purpose is to use a temporally short MIMO equalizer.

For this second approach, the GD spread is the parameter used to reduce the complexity in the FMF communication system detection (MIMO-DSP) [Savory, 2010], [Arik, 2015].

E.2. MIMO in weakly coupled

In the presence of a simple MIMO, the fiber must be designed so that the modes admit a weak couple. In this regime, some modes could be coupled due to their almost similar propagation constants, but others will never reach a coupling state.

The MDM channels in weakly-coupled regime do not need complex MIMO-DSP. In this regime [Sillard, 2015], we need to consider:

- Minimizing mode coupling to limit the crosstalk and obtain the minimal effective area of all modes.
- Choosing the appropriate fibers with a profile that allows low crosstalk and very large effective area, regardless of its large DMGD. One of the good candidates is the step-index (SI).

Weakly-coupled uses 2×2 or 4×4 MIMO with a small number of taps in order to separate each spatial mode, without requiring the differential mode delay compensation and digital signal processing. Thus, MIMO handles only the polarization diversity and modes with the same propagation constant (degenerate modes). To date, 4 LP mode fibers with low crosstalk have been reported [Sillard, 2011]. The main restrictions to increase the modes number in this system are A_{eff} , attenuation and crosstalk (~ 25 dB).

E.3. MIMO in strongly-coupled

In the presence of a MIMO complex, the fiber must be designed to admit a strong-coupling. In this regime, the modes have nearly identical propagation constants which allow a full coupling. To achieve this regime, external or intentional perturbation could be used.

The MDM channels in strongly-coupled regime required a MIMO-DSP. In this regime [Sillard, 2015], we need to consider:

- Minimizing the differential mode group delay (DMGD), regardless of mode coupling.
- Choosing the appropriate fibers with a profile that allows small differential mode delay. One candidate is the fibers with graded-index profile (GI).

The strongly-coupled regime uses $2N \times 2N$ MIMO techniques with 2 polarizations $\times N$ spatial modes that allow detecting all modes simultaneously and cross-talk compensation. This strategy is appropriated if the numbers of multiplexed modes is significant. To date, 10 SDM channels (6 LP modes) with a spectral efficiency of 58 b/s/Hz (chapter 1) have been reported [Chen, 2016]. The main limitations to increase the modes number are DGD and differential mode attenuation.

To overcome the complexity of MIMO, DMGD must be as small as possible. For example, [Zhao, 2015] has considered an ultra-low DMGD Fiber in spite of the difficulties to achieve a low DMGD once LP number is important. The channel spread can be reduced by introducing a strong coupling by an intentional perturbation. This reduction has an impact on the equalizer taps length [Ho, 2011], but mode-depend-loss could appear. Other approaches, such as [Sakamoto, 2013] use the DMGD-compensated fiber with a positive DMGD (P type) or a negative DMGD (N type) or finally introduce a computational efficient algorithms in the DSP side.

In table E.1 is summarized the characteristics of these approaches (Weakly-coupled and strongly-coupled).

Table E.1: Weakly-coupled and strongly-coupled in FMF [Sillard, 2016].

Criterion: Min $ \Delta n_{eff} $	FMF weakly-coupled	FMF strongly-coupled
Parameter	Step Index	Graded Index
A_{eff}	>80 μm^2 , increases with the modes	>80 μm^2
Attenuation	It increases with the modes $\sim 0.25\text{dB/km}$	It increases with the modes $\sim 0.25\text{dB/km}$
Bend losses	< 10dB/turn	< 10dB/turn
Losses	higher-order LP _{x1} modes >19.34dB	higher-order LP _{x1} modes >19.34dB
Min Δn_{eff}	Small	It can be minimized
$\Delta\beta$	High	
DSP-MIMO	Most cases (2x2MIMOs or 4x4MIMOs)	2N \times 2N MIMOs (MIMO complexity depend of DMGD)
Max DMGD	High $\gg 100\text{ps/km}$	Low <50ps/km
Crosstalk	Low, limits $\sim 25\text{dB}$ (high distance) $\sim 45\text{dB}$ (short distance-9LP)	Medium
Simplicity	Yes	No
Modes number limit	9LP (Impact on Crosstalk)	12LP (Impact on MDL)

The previous review highlights that the coupling in fibers has already been studied through many aspects. We propose to push these studies forward by adapting the coupling model to FMF in MDM communication system.

F. DGD in stochastic differential equation

The strong coupling depends on the combination of effects of mode coupling over the entire fiber [Poole, 1986]. Therefore, the group delay has a statistical behavior. To study the DGD, we need to solve stochastic differential equations. Firstly, we assume that the curvature represents a stationary random process, $R_K(u) = \langle K^*(z) K^*(z-u) \rangle$, by considering the average of the curvature over one section length. Here, the brackets are ensemble averages. Secondly, curvature has a characteristic correlation length such that $R(u) \approx 0$ for $|u| >$ correlation length, where u represents the elements of the matrix U . Third, amplitude are complex and their phase are sufficiently random.

$$\langle \mathbf{a}_m \mathbf{a}_n \rangle = \langle \mathbf{a}_m \mathbf{a}_n' \rangle = 0 \text{ for } m \neq n$$

We also express the power spectral density (PSD) of the curvature by :

$$S_K \left(\frac{\Delta\beta}{2\pi} \right) = \int R_K(u) \cdot e^{-\Delta\beta u} du \quad (\text{F.1})$$

By assuming an FMF with 2-LP modes (m, n), equation 3.14 becomes:

$$\vec{a}'_{(\omega, z)} = \begin{bmatrix} -i \cdot \beta_m & i \cdot K(z) \\ i \cdot K(z) & -i \cdot \beta_n \end{bmatrix} \vec{a}_{(z)} \quad (\text{F.2a})$$

$$\frac{\partial a_m(z)}{\partial z} = -i \cdot K(z) \cdot e^{-i\Delta\beta z} a_n^*(\omega, z) \quad (\text{F.2b})$$

$$\frac{\partial a_n(z)}{\partial z} = i \cdot K(z) \cdot e^{-i\Delta\beta z} a_m^*(\omega, z) \quad (\text{F.2c})$$

[Poole, 1988] describes the dispersion in an ensemble of fibers in terms of the second moment about the variance $\langle \Delta\tau(z)^2 \rangle$. Therefore, it can be expressed by considering the matrix element. Note that $\langle \Delta\tau(z)^2 \rangle$ is expressed in terms of the complex amplitude.

$$\langle \Delta\tau^2 \rangle = 4 \langle |a_m'|^2 + |a_n'|^2 \rangle$$

Then, we derive the equation with respect to z twice and later we use equations F.2b and F.2c and their frequency derivatives. Thereby, we obtain the differential equation of $\frac{d\langle \Delta\tau^2 \rangle}{dz}$ and $\frac{d^2\langle \Delta\tau^2 \rangle}{dz^2}$ as in [Poole, 1988].

$$\frac{d\langle \Delta\tau^2 \rangle}{dz} = i \cdot 4 \cdot \frac{d(\beta_m - \beta_n)}{d\omega} \cdot \langle a_m \cdot a_m'^* + a_n \cdot a_n'^* \rangle + 2 \cdot \left(\frac{d(\beta_m - \beta_n)}{d\omega} \right)^2 z \quad (\text{F.3})$$

where,

$\Delta\beta' = \frac{d(\beta_m - \beta_n)}{d\omega}$ corresponds to the difference in the group delay time per unit length.

By solving the stochastic coupled equation (3.53b and 3.53c) and assuming the complex amplitudes and their frequency derivatives are constant over intervals of the order of length section (weak-coupling approximation). We can obtain the perturbation solutions for the complex amplitudes that are later used to solve the differential equations that permit to obtain $\langle \Delta\tau(z)^2 \rangle$ (See equation F.4).

$$\frac{d^2\langle \Delta\tau^2(z) \rangle}{dz^2} = -2 \cdot h \cdot \frac{d\langle \Delta\tau^2(z) \rangle}{dz} + 2 \cdot \left(\frac{d(\beta_m - \beta_n)}{d\omega} \right)^2 \quad (\text{F.4})$$

Here, $h = \int R_K(u) \cdot e^{-\Delta\beta u} du \approx S_K \left(\frac{\Delta\beta}{2\pi} \right)$. h describes the ensemble-average ratio at which power is transferred between modes. The solution of the equation F.4 are obtained over the initial condition following $\langle \Delta\tau^2(0) \rangle = \frac{d\langle \Delta\tau^2(0) \rangle}{dz} = 0$, thus, we obtain the mean-square DGD (See equation F.5).

$$\langle \Delta\tau^2(z) \rangle = E[\Delta\tau^2] = \left(\frac{\partial\Delta\beta}{\partial\omega} \right)^2 \cdot \left[\frac{1}{2 \cdot h^2} \cdot (e^{-2 \cdot h \cdot z} + 2 \cdot h \cdot z - 1) \right] \quad (\text{F.5a})$$

$$\langle \Delta\tau^2(z) \rangle = E[\Delta\tau^2] = \left(\frac{d(\beta_m - \beta_n)}{d\omega} \right)^2 \cdot \left[\frac{1}{2 \cdot h^2} \cdot (e^{-2 \cdot h \cdot z} + 2 \cdot h \cdot z - 1) \right] \quad (\text{F.5b})$$

To study the coupling regime, we can find the limit $hz \rightarrow 0$ for low-coupling or $hz \rightarrow \infty$ for strong-coupling. If $z=L$, we have:

$$\lim_{hz \rightarrow 0} E[\Delta\tau^2(z)] = \left(\frac{\partial\Delta\beta}{\partial\omega} \right)^2 \cdot L^2 = \left(\frac{d(\beta_m - \beta_n)}{d\omega} \right)^2 \cdot L^2 \quad (\text{F.6a})$$

$$\lim_{hz \rightarrow \infty} E[\Delta\tau^2(z)] = \left(\frac{\partial\Delta\beta}{\partial\omega} \right)^2 \cdot \frac{L}{h} = \left(\frac{d(\beta_m - \beta_n)}{d\omega} \right)^2 \cdot \frac{L}{h} \quad (\text{F.6b})$$

It should be noted that the mean square DGD in low-coupling looks like the equation 3.51c. Here, DGD increases linearly. However, in strong-coupling DGD varies with the square root of the length and it varies inversely with h or power spectral density of curvature. Accordingly, there is a strong dependence on the fiber statistics.

The coupling regime in PM's will be relevant to understand the results of the next section.

NOTATIONS

➤ Refractive Indices and Related quantities

n	Refractive index function
n_{core}	Core refractive index
n_1	Maximum of the core refractive index
n_2	Cladding refractive index
n_0	Refractive index without perturbations
n_e	Equivalent refractive index
n_p	Perturbed refractive index
n_{trench}	Trench refractive index
n_{eff}	Effective refractive index
Δn_{eff}	Effective refractive-index differences
r	Radius parameter
a	Core radius
α	Power-law exponent
Δ	Relative refractive index difference
$f(r)$	Shape of the index profile

➤ Fields and related quantities

\vec{E}	Electric field
\vec{H}	Magnetic field
\vec{D}	Electric displacement field
\vec{B}	Magnetic induction
β	Propagation constant
β_m	Propagation constant of the guided mode m
β_0	Fundamental propagation constant
β_2	Second order dispersion
D	Chromatic dispersion
v_g	Group velocity
k_0	Free space wavenumber
k_t	Transverse wavenumber of the bent fiber

NOTATIONS

k_{te}	Transverse wavenumber of the equivalent fiber
ω, λ, t	Angular frequency, Wavelength, Time
\vec{J}, ρ	Free current density vector, Free charge density
$\varepsilon, \varepsilon_0, \varepsilon_r$	Permittivity, Vacuum permittivity, Relative permittivity
μ_0	Vacuum permeability
A_m^+	Amplitude of the progressive wave for the electric field
A_m^-	Amplitude of the regressive wave for the electric field
B_m^+	Amplitude of the progressive wave for the magnetic field
B_m^-	Amplitude of the regressive wave for the magnetic field
a_m	Amplitude of the mode m for the electric field
b_m	Amplitude of the mode m magnetic field

➤ Fiber, Modes and related quantities

L	Fiber length
ΔL	Length of a fiber segment
R	Bend radius
$\sigma_{1/R}$	Standard deviation of the curvature
τ	Group delay per unit length
σ_{GD}	Group delay standard deviation
N_m	Number of modes
U, W	Modal parameters
V	Normalized frequency
ν	Integer modal azimuthal number / angular quantization
μ	Radial quantization
J_ν	Bessel functions of the first kind
K_ν	Modified Bessel functions of the second kind
$F_\nu(r, \theta)$	Amplitude of the ν mode
L_q^l	Laguerre polynomial of order l and q
$H_\nu^{(i)}$	Hermite polynomial of order i
$\alpha_{\mu\nu}$	Mode bend losses
K'_{mn}	Coupling coefficient for the electric field
k'_{mn}	Coupling coefficient for the magnetic field

NOTATIONS

➤ Matrix notations and related quantities

$[\mathbf{B}(\omega)]$	Uncoupled propagation matrix: Propagations matrix of a degenerate mode group
$[\mathbf{K}]$	Coupling coefficients between modes
$[\mathbf{a}(\mathbf{z})]$	Wave amplitude
$[\boldsymbol{\alpha}]$	Propagation losses
$[\mathbf{M}(\boldsymbol{\omega})]$	Propagation matrix
$[\mathbf{U}(\boldsymbol{\omega})]$	Lossless propagation matrix
Φ_1	Phase of the fundamental mode
$\Delta\alpha_N$	Difference between the propagation constants of the fundamental mode and mode, N
$\Delta\beta_N$	Difference between the propagation constants of the fundamental mode and mode, N
$[\mathbf{T}(\boldsymbol{\omega})]$	Group delay matrix
$[\boldsymbol{\tau}]$	Delay per unit of length
$[\mathbf{G}(\boldsymbol{\omega})]$	Group delay operator matrix
$[\mathbf{I}]$	Identity matrix

BIBLIOGRAPHY

[Agrawal, 2002] G. P. Agrawal. *Fiber-Optic Communication Systems*, Third Edition, New York: John Wiley (2002).

[Agrawal, 2000] G. P. Agrawal. *Nonlinear fiber optics*, Nonlinear Science at the Dawn of the 21st Century-Springer (2000).

[Agrawal, 2010] G. P. Agrawal. *Fiber-Optic Communication Systems*, 3rd ed. Hoboken, NJ: Wiley-Interscience (2010).

[Ali, 2015] T. A. Ali, M. I. Shehata and N. A. Mohamed. "Design and performance investigation of a highly accurate apodized fiber Bragg grating-based strain sensor in single and quasi-distributed systems," *Appl. Opt.* 54, 5243-5251 (2015)

[Arik, 2014] S. O. Arik, J. M. Kahn and K. P. Ho. "MIMO signal processing for mode-division multiplexing," *IEEE Signal Process. Mag.* 31(2), 25-34 (2014)

[Arik, 2015] S. O. Arik, D. Askarov and J. M. Kahn. "MIMO DSP Complexity in Mode-Division Multiplexing," in *Optical Fiber Communication Conference*, OSA Technical Digest (online) (Optical Society of America), paper Th1D.1 (2015)

[Bai, 2011] N. Bai, E. Ip, Y. K. Huang, E. Mateo, F. Yaman, M. J. Li, S. Bickham, S. Ten, J. Liñares and C. Montero. "Mode-division multiplexed transmission with inline few-mode fiber amplifier," *Optics express* 20, 2668-2680 (2012)

[Bai, 2013] N. Bai. *Mode-division multiplexed transmission in few-mode fibers*. Florida: University of Central Florida Orlando. (2013)

[Barré, 2013] N. Barré, B. Denolle, J. Pu, Morizur, J-F. and Labroille, G. *Broadband, mode-selective 15-mode multiplexer based on multi-plane light conversion*. *Optical Fiber Communication Conf. and Exposition, Los angeles*. (2017)

[Beppu, 2014] S. Beppu, K. Kasai, M. Yoshida and M. Nakazawa. "2048 QAM (66 Gbit/s) single-carrier coherent optical transmission over 150 km with a potential SE of 15.3 bit/s/Hz". In Proc. *Optical Fiber Communication Conf. and Exposition*, San Francisco, CA, 9–13 March. (2014)

BIBLIOGRAPHY

[**Bigo, 2006**] S. Bigo. "Modelling of WDM Terrestrial and Submarine Links for the Design of WDM Networks," in *Optical Fiber Communication Conference and Exposition and The National Fiber Optic Engineers Conference*, paper OThD1. (2006)

[**Bigo, 2015**] L. Bigot, G. Le Cocq and Y. Quiquempois, "Few-mode Erbium-doped fiber amplifiers: A review," *IEEE J. Lightw. Technol.*, vol. 33, no. 3, pp. 588–596. (2015)

[**Bromage, 2011**] J. Bromage, J. M. Fini, C. Dorrer and J. D. Zuegel, "Characterization and optimization of Yb-doped photonic-crystal fiber rod amplifiers using spatially resolved spectral interferometry," *Appl. Opt.* 50, 2001-2007. (2011).

[**Bures, 2009**] J. Bures. *Guided Optics*, WILEY-VCH (2009).

[**Chen, 2014**] H. Chen, N. K. Fontaine, R. Ryf, B. Guan, S. J. B. Yoo and A. M. J. Koonen, "A fully-packaged 3D-waveguide based dual-fiber spatial-multiplexer with up-tapered 6-mode fiber pigtails," in *the European Conference on Optical Communication (ECOC)*, Cannes, 2014, pp. 1-3. (2014).

[**Chen, 2016**] H. Chen, R. Ryf, N. K. Fontaine, A. M. Velázquez-Benítez, J. Antonio-López, C. Jin, B. Huang, M. Bigot-Astruc, D. Molin and F. Achten., P. Sillard, R. Amezcua-Correa, "High Spectral Efficiency Mode-Multiplexed Transmission over 87-km 10-Mode Fiber," in *Optical Fiber Communication conference*, OFC'16, paper Th4C.2. (2016).

[**Djafar, 2001**] K. Djafar, Mynbaev and L. L. Scheiner. *Fiber-optic communications* Technology New York: Prentice Hall. (2001).

[**Djordjevic, 2016**] I. B. Djordjevic and Z. Qu. "Coded Orbital Angular Momentum Modulation and Multiplexing Enabling Ultra-High-Speed Free-Space Optical Transmission," in *Optical Wireless Communications*, pages 363-385. Springer, 2016.

[**Ellis, 2010**] A. D. Ellis, J. Zhao and D. Cotter. "Approaching the non-linear Shannon limit," *J. Lightw. Technol.*, vol. 28, no. 4, pp. 423–433. (2010)

[**Ellis, 2013**] A. Ellis and N. Doran."Are few-mode fibres a practical solution to the capacity crunch?" in *15th International Conference on Transparent Optical Networks, ICTON 2013.*, Tu.C2.1, IEEE conference publications, IEEE, Cartagena, Spain. (2013)

BIBLIOGRAPHY

[Erdogan, 1997] T. Erdogan. "A Cladding-mode resonance in short- and long-period fiber grating filters," *J. Opt. Soc. Am. A* 14, 1760-1773 (1997)

[Essiambre, 2009] R. J. Essiambre, P. Foschini G. and Winzer and G. Kramer. "Capacity Limits of Fiber-Optic Communication Systems," in *Optical Fiber Communication Conference and National Fiber Optic Engineers Conference*, OSA Technical Digest (CD) (Optical Society of America, 2009), paper OThL1. (2009)

[Essiambre, 2010] R. J. Essiambre, G. Kramer, P. J. Winzer, G. J. Foschini and B. Goebel. "Capacity limits of optical fiber networks" *J. Lightw. Technol.* vol. 28 no. 4 pp. 662-701 (2010).

[Fan, 2005] S. Fan and J. M. Kahn. "Principal modes in multimode waveguides," *Opt. Lett.* 30, 135-137 (2005).

[Fang, 2014] L. Fang and H. Jia. "Coupling analyses of LP_{0m} modes with optical fiber gratings in multimode fiber and their application in mode-division multiplexing transmission", *Optics Communications*, Volume 322, 2014, Pages 118-122 (2014).

[Ferreira, 2015] F. Ferreira, S. Stylianos and E. Andrew. "Impact of linear mode coupling on the group delay spread in few-mode fibers." *Optical Fiber Communications Conference and Exhibition (OFC)*, 2015. IEEE, (2015).

[Fini, 2013] J. M. Fini, J. W. Nicholson, R. S. Windeler, E. M. Monberg, L. Meng, B. Mangan, A. DeSantolo and F. V. DiMarcello. "Low-loss hollow-core fibers with improved single-modedness," *Optics Express*, 21 (5), pp. 6233-6242. (2013).

[Flamm, 2012] D. Flamm, D. Naidoo, C. Schulze, A. Forbes and M. Duparré. "Mode analysis with a spatial light modulator as a correlation filters," *Opt. Lett.* 37, 2478-2480 (2012).

[Friesem, 1989] A. A. Friesem, E. Lichtman, R. G. Waarts and H. H. Yaffe. "Nonlinear Effects In Optical Fiber Communication". Proc. SPIE 1033, *Trends in Quantum Electronics*, 372. (1989).

[Frignac, 2002] Y. Frignac, G. Charlet, W. Idler, R. Dischler, P. Tran, S. Lanne, S. Borne, C. Martinelli, G. Veith and A. Jourdan, J. Hamaide and S. Bigo. "Transmission of 256 wavelength-division and polarization-division-multiplexed channels at 42.7Gb/s (10.2Tb/s

BIBLIOGRAPHY

capacity) over 3x100km of TeraLight fiber,” in *Optical Fiber Communications Conference*, A. Sawchuk, ed., Vol. 70, paper FC5. (2002).

[Frignac, 2003] Y. Frignac “Contribution à l'ingénierie des systèmes de transmission terrestres sur fibre optique utilisant le multiplexage en longueur d'onde de canaux modulés au débit de 40 Gbit/s” Paris tech, (2003).

[Gallawa, 1991] R. L. Gallawa, I. C. Goyal, Y. Tu, and A. K. Ghatak, “Optical waveguide modes: an approximate solution using Galerkin's method with Hermite-Gauss basis functions”, *IEEE Journal of Quantum Electronics*, Vol. 27. (1991).

[Gloge, 1972] D. Gloge. “Optical Power Flow in Multimode Fibers”. *Bell System Technical Journal*, 51: 1767–1783. (1972)

[Gloge, 1973] D. Gloge and E. A. J. Marcatili. “Multimode Theory of Graded-Core Fibers”. *Bell System Technical Journal*, 52: 1563–1578. (1973).

[GoldBai, 1997] H. Meyr, M. Moeneclaey and S. Fechtel. *Digital communication receivers*, John Wiley & Sons, New York, vol. 1, 1990. (1997).

[Golub, 1982] M. A. Golub, A. M. Prokhorov, I. N. Sisakian and V. A. Soifer, "Synthesis of spatial filters for investigation of the transverse mode composition of coherent radiation," *Sov. J. Quantum Electron.* 12, 1208-1209 (1982).

[Goldfarb, 2007] G. Goldfarb and G. Li “Chromatic Dispersion Compensation Using Digital IIR Filtering With Coherent Detection”. *IEEE Photonics Technology Letters*, vol. 19, no. 13, pp. 969-971. (2007).

[Graham Bell, 1876] Graham, Bell Alexander. "Improvement in telegraphy." U.S. Patent No. 174,465. 7 Mar. (1876).

[Gross, 2014] S. Gross, B. R. Norris, N. Cvetojevic, N. Jovanovic, A. A. Martiarena, P. N. Stewart, J. S. Lawrence, M. J. Withford and P. G. Tuthill. “High performance 3D waveguide architecture for astronomical pupil-remapping interferometry”. *Proc. SPIE 9146, Optical and Infrared Interferometry IV*, 91461B. (2014).

[Gruner-Nielsen, 2012] L. Gruner-Nielsen, J. W. Nicholson, K. Jespersen, Y. Sun, R. Lingle, D. Jacobsen and B. Pálsdóttir. "Measuring distributed mode scattering in few mode fibers

BIBLIOGRAPHY

with high and low differential group delay" Proc. *IEEE Photon. Soc. Summer Topical Meeting* pp. 193-194 Jul (2012).

[Heck, 2013] M. J. R. Heck, J. F. Bauters, M. L. Davenport, J. K. Doylend, S. Jain, G. Kurczveil, S. Srinivasan, Y. Tang and J. E. Bowers. "Hybrid Silicon Photonic Integrated Circuit Technology," in *IEEE Journal of Selected Topics in Quantum Electronics*, vol. 19, no. 4, pp. 6100117-6100117, July-Aug. (2013).

[Ho, 2011] K. Ho, and J. Kahn. "Statistics of group delays in multimode fiber with strong mode coupling," *J. Lightw. Technol.*, vol. 29, no. 21, pp. 3119–3128. (2011).

[ISO/IEC 11801, 2011] ISO/IEC 11801 ed2.2 - Information technology - Generic cabling for customer premises (2011)

[IEC 60793-2-10, 2011] IEC 60793-2-10 Ed. 4.0: Optical fibres - Part 2-10: Product specifications – Sectional specification for category A1 multimode fibres (2011)

[Igarashi, 2014] K. Igarashi, T. Tsuritani, I. Morita, Y. Tsuchida, K. Maeda, M. Tadakuma, T. Saito, K. Watanabe, K. Imamura, R. Sugizaki and M. Suzuki. "Super-Nyquist-WDM transmission over 7,326-km seven-core fiber with capacity-distance product of 1.03 Exabit/s·km", *Opt. Express* 22, 1220-1228 (2014).

[Inan, 2012] B. Inan, S. L. Jansen, B. Spinnler, F. Ferreira, D. Borne, van den, M. Kuschnerov, A. Lobato, S. Adhikari, V. A. J. M. Sleiffer and N. Hanik. "DSP requirements for MIMO spatial multiplexed receivers". *IEEE Photonics Society Summer Topical Meeting Series*, Seattle, pp. 187-188. (2012).

[Inao, 1979] S. Inao, T. Sato, H. Hondo, M. Ogai, S. Sentsui, A. Otake, K. Yoshizaki, K. Ishihara and N. Uchida. "High density multicore-fiber cable," in Proc. *Int. Wire Cable Symp.*, pp. 370–384. (1979).

[Ismaeel, 2014] R. Ismaeel, T. Lee, B. Oduro, Y. Jung and G. Brambilla. "All-fiber fused directional coupler for highly efficient spatial mode conversion," *Opt. Express* 22, 11610-11619. (2014).

[ITU-T, 2009] ITU-T manual "optical fibers, cables and system" (2009).

BIBLIOGRAPHY

- [**Juarez, 2014**] A. A. Juarez, E. Krune, S. Warm, C. A. Bunge, and K. Petermann, "Modeling of Mode Coupling in Multimode Fibers With Respect to Bandwidth and Loss," *J. Lightwave Technol.* 32, 1549-1558 (2014)
- [**Jung, 2013**] Y. Jung, R. Chen, R. Ismaeel, G. Brambilla, S. U. Alam, I. P. Giles and D. J. Richardson. "Dual mode fused optical fiber couplers suitable for mode division multiplexed transmission" *Opt. Exp.* vol. 21 no. 20 pp. 24326-24331 (2013).
- [**Jung, 2014**] Y. Jung, Q. Kang, J. K. Sahu, B. Corbett, J. O'Callaghan, F. Poletti, S. U. Alam and D. J. Richardson. "Reconfigurable modal gain control of a few-mode EDFA supporting
- [**Jung, 2014**] Y. Jung, E. L. Lim, Q. Kang, T. C. May-Smith, N. H. L. Wong, R. Standish, F. Poletti, J. K. Sahu, S. U. Alam and D. J. Richardson. "Cladding pumped few-mode EDFA for mode division multiplexed transmission" *Opt. Exp.* vol. 22 no. 23 pp. 29008-29013 (2014).
- [**Kaiser, 2009**] T. Kaiser, D. Flamm, S. Schöter and M. Duparré. "Complete modal decomposition for optical fibers using CGH-based correlation filters" in *Optical Express* 17, 9347-9356 (2009).
- [**Kobayashi, 2013**] T. Kobayashi, H. Takara, A. Sano, T. Mizuno, H. Kawakami, Y. Miyamoto, K. Hiraga, Y. Abe, H. Ono and M. Wada. "2 × 344 Tb/s propagation-direction interleaved transmission over 1500-km MCF enhanced by multicarrier full electric-field digital back-propagation". *39th European Conference and Exhibition on Optical Communication*, London, 2013, pp. 1-3. (2013).
- [**Koonen, 2012**] A. M. J. Koonen, H. Chen, H. P. A. Van den Boom and O. Raz. "Silicon Photonic Integrated Mode Multiplexer and Demultiplexer" in *IEEE Photonics Technology Letters*, vol. 24, no. 21, pp. 1961-1964, Nov.1. (2012).
- [**Krummrich, 2011**] P. Krummrich. "Optical amplification and optical filter based signal processing for cost and energy efficient spatial multiplexing ", *Opt. Express* 19, 16636-16652. (2011).
- [**Lee, 2000**] K. Lee. "Mode coupling in tilted planar waveguide gratings," *Appl. Opt.* 39, 6144-6149 (2000).

BIBLIOGRAPHY

- [Lee, 2003] B. Lee. "Review of the present status of optical fiber sensors", *Optical Fiber Technology*, vol. 9, 57–79 (2003).
- [Leon-Saval, 2014] S. G. Leon-Saval, N. K. Fontaine, J. R. Salazar-Gil, B. Ercan, R. Ryf and J. Bland-Hawthorn. "Mode-selective photonic lanterns for space-division multiplexing," *Opt. Express* 22, 1036-1044 (2014).
- [Li, 2014] K. Nishiguchi, C. H. Li, A. Guzik and K. Kishida, "Synthetic spectrum approach for Brillouin optical time-domain reflectometry," *Sensors (Switzerland)*, 14 (3), pp. 4731-4754. (2014).
- [Liu, 1995] Y. Liu, B. M. A Rahman, Y. N. Ning and K. T. V. Grattan. "Accurate mode characterization of graded-index multimode fibers for the application of mode-noise analysis". *Appl. Opt.* 34 1540-1543. (1995).
- [Logie,1925] W. Raymer. "The silicom web: physics for the Internet Age", Taylor and Francis, New York (2009).
- [Ly-Gagnon, 2005] D. S. Ly-Gagnon, K. Katoh and K. Kikuchi. "Unrepeated 210-km transmission with coherent detection and digital signal processing of 20-Gb/s QPSK signals", *Optical Fiber Communication (OFC)*. (2005).
- [Masaki, 1978] Y. Masaaki. "Hypergeometric functions, modular interpretations of configuration spaces", *Aspects of mathematics*, vol. E32 (1978).
- [Marconi,1901] G. Marconi. "Apparatus for wireless telegraphy." U.S. Patent No. 676,332. 11 Jun (1901)
- [Marcuse, 1973] D. Marcuse. "Coupled mode theory of round optical fibers," *Bell System Technical Journal*, vol. 52, no. 6, pages 817-842 (1973).
- [Marcuse, 1976] D. Marcuse. "Curvature loss formula for optical fibers", in *J. Opt. Soc. Am.*, vol. 66 , no. 3, pages 216-220 (1976).
- [Marcuse, 1984] D. Marcuse. "Microdeformation losses of single-mode fibers," *Appl. Opt.* 23, 1082-1091 (1984).

BIBLIOGRAPHY

[**Marcuse, 1991**] D. Marcuse. "Single-channel operation in very long nonlinear fibers with optical amplifiers at zero dispersion." *Journal of lightwave technology*, vol. 9, no. 3, pages 356-361 (1991).

[**Maruyama 2014**] R. Maruyama, N. Kuwaki, S. Matsuo and M. Ohashi. "Two mode optical fibers with low and flattened differential modal delay suitable for WDM-MIMO combined system," *Opt. Express* 22, 14311-14321 (2014).

[**Maruyama, 2015**] R. Maruyama, N. Kuwaki, S. Matsuo and M. Ohashi. "Experimental investigation of relation between mode-coupling and fiber characteristics in few-mode fibers". In *Optical Fiber Communications Conference and Exhibition (OFC)*, IEEE, 2015. p. 1-3. (2015).

[**Mitra, 2001**] P. P. Mitra and J. B. Stark. " Nonlinear limits to the information capacity of optical fibre communications", *Nature*, vol. 411, pp. 1027–1030. (2001).

[**Mizuno, 2017**] T. Mizuno, K. Shibahara, T. Kobayashi and Y. Miyamoto. "High-capacity Dense Space Division Multiplexed Multicore Fiber Transmission", in *Photonic Networks and Devices*, pages NeTu2B-3. Optical Society of America, (2017).

[**Molin, 2010**] D. Molin, M. Bigot-Astruc, K. de Jongh and P. Sillard. "Trench-assisted bend-resistant OM4 multi-mode fibers" (2010) *European Conference on Optical Communication, ECOC*, 1-2, art. no. 5621099.(2010).

[**Molin, 2016**] D. Molin. *Next generation multimode fiber for high speed data networks with improved bend resistance and chromatic dispersion compensation*. PhD thesis, University of Lille 1, (2016).

[**Mori, 2014**] T. Mori, T. Sakamoto, M. Wada, T. Yamamoto and F. Yamamoto. "Few-mode fibers supporting more than two LP modes for mode-division-multiplexed transmission with MIMO DSP," *Journal of Lightwave Technology*, vol. 32, no 14, p. 2468-2479. (2014)

[**Morizur, 2015**] Morizur, J-F., J. Pu, B. Denolle, O. Pinel, N. Barré and Labroille, G. *Efficient and mode-selective spatial multiplexer based on multi-plane light conversion*. *Optical Fiber Communication Conf. and Exposition*, Los angeles, W1A.4 (2015)

BIBLIOGRAPHY

- [**Nakazawa, 2014**] Nakazawa M., Masato Y., and Toshihiko H. "Measurement of mode coupling distribution along a few-mode fiber using a synchronous multi-channel OTDR." *Optics express*, vol. 22, no. 25, pages 31299-31309, (2014).
- [**Nazarathy, 2013**] M. Nazarathy and A. Amos. "Doubling direct-detection data rate by polarization multiplexing of 16-QAM without a polarization controller." *Optical Communication (ECOC 2013), 39th European Conference and Exhibition on. IET*, (2013)
- [**Nguyen, 2012**] D. Nguyen, S. Blin, T. Nguyen, S. Le, L. Provino, M. Thual, and T. Chartier, "Modal decomposition technique for multimode fibers," *Appl. Opt.* **51**, 450-456 (2012).
- [**Nicholson, 2009**] J. W. Nicholson, A. D. Yablou, J. M. Fini and M. D. Mermelstein. "Measuring the modal content of large-mode-area fibers". *IEEE journal of selected topics in quantum electronics*, vol. 15, no 1, p. 61-70.(2009)
- [**Nicholson, 2013**] J. W. Nicholson, J. M Fini, X. Liu, A. DeSantolo, P. Westbrook, R. Windeler, E. Monberg, F. DiMarcello, C. Headley and D. Di-Giovanni. "Single-frequency pulse amplification in a higher-order mode fiber amplifier with fundamental-mode output". In *CLEO: Science and Innovations*. Optical Society of America, p. CW3M. 3.(2013)
- [**Olshansky, 1975**] R. Olshansky. "Mode coupling effects in graded-index optical fibers." *Appl. Opt.*, vol. 14, no. 4, pages 935-945, (1975).
- [**Olshansky, 1976**] Olshansky, R., and Donald B. "Pulse broadening in graded-index optical fibers." *Applied Optics*, vol. 15, no. 2, pages 483-491, (1976).
- [**Ono, 2015**] H. Ono, T. Hosokawa, K. Ichii, S. Matsuo and M. Yamada. "Improvement of differential modal gain in few-mode fibre amplifier by employing ringcore erbium-doped fibre, *Electron. Lett.*, vol. 51, no. 2, pp. 172–173. (2015).
- [**Otto, 2013**] C. Otto. "Dynamic of Quantum dot lasers, effects of optical feedback and external optical injection". *Technical university of Berlin, Germany, springer*. (2013).
- [**Pal, 1992**] B. P. Pal, R. L. Gallawa and I. C. Goyal. "LP/sub 11/-mode leakage loss in coated depressed clad fibers." *IEEE photonics technology letters*, vol. 4, no. 4, pages 376-378 (1992).
- [**Petterman, 1976**] K. Petermann. "Microbending loss in monomode fibres." *Electronics Letters*, vol. 12, no. 4, pages 107-109. (1976).

BIBLIOGRAPHY

[Phogat, 2013] A. Phogat, T. Gulati et D. Malik "Q-Factor and Jitter performance in WDM systems using RZ, NRZ and Duo binary modulation formats at different distances". *International Journal of Latest Trends in Engineering and Technology (IJLTET)*, Vol. 2 Issue 4, (2013).

[Poole, 1986] C. D. Poole and R. E. Wagner. "Phenomenological approach to polarisation dispersion in long single-mode fibres" *Electronics Letters*, vol. 22, no. 19, pages 1029-1030, (1986).

[Poole, 1988] C. D. Poole. "Statistical treatment of polarization dispersion in single-mode fiber", *Optics Letters*, vol. 13, no. 8, pages 687-689, (1988)

[Poole, 1991] C. D. Poole, J. H. Winters and J. A. Nagel. "Dynamical equation for polarization dispersion," *Optics Letters*, vol. 16-6, pp. 372-374. (1991)

[Puttnam, 2015] B. J. Puttnam, R. S. Luís, W. Klaus, J. Sakaguchi, J. M. D. Mendinueta, Y. Awaji, N. Wada, Y. Tamura, T. Hayashi and M. Hirano. "2.15 Pb/s transmission using a 22 core homogeneous single-mode multi-core fiber and wideband optical comb". In *Proc. European Conf. on Optical communication (ECOC)*, Valencia, Spain. (2015)

[Qian, 2004] X. Qian and A. C. Boucouvalas. "Propagation characteristics of single-mode optical fibers with arbitrary complex index profiles," *IEEE journal of quantum electronics*, vol. 40, no. 6, pages 771-777, (2004).

[Qian, 2011] D. Qian, M. F. Huang, E. Ip, Y. K. Huang, Y. Shao, J. g Hu and T. Wang. "101.7-Tb/s (370 x 294-Gb/s) PDM-128QAM-OFDM transmission over 3 x 55-km SSMF using pilot-based phase noise mitigation", *Optical Fiber Communication Conference (OFC)*. (2011).

[Richardson, 2013] D. J. Richardson, J. M. Fini and L. E. Nelson. "Space-division multiplexing in optical fibres" *Nature Photon.* vol. 7 pp. 354-362 Apr. (2013).

[Ryf, 2013] R. Ryf, S. Randel, N. K. Fontaine, M. Montoliu, E. Burrows, S. Chandrasekhar, A. H. Gnauck, C. Xie, R. J. Essiambre and P. Winzer. "32-bit/s/Hz spectral efficiency WDM transmission over 177-km few-mode fiber". In *Optical fiber communication conference*. Optical Society of America, p. PDP5A. 1.(2013).

BIBLIOGRAPHY

- [Ryf, 2014]** . Ryf, N. K. Fontaine, H. Chen, B. Guan, S. Randel, N. Sauer, S. J. B. Yoo, A. M. J. Koonen, R. Delbue, P. Pupalaikis, A. Sureka, R. Shubochkin, Y. Sun and R. Lingle. “23 Tbit/s transmission over 17-km conventional 50 um radedindex multimode fiber”, in *Optical Fiber Communication Conference/National Fiber Optic Engineers Conference*. (2014).
- [Sakamoto, 2013]** T. Sakamoto, T. Mori, T. Yamamoto and S. Tomita. “Differential Mode Delay Managed Transmission Line for WDM-MIMO System Using Multi-Step Index Fiber”, *Journal of Lightwave Technology*. 30(17), 2783–2787. (2013).
- [Sammut, 1976]** R. Sammut and A. W. Snyder. "Leaky modes on a dielectric waveguide: orthogonality and excitation." *Applied Optics* 15.4: 1040-1044. (1976).
- [Sano, 2012]** A. Sano, T. Kobayashi, S. Yamanaka, A. Matsuura, H. Kawakami, Y. Miyamoto, K. Ishihara and H. Masuda. “102.3-Tb/s (224 ×548-Gb/s) C- and extended L-band all-Raman transmission over 240 km using PDM-64QAM single carrier FDM with digital pilot tone”. In Proc. *Optical Fiber Communication Conf. and Exposition*, Los Angeles, CA, 4–8 March (2012).
- [Savory, 2010]** S. J. Savory, "Digital coherent optical receivers: Algorithms and subsystems." *IEEE Journal of Selected Topics in Quantum Electronics* 16.5: 1164-1179. (2010)
- [Schimpf, 2011]** D. N. Schimpf, R. A. Barankov, and S. Ramachandran, "Cross-correlated (C^2) imaging of fiber and waveguide modes," *Opt. Express* 19, 13008-13019. (2011).
- [Schulze, 2013]** C. Schulze, D. Flamm, M. Duparré, and A. Forbes, “Using spatial light modulators to measure laser beam quality”, *SPIE Newsroom*. DOI: 10.1117/2.1201304.004799. (2013).
- [Schulze, 2015]** C. Schulze, R. Brüning, S. Schröter, and M. Duparré. "Mode Coupling in Few-Mode Fibers Induced by Mechanical Stress," *J. Lightwave Technol.* 33, 4488-4496 (2015).
- [Sévigny, 2014]** B. Sévigny, G. Le Cocq, C. C. Castineiras Carrero, P. Sillard, C. Valentin, G. Bouwmans, L. Bigot, and Y. Quiquempois, "A novel take on the s 2 dataset modal analysis". In *Optical Communication (ECOC), European Conference on. IEEE*, 2014. p. 1-3. (2014)

BIBLIOGRAPHY

- [Sévigny, 2015] B. Sévigny, *Fibres à cristaux photoniques et generation d'ultraviolets par mélange à quatre ondes*, PhD thesis, University of Lille (2015)
- [Shannon, 1948] C. Shannon. " A mathematical theory of communication". *Tech. J.* vol. 27, p. 379–423. (1948).
- [Shemirani, 2009] M. B. Shemirani, W. Mao, R. A. Panicker, and J. M. Kahn, "Principal Modes in Graded-Index Multimode Fiber in Presence of Spatial- and Polarization-Mode Coupling", *J. Lightwave Technol.* 27, 1248-1261. (2009).
- [Sillard, 2011] P. Sillard, M. Astruc, D. Boivin, H. Maerten, and L. Provost, "Few mode fiber for uncoupled mode-division multiplexing transmissions," in *European Conference and Exposition on Optical Communications*, pp. Tu-5, Optical Society of America, 2011.
- [Sillard, 2014] P. Sillard, D. Molin, M. Bigot-Astruc, A. Amezcua-Correa, K. De Jongh, and F. Achten, DMGD-compensated links (2017) *Optics InfoBase Conference Papers*, Part F40-OFC 2017, 3 p. (2014).
- [Sillard, 2015] Sillard, P., Molin, D., Bigot-Astruc, M., Amezcua-Correa, A., De Jongh, K., Achten, F. "50 μ m multimode fibers for mode division multiplexing" . *European Conference on Optical Communication, ECOC*, 2015-November, art. no. 7341642, (2015).
- [Sillard, 2016] Sillard, P. "Few-Mode Fibers for Space Division Multiplexing", *Optical Fiber Communication conference, OFC'16*, Th1J.1. (2016).
- [Singh, 2001] H. Singh. *Photodetectors and Fiber Optics*, academic press. (2001).
- [Snyder, 1978] A. W. Snyder, and J. Love. *Optical Waveguide Theory*. Springer US. (1978).
- [Snyder, 1983] A. W. Snyder, and J. Love. *Optical Waveguide Theory*. Springer Science & Business Media. (1983).
- [Soares, 2011] F. M. Soares, N. K. Fontaine, R. P. Scott, J. H. Baek, X. Zhou, T. Su, S. Cheung, Y. Wang, C. Junesand, and S. Lourdudoss, "Monolithic InP 100-Channel \times 10-GHz Device for Optical Arbitrary Waveform Generation", in *IEEE Photonics Journal*, vol. 3, no. 6, pp. 975-985. (2011).

BIBLIOGRAPHY

- [**Soma, 2015**] D. Soma, K. Igarashi, Y. Wakayama, K. Takeshima, Y. Kawaguchi, N. Yoshikane, T. Tsuritani, I. Morita, and M. Suzuki, "2.05 Peta-bit/s super-nyquist-WDM SDM transmission using 9.8-km 6-mode 19-core fiber in full C band", *Optical Communication (ECOC), 2015 European Conference on*, Valencia, 2015, pp. 1-3. (2015).
- [**Stoltz, 1982**] B. Stoltz, and Y. David. "Calculated pulse responses of perturbed fiber profiles." *Applied optics*, vol. 21, no. 23, pp. 4235-4240. (1982).
- [**Tang, 2006**] J. Tang. "A Comparison Study of the Shannon Channel Capacity of Various Nonlinear Optical Fibers," *J. Lightw. Technol.*, vol. 24, no. 5, pp. 2070–2075. (2006)
- [**Takenaga, 2011**] K. Takenaga et al. "A large effective area multi-core fibre with an optimised cladding thickness, *37th European Conference and Exhibition on Optical Communication*", pp. 1-3. (2011).
- [**Tottori, 2012**] Y. Tottori, H. Tsuboya, and T. Kobayashi. "Low Loss Optical Connection Module for Seven-Core Multicore Fiber and Seven Single-Mode Fibers", in *IEEE Photonics Technology Letters*, vol. 24, no. 21, pp. 1926-1928. (2012).
- [**Tottori, 2014**] Y. Tottori, H. Tsuboya, and T. Kobayashi. "Multi functionality demonstration for multi core fiber fan-in/fan-out devices using free space optics", *OFC'14*, San Francisco, CA, USA. (2014).
- [**Thyagarajan, 1991**] K. Thyagarajan, S. Diggavi, A. Taneja, and A. K. Ghatak, "Simple numerical technique for the analysis of cylindrically symmetric refractive-index profile optical fibers". *Applied optics*, vol. 30, no 27, p. 3877-3879 (1991).
- [**Trinel, 2017**] J. B. Trinel, G. Le Cocq, Y. Quiquempois, E. R. Andresen, O. Vanvincq, and L. Bigot, "Theoretical study of gain-induced mode coupling and mode beating in few-mode optical fiber amplifiers," *Opt. Express*, vol. 25, pp. 2377-2390 (2017).
- [**Vengsarkar, 1996**] A. M. Vengsarkar, P. J. Lemaire, J. B. Judkins, V. Bhatia, T. Erdogan, and J. E. Sipe, "Long-period fiber gratings as band-rejection filters." *Journal of lightwave technology* 14.1: 58-65. (1996)
- [**van Uden, 2014**] R. van Uden, C. M. Okonkwo, H. Chen, H. de Waardt, and A. M. Koonen, "6×6 MIMO Frequency domain equalization of 28GBaud 128-SP-QAM Few-Mode Fiber Transmission", *Advanced Photonics for Communications*, paper SM2D.2. (2014).

BIBLIOGRAPHY

[Wang, 2014] J. Wang, and A. Willner. "Using orbital angular momentum modes for optical transmission" *Optical Fiber Communication Conference, W4J-5*, Optical Society of America, 2014.

[Weng, 2016] Y. Weng, T. Wang, and Z. Pan. " Optimization of mode-dependent gain efficiency based on intermodal Raman scattering for few-mode distributed Raman amplifier"; *CLEO San Jose*, CA, USA. 5–10. (2016).

[Widrow, 1985] B. Widrow, and S. Stearns, " Adaptive Signal Processing", Prentice Hall, Englewood Cliffs, NJ. (1985).

[Wu, 2012] C. Wu, Z. Liu, K. M. Chung, M. L. V. Tse, F. Y. M. Chan, A. P. T. Lau, C. Lu, and H. Y. Tam," Strong LP 01 and LP 11 mutual coupling conversion in a two-mode fiber Bragg grating " *IEEE Photon. J.* vol. 4 no. 4 pp. 1080-1086 Aug. (2012).

[Yun, 1996] S. Yun, H. In Kag, and Y. Byoung" All-fiber tunable filter and laser based on two-mode fiber." *Optics letters*, vol.21, no. 1, pp. 27-29. (1996).

[Zhao, 2015] J. Zhao, B. Li, M. Tang, S. Fu, D. Liu, P. P. Shum, and S. Liu, "Design and analysis of hole-assisted few mode fiber with ultra-low differential mode group delay (DMGD)," in *Asia Communications and Photonics Conference 2015*, pp. ASu2A-68, Optical Society of America. (2015).

[Zhang, 2013] Zhang,J.,Yu, J., Chi,N., Dong,Z., and Li,X. "Nonlinear compensation and crosstalk suppression for $4 \times 160.8\text{Gb/s}$ WDM PDM-QPSK signal with heterodyne detection," *Opt. Express* 21, 9230-9237. (2013)

[Zhu, 2011] B. Zhu, T. F. Taunay, M. Fishteyn, X. Liu, S. Chandrasekhar, M. F. Yan, J. M. Fini, E. M. Monberg, and F. V. Dimarcello,"112-Tb/s Space-division multiplexed DWDM transmission with 14-b/s/Hz aggregate spectral efficiency over a 76.8-km seven-core fiber", *Opt. Express* 19, 16665-16667. (2011)

[Zhi, 2003] W. Zhi, R. Guobin, L. Shuqin, and J. Shuisheng,"Loss properties due to Rayleigh scattering in different types of fiber". *Optics express*, 2003, vol. 11, no 1, p. 39-47.